A Leaky Waveguide All-Optical Analog-to-Digital Converter

A Thesis

Submitted to the Faculty

of

Drexel University

by

Xiaobo Hou

in partial fulfillment of the

requirements for the degree

of

Doctor of Philosophy

December 2004

DEDICATIONS

I would like to dedicate this work to my father Guoqing Hou, my mother Shuqing Huang, and my brother Xiaoshan Hou, for their continuous support, love and believe in me.

ACKNOWLEDGMENTS

I would like to thank Dr. Warren Rosen and Dr. Afshin Daryoush for their tireless motivation, continuous guidance, and neverending support of my work. I am also extremely grateful to Dr. Peter Zalud, Dr. Herschel Burstyn and Dr. Arye Rosen for their support to this project.

I very much appreciate Dr. Peter Herczfeld and Dr. Bahram Nabet for their help in my research, Dr. El Sherif for providing the facilities of his photonic laboratory.

Many thanks to my friends Ms. Cuiping Zhang, Ms. Xia Zhao, Mr. Liming Zhou, Dr. Mohammad-Reza Tafighi, Dr. Yifei Li, Dr. Samuel Goldresser, Mr. Eric Gallo for the helpful discussions.

I would also to thank many of my friends for their continuous support and friendship. I would specially thank Mr. Chunlong Hu for his support, care and encourage.

Table of Contents

List of Tables

List of Figures

Abstract

An Ultra High-Speed Spatial Sampling All-Optical Analog-to-Digital Converter

Xiaobo Hou

Warren A. Rosen, Ph.D. Afshin S. Daryoush, Ph.D.

In this thesis we describe a novel all-optical analog-to-digital converter (AOADC) based on a leaky waveguide deflector. The principle of the spatial sampling AOADC is to convert an electrical signal to its corresponding optical deflection angle and then sample and quantize this angle in the spatial domain, instead of the amplitude domain. This AOADC is designed for broadband digital receivers working at frequencies above 20 GHz (a minimum 40 GS/s sampling rate) and provides a resolution higher than 6 bits. An original design based on GRISM (Grating and pRISM) is investigated for a high-resolution ADC implementation; and its challenges have been identified. The investigation provides a general model of spatial sampling AOADCs and highlights their advantages of immunity to optical intensity fluctuation. Later we proposed an AOADC that employs a leaky waveguide structure that is different from any other optical ADC. The AOADC consists of a sampler based on a mode-locked laser and a leaky waveguide deflector driven by traveling wave electrodes, a quantizer based on an integrated optical collector array and broadband photodetectors. These components provide the AOADC with a higher deflection angle and angular resolution resulting in high bit resolution without consuming significant power. The quantization of the deflection angle is done by a simple spatial quantizer that digitizes as well as encodes the signal simultaneously. A detailed design of the E-O deflector and the spatial quantizer has been analyzed and simulated; and some preliminary tests have been conducted. This thesis summarizes our contributions in designing and modeling this novel spatial sampling AOADC.

1. Introduction

1.1 Introduction

The majority of signals encountered in nature are continuous in both time and amplitude. The analog-to-digital converter (ADC) converts analog signals to discrete time digitally-coded form for digital processing and transmission. An A-to-D converter is usually located at the very end of an analog chain in a receiver and deals with the baseband signals as shown in Figure 1-1. Usually analog-to-digital conversion includes two major processes: sampling and quantization, as shown in the sub-block in the figure. The extracted baseband signal is sampled and held at discrete time intervals, then approximated as discrete amplitude levels and represented in a digital code. Associated with these two processes, two fundamental measures are used to characterize an ADC's performance, sampling rate and quantization resolution. Sampling theory states that a band-limited signal with bandwidth of B can be uniquely represented by sampling the signal at a rate of $f_s \geq 2B$ samples/s. The minimum rate $f_N = 2B$ samples/s is called the Nyquist rate, and ADCs sampling at speed near the Nyquist rate are called Nyquist-rate converters. It is clear that the wider the analog signal bandwidth, the higher the sampling rate that is required.

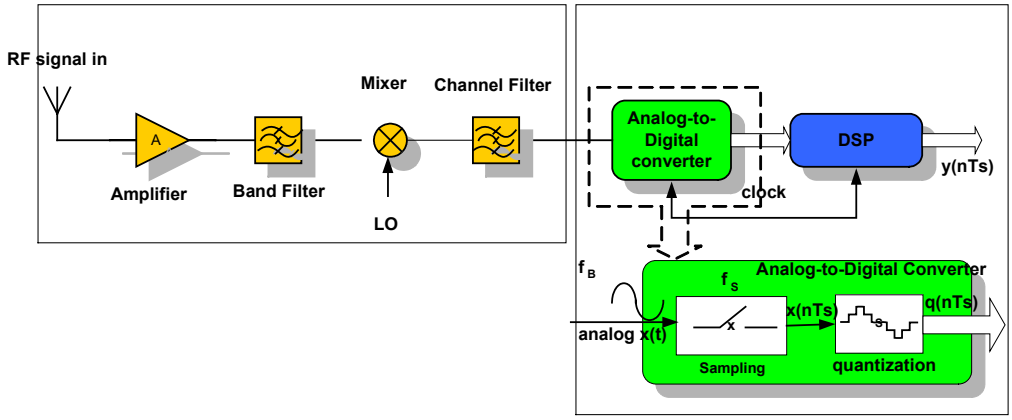

Figure 1-1: Basic system diagram of a conventional digital receiver.

ADCs are widely used in numerous applications. Figure 1-2 shows several examples in terms of sampling rate and resolution. Consumer products, such as high-fidelity audio and image processing, require very high resolution, while advanced radar systems and satellite communications with ultra-wide-bandwidth require sampling rates above 1 GHz.

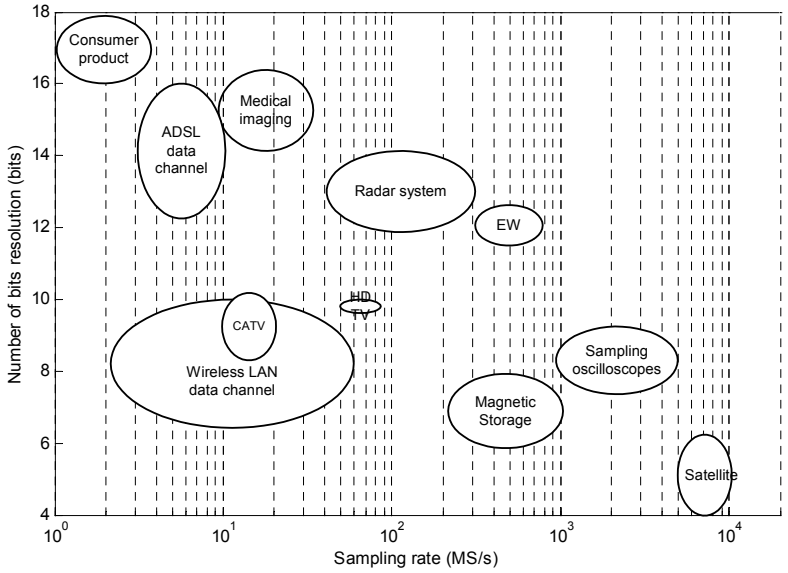

Figure 1-2: Applications and their performance requirement. [1]

As the spectrum becomes crowded, the need for operation at higher frequencies increases. Not only is the carrier frequency increasing, the baseband has increased to GHz to accommodate more information. For example, UWB (ultra wideband) technology operating from 3.1 GHz up to 10.6 GHz emerged as a new standard of wireless products whose bandwidth is greater than 20% of the center frequency, or at least 500 MHz [2]. Advanced radar, surveillance, and intelligence systems, which demand even higher frequency and wider bandwidth, would benefit significantly from high resolution ADCs having broad bandwidths.

In contrast to conventional digital receivers that perform RF signal amplification, conditioning and channelization in the analog domain as shown in Figure 1-1, an emerging trend is to directly process the raw signal at the front end rather than converting the RF signal to baseband. This concept will benefit a receiver system by eliminating complicated analog parts and providing protocol flexibility. In conventional receivers hardware is usually dedicated to a specific standard characterized by carrier frequency, bandwidth, and modulation. As a consequence, we are not able to build a single 'universal' terminal to accommodate diverse standards and get 'universal' services based on conventional technology. As more powerful digital signal processors (DSPs) become available, performing direct down-conversion as well as channelization and demodulation in the digital domain by reconfiguring DSP software becomes possible. In the ultimate digital receiver, the ADC will be pushed closer to the front end, right after the antenna and RF amplifier. Dealing with the raw analog signal at carrier frequencies, the receiver

will require a very high-sampling rate. If the Nyquist band of the ADC is wide enough to cover the whole frequency band from the antenna, all operations could be performed entirely in the digital domain by the powerful DSP. This concept is often referred to as a "software radio," which is able to adapt to various radio environments dynamically and more reliably, flexibly and robustly; any future changes due to new protocols or upgrades can be easily carried out by modifying the software [4]. This is especially useful for other applications such as antenna arrays or digital beamforming systems, which contain a large number of elements.

1.2 Motivation of the all-optical ADC

Currently there are 3 candidates for high sampling rate ADCs: electronic, optical, and superconductor ADCs. Conventional electronic ADCs are successful in relatively low frequency applications. A large effort has been made to improve their performance to accommodate high frequency applications. However, limited by time jitter and comparator ambiguity of the electronic devices in the high frequency region, electronic ADCs are difficult to push beyond 10 GS/s, and so electronic ADCs have failed to keep pace with rapidly evolving digital integrated circuit and digital signal processing (DSP) technologies. On average electronic ADCs improve by only 1.5 bits in resolution every 8 years [5]; and electronic ADCs have been a major bottleneck for emerging broadband applications. In theory, superconductor ADCs can dramatically reduce many kind of noise and achieve very high speed [7], but the ultra-low temperature requirement has been a major drawback from the very beginning. Therefore, superconductor based ADCs find applications only in specialized systems. To break this bottleneck, optical ADCs have gained more and more attention in recent years.

Optical analog-to-digital converters (OADCs) have long intrigued researchers because of their high sampling rate and potential for high resolution. Taylor [6] designed the first AOADC as early as 1975. Although Taylor's AOADC has never been applied to any real applications because of its complexity and limited resolution, it opened a new avenue to achieve ultra-high sampling rates in the optical domain. Since then, various AOADC structures have been proposed to improve performance and feasibility.

Optical ADCs surpass their electronic counterparts in their superb high-speed capability, and they are superior to the superconductor ADCs in terms of feasibility. However all-optical ADCs also face great challenges. Existing all-optical ADCs are generally limited in resolution to a few bits of resolution. Some researchers have proposed hybrid optical ADCs that combine optical sampling and electronic quantization techniques. On the other hand, more all-optical schemes have been developed to take advantage of simplicity and low power consumption.

After a comprehensive review of state-of-the-art AOADCs, it becomes apparent that few of these devices could be feasibly realized to achieve their claimed performance. Furthermore, most of the AOADC schemes that have been demonstrated work in the amplitude domain, i.e., the input analog signal is modulated onto the intensity of the optical sampling pulses. Amplitude-domain AOADCs suffer from intensity fluctuations of the optical signal and uneven power splitting from bit to bit. In this work we propose a novel AOADC working in the spatial domain based on an electro-optic (E-O) leaky

waveguide deflector. The principle of the proposed AOADC is to convert the amplitude of the electrical analog signal into a corresponding angular displacement of an optical beam. Figure 1-3 depicts the general configuration of a spatial-domain AOADC. Pulses from a mode-locked laser are sent to an optical deflector, which deflects the pulses through an angle θ that is proportional to the magnitude of the signal to be digitized. A spatial coder employing an optical collector array connected to remote photodetectors is then used to quantize the deflection, and hence the signal to be digitized. The E-O deflector in our device is implemented using a leaky waveguide driven by traveling wave electrodes, which I propose in the thesis. The AOADC offers several unique advantages:

- It provides immunity from optical power fluctuations.
- The traveling wave scheme is inherently broadband.
- It improves resolution by eliminating channelization mismatch.
- Any digital code may be easily generated by the spatial quantizer/encoder.
- It requires low driving voltage and consumes less power

This novel AOADC has potential to be able to work at 40 GS/s with a minimum of 6 bits of resolution. The thesis will discuss its operation, design and implementation in detail.

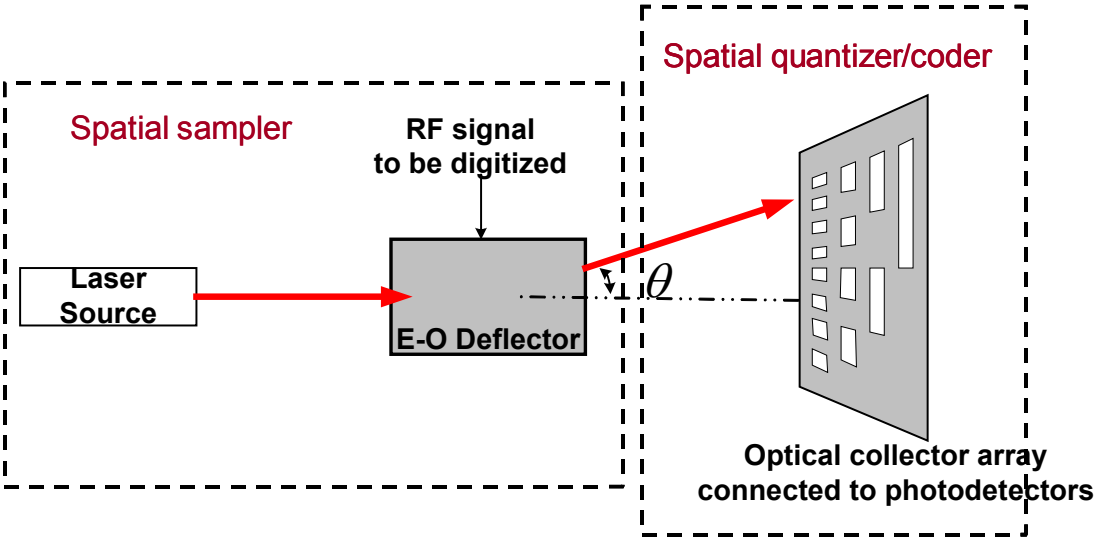

Figure 1-3: Conceptual system diagram of a general spatial-domain AOADC.

1.3 Overview of the project and contributions of the thesis

The main objective of this research effort has been to develop a feasible, low cost, high resolution, high-sampling rate all-optical ADC for broadband receiver applications. The original design [8, 9] used an electro-optically steerable diffraction grating that diffracts light into angles according to the applied electrical signal voltage. Taking advantage of high diffraction orders, the steerable angle could be fairly large and hence enable a high resolution spatial-domain AOADC. However our later study indicated that this structure encountered two major problems. First, the diffracted light losses its pulse shape, because the grating splits the multi wavelength light into different directions and breaks the short optical pulse condition. Second, its bandwidth is limited by the capacitance, which is proportional to the size of the grating. The original design with detailed implementations and solutions are attached as Appendix A at the end of the thesis.

The research on how to solve the two problems led to an improved design employing a leaky waveguide deflector [10,11]. The new design combined a leaky strip waveguide and traveling electrodes as a spatial sampler. To my knowledge, this structure has never been demonstrated previously. In this design the leaky wave of all wavelengths leaks in the same direction and so the mode-locked condition obtains, ensuring that the leaky wave is still pulsed. Thus it solves the first problem. At the same time because of its waveguide structure, traveling wave electrodes can be driven by high frequency signals, solving the second problem. Moreover, the overall size and power dissipation can be significantly reduced as well.

In this thesis we have made several important contributions. First, this thesis and investigates the spatial sampling AOADC at the system level. Key design issues, modeling, and enabling components have been identified. The research was focused on the two components that are not currently available: the E-O steerable component and the spatial quantizer.

Second, we propose and analyze a novel high-frequency optical deflector based on a leaky waveguide and traveling electrodes. This structure is capable of operating above 20 GHz (40 GS/s) and quantization of at least 6-bits of resolution. Because of the small size of the waveguide, the driving voltage is 1~2 orders-of-magnitude lower than conventional prism-based E-O deflectors. Simulations of deflection capability, angular resolution and leaky coefficient have been performed. Different implementations,

including $LiNbO_3$ waveguide with strip line electrodes, polymer waveguide with strip line electrodes and $LiNbO_3$ waveguide with coplanar electrodes, are proposed and compared.

Third, we develop an approximate model for the strip waveguide leaky coefficient analysis and give a simple analytical expression. The expression provides clear insight for understanding the behavior of the leaky waveguide and clearly shows the factors that determine the leaky coefficient. My theoretical analysis of the strip leaky waveguide provides a detailed guideline of how to design the spatial domain AOADC.

Fourth, we investigate a simple and efficient optical collector array as a spatial quantizer and encoder. The collector apertures are arranged in a binary fashion and able to generate any code easily. When an optical beam moves across these apertures, the optical power intensity signal collected is a parallel *n*-bit encoded optical digital signal. The static characteristics of the collector were investigated experimentally. This study also provided a possible implementation using integrated arrayed waveguide technology.

The combination of these contributions results in a successful analysis and design of the high-speed AOADC. The thesis discusses its novelty and issues in detail.

1.4 Outline of the thesis

In Chapter 2, the basic general issues of A-to-D converters are described and a comprehensive literature review of electronic and optical ADCs is provided. We start by introducing the two key performance measures of ADCs: sampling rate and resolution.

The following section summarizes general limitations of analog-to-digital converters and shows the trade-off between sampling rate and resolution. We reviewed electronic ADCs and indicate that poor electronic sampling timing jitter and device speed limit the performance of electronic ADCs. Then we provide a summary of state-of-the-art of hybrid optical and all-optical ADCs. We show the advantages of optical ADCs by comparing them with their electronic counterparts. The limitations of existing optical ADCs are summarized as a critique of the existing techniques. we conclude the chapter by outlining goals for this thesis.

The system-level design of a spatial domain AOADC is introduced at the beginning of Chapter 3. We provide the general concerns of designing a spatial-domain AOADC. Its advantages of immunity from intensity fluctuation are verified by a theoretical derivation of its error probability. Then four enabling components, mode-locked laser (MLL), E-O deflector, optical collector array, and photodetectors, are identified. Among them, the deflector and collector array need to be designed. For the E-O deflector, we present the original design of the E-O steerable grating using a GRISM (Grating and Prism) and indicate its advantages, drawbacks and possible solutions. Then we introduce the leaky waveguide E-O deflector with a brief description of its principles of operation.

The proposed E-O leaky waveguide deflector, one of the major contributions of my thesis, is described in detail in Chapter 4. In this design the effective refractive index of the propagation mode in the waveguide is modulated by the voltage applied to traveling wave electrodes. In the presence of a high index superstrate, part of the optical power

leaks out towards a unique direction corresponding to the index change in the waveguide. The design shows the advantages of high speed, low mismatch, easy encoding, low driving voltage and low power dissipation. We have determined the resolution of the AOADC by deriving the total steering angle and minimum resolvable angle of the E-O deflector. we have analyzed an *x*-cut $LiNbO_3$ leaky waveguide, the simplest implementation, and show its high-resolution capability. An electrical performance study of the *x*-cut $LiNbO_3$ leaky waveguide shows that it is difficult to achieve velocity match between the RF and optical signals. Therefore two other structures have been proposed to obtain 20 GHz of bandwidth and more than 6 bits of resolution. At the end of Chapter 4 we summarize the design tradeoffs of the E-O leaky waveguide deflector.

Chapter 5 focuses on the design, simulation, and implementation of the two possible realizations of a steerable deflector based on the concept of a leaky wave waveguide as introduced in Chapter 4: a polymer stripline structure and a *z*-cut Ti:$LiNbO_3$ coplanar structure. A comprehensive analysis is presented beginning with a leaky wave slab model and simulations of a $LiNbO_3$ slab leaky waveguide. We have developed an approximate model of a general leaky strip waveguide to provide a physical understanding of the factors that affect the leaky coefficient. The following sections show the simulations of the 2 structures in terms of leaky coefficient, deflection angle and bandwidth of the traveling wave electrodes. We conclude the chapter by comparing these two different structures.

In Chapter 6, we present other key components, including the new spatial quantizer/coder, MLL and photodetectors. We analyze the performance of the optical collector and verify it experimentally using a static experiment. Then we describe the available components, MLL and photodetectors, in terms of their function, requirement, the state-of-the-art and availability.

Finally, Chapter 7 summarizes the contributions of the thesis and gives a detailed design guideline for the proposed AOADC. At the end of the chapter, we provide recommendations to build the leaky waveguide deflector AOADC and to further enhance its performance.

2. Review of Literature

In this chapter we first introduce basic requirements and constraints for designing analog-to-digital converters and use them as a basis for the following discussion. Secondly, we review existing electronic and optical ADCs, which are further divided into hybrid and all-optical ADCs. We compare them in terms of advantages and disadvantages.

2.1 Performance measures

ADCs are a critical component in systems such as digital receivers, as their performance has great impact on the system bandwidth, accuracy and signal-to-noise-ratio (SNR). Despite the diversity of ADCs, their overall performance can be characterized by a relatively small number of parameters.

2.1.1 Sampling rate

In any A-to-D conversion, a periodic impulse train, either electrical or optical, samples a continuous time signal at regular intervals to obtain a discrete-time signal. According to Nyquist's theorem, the sampling rate has to be equal to or greater than twice the bandwidth of the analog signal to recover the signal from the discrete-time signal. This minimum sampling rate is called the Nyquist rate. To process signals with larger bandwidth the ADCs must have higher sampling rates.

Another parameter, conversion rate, describes the speed of the ADC from a different aspect. Conversion rate, which is in units of conversions/second, specifies how fast a final digitized code is generated by an ADC. In Nyquist-rate ADCs this parameter is identical to sampling rate, while in subsampling and oversampling ADCs where the code is based on multiple samples, the conversion rate is a fraction of the sampling rate.

2.1.2 Resolution

The sampled signal is discrete in time and must be quantized in amplitude. Usually the full-scale voltage is divided into 2^b quantization levels, where b is the number of bits of resolution in the ADC. b is also called the stated resolution, which is the physical number of output bits. A more accurate measure of the resolution is "effective bit number," which refers to the actual dynamic range, or the noise performance of the converter. For high-speed applications SNR (Signal-to-Noise Ratio) and SFDR (Spurious-Free Dynamic Range) provide more accurate measures of dynamic performance of ADCs.

2.1.3 SNR effective bit resolution

In an ideal ADC, the only noise is caused by quantization, which chops the initial analog signal into samples of finite precision and therefore loses information. Figure 2-1 shows a sinusoidal wave and its digital representation by a 3-bit (8-level) quantizer.

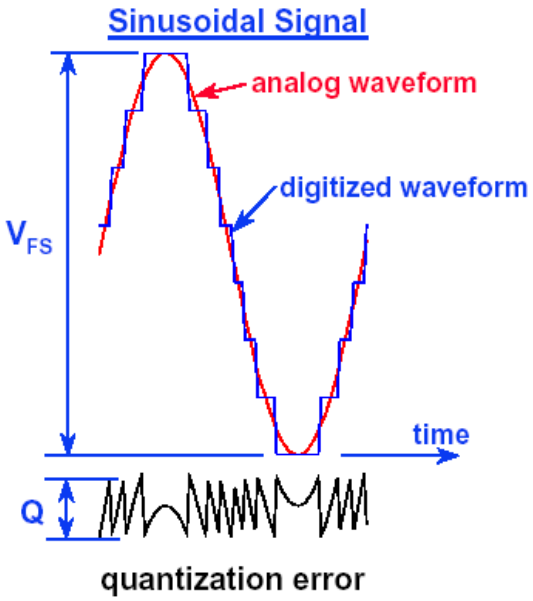

Figure 2-1: Example of quantization noise for a sinusoidal signal. V_{FS} is the full-scale voltage and Q is the size of quantization level.

Quantization noise is defined as the difference between the analog signal and its digitized amplitude level. In an ideal A-to-D converter, the error associated with this quantization process is within ± ½Q range, where Q is the smallest quantizing step. To reduce the quantization noise, a high-resolution converter requires an extremely accurate quantizer. For instance, given a full-scale of 1V, the LSB (Least Significant Bit) of an 8-bit A-to-D converter is 16 mV, while for 16-bit and 24-bit A-to-D converters; it is 15.3 µV and 59.6 nV, respectively.

Signal-to-quantization noise ratio (SQNR) is the SNR with the presence of only quantization noise. To compute a closed-form analytic solution for the SQNR, the input to the ADC is assumed to be a sinusoidal signal $x(t)=A\cos(\omega_0 t+\phi)$. The full-scale voltage

is divided into $M=2^b$ uniform levels, and the amplitude can be expressed $A=½MQ$. The input signal power can be represented as the variance of the input signal:

$$\sigma_x^{\,2} = \frac{A^2}{2} = \frac{(\frac{1}{2}MQ)^2}{2} = \frac{Q^2}{8}\cdot 2^{2b}. \qquad (2\text{-}1)$$

The variance of quantization error, which is the quantization noise power, is:

$$\sigma_q^{\,2} = \int_{-Q/2}^{Q/2} \frac{1}{Q} e^2 de = \frac{Q^2}{12}. \qquad (2\text{-}2)$$

The SQNR is, therefore:

$$SQNR = \frac{\sigma_x^{\,2}}{\sigma_q^{\,2}} = 3\cdot 2^{2b-1} \quad \text{or } SQNR(dB) = 6.02b+1.76\,. \qquad (2\text{-}3)$$

Equation (2-3) shows that by increasing the resolution by1 bit, the SQNR is improved by about 6 dB.

In the real world there are many other noise sources degrading the SNR performance of an ADC. All the additional errors can be modeled as additive white noise and counted as equivalent quantization noise when evaluating the SNR. The actual resolution, as a function of SNR, can be expressed as effective number of bits:

$$b_{eff} = \frac{SNR(dB)-1.76}{6.02}. \qquad (2\text{-}4)$$

Obviously the SNR is always lower than SQNR, and therefore the effective bit number is less than the claimed bit number. The SNR effective bit number is one of the most important specifications of an ADC.

2.1.4 Spurious-free dynamic range (SFDR) effective bit resolution

Spurious-free dynamic range (SFDR) is a nonlinear measure defined as the ratio of a single-tone signal amplitude to the largest harmonic component within the frequency band of interest. It is usually expressed in dBc. SFDR describes the ability of an ADC to convert high frequency signals without adding distortion. In communication applications, it quantifies the separation of channels in a digital receiver. Figure 2-2 shows the difference between SNR and SFRD. Usually, the SFDR is less than SNR and degrades the performance at a specific frequency. The SFRD effective bit number is given as:

$$b_{eff} = \frac{SFDR(dBc)}{6.02}. \qquad (2\text{-}5)$$

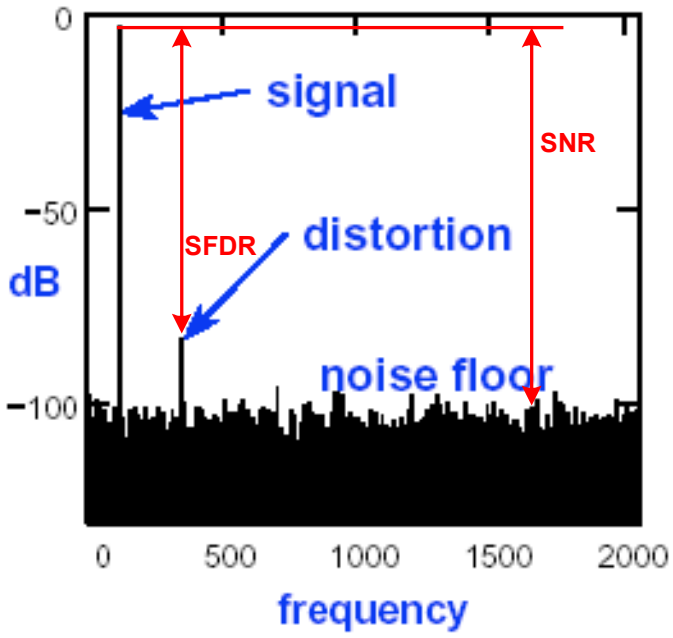

Figure 2-2: Typical SNR and SFDR represented in the frequency domain.

2.1.5 Resolution-sampling-rate-product

ADCs' sampling rates extend from DC to GHz, while resolution can be a few bits to more than 20 bits. Resolution-sampling-rate-product is one of the parameters to evaluate the overall performance. The resolution-sampling-rate-product is defined as:

$P = 2^{b_{eff}} \times f_{samp}$, where b_{eff} is the effective SNR bit number [5]. The product clearly shows a common tradeoff between bandwidth and dynamic range of any electronic component.

In any system or component, power is a very important parameter to evaluate efficiency. In terms of the power dissipation, P_{diss}, a figure of merit [5] of overall performance is given as:

$$F = \frac{2^{b_{eff}} \times f_{samp}}{P_{diss}}. \qquad (2\text{-}6)$$

Any ADC design has to compromise between the bandwidth, the dynamic range and the power dissipation.

2.2 Performance limitations

Increasing the resolution bit number can reduce quantization noise arbitrarily but it is noise from various internal and external sources that sets the noise floor of an ADC. To fully utilize the available SNR, usually the quantization step is chosen so that the quantization noise is equal to total noise level. In the following sections, we discuss four major factors limiting the maximum achievable bit number. The design criteria we derive in these sections can be applied to both electronic and optic ADCs.

2.2.1 Thermal noise

A variety of noise sources contribute to the noise level at the input of an ADC, including thermal noise, shot noise, 1/f noise and input referred noise. All of them can be modeled as a noise generated by an equivalent thermal resistor R_{eff}. The noise level can be calculated by integrating the noise density spectrum over the full Nyquist band $f_{samp}/2$. It is given as:

$$\sigma^2{}_{thermal} = 4kTR_{eff} f_{samp} / 2 . \qquad (2\text{-}7)$$

Where k is Boltzmann's constant, $1.38 \times 10\text{-}23$ J/K; T is the temperature in Kelvin, and R_{eff} is an effective thermal resistance that lumps together the effects of all noise sources. If an ADC's quantization noise is below the noise floor, its LSB is meaningless. By equating the thermal noise and an equivalent quantization noise, $\sigma^2{}_{thermal} = \sigma^2{}_q$, where $\sigma_q{}^2 = \frac{Q^2}{12} = \frac{1}{12} V_{FS}{}^2 2^{-2b_{thermal}}$, the maximum achievable bit number is given as:

$$B_{thermal} = \log_2 (\frac{V_{FS}^2}{6kTR_{eff} f_{samp}})^{1/2} - 1 , \qquad (2\text{-}8)$$

where V_{FS} is the full scale voltage quantized by the ADC. Equation (2-8) shows that the thermal noise-limited effective bit number is inversely proportional to $1/f^{1/2}$, therefore a trade-off between sampling rate and resolution must be made.

2.2.2 Aperture jitter

Jitter noise comes from uncertainty in sampling time and interval, which vary from sample to sample. The time jitter is caused by phase noise on the sampling clock or phase noise in the input signal. The standard deviation of the timing offset Δt is called aperture

jitter, or timing jitter, expressed as τ_a. As shown in Figure 2-3, timing jitter introduces sample error in amplitude. If the input is a sinusoidal signal, then the error is:

$$\Delta V = A\sin[2\pi f_x(t+\Delta t)] - A\sin\{2\pi f_x t) \approx 2\pi f_x \Delta t \cos(2\pi f_x t). \quad (2\text{-}9)$$

Under the assumption that the timing jitter is an uncorrelated Gaussian random process, the power of the error signal is the standard deviation of ΔV, which is

$$\sigma^2{}_{jitter} = \frac{V_{FS}{}^2}{2}(2\pi f_{samp}\cdot\tau_a)^2, \quad (2\text{-}10)$$

where $V_{FS}=2A$, is the full-scale signal amplitude.

Equaling the error induced by timing jitter to the equivalent quantization noise, the achievable bit number is limited by

$$B_{aperture} = log_2(\frac{2}{\sqrt{3}\pi f_{sample}\tau_a}) - 1. \quad (2\text{-}11)$$

Equation (2-11) is very similar to (2-8), except that now the bit number, $B_{aperture}$, drops at a greater rate of $1/f_{sample}$ as the sampling rate increases, so the aperture jitter noise dominates the SNR over the thermal noise at high frequencies.

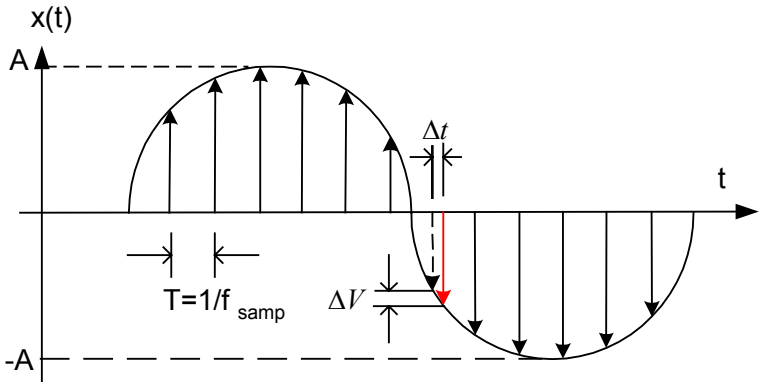

Figure 2-3: Model for sampling jitter. The red pulse indicates the position of an ideal pulse. The figure shows an offset of Δt and corresponding error of ΔV.

2.2.3 Comparator ambiguity

Usually quantization is performed by comparing the analog input to certain references. A simplified conceptual model divides the quantizer into a comparator and logic circuits. The comparator is primarily an amplifier and a regenerator. In a signal acquisition state, the voltage difference between the analog and reference input is amplified by gain *A*. Upon receipt of a latch command the regenerator disconnects its output from the input and multiplies the signal by a growing exponential, $e^{t/\tau}$, until saturation is reached. At a sufficient time after latch the comparator output signal becomes and remains a digital '1' or '0'. However if the growing time is not sufficient, the latched signal may fall in the neighborhood of the threshold value and the logic circuits following the comparator cannot distinguish unambiguously, causing ambiguity errors. The indecision probability, and hence the error power density, is determined by the variation of the input and the regeneration time, i.e., the speed of the comparator.

Assuming the minimum difference that the logic circuits can discriminate unambiguously is $\pm V_L$ and the gain of the comparator is *A*, the input within $+V_L/A \sim -V_L/A$ around threshold will result in indecisive output. Assuming the input signal is uniformly distributed and the quantization step is *Q*, the probability that signal falls into this region is:

$$P_i = \frac{2V_L}{AQ}. \qquad (2\text{-}12)$$

The gain is a time variant value, $A=A_0 \times e^{t/\tau}$ ($t \geq 0$). The indecisive probability of a single comparator is:

$$P_i = \frac{2V_L}{A_0 Q} e^{-t/\tau} \text{. [12]} \qquad (2\text{-}13)$$

In an ideal case, τ equals 0, implying an infinitely fast comparator, so the logic circuit can determine the binary value without any ambiguity. τ is a device parameter; it can be estimated by: $\tau \approx \frac{1}{2\pi f_T}$, where f_T is the unit current gain of the transistor in the comparator, determined by transistor technology and interconnection capacitance. It is a common practice to use a set of experimental values: amplification, regeneration time, and addictive noise degradation, to estimate the effective bit number limitation due to ambiguity error [12]:

$$B_{ambiguity} = \frac{\pi f_T}{6.93 f_{sample}} - 1.1. \qquad (2\text{-}14)$$

Again, the number of effective bits is inversely proportional to the sampling rate. Therefore at high frequencies comparator ambiguity is the dominant in resolution limitation.

2.2.4 Heisenberg uncertainty

The three factors discussed above strongly depend on currently available technologies. Adopting new technologies and approaches may improve the performance of ADCs, unless a physical limitation is reached. Ultimately, the resolution-sampling rate product is limited by Heisenberg uncertainty. The Heisenberg uncertainty principle states that energy and time cannot be measured with infinite precision at the same time, i.e.

$\Delta E \cdot \Delta t \geq \hbar/2$, where ΔE is the uncertainty in energy, which for an ADC is the smallest resolvable energy, equivalent to *0.5 LSB*; Δt is 0.5 sampling period *(T/2),* and $\hbar = \frac{h}{2\pi} = 1.0546 \times 10^{-34}$ *J-s* (h is Planck's constant).

Assuming the input resistance is R, ΔE is calculated as

$$\Delta E = \frac{(\frac{1}{2} LSB)^2}{R} \cdot \frac{T}{2} = \frac{(V_{FS}/2^b)^2}{4R} \cdot \frac{1}{2 f_{samp}}. \quad (2\text{-}15)$$

Therefore Heisenberg's uncertainty principle is written as

$$\Delta E \cdot \Delta t \geq \frac{1}{R}\left(\frac{V_{FS} 2^{-b}}{4 f_{samp}}\right)^2 \geq \frac{\hbar}{2}, \quad (2\text{-}16)$$

so the resolution-sampling rate product can be evaluated by

$$2^b f_{samp} \leq \frac{V_{FS}/4}{\sqrt{\hbar R/2}} = 4.86 \times 10^{15} \quad \text{(Assuming } V_{FS}\text{=1V and R=50 } \Omega\text{)}, \quad (2\text{-}17)$$

which is 3-4 orders-of-magnitude higher than the current state of the art. For example, theoretically a 12-bit ADC can be used with a sampling rate at 850 GS/s [5].

2.2.5 Summary of limitation factors

Figure 2-4 shows the maximum bit resolution achievable under some typical conditions of thermal noise, aperture jitter and comparator ambiguity. The resolution decreases as the sampling rate increases. It should be noted that in the low frequency region, the resolution of ADCs are limited by the equivalent thermal noise, e.g., a ~1KΩ resistor limits the resolution to 16 bits at a sampling rate 2 MS/s. Aperture jitter, in the range of 0.5 ps to 2 ps, limits SNR for the sampling frequency range of ~2Ms/s to 4 Gs/s.

Broadband ADCs above 4 Gs/s are limited by comparator ambiguity with f_T>50GHz. For example, if the sampling rate is 40 GS/s, using a comparator with f_T=250 GHz the resolution is limited to only 2 bits [5].

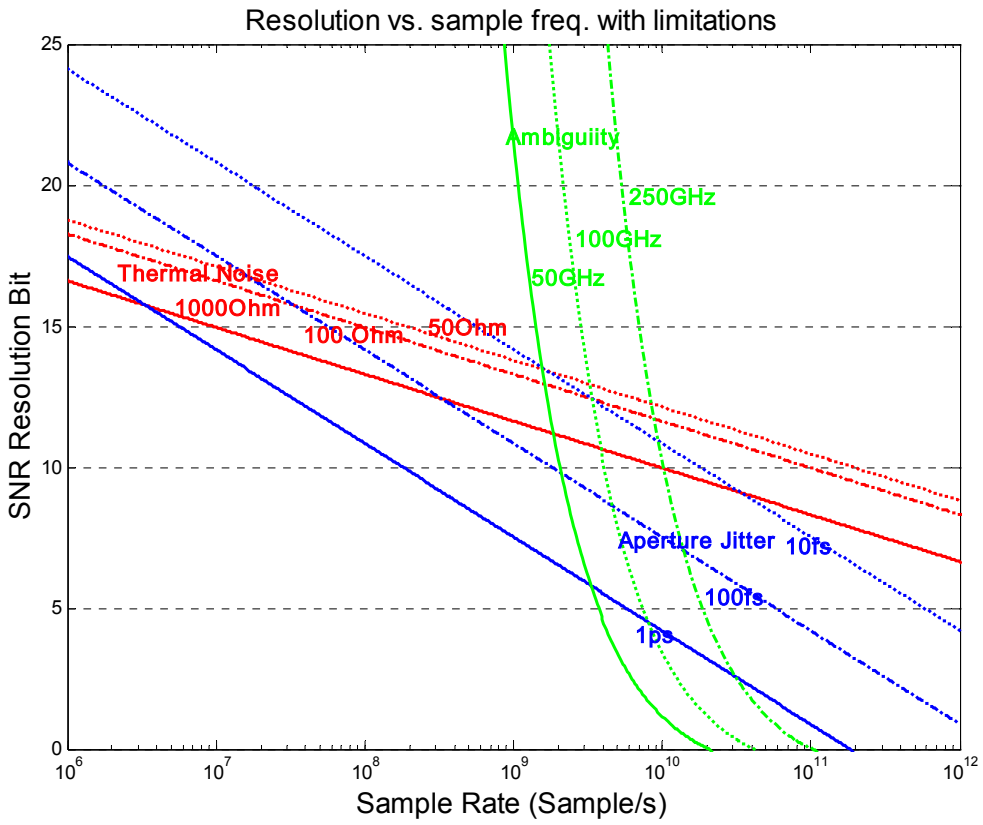

Figure 2-4: Achievable resolution vs. sampling rate limited by thermal noise (red), aperture jitter (blue) and comparator ambiguity (green).

2.3 Review of electronic analog-to-digital converters

The most popular ADCs are Nyquist A-to-D converters, in which the sampling operation is chosen around the minimum Nyquist criterion: $f_{samp}=f_N=2f_B$. Nyquist rate ADCs are used for high-frequency applications, which of interest in this thesis. Low sampling rate, $f_{samp}<f_N$, is also acceptable if the input signal is known to be periodic. This is called

subsampling. Subsampling ADCs are usually used in oscilloscopes, which process periodic signals. Another class of ADC is oversampling, in which $f_{samp} >> f_N$. The ratio of f_{samp}/f_N is called the oversampling ratio (OSR) and usually chosen as 2^M, where M is an integer. A final digital code is obtained by subsequently processing 2^M quantization results; therefore its conversion rate is $f_{samp}/2^M$. The idea of oversampling A-to-D conversion is to trade sampling rate for resolution, and it is widely used in very high-resolution ADC designs.

Researchers keep pushing the performance of ADCs to higher sampling rate and resolution. Some GS/s products have recently emerged in the market. In the past few years several off-the-shelf products have met the lowest requirements for direct conversion applications around 1GS/s. Some of these are shown in Table 1. The Rockwell and Atmel's ADC chips are able to sample an RF signal at rates higher than 2GS/s with sufficient bits of resolution and spurious-free-dynamic range. Agilent has implemented a 20GS/s 8-bit ADC module in their oscilloscopes by using 80 parallel ADCs running at 250MS/s, 1MB on-chip sample memory, and signal processing software [13].

Table 2-1: High-speed ADC products

Manufacturer	Part Number	Sampling Rate (S/s)	Claimed number of bits	SFDR (dB)	Power
Maxim [14]	MAX108	1.5G	8	-54	5.25W
Rockwell [15]	RAD008	3G	8	-55	5.5W
Rockwell [16]	RAD006	6G	6	-40	3.8W
Atmel [17]	TS83102G0B	2G	10	-54	4.6W

Researchers have demonstrated better performance in laboratories during the past decade. However, as the sampling rate has been pushed into the 10GS/s range, very slow progresses been made. In the following sections, we discuss three typical Nyquist rate electronic ADC techniques: a) flash, b) pipeline, and c) folding and interpolating, as well as their performance.

2.3.1 Flash ADC

Conceptually the simplest and potentially the fastest way to quantize an analog signal is by simultaneously comparing it to 2^b-1 different reference levels, where b is the resolution bit number. This is called a flash ADC. Its block diagram is illustrated in Figure 2-5. The ADC consists of a 2^b-1 resistor ladder and 2^b-1 comparators followed by a decoder. When the analog input is between V_j and V_{j+1}, the j-th and $j+1$-th references, the comparators from 1st (lowest) to j-th produce ONEs while the rest produce ZEROs. Consequently, the 2^b-1 comparators generate a thermometer code, which is converted to binary or other code by the following decoder.

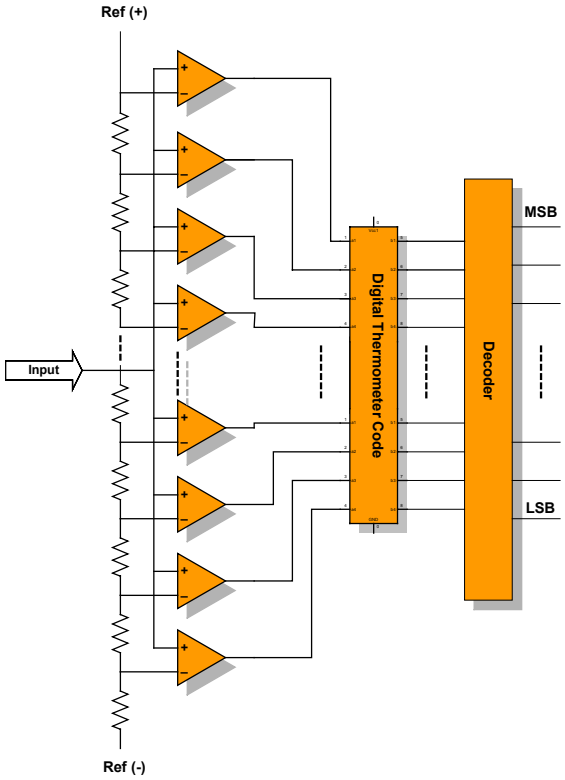

Figure 2-5: Diagram of a flash ADC.

The flash ADC is the fastest scheme of all electronic ADCs. First of all, the fully parallel architecture accomplishes a conversion in a single stage. Second, in principle, it does not need an explicit front-end sample-and-hold circuit, which requires high linearity and hence can only be implemented at lower frequency.

On the other hand, the resolution of flash ADCs is limited by circuit complexity, high power dissipation and comparator reference mismatch. Its complexity grows exponentially as the resolution bit increases. High-resolution flash ADCs need very large chip size and consume high power. For instance, a 10-bit flash ADC requires 2^{10}-1 comparators and resistors. The total number of transistors may exceed 20,000.

Consequently it requires complex IC design and excessively large power dissipation. Therefore, flash ADCs are usually employed for moderate resolution and high sampling rates, typically above 4GS/s. Moreover, the large amount of comparators causes serious matching problem and kickback noise. For these reasons, flash converters are typically limited to approximately 8 bits of resolution [1].

The performance of flash ADCs strongly depends on IC technology, or more specifically, the cutoff frequency of transistors in the comparators. Most ADCs have been fabricated in silicon, while a few flash ADCs have taken advantage of high-speed gallium arsenide (GaAs), silicon germanium (SiGe) or indium phosphide (InP) technologies. A flash ADC of 8 GS/s with effective 3bits of resolution fabricated using AlInAs/GaInAs HBT with f_T=75GHz, has been reported by Baringer et al. at HRL laboratory [18]. An ADC of 8 GS/s with effective 4 bits of resolution has been implemented by SiGe bipolar technology of IBM [19]. In 2001, HRL laboratory reported flash ADC of 10 GS/s with 2.4 effective resolution bits fabricated in InP HBT with f_T=150GHz [20]. The 3 GS/s and 6 GS/s ADC products from Rockwell in Table 1 are both based on a flash architecture. [11, 12]

2.3.2 Pipeline ADC

A pipeline ADC is composed of a series of low-resolution ADCs and DACs (digital-to-analog converters), as shown in Figure 2-6. Each stage quantizes the analog signal from the preceding stage into *m* bits, calculates the residue value and then sends it to next stage. Pipeline converters can provide moderate resolution and speed. Each stage performs a conversion using a lower resolution high-speed flash ADC and a DAC. Its complexity is $2^m \times k$, where *m* is the resolution bit number of a single stage and *k* is the

number of stages. However it requires a D-to-A converter and a track-and-hold circuit in every stage. This means pipeline ADCs achieve less complexity and higher resolution at a cost of latency due to its multiple stage architecture. The highest performance of 3 GS/s with *6.5* effective bits was implemented using an AlGaAs/GaAs HBT [21]. An impressive ADC product at 20 GS/s with 8 bits has been used in Agilent's 20 GS/s oscilloscope. It uses 80 pipelined ADCs at 250 MS/s and employs time interleaving of 50 ps. In this ADC comprehensive calibration of signal voltage and timing is accomplished by signal processing software and another 16 separate DACs[13], this chip contains more than 5 millions transistors and consumes more than 10 Watts of power.

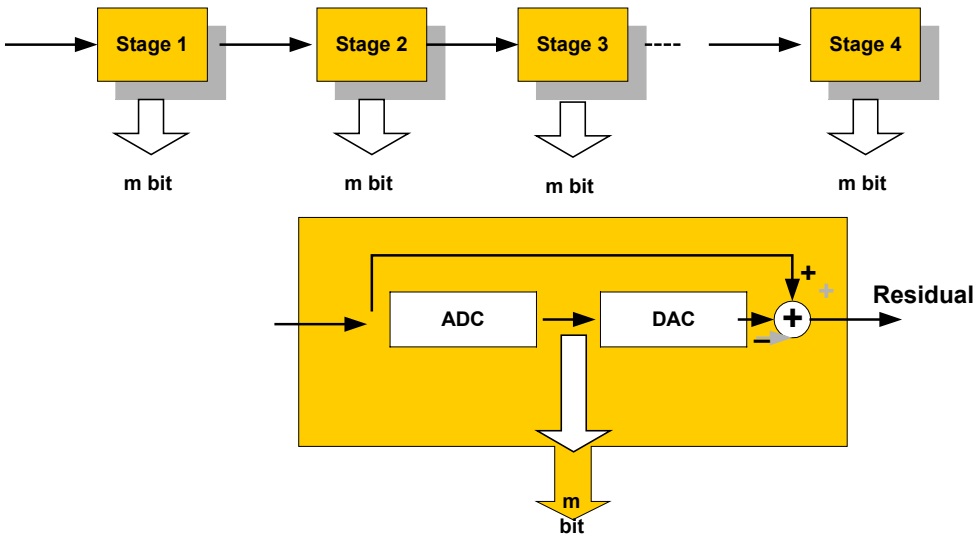

Figure 2-6: System diagram of pipeline ADC (upper) and a single stage is shown in lower part.

2.3.3 Folding and interpolating (F&I) ADC

Folding architectures have evolved from fully parallel and two-step architectures, as shown in Figure 2-7. In an F&I ADC, the input signal is converted into *f* folds. Then the folded voltage is subsequently digitized using an interpolating resistor network and comparators to generate *k* least significant bits (LSBs). The most significant bits (MSBs) can be resolved using an *m*-bit coarse flash stage that operates in parallel with the folding circuits and hence samples the signal at approximately the same time that the folded signal is sampled. Folding architectures have become popular because of their simplicity and speed. The folding architecture eliminates the need for D-to-A converters and subtraction circuitry in pipeline ADCs.

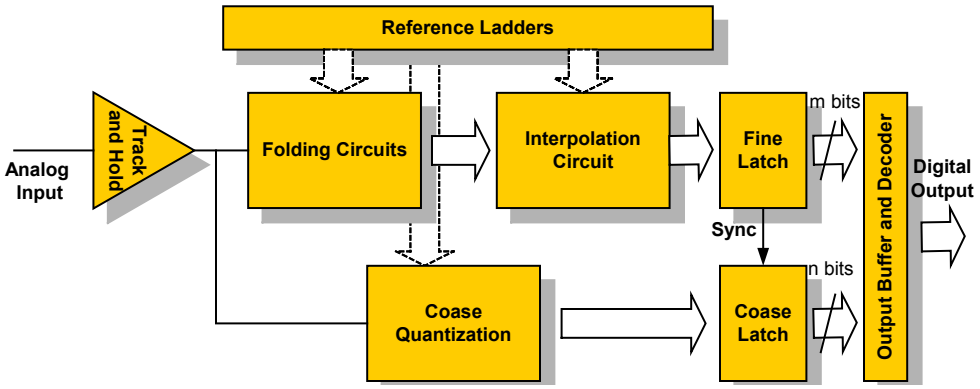

Figure 2-7: System diagram of folding & interpolating A-to-D converter.

The folding block contains a series of folding cells. A folding cell is simply a coupled differential pair with different references, as shown in Figure 2-8. The output is folded into two segments that are symmetric to $V_{in}=(V_{high}+V_{low})/2$. The interceptions of the

folded curve and the threshold, at $V_{in}=V_{high}$ and $V_{in}=V_{low}$, are called zerocrossings. Thus, when $V_{out}>V_{th}$, its quantized level is '1', otherwise it is '0'.

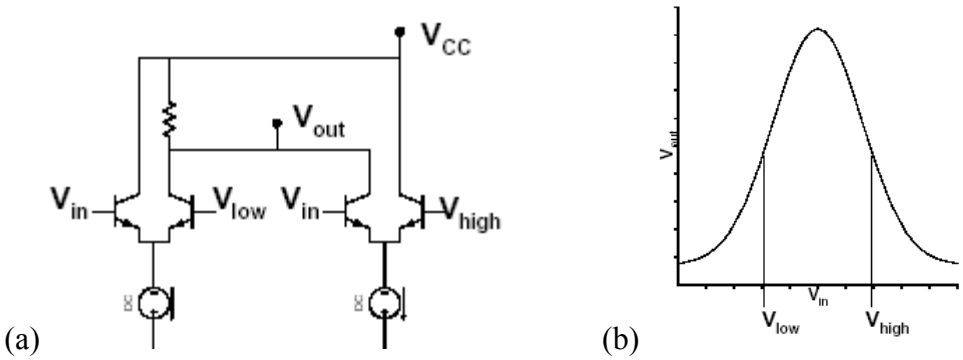

Figure 2-8: (a) folding cell and (b) its folded output.

The input full-scale voltage can be divided into 2^m quantization levels by using 2^m equally spaced references and introducing 2^m zerocrossings. Figure 2-9 shows an 8-time folded output using references V_1~V_8.

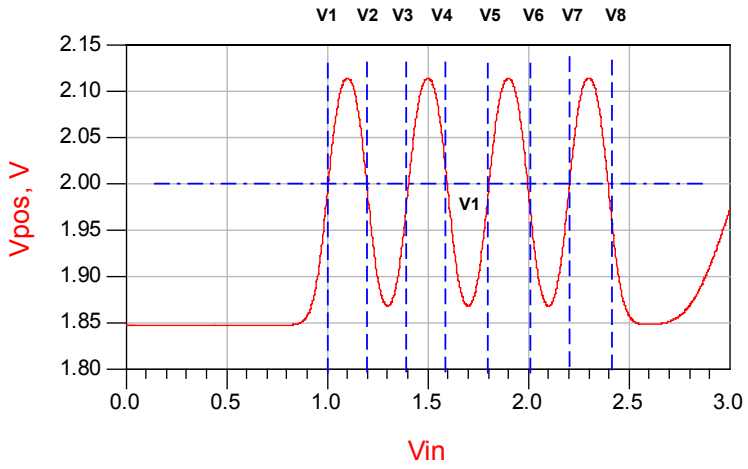

Figure 2-9: Output of folding block with 8 reference voltages.

In an F&I ADC, the number of quantization levels is equal to the number of zerocrossings. To get twice the number of zerocrossings, we can use a duplicated folding block with a set of shifted references $V_1 + \Delta V \sim V_8 + \Delta V$, where ΔV is half of the original reference difference. This procedure can be repeated and more zerocrossings can be inserted by shifts of ¼ and ¾ of the reference differences.

To achieve finer quantization, F&I ADCs use voltage interpolating to get more zerocrossings without using any transistors. A resistive network inserts zerocrossings in between folding blocks, as illustrated in Figure 2-10. The outputs of this F&I block are *V1, V1+1/4ΔV, V1+2/4ΔV, V1+3/4ΔV, V*. Thus 3 more zerocrossings are inserted in between the curve *V1* and *V2*.

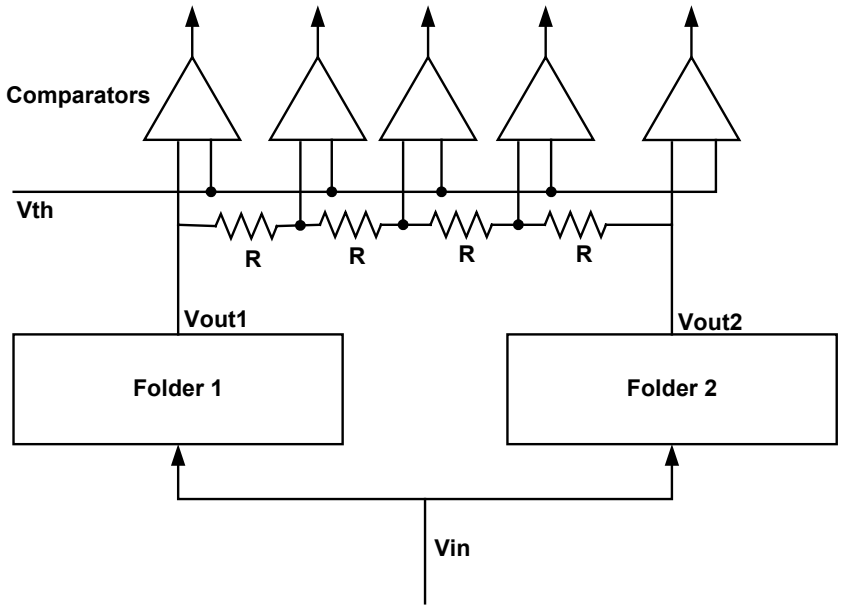

Figure 2-10: Interpolating network inserting 3 zerocrossings between *Vout1* and *Vout2*.

An example implementation of a 10-bit F&I ADC can be designed with the following arrangement. The folding factor can be chosen as 8, which means the coarse ADC is 3 bits. 4 folding blocks with shifted references can generate totally 32 zerocrossings. Then 32 resistors in between every adjacent folding block will insert 32 times more zerocrossings. Thus the full-scale voltage is divided into 2^{10} (=32×32) quantization levels. This ADC needs only 136 comparators and moderate power dissipation. The total number of transistors is estimated to be 3000, which is far less than equivalent flash ADCs.

Folding and interpolating is a high speed ADC architecture because of its flash-like structure where only 2 stages are employed. Meanwhile, the resolution remains high because of the reduced requirement for linearity, since it does not need accurate residues as the pipeline ADC does. The cost of a folding architecture is that it requires high-speed devices. Because the input signal is folded *f* times, and consequently the frequency of the folded signal is *f* times the original input, it therefore requires *f*-times faster semiconductor devices.

F&I ADCs achieve good overall performance. As a result, at GS/s or sub-GS/s applications, F&I ADCs have gained a lot attention and effort (see appendix). High performance F&I ADCs of 4GS/s with 6 effective bits and 2GS/s with 8 effective bits were reported. [22,23]

2.3.4 Summary of high-speed electronic ADC

Table 2-1 compares ADC architectures discussed above in terms of sampling rate, resolution, power dissipation and complexity. According to different applications, proper architecture and IC technology should be chosen to optimize performance and cost. Flash ADCs are the fastest, and pipeline and F&I ADCs are attractive with their moderate resolution and fairly fast speed.

Table 2-2 Comparisons of ADC architectures

	Flash ADC	Pipeline ADC	F&I
Sample rate	Fastest in electronic ADCs Up to 10Gs/s	Fast Up to several Gs/s	Fast Up to several Gs/s
Resolution	Low 6-8 bits	Medium 8-12 bits	Medium 8-12 bits
Power	High	Medium	Medium
Complexity	Exponential 2^b	$2^m \times$ k comparator high resolution DAC	2^m+2^k-1 comparator interpolating

In summary, the overall performance of current electronic ADCs appears to reach its limit at frequencies near 10GS/s, and therefore have not kept pace with other semiconductor devices during the past a few years. For example, f_T's of 350 GHz for SiGe HBT [24], 500 GHz for InP/InGaAs HBT [25], 550 GHz for InP HEMT and 562 GHz for InAlAs/InGaAs HEMT [26] have been achieved. This implies that while the comparator ambiguity limit has raised its bar, the performance is still limited by the relatively poor electronic sampling clock jitter. That is why fast yet clean optical pulse sources look so attractive to ADC researchers.

2.4 Review on Optical Analog-to-Digital Converters

The high-speed electronic ADCs discussed in the previous section offer at best 10 GS/s sampling rate with only a few bits of resolution. Promising to breakthrough the bottleneck of the electronic ADCs, optoelectronic devices have demonstrated ultra-fast switching speed and mode-locked lasers have achieved high speed accurate optical pulses. Many optical ADCs have been proposed and have shown a number of advantages over their electronic counterparts. First of all, the time jitter of optical sources is in the order of a few picoseconds or in the range of femtoseconds, which is about 2 orders lower than electronic clocks, making ADCs above 100 GS/s possible. That implies RF signals with 50 GHz of bandwidth can be directly converted. Second, optical ADCs decouple the electrical signal to be sampled and the optical signals of post sampling, and hence reduce interference. Third, post sampling or quantized optical signals are easy to distribute by fiber and can be controlled remotely. Also, many optical ADC approaches produce digital outputs as Gray-codes directly, eliminating the need for additional encoding circuits.

However, current optical quantization has been generally limited to a few bits and remains a major challenge because of implementation issues. According to whether the quantization function is accomplished optically or electrically, optical ADCs fall into two categories: hybrid optic-electronic ADCs or all-optical ADCs.

2.4.1 Hybrid optic-electronic ADC

Hybrid optio-electronic ADCs, which are known as optically assisted ADCs, employ optical sampling followed by electronic quantization. They attempt to combine the high

speed of optical sampling and the high resolution of electronic quantization. A hybrid ADC modulates the electrical signal onto the power intensity of an optical impulse train. The optical pulses are then detected by photodetectors and quantized by electronic ADCs. Since the speed of electronic devices is much lower than the optical sampling rate, hybrid ADCs have to split fast optical pulses into multiple parallel channels to get lower speed at each channel. For example, 100 GS/s sampled pulses can be split into 10 channels in the time domain; the pulse rate in every channel is 10 GS/s, which an electronic ADC is able to handle.

Usually a hybrid ADC uses a Mach-Zehnder modulator to perform the electrical-to-optical conversion. Figure 2-11 shows a Mach-Zehnder interferometer and its modulation characteristics. The applied electrical field changes the refractive index of the electro-optic material and introduces phase difference between the two arms. Its output is the interfered signal of the two optical beams. As a result, the output intensity of the Mach-Zehnder interferometer is a function of the applied voltage:

$$I_{out} = I_i \cos^2\left(\frac{\varphi_0}{2} - \frac{\pi V}{2V_\pi}\right), \tag{2-1}$$

where $\varphi_0 = 2\pi nL/\lambda_0$, the optical distance of a branch, and V_π is the half-wave voltage, defined as the applied voltage at which the phase shift changes by π. In a small range around V_π, the output is approximately linearly proportional to the applied voltage. That is the region where optical sampling is used. To extend the linear range of a Mach-Zehnder modulator, a number of linearization approaches have been proposed. In optical ADCs, the linearization can be done in the digital domain by directly inverting the transfer function in the DSP.

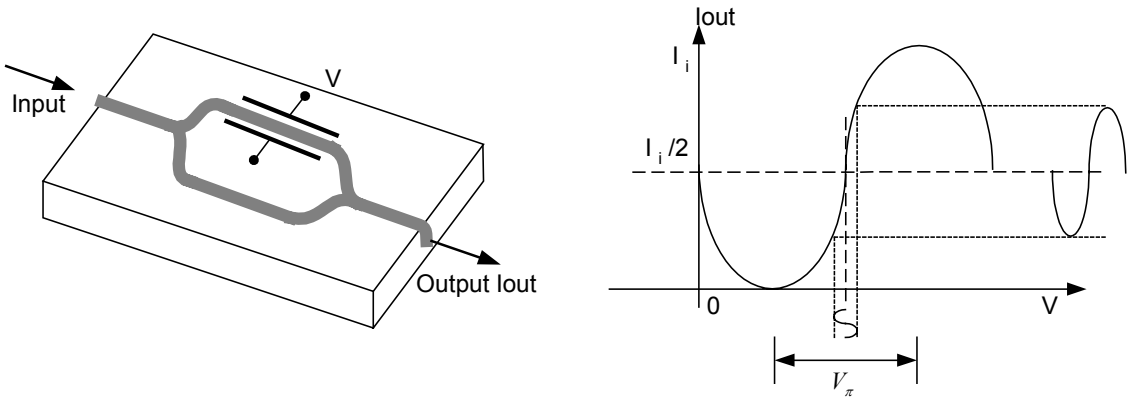

Figure 2-11: M-Z interferometer and its modulation characteristics.

The key issue in hybrid ADCs is to channelize the high-speed sampled optical pulses and ensure channels match in amplitude and time. Based on approaches of channelization, three major schemes have been proposed, as we discuss each in the following sections.

2.4.1.1 Time interleaving

The concepts of optical sampling and time interleaving were first combined by Bell et al. to realize a 2-Gs/s ADC that achieved a relatively poor resolution of 2.8 effective bits. Following this pioneering work, J. C. Twichell and P. W. Juodawlkis, et al. at Lincoln Laboratory, MIT, proposed an ADC using 1:4 optical time division demultiplexers that achieved 208 MS/s [27]. Later they extended the bandwidth to 505 MS/s by using two 1:8 demultiplexers and 16 electronic ADCs with 14-bit at 63 MS/s [28] (Figure 2-12). A dual-output $LiNbO_3$ M-Z modulator was used for linearization processing. The sampled optical pulses are split into 8 channels by optical time division demultiplexers, which are composed of 3 stages of 1×2 switches controlled by 505 MHz driving signals. This ADC

obtains 65 dB of SFDR and 47 dB SNR, corresponding to an effective resolution of 7.5 bits. The electronic quantizers used in this ADC are very good in terms of resolution-sampling rate product, which was $P=1.03\times10^{12}$ LSBs-Hz, but the optically assisted ADC shows an overall performance of only $P=9.14\times10^{10}$ *LSBs-Hz*, which is one order lower than that of electronic ADCs due to a degradation of resolution.

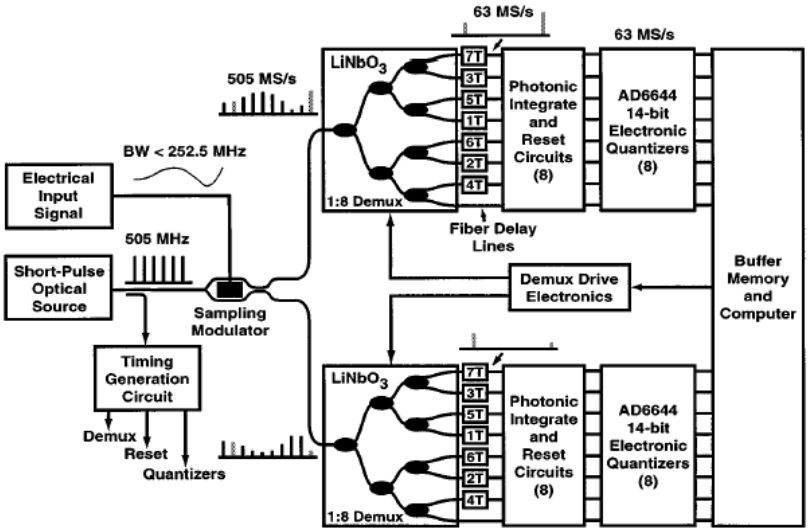

Figure 2-12: Block diagram of time interleaving ADC working at 505 Ms/s [28].

The degradation comes from time skew between channels, uneven power splitting, and different amplifications of the electronic ADCs, etc. To achieve high resolution (or large SFDR) in a time-interleaving ADC, the following condition must be met [27]:

- The sampling time of the interleaved ADCs must be uniform.
- The converter-to-converter gains and offset must be precisely matched.
- The crosstalk between electronic ADC converters and sample-to-sample memory effects must be minimal.

For example, to achieve an interleaving ADC with SFDR of 80 dB, the converter-to-converter gains must be matched to ~0.01%, the offset must be matched to ~0.01% of the signal amplitude, and the converter-to-converter crosstalk must be less than one part in 10^4 [27]. Because of the limitations of electronic driving circuits used in the electronically controlled 1×2 optical switches, it is difficult to further increase its sampling rate. However this scheme opened an avenue to design optically assisted ADCs.

2.4.1.2 WDM channelized ADC

Borrowing from the concept of WDM (wavelength division multiplexing) communication, the sampled optical signal can be channelized in both the wavelength and time domains. Using optical dispersive components, a multi-wavelength optical signal is smeared (for continuous spectrum) or split (for discrete wavelengths) in time. The RF signal is sampled by the WDM pulses and then channelized by a WDM demultiplexer.

T. R. Clark, J. U. Kang, et al. at the Naval Research Laboratory demonstrated a 100-GS/s photonic ADC based on the wavelength-interleaved scheme as shown in Figure 2-13[29].

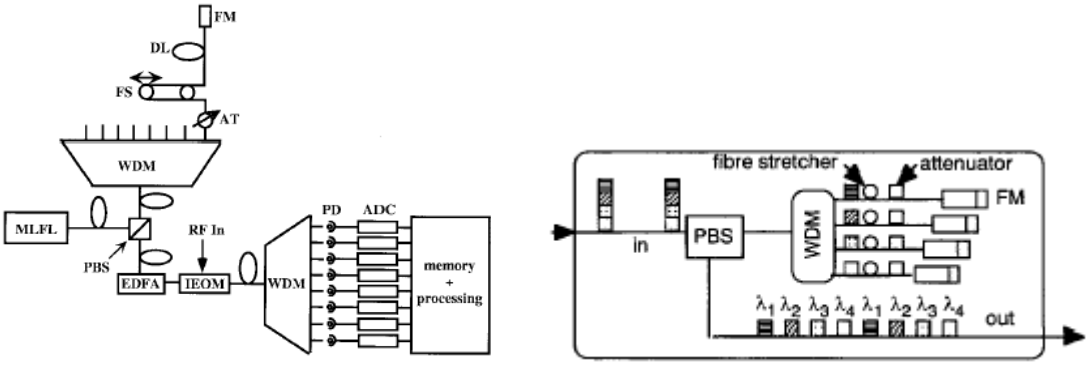

Figure 2-13: (left) Block diagram and (right) wavelength interleaving [29].

Their ADC architecture is shown on the left in Figure 2-13. There are 2 wavelength division multiplexers (WDM): the first one is used to generate the 100GHz sampling pulses from a 12.5 GHz pulse train; the second WDM splits the 100GHz post sampled pulses into 8 electronic channels. In this design a mode-locked fiber laser (MLFL) generates the 12.5 GHz pulse train. The pulse train is then sent to a polarizing beam splitter (PBS) followed by the first WDM (, right, only 4 channels are shown instead of 8). Every single pulse contains 8 wavelengths and is split into 8 fibers with different lengths, which are terminated by variable fiber inline attenuators and Faraday mirrors (FM). The pulses propagate through fibers yielding a 10ps delay difference from fiber to fiber, reflected by the FMs. Coming back to the first WDM, the 8 pulses recombine into a single channel, which is coupled out from the orthogonal output of the PBS forming a 10ps time interweaved 100 GHz pulse train. The delay and attenuation can be adjusted for time matching and amplitude equalizing respectively. The resulting 100 GHz pulses pass through a M-Z modulator and sample the applied electrical signal to be converted. The second WDM splits the sampled pulses into 8 electronic channels according to their wavelengths. The resulting parallel pulses are then quantized by 8 high-speed quantizers

(>12.5 Gs/s), which were assumed to be available by the authors at their time. The actual hybrid ADC was built using 8-bit MAX104 electronic ADCs operating at only 781MS/s and measured by a 1-GHz state analyzer, therefore its actual measured sampling rate is $781MS/s \times 8 = 6.25\ GS/s$. The experiment result showed a SNR of 22~26 dB, corresponding to about 4 bits of resolution. The resolution-sampling rate product of the ADC is about $P=1.6\times10^{12}$ LSBs-Hz. It is one order higher than the best high-speed (~10 GS/s) electronic ADC.

This wavelength-channelized ADC faces similar difficulties as the time interleaving ADC. They are different only in the approaches of channelizing the post sampled optical signal; one splits optically while the other one splits electrically. The matching requirements described in the last section still hold.

2.4.1.3 Time stretching ADC (TSADC)

A. S. Bhushan and F. Coppinger, et al. at UCLA proposed a record ultra-fast sampling rate of 130 GS/s using a time stretching approach in 2002 [30]. Its concept is similar to a wavelength channelized ADC, but in the TSADC the RF signal modulates an optical signal with a broadband continuous spectrum rather than modulating optical pulses with discrete wavelengths. Figure 2-14 shows the TSADC signal single channel diagram. The analog optical signal detected by a photodetector is sampled and quantized using an electronic ADC, which is not shown in the figure.

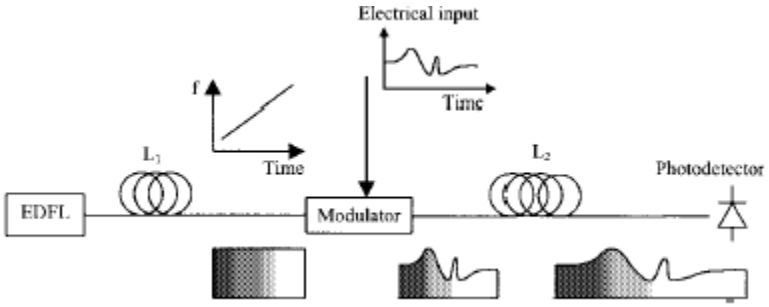

Figure 2-14: Time limited signal converted by time stretching ADC [31].

The single channel architecture can be used in applications featuring limited-time signals, such as a pulsed signal. A passively mode-locked fiber laser with 20-MHz repetition rate followed by a 17-nm wavelength filter generates broadband short pulses. The optical pulses propagate through a dispersive fiber of length *L1*, stretch in time and get 0.8 ns of time aperture. The 0.8-ns pulse is then modulated by the RF signal to be converted. Then the modulated wave is sent to another piece of dispersive fiber of length *L2* to be further stretched in the time domain. After *L2* the pulse is stretched 16.2 times and its pulse width becomes 12.96 ns. Finally the stretched signal is detected and digitized by an 8 GS/s electronic ADC of a high-speed oscilloscope. Therefore the effective sampling rate for the TSADC can be derived as *8Gs/s×16.2=129.6GS/s*.

Note that, without channelizing and multiple electronic ADCs this TSADC is suitable for only signals limited in time since it samples only in a time aperture of 0.8 ns. The TSADC showed a simple system design and obtained SNR of 45 dB, corresponding to 7.5 bits of resolution. The resolution-sampling rate product of this TSADC is 2.4×10^{13} LSBs-Hz, which is much higher than any current ADC.

If the input signal is continuous in time, then a parallel architecture, similar to the previous two architectures, must be used in order to preserve the information (Figure 2-15).

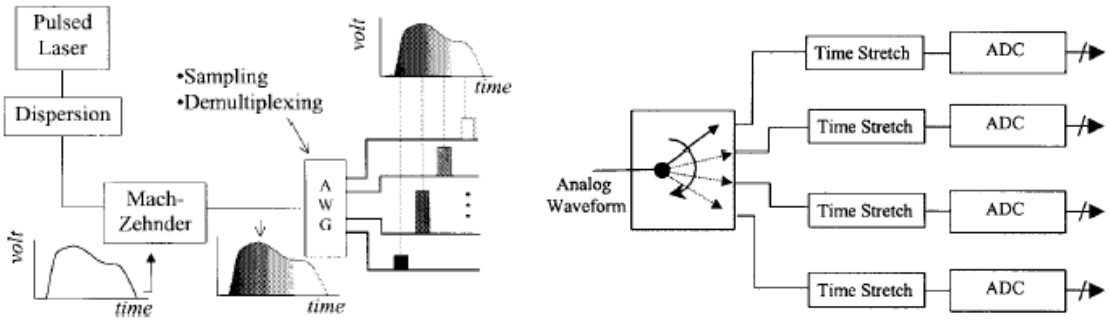

Figure 2-15: Continuous RF signal application implemented by time stretch ADC [31].

The output optical signal from the M-Z modulator is continuous in both intensity and time. The analog signal is segmented by an arrayed waveguide grating (AWG). Each output port of the AWG filter gets a portion of the optical spectrum, or small piece of information of the original RF signal. Then each of the segments is time stretched by the second piece of dispersive fiber of length *L2*, and enters an electronic ADC (, right).

No experiment result has been reported. One challenge they could have encountered is that to sample a continuous RF signal in their approach the input optical wave must be continuous. At the same time to get enough dispersion the spectral bandwidth must be very wide. However, signals that are continuous in time end up having very narrow bandwidth in the spectral domain, and vise versa. This conflict may prohibit the TSADC from converting continuous electrical signals. Moreover, similar to the channelization approach described in time interleaving and wavelength channelization, difficulties are

always associated with the channel mismatch. However, this TSADC has clearly shown the extremely high sampling rate potential of optical ADCs.

2.4.1.4 Summary of hybrid ADCs:

Hybrid opto-electronic ADCs attempt to take advantage of the ultra-fast speed of optical sampling together with the high-resolution of electronic ADCs. They have achieved remarkable performance. However using N electronic ADCs definitely does not imply an enhancement of N times in resolution-sampling rate product. The time uncertainty and amplitude mismatch between channels still limit the resolution of hybrid ADCs. Moreover, in hybrid ADCs the digitized output signals are electrical and are not distributed as easily as optical signals. Finally, but not least, hybrid architectures usually use multiple electronic ADCs making power dissipation much higher.

2.4.2 Review of all-optical ADCs

2.4.2.1 Mach-Zehnder based AOADCs

All-optical ADCs were actually proposed earlier than the hybrid ADCs. Many schemes have been demonstrated. Probably the best known optical ADC, also the first optical ADC, was developed based on a Mach-Zehnder interferometer by H. F. Taylor in 1975 and patented in 1977 [6].

Observing the transfer function of a Mach-Zehnder interferometer (see Figure 2-11), one can identify a periodic behavior similar to a binary code. Its period is determined by the half-wave voltage, V_π, which is in turn determined by the electrode length, or more

accurately, the interaction length. Taylor's opto-electronic quantization scheme was based on an array of electrooptic interferometers with electrode lengths organized in a binary ladder (Figure 2-16). The input RF signal is simultaneously applied to the parallel Mach-Zehnder interferometer array. The resulting parallel optical outputs are a Gray code representing the input signal amplitude. This elegant and simple idea highlighted the benefits of all-optical ADCs including high sampling rate and direct encoding, as well as isolation of input and sampled signals. Mach-Zehnder interferometers have achieved speeds higher than 100 Gb/s in communications and this makes the M-Z based AOADC very attractive [1]. However its resolution is limited to just a few bits. The limitation is primarily caused by modulator electrode length. Since each additional bit of resolution requires a doubling of the electrode length, this produces a transit-time limitation. Moreover, different bits are generated separately, so mismatch from bit to bit may cause errors and further degrade the performance. Resolution of approximately 6 bits at 1 GHz using $LiNbO_3$ Mach-Zehnder interferometer has been reported.

A revised ADC based on Mach-Zehnder modulator, named the optical folding-flash A-to-D converter, was proposed and demonstrated by B. Jalali and Y. Xie in 1995 [32]. Figure 2-17 shows a block diagram of a 4-bit optical folding-flash ADC.

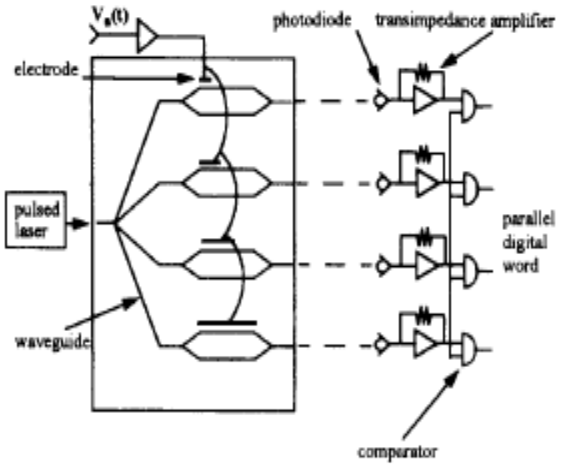

Figure 2-16: All-optical ADC using MZ interferometers.

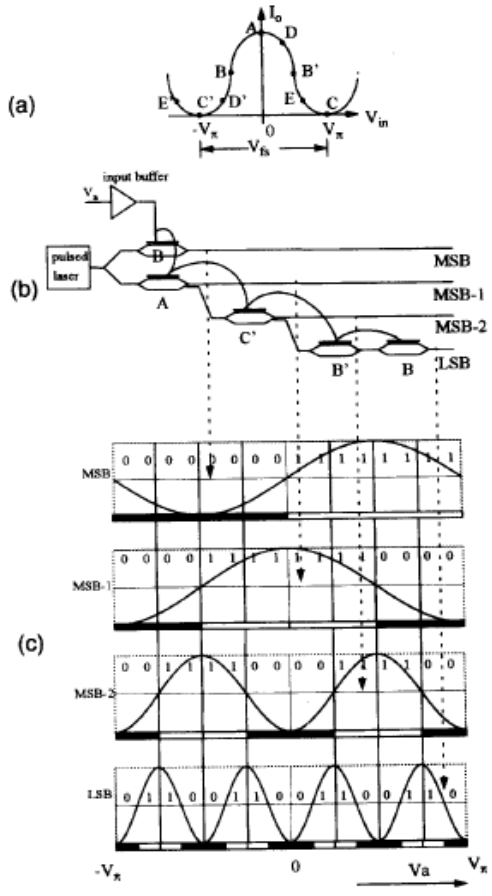

Figure 2-17: Modified all-optical ADC: (a) operating point, (b) ADC architecture, (c) output waveform.

The geometrical scaling problem of electrode length is eliminated by a parallel-serial combined configuration. This scheme used identical electrode lengths but sets the DC bias at different points on the interferometer transfer characteristic curve. The output from MSB-1 is sent to another interferometer, whose bias is set *C'* in the figure (a) and thus generate MSB-2 with a doubled frequency, since the total equivalent length of electrodes is doubled. In the same way the LSB is generated.

This solves some problems, but others still remain. First the transit time limitation is still not eliminated. Second the mismatching problem is still there. Additionally, the hardware complexity is increasing exponentially as $2^{(b-2)}+1$ in terms of the number of interferometers. Moreover, it strongly relies on the accuracy of the bias points.

2.4.2.2 Flash AOADC

A flash AOADC is an exact copy of a flash electronic ADC of the optical version. The flash AOADC quantizes the optical signal using variable electro-absorption semiconductor absorbers, as demonstrated by M. J. Hayduk, et al [33,34] (Figure 2-18).

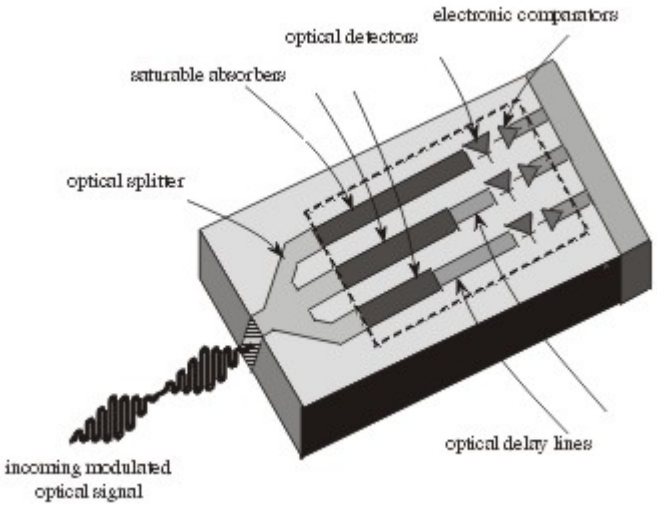

Figure 2-18: Optical ADC using variable electro-absorption semiconductor modulators.

A conceptual design of the flash AOADC is shown in Figure 2-18. The front end of the system uses an ultra-stable mode-locked laser to sample the RF electronic data using an EO modulator. The optical signal is then sent in parallel to a series of semiconductor saturable absorber light channels. The optical properties of the saturable absorber channels are tailored so that the nonlinear absorbance can be scaled monotonically over the entire range of absorbers. As in electronic flash ADC systems, the total number of saturable absorbers or comparators required is equal to $2^b - 1$, where b is the number of bits of resolution The authors claimed that the ADC is potentially able to operate at more than 100 GS/s combined with resolution as high as 10-12 bits ideally. However no prototype or experiment has been reported. Actually this scheme may not be very feasible. The number of channels grows exponentially as the number of bits increases. For instance, a 10-bit flash AOADC split optical power into 1024 channels; implying that the power in each channel is only 1/1024 of the total. Moreover the already very weak optical signal needs to be quantized into 1024 quantization levels, requiring 1024

extremely sensitive and accurate semiconductor absorbers. In my opinion, the optical flash ADC was an incondite copy of electronic flash ADC and might not succeed.

A similar idea was also employed in all-optical ADC quantization using photodetectors with different sensitivities [35] as optical comparators. In summary, any AOADC that quantizes the optical power intensity strongly depends on optical source fluctuation, device linearity, optical loss and channel mismatch.

2.4.2.3 OADCs based on tunable lasers

Several all-optical ADC schemes take advantage of the stable and accurate spectra of optical sources. One of them uses a tunable laser for sampling and optical filters for quantizing. A system was demonstrated by H. Zmuda, E. N. Toughlian, et al., in 2001 [36] (cf. Figure 2-19).

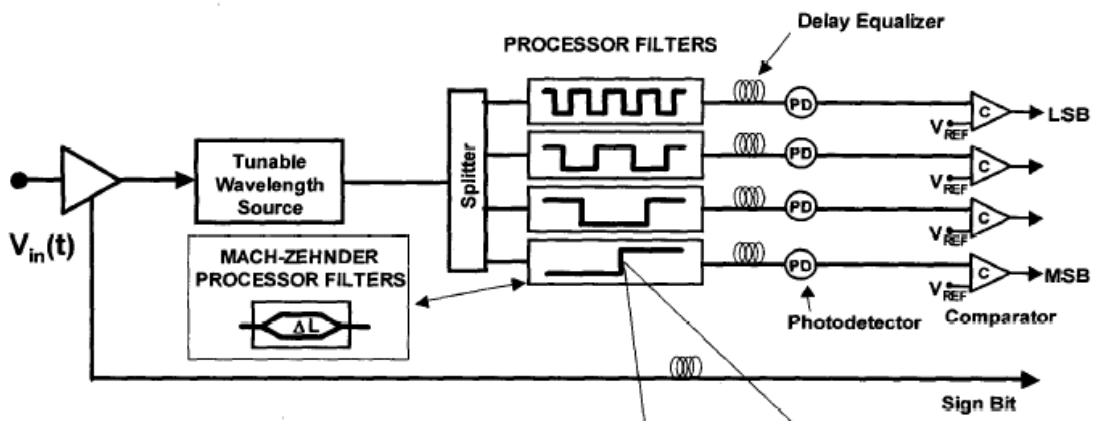

Figure 2-19: Optical ADC using tunable laser and filters [36].

The input RF signal is applied to a tunable laser, which changes its wavelength according to the voltage. The optical signal is then sent in parallel to a series of processor filters. The passband in the spectral domain of each filter is a periodic pattern, and the period is doubled from one bit to next. As shown in Figure 2-20, the passbands behave like digital codes. The passband and stopband of the filters can be organized as either binary code or Gray code. If the spectral line carrying information of the RF signal falls into the passband, the output is "1," otherwise it is a "0".

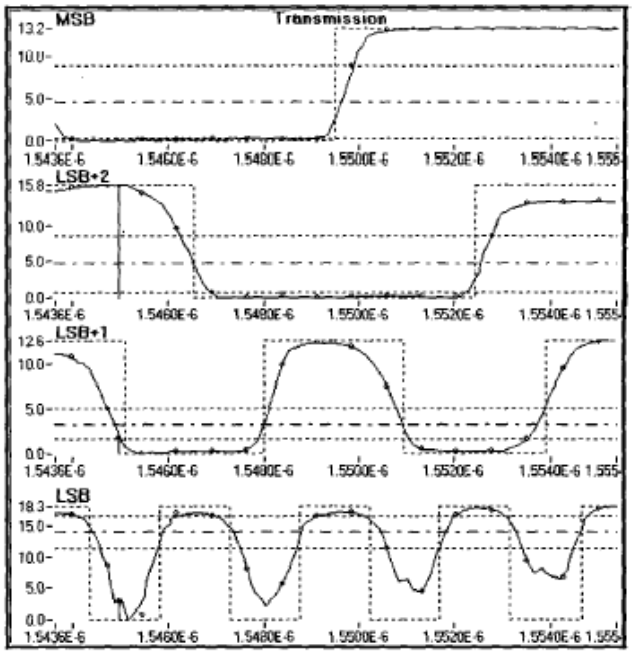

Figure 2-20: Performance of Bragg grating filters.

The total tunable range of the laser and the filter resolution determine the resolution of this ADC. A 4-bit optical ADC using a ring cavity tunable laser and Bragg grating filters has been proposed and analyzed. Because of the convergence time limitation of the

Fabry-Perot cavity, only 4 bits of resolution can be achieved at 10 GS/s, and the performance of Bragg grating filters (Figure 2-20) limit resolution. The author claimed that the ADC would be able to operate at sampling speeds in excess of 10 GHz with up to 10 to 12 bits of resolution, but this requires either an ultra broadband tunable laser or extremely fine grating filters. Since the authors did not continue their work we don't know what the ultimate feasible performance is.

Another all-optical ADC based on a tunable laser was proposed by M. Johansson and B. Löfving, et al. in 2000 [37]. This ADC is show in Figure 2-21. In this approach the analog voltage controls a multi-electrode tunable diode laser such that the wavelength changes accordingly. The laser beam is then fed to a diffraction grating. Therefore the beam is diffracted into an angle that is determined by the wavelength, and hence controlled by the applied voltage. The diffracted beam is focused on an image plane where a row of 2^b (b is the number of bits) diffractive optical elements are placed. A diffractive element is a pattern containing $2b+1$ spots, either transparent or opaque, representing a digital code (shown in Figure 2-22). Depending on the angle, i.e. the applied voltage of tunable laser, one of the diffractive elements is illuminated and corresponding code is generated.

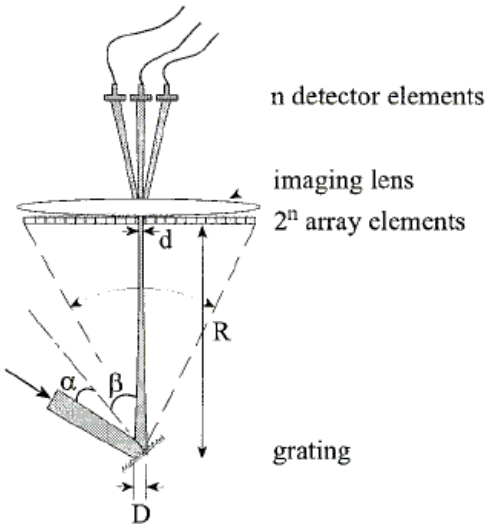

Figure 2-21: Schematic of the optical part of the ADC.

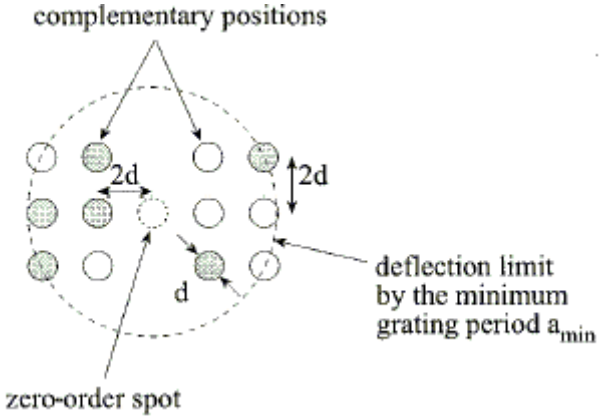

Figure 2-22: Example of designed spot pattern (6 bits) for the tunable laser ADC. The 6 spots on the left are the complement of the 6 spot on the right. The redundancy and zero-order spot are used for bit error check/correction.

A principle-proof experiment was carried out on a 6-bit ADC system by using a DC voltage instead of an RF signal. A continuously tunable diode laser system in the 1.5 μm

range served as the light source. Observing the 64 spot patterns by applying 64 DC voltage levels 62 out of 64 spot patterns were generated correctly.

This approach converts the signal voltage into wavelength and then further translates it into an angle in the spatial domain. It is interesting to observe that the diffractive element in serves as a quantizer, as well as an encoder. The code can be anything and that makes its encoding scheme very flexible. However a problem may arise for scenarios in which the diffracted beam falls in between two elements. In this case, the code part of one element and complementary code part of another element are illuminated at the same time, so the output code could be wrong. It was not clear how the authors solve this problem.

A general problem associated with the tunable laser based AOADCs is that they require a tunable mode-locked laser with wide tunable range and fast accurate optical pulses at the same time, which has not been demonstrated in current laser technology. Moreover, the sampling rate of this approach is limited by the tuning speed of the laser, which is about 10 GHz for a state-of-the-art device.

2.4.2.4 Other AOADCs

There are some alternative approaches to quantizing optically. L. Brzozowski and E. Sargent demonstrated a novel all-optical ADC architecture based on an optical logical gate array with different thresholds [38]. M. Currie and T. R. Clark, et al. proposed an ADC based on distributed phase modulation, in which the modulated phase shift is

detected by polarizers and converted to amplitude [39]. Optical sampling has also been performed using photodiodes as high-speed opto-electronic switches; the sampled amplitude is converted to proportional width of the pulse [40].

To complete the review, we should mention the optical oversampling ADC as a counterpart of electronic oversampling ADCs, although their point is to achieve high resolution rather than high sampling rate. Optical oversampling ADCs take advantage of the ultra high rate of photonic sampling and have the potential to improve the overall ADC performance significantly. B. L. Shoop, et al., proposed a parallel implementation of an oversampling ADC incorporating a neural network architecture and oversampling error diffusion A-to-D converter [41].

2.4.2.5 Spatial sampling AOADC

An AOADC actually performs two conversions, electrical-to-optical and analog-to-digital. The information carried by the input RF signal must be modulated onto an optical signal. Usually the amplitude of the RF signal is converted to intensity of the optical signal using a Mach-Zehnder modulator. The tunable laser based AOADCs converts the amplitude of the RF signal into a wavelength shift. It is also possible to translate the amplitude to a spatial displacement of the optical beams. Spatial sampling AOADC is a new category in optical ADCs in which the information is represented by the steered angle in the spatial domain. The angle can also be sensed and quantized in the spatial domain. We have proposed spatial sampling in 2002 [8, 9]. At the same time, Nunnally filed a similar idea for a patent witch was granted in 2004 [42]. Nunnally's ADC used a

prism-based deflector, as shown in Figure 2-23. This design is conceptual without giving any implementation issues. Also there are no any further publications discussing its modeling or performance. We will introduce our spatial sampling AOADC in the next chapter and then devote Chapter 4 and Chapter 5 to the proposed leaky waveguide deflector design, modeling and simulation.

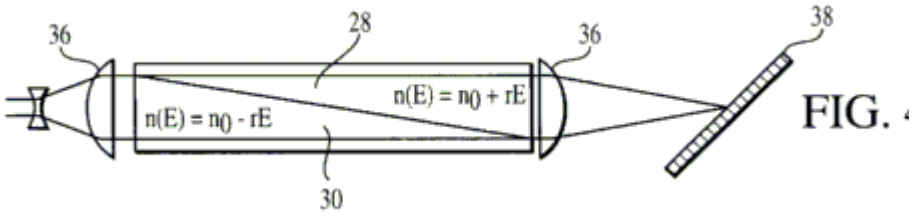

Figure 2-23: Nannally's AOADC based on prism-based E-O deflector [42].

2.5 Comparison of electronic and optical ADCs

As a summary, we compare existing electronic and optical ADCs. Figure 2-24 shows all categories along with their best-reported performance. Electronic ADCs are mature, commercially available and high in resolution but they are not capable of A-to-D conversion at sampling rates above 10 GS/s at present. Optical ADCs have shown incomparable sampling rates but they need to improve their resolution and feasibility.

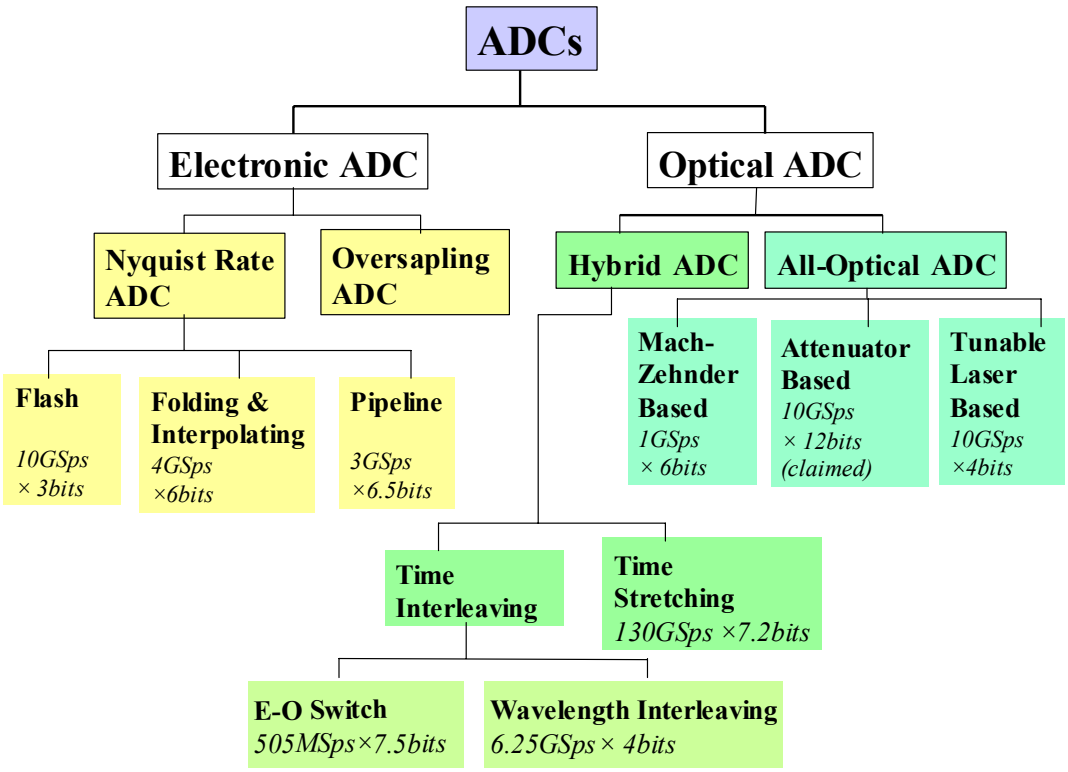

Figure 2-24: An ADC taxonomy and best performance.

All-optical ADCs are the direction of ultimate ultra high speed ADCs. However no all-optical ADC has ever achieved the desirable performance promised by their capability. They face severe problems for either practical reasons or fundamental issues. This thesis proposes a new approach for an all-optical ADC that has a great potential to be broadband, high-resolution and feasible. Unlike other approaches, the proposed novel AOADC is working in the spatial domain.

3. Spatial Sampling AOADC

In this chapter we introduce the spatial-sampling AOADC at the system level. A quantitive simulation shows that the spatial-sampling AOADC provides better tolerance to intensity fluctuation and shot noise than conventional amplitude sampling OADCs. The most important part in a spatial sampling AOADC is the E-O steerable component, which converts the amplitude of the input RF signal into an angular displacement in the spatial domain. In our first approach we designed a steerable grating array, which is implemented using GRISMs for the spatial sampler. We will discuss its operation, advantages, and challenges. Then we introduce a novel leaky waveguide deflector as a high speed, low-power spatial sampler but leave its investigation to Chapters 4 and 5. We will discuss other enabling components such as the optical quantizer, MLL and photodetectors in Chapter 6.

3.1 System diagram of spatial sampling AOADC

Figure 3-1 shows a general system diagram of an AOADC working in the spatial domain. There are three basic blocks, a mode-locked laser, an E-O deflector, and an optical collector array, which is connected to photodetectors at a remote end. The MLL and the deflector compose a spatial sampler, which steers an optical beam into a direction according to the amplitude of the input electrical signal. The optical pulses at certain time intervals sample the signal, and the position at the sensor array where a pulse appears represents the amplitude it experienced at its sampling instances. Thus the spatial sampler converts the analog signal into time-discrete angular information. The angular

information is then collected and detected by a sensor array at a fixed position, which performs as a spatial quantizer. The full span of the optical beam at the sensor array can be divided into 2^b segments, where b is the designed resolution bit number. Optical collector apertures in each segment correspond to a unique digital code, so the collected optical power is essentially an optical binary signal and can be delivered to a remote end to be detected, regenerated and further processed.

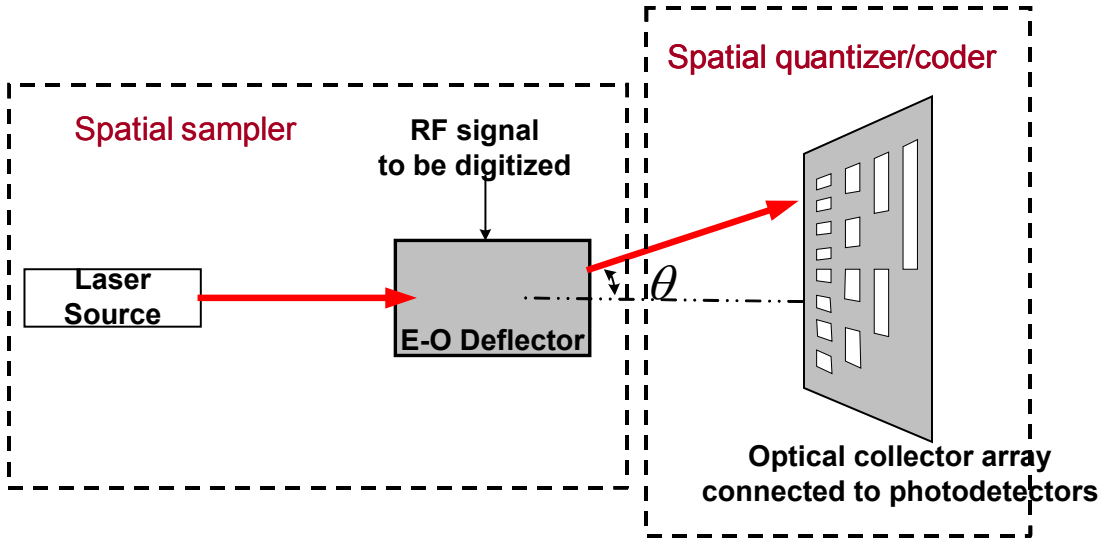

Figure 3-1: System diagram of a general AOADC working in the spatial domain.

A laser with a range of radiated frequencies and an E-O steerable component were selected as the spatial sampler. Since the state of the art of repetition rates of mode locked lasers and the RF bandwidth of photodetectors can be on the order of 100 GHz, the missing component is the high-speed E-O based steerable deflector and the optical collector array.

The resolution of the AOADC is mainly determined by the angular resolution of the optical spatial sampler. Its maximum number of quantization segments is equal to the total resolvable number of image spots within the full-scale deflection. The resolution performance is also affected by the position and size accuracy of the optical collector array, whose spatial error introduces quantization error, which is very similar to performance limitations of the comparator reference error in the electronic ADCs. Through our design, the trade-off between resolution and sampling rate has been a major challenge, which we will discuss later.

3.2 Error calculation of the spatial domain based OADC

When an optical beam is swept across a collector array, the detectors sense digital-like optical pulses. It can be proved that the spatial sampling AOADC is less impacted by fluctuation in the laser source and noise in the detectors, so it is potentially a high-resolution technique. Furthermore, the sampling rate and jitter are determined by the characteristics of the mode-locked laser, which could be extremely fast and stable. We will compare the AOADC and amplitude sampling OADCs in terms of detected error rate to demonstrate their tolerance of fluctuations.

In the AOADC, the digital codes are generated by comparing the received pulse power to a predetermined threshold, usually half of the maximum power, so when the optical power intensity varies, errors may occur near the threshold, if the threshold does not change accordingly. When the intensity slowly undulates, as conventional optical modulators usually do, the proposed AOADC can use a power monitoring and feedback scheme to adjust the laser power or the threshold dynamically, so that slow change of

optical intensity can be corrected. When the intensity fluctuates instantaneously, errors are inevitable, but only happen at the edge near to the threshold. That is why the AOADC suffers from less error probability than other ADCs.

Shot noise is caused by fluctuations in the detected current. Similar to the impact of fluctuation of input optical intensity, it also causes error at the edge due to the threshold offset. The impact of shot noise can be derived as following and the reasoning can be applied for intensity fluctuation, too. Usually the shot noise is Poisson distributed, so the variance in the optical induced voltage is related to the mean number of detected electrons N in $\sigma^2_{shot} = (\frac{qG}{C})^2 N$, where q is the electron charge, C is the integration capacitance of the photodetector, and G is any additional voltage gain. N is determined by power of the light to be detected.

A discrimination circuit following the detector digitizes the voltage by comparing it to a preset threshold, V_{th}. The error occurs with certain probabilities depending on the voltage, V, and logic circuit ambiguity range. At any given ideal signal level, V, assuming the actual detected level, v, is a Gaussian distribution with mean of V and variance of σ_{shot}, the probability density of v is:

$$p(v) = e^{-\frac{v-V}{2\sigma_{shot}^2}}. \qquad (3\text{-}1)$$

When the ideal voltage, V, is greater than V_{th}, the quantizer should output a '1'. But the actual detected voltage may be below V_{th} and causes false '0', so the probability of error at ideal voltage V is the probability that v is less than V_{th} :

$$P_e(V) = \int_{-\infty}^{V_{th}} p(v)dv = \frac{1}{\sqrt{2\pi}} \int_{-\infty}^{-\sqrt{(V-V_{th})/\sigma_{shot}}} e^{-u^2/2} du = Q\left(\sqrt{\frac{V-V_{th}}{\sigma_{shot}}}\right), \text{ if } V>V_{th}. \quad (3\text{-}2)$$

Similarly, when V is less than V_{th}, the quantizer should output a '0'. The probability of false '1' output is equal to the probability of v acceding V_{th}:

$$P_e(V) = \int_{V_{th}}^{\infty} p(v)dv = \frac{1}{\sqrt{2\pi}} \int_{\sqrt{(V_{th}-V)/\sigma_{shot}}}^{\infty} e^{-u^2/2} du = Q\left(\sqrt{\frac{V_{th}-V}{\sigma_{shot}}}\right), \text{ if } V<V_{th}, \quad (3\text{-}3)$$

where Q is related to the error function of the Gaussian process by $Q(x) = \frac{1}{2} erfc\left(\frac{x}{\sqrt{2}}\right)$.

Typically the photodetector has a noise current on the order of nA. In order to obtain sufficient signal to noise ratio, the photocurrent is usually more than 1000 times higher than the noise level. Figure 3-2 illustrates the error probability vs. detected voltage, $P_e(V)$, for a full-scale photocurrent $I_{max}=1\ \mu A$ through a 50 Ω load. The red and magenta curves are the error functions when the noise current is 1/1000 and 1/100 of the maximum photocurrent, respectively. It is clearly shown that error occurs mostly around the threshold point.

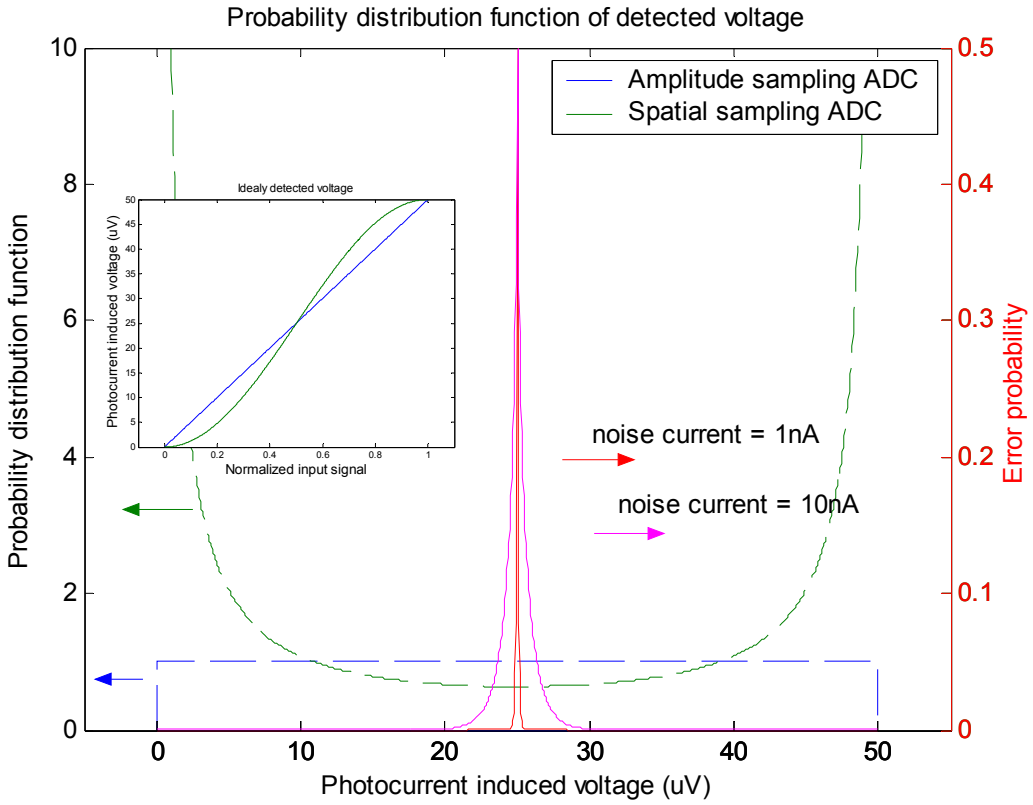

Figure 3-2: The uniform shape and concave shape pdf of output voltage for amplitude sampling and spatial sampling AOADCs respectively, along with error probability vs. voltage.

The total probability of errors of an OADC is the integral of $P_e(V)$ over all possible detected voltage in the full-scale range,

$$P_e = \int_0^{V_{\max}} P_e(V) f_V(V) dV \,, \tag{3-4}$$

where $f_V(V)$ is the probability distribution function of the detected voltage. Therefore if we can reduce the probability that the voltage falls into the vicinity of V_{th}, the total error will be decreased. In the conventional amplitude sampling OADC, the detected voltage is usually linear in the signal level, as shown as the blue line in the small drawing in Figure 3-2. Therefore it is evenly distributed within the full-scale range as shown as a blue

dashed line in Figure 3-2. In contrast, in the spatial-sampling AOADC, the transfer function of detected voltage vs. input signal level is a digital-like waveform, in the sense that most time the detected voltage is well above or well below the threshold. The green line in the small drawing shows a cosine shape transfer function, which results in a concave voltage distribution as shown as the green dash line in Figure 3-2. Therefore the detected voltage falls with least probability around the threshold, where errors most likely to happen. If the transfer function becomes steeper, the total error rate is even less. To compare immunity to shot noise or other equivalent fluctuation of the two types of OADCs the total error probability is calculated. When the photodetector is very quiet, as the noise current is 1 nA in the example, the total error probability is close for the two OADCs. It is 0.12% for the amplitude sampling OADC, and 0.07% for the spatial sampling AOADC. As the fluctuations become severer, the error probability increases to 1.01% and 0.64% respectively. It is shown that the spatial sampling AOADC provides better immunity from intensity fluctuation.

3.3 Spatial sampling AOADC design based on steerable gratings

In this approach, as shown in Figure 3-3, we have proposed an E-O grating/prism (GRISM) to translate the applied electric field into diffraction angle. The input light contains multiple discrete spectral lines, so when the light is diffracted by the grating, it is split into different angles according to the wavelengths, shown in colors in the figure. The RF signal to be converted is applied in parallel to an array of GRISMs. The RF electric field modulates the refractive index of the electro-optic material. Therefore the diffraction angle of the whole set of spectral lines is changed by the refractive index corresponding

to the RF signal amplitude. Steered by the linear Pockel's effect, the electric signal is linearly converted into a unique diffraction angle according to its amplitude. In the quantization part, since there are multiple spectral lines for each bit, we just need to use one optical collector to sense and quantize the image positions for each bit. In comparison with AOADCs based on tunable lasers, we have separated the tunable mode-locked laser challenge to a mode-locked laser source and steerable grating components respectively.

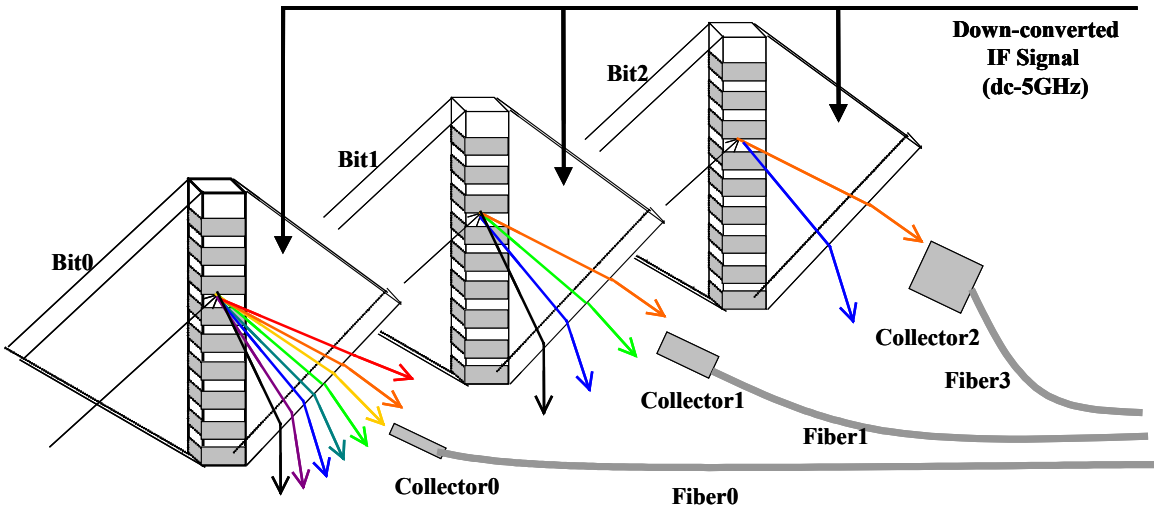

Figure 3-3: GRISM based AOADC.

Figure 3-3 shows the first three bits of the AOADC. Each bit has the same electro-optically steerable grating but different spectral line spaces and optical collector sizes. The line spaces of the spectra and apertures of the optical collectors are organized in a modulo 2 fashion, for example, if the line spacing is 50 GHz for the least significant bit (LSB), bit0, the line spaces for bit1, bit2, bit3… are then 100 GHz, 200 GHz, 400 GHz etc. And the spatial apertures of the collectors are set at half of the line space in the

diffracted pattern. Therefore, the detector will observe a digital sequence of "01010101…" when the diffracted pattern is steered by the electrical field.

A Grating/prism (GRISM) is a holographic volume grating sandwiched between two pieces of prisms. The electrodes will be placed in the prism region and the refractive index is modulated accordingly. The resolution of the AOADC depends on the number of resolvable lines of the E-O steerable grating at a given electric field. Figure 3-4 shows the grating only and its diffracted spectral pattern. Assuming a diffraction grating with M grooves with period of d, the diffraction angle corresponding to a specific λ_0 is given by:

$$nd\sin\theta - nd\sin\theta_i = m\lambda_0\,, \qquad (3\text{-}5)$$

where θ_i is the incident angle, which is 0 in the figure; θ is the diffracted angle, λ_0 is the wavelength in vacuum, n is the index of refraction and m is the diffraction order. Figure 3-4 shows that the grating split adjacent wavelengths by an angle of $\delta\theta$, while the angular spectral line width is $d\theta$.

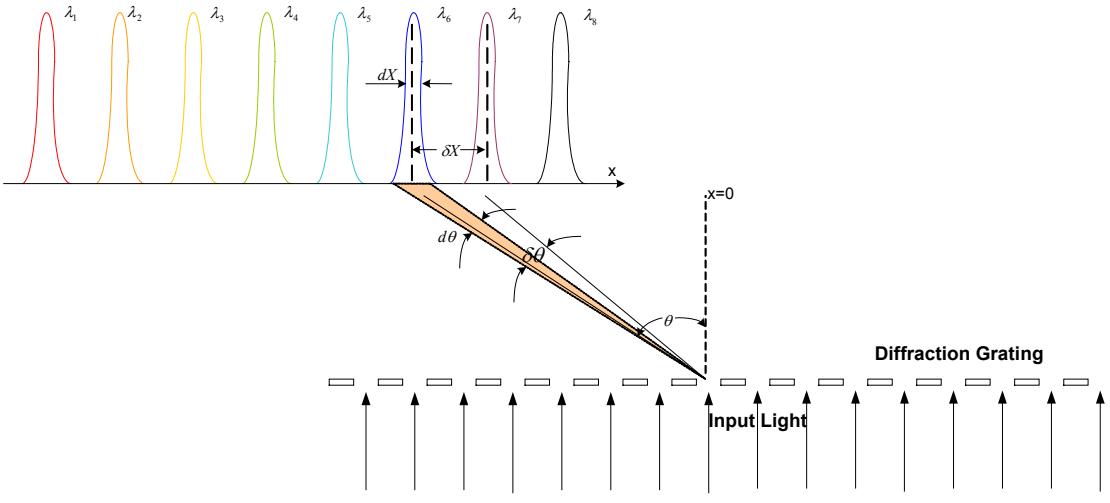

Figure 3-4: Diffraction pattern of a standard phase grating.

Equation (3-5) can be rewritten as $\sin\theta = \frac{m\lambda_0}{nd} + \sin\theta_i$. Taking the derivative with respect to *n*, the angular displacement caused by a change in refractive index is

$$\Delta\theta = -\frac{m\lambda_0}{n^2 d\cos\theta}\Delta n \qquad (3\text{-}6)$$

On the other hand, the angular resolution of a grating depends, theoretically, on the spectral characteristics of optical sources and parameters of the grating:

$$d\theta = \frac{\delta\lambda_0}{nd\cos\theta} + \frac{\lambda_0}{Mnd\cos\theta}. \qquad (3\text{-}7)$$

$\delta\lambda$ is the spectral linewidth. The linewidth of a laser is usually very narrow; therefore the first term in equation (3-7) can be neglected. Then the angular beam width can be written as

$$d\theta = \frac{\lambda_0}{Mnd\cos\theta}, \qquad (3\text{-}8)$$

which represents the Fraunhofer diffraction limitation caused by the total aperture size *Md* of the grating. Therefore the total number of resolvable lines is

$$N = \frac{\Delta\theta}{d\theta} = \frac{\Delta n}{n} \times mM\ . \qquad (3\text{-}9)$$

Equation (3-9) shows that the number of resolvable spectral lines is proportional to the refractive index modulation depth, the number of grooves and the diffraction order. In a non-linear optical material like $LiNbO_3$, the change of refractive index is modulated by the electric field ΔE via the electro-optic effect:

$$\Delta n = \frac{1}{2} n^3 \gamma \Delta E, \qquad (3\text{-}10)$$

where γ is the appropriate electro-optic coefficient. Substituting (3-10) into (3-9), the number of resolvable spectral lines can be rewritten as:

$$N = \frac{1}{2} mMn^2 \gamma \Delta E . \qquad (3\text{-}11)$$

There are two design issues that must be addressed to maximize the number N in equation (3-11), material selection and grating design. The material characteristics limit the resolution of the AOADC in terms of refractive index, n, electro-optic coefficient γ, and the maximum applicable voltage of the material. Most nonlinear electro-optic materials are able to achieve refractive index modulation, $\frac{\Delta n}{n}$, on the order of 10^{-4}. To compensate for the weak electro-optic effect, the resolving power of the diffraction grating has to be large, which, in an ideal case, is simply equal to mM. Therefore by taking advantage of high diffraction order, the resolution can be significantly improved.

In a practical diffraction grating, however, the resolving power not only depends on the number of grooves, but also the quality and shape of the grooves. Therefore the parameter mM in equation (3-11) should be substituted with a general expression of the resolving power, which is $\frac{\lambda}{d\lambda}$. $d\lambda$ is the minimum resolvable wavelength difference in the spectrum. Then equation (3-11) can be rewritten as:

$$N = \frac{1}{2} n \gamma \frac{\lambda_0}{d\lambda} \Delta E \qquad (3\text{-}12)$$

Some large size gratings have shown wavelength resolutions as small as 0.01 nm, implying a potential for the steerable grating to be high-resolution, but equation (3-12) is based on a static analysis. Its dynamic performance, however, faces some challenges:

● The RF bandwidth of the GRISM is limited by its size. To steer the diffracted light with the full aperture size of the length of the grating, electrode metal layers must cover the entire top and bottom surfaces of the GRISM. Therefore the size of the grating will significantly affect its steering speed. Because of its triangle shape, traveling wave electrodes are not suitable for the GRISM, so its speed is primarily limited by the RC time of a large electrode capacitance, $C = \frac{A\varepsilon}{t}$. Therefore large bandwidth requires the electrode size as small as possible. But to achieve sufficient resolution, the GRISM is usually designed to be a few centimeters, which usually limits the bandwidth to a few hundreds MHz. It is seen that there is a trade-off between resolution and sampling rate: the higher the resolution, the larger the size, and consequently the lower the speed.

● The second challenge is that the diffracted light loses its impulsive property in the time domain. The pulse train from a mode-locked laser is indeed a beat pattern of a series of continuous waves with fixed frequency difference, whose phases are locked. Since the grating splits different wavelengths (i.e. frequency) into different directions, at a specific position on the image plane only one frequency component is collected, thus a continuous wave of that frequency is observed. Therefore the diffracted beams are CW waves in different directions that continuously swept across the collector array as the RF signal varies. This means that a collector receives the spectral lines one after another continuously, and hence generates ultra fast optical pulses. For example, when a 20 GHz sinusoidal signal is applied to the GRISM, the beam sweeps from its minimum to its maximum angle in 25 ps. For resolution of 6-bit, there are 32 spectral lines in the LSB,

and all of them will pass the collector successively in the 25 ps, resulting a collected short pulse every 780 fs in average, corresponding to a frequency of 1.28 THz. The ultra-short pulses cannot be properly sensed by a practical photodetector. To solve this problem, a gated wave approach has been proposed to generate pulses without mode-locked, so every wavelength is impulsive in time. (See Appendix A) But solving the CW problem by the gated approach may sacrifice the advantage of low time jitter from mode-locked lasers.

3.4 Spatial sampling design based on an E-O leaky waveguide deflector

To enhance the RF bandwidth, a traveling wave electrode approach is a must and consequently an optical waveguide should be used. This is a structure similar to a conventional M-Z modulator. However there is only phase shift along the waveguide and no angular displacement in an M-Z modulator. However, if we made the waveguide leaky, the index change in the core region will result in an angular shift. This idea leads to an E-O leaky waveguide, in which the guided mode in the waveguide can be coupled into a radiation mode by introducing a prism whose refractive index is higher than that of the waveguide, as shown in Figure 3-5. Additionally, introducing a high index medium also solves the second problem of CW waves associated with steerable gratings. By choosing a non-dispersive material, all frequency components of the mode-locked pulses leak towards the same direction, so the leaky waves remain impulsive. Or, from the time domain point of view, a pulse leaking earlier from the waveguide travels slower in a denser medium but travels a shorter path, while the remaining power of the pulse propagating faster in the waveguide and leaks out later. Therefore there exists a plane, at which all leaked pulses arrived at the same time; hence a time-domain pulse can be

obtained at the image plane. It can be compared to a grating leaky waveguide exposed to the air. In that case, only -1, -2 … diffraction orders exist, but not the 0^{th} order, so the pulses arrive at the image plane one after another and actually compose an image line that is continuous in the time domain (no pulse). The designed leaky waveguide deflectors keep the impulsive characteristic of the optical signal in both spectral and time domain concerns.

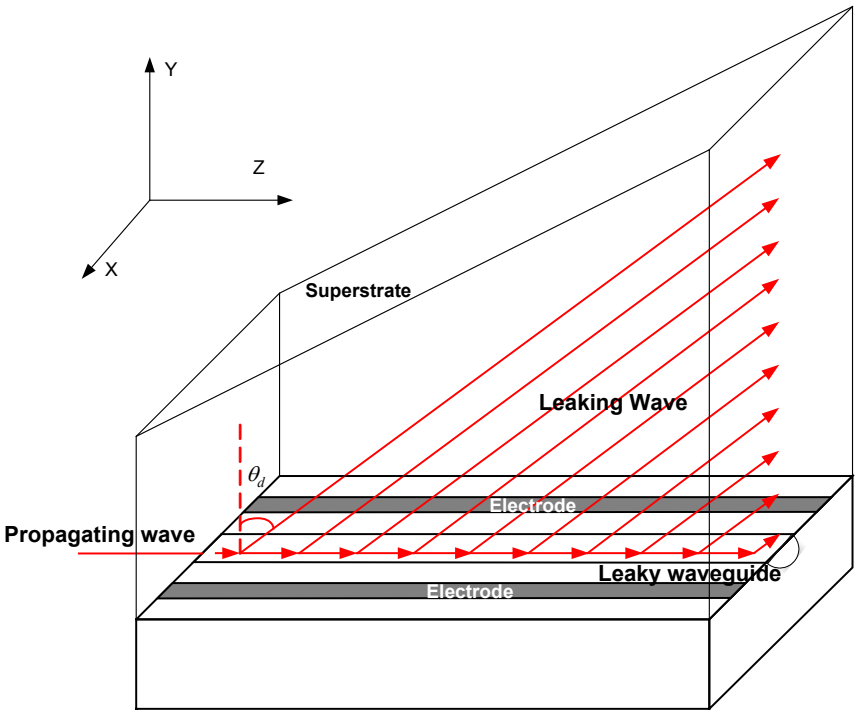

Figure 3-5: An E-O controlled leaky waveguide deflector working as a spatial sampler.

Another difference of the leaky waveguide deflector design is that it projects only a single image line to the image plane and thus requires multiple collector apertures in each bit of the sensor array. The design of the E-O leaky waveguide deflector is one of the major contributions of the thesis. We will discuss its operation in Chapter 4 and its design

and simulation in Chapter 5. Another important contribution, the investigation of the optical collector array, will be discussed in Chapter 6.

4. Leaky Waveguide Based All-Optical Analog-to-Digital Converter

4.1 Operation of the leaky waveguide based AOADC

The spatial sampler is the most important component in an AOADC working in the spatial domain. The speed and resolution of the sampler determine the overall performance of the AOADC. Our goal is to design an all-optical ADC operating at 40 GS/s with at least 6-bit of resolution that is able to process RF signals with a maximum instantaneous bandwidth of 20 GHz with SNR >38 dB.

A high-speed spatial sampler has been designed using an E-O leaky waveguide deflector as mentioned in section 3.3.3. The deflector incorporated with a collector array comprises the sampling and quantization of the AOADC, as shown in Figure 4-1, when short optical mode-locked pulses are inputted to the leaky waveguide.

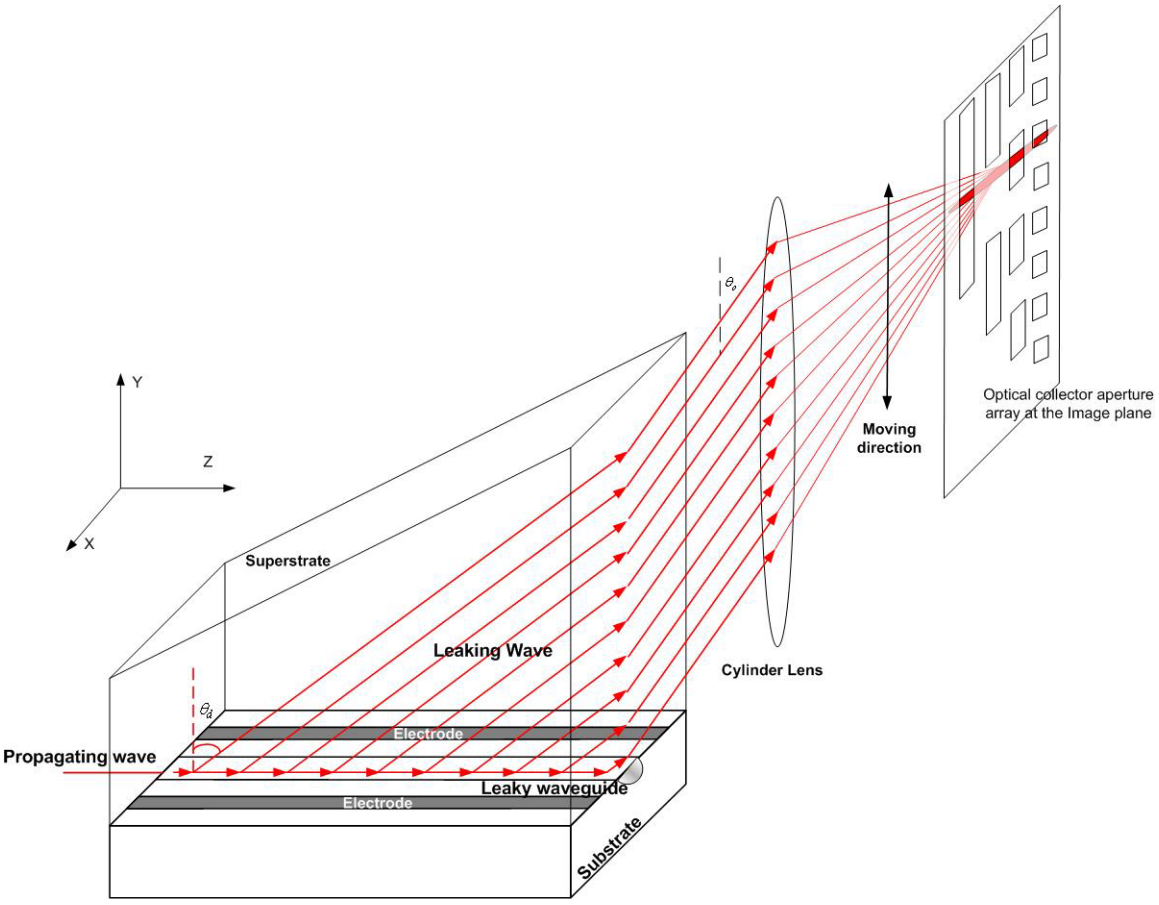

Figure 4-1: Conceptual diagram of the leaky waveguide all-optical ADC (laser source and detectors are not included). θ_d is the leaky angle, which is changed by the applied electric field. This shifts the position of the focused light at the image plane.

The leaky waveguide deflector on the left is composed of an embedded strip waveguide on the bottom, a superstrate on the top, and a buffer layer in between. When pulses from a mode-locked laser (not shown in the figure) propagate through the waveguide, part of the optical power leaks to the superstrate at angle θ_d and is transmitted into the air at θ_o. The leaked waves are then focused onto an image plane, where an optical aperture array is employed to collect the optical power and deliver it to remote photodetectors (not shown in the figure).

The sampling of the AOADC at rates above gigasamples per second is accomplished by the mode locked laser (MLL) and the leaky waveguide. The mode-locked-laser generates short optical pulses at a sampling rate f_{samp}. These pulses are sent through the leaky waveguide and are modulated by the electrical signal intended for A-to-D conversion. When the signal is applied to the traveling wave electrodes, an electrical field is created whose strength is proportional to the applied voltage. Due to electro-optical effect the refractive index of the waveguide will change accordingly. This structure is very similar to a conventional electro-optical phase modulator, except for the presence of a superstrate, whose refractive index is slightly greater than the index of the waveguide. As a result part of the optical power leaks out during its propagation. The leaked waves along the propagation path are focused on the image plane and become an image line that appears at time intervals of $1/f_{samp}$. The position of the image line is determined by the electric field the optical pulse experiences in the waveguide, so the leaky waveguide is essentially an electro-optical deflector. A detailed derivation will show that the leaky angle is linear in the applied voltage. By propagating the optical pulses generated by the MLL through the waveguide, the electrical signal to be converted is translated into line images at discrete times, and their positions reflect the voltage at sampling instances. In this way the sampling of the AOADC is accomplished in the spatial domain.

The leaky waves exit the superstrate at an angle of θ_o, as shown in Figure 4-1. A cylindrical lens focuses the leaky waves into an image line. The line moves up and down according to the applied voltage as illustrated in the figure. The position is digitized into 2^b quantization levels by b rows of aperture arrays. The maximum number of

quantization levels, as well as the resolution of the AOADC, is determined by the number of resolvable lines,

$$N = \frac{full - scale\ angular\ swing}{angular\ resolution}. \qquad (4\text{-}1)$$

4.2 Advantages of the AOADC

The AOADC is designed for sampling rates up to 40 GS/s and at least 6 bits of resolution. The digitized optical signals are easy to distribute in parallel using optical ribbon cable. Its designed resolution-sampling rate product is 1.28×10^{12} LSBs-Hz, which is higher than any other all-optical ADC. The proposed AOADC offers the general advantages of all-optical ADCs. First, the binary output signal and the sampling signal may be conveyed by optical fiber, so that both the detectors and the optical source may be remotely located for better space and thermal management. Secondly, the all-optical approach offers the added advantage of increased EMI immunity. Thirdly, because it is working in the spatial domain, it provides good immunity from optical transmitted optical power fluctuations and shot noise in the detectors. Furthermore, it solves some basic problems of existing all-optical ADCs and offers the following additional advantages:

- The AOADC is inherently high sampling

As with other hybrid or all-optical ADCs, the AOADC takes advantages of advanced mode-locked lasers, which can generate accurate optical pulses at ultra-high repetition rates. It employs traveling wave electrodes to sample the RF signal, enabling broadband modulation. As E-O materials and modulation techniques keep improving, the proposed ADC can easily take advantage of the increased speed.

- The AOADC improves resolution by using a single-channel configuration

First, recall the optical ADC schemes in the literature review. The hybrid ADCs have to split the post-sampled optical pulses into several electronic channels, causing intensity and timing mismatch [43]. M-Z based all-optical ADCs use individual interferometers to implement different bits; and similarly, tunable laser based all-optical ADCs generate different bits using different Bragg gratings, causing mismatch from bit to bit. It has been shown that channelization or splitting significantly degraded their resolution. The proposed AOADC just employs a single waveguide and generates a single image line, so there is not any time difference between different bits. Its quantization is accomplished by an integrated optical collector array, which can be precisely fabricated. The position and inclination of the image line on the collector array can be calibrated in advance, compensating for nonlinearities in the system and therefore allowing higher resolution.

- The AOADC allows easy generation of any digital code

The proposed AOADC is able to generate any code easily by simply changing the pattern of the optical collector apertures, which looks like a series of barcodes at different positions. Encoding is accomplished without adding any new hardware or software, so the collector array is essentially a spatial quantizer/coder. For the purpose of comparison, let's look at how other ADCs implement encoding. Every hybrid optical ADC and most of the existing all-optical ADCs which are working in the intensity domain have to use extra electronic circuitry or a piece of software to perform encoding, which significantly increases the system complexity and power dissipation. Taylor's M-Z based all-optical

ADC was able to obtain either a binary code or Gray code directly, but it is not flexible enough to achieve any other code. It is concluded that the proposed AOADC surpasses all the other competitors in terms of simple yet flexible encoding.

- The AOADC requires lower driving voltage

Because of its waveguide structure and traveling wave electrode configuration, the electro-optical leaky waveguide deflector requires about 20 V to achieve more than 40 resolvable lines. As a deflector, its driving voltage is much lower than existing electro-optical deflectors. Most E-O deflectors are based on cascaded prisms, which were bulky and expensive in the past [44]. Current advancements in material technologies have allowed prisms integrated on a $LiTaO_3$ wafer or polymer films, whose thickness is just a few hundred micrometers. An E-O deflector composed of tens of micro prisms generated by a domain inversion process on a $LiTaO_3$ wafer has been reported to obtain more than a 15^o angular sweep and 17 resolvable spots [45]. It is one of the largest deflection angles ever demonstrated. However its driving voltage is ±4.29KV and all of their experiments were done at DC. Using a similar process in a polymer, integrated E-O polymer beam deflectors have been proposed. L. Sun, et al. has built a polymer deflector with maximum deflection angle of ±8.4mrad at ±300V (DC) [46]. But it only provided 1.8 resolvable spots, and hence it is only barely suitable for switching applications. The existing prism-based optical deflectors show two major drawbacks: high driving voltage and low frequency. These problems arise from their dimensions. Usually the thickness of a wafer is at least several hundred micrometers, therefore very high voltage must be applied to achieve sufficient electric field, which are on the order of V/μm to obtain enough sweep

angle. On the other hand, to achieve sufficient resolution, the size of the prisms is usually on the order of millimeters or a few hundred micrometers. Since the electrodes must cover the entire prism region, its bandwidth is limited by the huge lumped capacitance or velocity mismatch between the optical wave and microwave signal, as well as the high voltage requirement, as discussed in Appendix C.

Some E-O deflectors for switching functions are based on Bragg diffraction [47]. These devices are very similar to an acousto-opitc beam deflector, in that a standing microwave induces a Bragg grating via electro-optic index modulation. The grating diffracts an optical beam at an angle associated with the microwave frequencies. This type of deflector was reported at frequencies in the frequency range of GHz. However, they were working in the on/off mode for applications like short optical pulse generation. Also, they usually use a pulsed magnetron with power of KiloWatts, which is prohibitive for ADC applications.

The proposed leaky waveguide deflector employs a waveguide structure with traveling wave electrodes. The typical gap between electrodes is 10~20 μm, which is one order of magnitude smaller than the thickness of prism-based deflectors (cf. Appendix C), therefore the leaky waveguide deflector requires much lower driving voltage. Also, the traveling wave electrodes can be carefully designed to obtain velocity match and impedance match, as conventional M-Z modulators have done for years. The electro-optically controlled leaky waveguide itself is a revolutionary design for an optical deflector.

- The AOADC consumes lower power

The proposed AOADC is designed to use a full-scale voltage of ± 20 V for a 50 Ω system, resulting in a power dissipation of about 4 Watts. The total power dissipation should also include the power consumed by the mode-locked laser and photodetectors. Since these two components are common devices used in most hybrid or all-optical ADC they will consume a similar amount of power for the same specified speed, therefore only the power dissipation of the sampler and quantizers need to be compared among different ADCs. For a hybrid ADC using conventional M-Z modulators, the driving voltage is fairly low; a typical V_π is 2~5V. Therefore its sampling part does not consume much power, but hybrid ADCs have to use multiple electronic ADCs as quantizers, which adds a significant power load to the system. For example, the wavelength-interleaving hybrid ADC was designed to generate digital codes at 100 GS/s by 8 electronic ADCs operating at 12.5 GS/s. Since usually a 10 GS/s electronic ADC consumes more than 4 Watts, then that makes the total power consumption in excess of 32 Watts. In the all-optical ADC part, M-Z based ADCs use multiple interferometers and hence consumed a lot power. The proposed AOADC requires much less power because of its low driving voltage, single channel configuration and passive quantizers.

4.3 Resolution of the E-O leaky waveguide deflector

4.3.1 Leaky angle

In the sampling stage, the leaky waveguide is the key component. It contains an embedded strip waveguide covered by a superstrate whose index of refraction is higher than that of the waveguide. The cross section of the leaky waveguide optical deflector

with its electrodes is shown in Figure 4-2. The optical power slowly leaks out to the upper space from the core region along a coupling length of about 3 cm. The long coupling length requires a weakly leaky condition, meaning that the optical wave is still well confined in the waveguide core region. To achieve the optical confinement, a thin buffer layer with refractive index $n_b < n_{eff}$ is deposited on top of the waveguide to separate it from the superstrate, otherwise the leaky coefficient would be too high, resulting in very short interactive length. The thickness of the buffer layer is one of the key parameters that control the leaky coefficient and we will discuss it in a great detail in the next chapter.

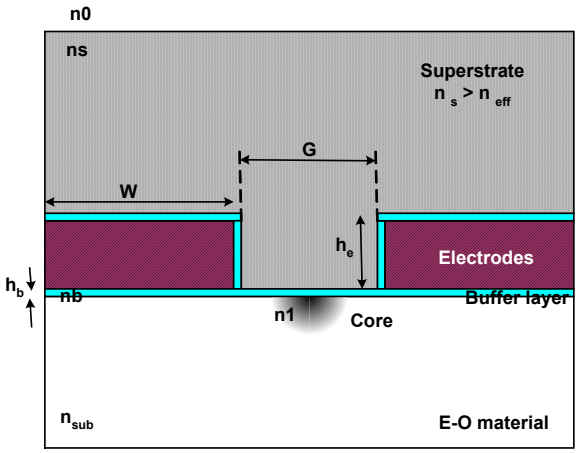

Figure 4-2: The cross section of a leaky waveguide with electrodes.

When an optical wave is propagating through the waveguide, in the presence of the buffer layer, the optical field is well confined in the core region and a small portion of it extends to the superstrate layer. Because the index of the buffer layer is less than the effective index in the waveguide, according to the boundary condition in the core/buffer interface, the orthogonal component of the propagation constant in the buffer layer is

imaginary and the amplitude declines exponentially, so there is no loss in the buffer layer assuming the buffer material is lossless at the operating wavelength. But when the buffer layer is thin, a tail of the optical power extends into the superstrate where the refractive index is greater than the effective index of the waveguide resulting in a real orthogonal component of propagation constant in the superstrate, which means radiation occurs in a direction normal to the propagation direction causing leakage.

The leaky angle, θ, is shown in Figure 4-1, is determined by satisfying Snell's law of refraction for the propagation constant along z, β, and the propagation constant in the superstrate, k_s, based on the dispersion relationship. Figure 4-3 shows the propagation constants in a phase matching diagram. Because the boundary condition forces a phase match along the tangential direction of the interfaces and all interfaces are parallel to each other, the z components are identical in every medium, thus $k_{eff\_z}=k_{1z}=\beta$. The index and the thickness of the buffer layer affect the leaky coefficient but do not change the leaky angle; therefore the buffer layer is not shown in the phase mach diagram. At the superstrate/air interface, the leaky waves hit the edge at an incident angle θ_i, and are transmitted into the air at an output angle θ_o.

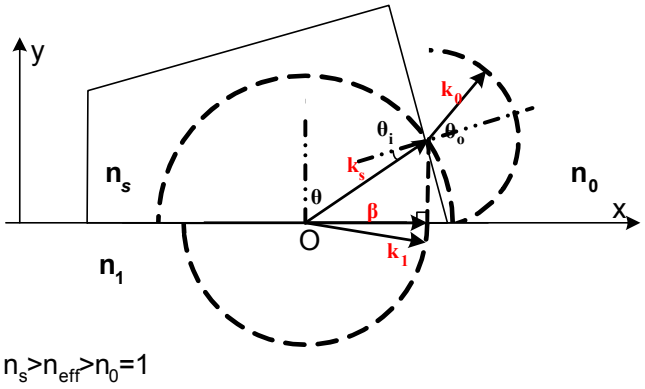

Figure 4-3: Phase matching diagram and leaky angle.

Following the boundary condition that tangential electric fields are continuous at interfaces, the leaky angle, θ, can be derived using the index of the waveguide, n_{eff}, and the index of the superstrate, n_s:

$$sin\theta = \frac{\beta}{k_s} = \frac{n_{eff}}{n_s} \qquad (4\text{-}2)$$

Generally, a waveguide supports multiple modes, and every mode corresponds to a different effective index of refraction, consequently modes are leaky at different angles, resulting in broadening of the beam width. Therefore, the waveguide should be designed for single mode operation only.

4.3.2 Total angular swing

The electrical signal applied to the traveling wave electrodes induces a refractive index modulation, Δn, and hence changes n_{eff} and further alters the leaky angle, as well as the angle at the superstrate/air interface. Because the induced refractive index modulation is very small, the output angle displacement is approximately linearly proportional to the electric field, thus the applied voltage is translated into angular displacement in the

spatial domain almost linearly, and any nonlinearity can be compensated in the spatial quantizer.

The leaky angle and output angle deviation induced by the electric field can be derived in the following way. Take the derivative of the leaky angle in equation (4-2) with respect to n_{eff}. The differential angle is given as:

$$d\theta = \frac{dn_{eff}}{n_s \cos\theta}. \tag{4-3}$$

This shows that when θ is near 90^o, the derivative $\frac{d\theta}{dn_{eff}}$ is approaching its maximum. Referring to equation (4-2), the maximum condition implies that n_s is just slightly greater than n_{eff}. But very small index difference leads to very small power leakage along the y direction, so the selection of superstrate material must be optimized for a large angular swing and sufficient leaky power.

The output angle at the superstrate/air interface can be calculated from Snell's law. Assuming the incident angle without applied electrical field is θ_i, the output angle θ_o is related to θ_i by:

$$n_0 \sin\theta_o = n_s \sin\theta_i. \tag{4-4}$$

The output angle displacement is therefore related to the change of θ_i by:

$$d\theta_o = \frac{n_s \cos\theta_i}{n_0 \cos\theta_o} d\theta_i = \frac{n_s \cos\theta_i}{n_0 \sqrt{1 - (\frac{n_s}{n_0} \sin\theta_i)^2}} d\theta_i. \tag{4-5}$$

Note that $d\theta_i$ is equal to $d\theta$, the angular displacement of the leaky angle. It is seen that the leaky angle swing is magnified at the interface by a factor of

$$f(\theta_i) = \frac{n_s \cos\theta_i}{n_0 \sqrt{1-(\frac{n_s}{n_0}\sin\theta_i)^2}}.$$

When the incident angle at the interface is near the total reflection condition, $f(\theta_i)$ is arbitrarily large. However, the selection of θ_i should be a compromise between the angular swing and output optical power, since near to total refection most optical power will be reflected.

Since $d\theta=d\theta_i$, equations (4-3) and (4-5) can be combined to obtain the direct relation between output angle alteration and index modulation dn_{eff}:

$$d\theta_o = \frac{n_s \cos\theta_i}{n_0 n_1 \cos\theta \sqrt{1-(\frac{n_s}{n_0}\sin\theta_i)^2}} dn_{eff}. \qquad (4\text{-}6)$$

The index modulation is linearly proportional to the applied electric field via the Pockel's effect:

$$dn = \frac{1}{2} n^3 \gamma d\vec{E}. \qquad (4\text{-}7)$$

Usually the effective index change is approximately equal to the change of refractive index of the waveguide material, i.e. $dn_{eff} \approx dn_1$. Substituting dn_{eff} into equation (4-6), $d\theta_o$ is related to applied field by

$$d\theta_o = \frac{1}{2} \frac{\cos\theta_i}{n_0 \cos\theta \sqrt{1-(\frac{n_s}{n_0}\sin\theta_i)^2}} n_1^3 \gamma dE \qquad (4\text{-}8)$$

Using a magnification factor $f(\theta_i)$ for conciseness, equation (4-8) can be rewritten as:

$$d\theta_o = \frac{1}{2}\frac{f(\theta_i)}{n_s \cos\theta} n_1^3 \gamma dE \qquad (4\text{-}9)$$

The Pockel's effect is usually weak and the typical induced index modulation $\frac{\Delta n}{n}$ is on the order of 10^{-4}. Because of the small index change range, the angle alteration $d\theta_o$ is almost linearly proportional to the applied electric field. This justifies the assumption that the input voltage is linearly translated into spatial angular displacement.

If the traveling velocity of the microwave signal is the same as the velocity of the optical wave in the waveguide, an optical pulse experiences the same index change everywhere through its propagation, and the leaky wave appears at the image plane as a clean and short pulse resembling the original. Therefore the physical dimensions of the electrodes must be carefully designed so that the RF signal velocity matches the velocity of the optical signal.

Two widely used electro-optical materials are $LiNbO_3$ and E-O polymers. Simulations were performed to illustrate their steering capabilities. The $LiNbO_3$ waveguide is assumed to be *x*-cut, for which the refractive index of the TE mode is typically 2.137. The applied electric field is parallel to the *z* orientation of the $LiNbO_3$ crystal to utilize its highest E-O coefficient γ_{33}, which is 30 pm/V. ZnS is considered for the superstrate, with refractive index of 2.282. The reasons for choosing ZnS will be discussed in chapter 5 as part of an implementation issue. Typical parameters for E-O polymer waveguides are chosen as following: the refractive index of core, cladding and superstrate are 1.62, 1.55

and 1.7, respectively, and its E-O coefficient is 100 pm/V. Figure 4-4 shows the angular swing simulations for the $LiNbO_3$ and E-O polymer based waveguides when the applied electric field changes from –3V/um to 3V/um, which is far below the dielectric breakdown and normal for various applications.

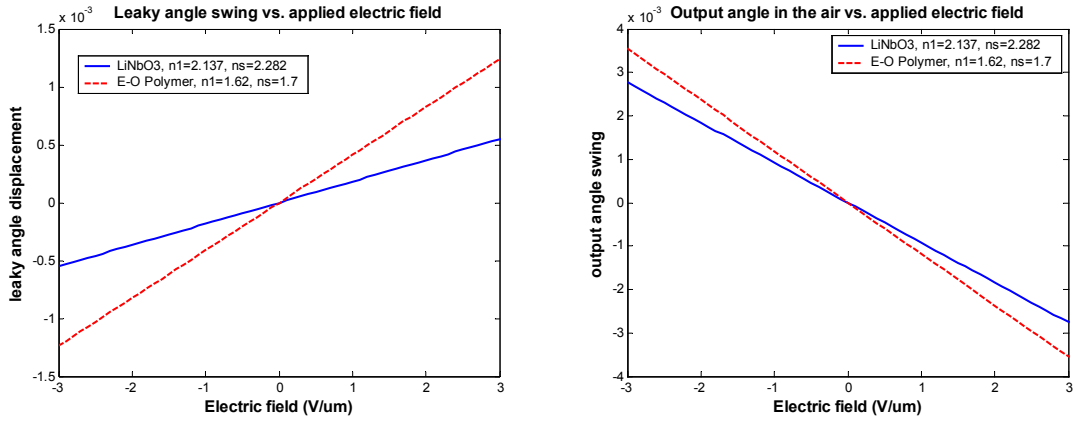

Figure 4-4: The leaky angle (left) and output angle (right) swing vs. applied electric field. Leaky angle is defined as the angle between wave propagation direction and the normal of the waveguide. The output angle is defined as the angle between the output optical wave propagation direction and the normal of the superstrate/air interface.

In the $LiNbO_3$ waveguide, the full-scale 6 V/um swing of the electric field induces 0.41‰ of change in the refractive index, corresponding to $\Delta n=8.4\times10^{-4}$. The refractive index change causes a leaky angle swing of 1.1 mrad as indicated by the blue line on the left in Figure 4-4, and an output angle swing of 5.5 mrad at incident angle $\theta_i=23.5^o$, as plotted in blue line on the right. It is seen that the superstrate/air interface magnifies the angular swing by a factor of 5. The angular swing per unit electric field in the $LiNbO_3$ waveguide is then 0.92 mrad/(V/m). A similar analysis is done for the E-O polymer waveguide. Because of the high electro-optical coefficient of the E-O polymer material, its induced refractive index is 0.8‰, corresponding to $\Delta n=0.0013$, which causes a greater

leaky angle swing of 2.5 mrad and output angle swing of 7.1 mrad, as indicated by red lines in Figure 4-4. The plots also demonstrate a linear function of angular displacement over the full-scale range of the applied electric field.

4.3.3 Angular resolution

The calculations of the total angular displacement show small angular swings on the order of a few millirads. According to equation (4-1), to achieve sufficient bit resolution, the angular linewidth of the output beam has to be very small. The minimum resolvable linewidth and its line shape are determined by the total length of the leaky region and the loss coefficient.

The magnitude of the leaky waves decays as an exponential function with loss coefficient, α, as shown in Figure 4-5. Here we have to define and distinguish the leaky coefficient and the loss coefficient. The leaky coefficient represents the loss caused by leakage only, while the loss coefficient considers all attenuation factors, including the leaky coefficient, waveguide loss and material loss. Therefore the loss coefficient is usually greater than the leaky coefficient.

Assuming the complex magnitude of the leaky wave at the origin is A, the contribution to an optical EM field from a segment of length dz in the leaky waveguide at angle θ can be written as:

$$u(z,\theta) = Ae^{-\alpha z} \cdot e^{-j(k_1 z - k_s z \sin\theta)} e^{-jk_s r} dz \qquad (4\text{-}10)$$

The leaky wave will be focused on an image plane by a lens. The magnitude at angle θ is the integral of contributions of all segments along the leaky waveguide:

$$U(\theta) = \int_0^L Ae^{-\alpha z} \cdot e^{-j(k_1 z - k_s z \sin\theta)} e^{-jk_s r} dz = \frac{Ae^{-jk_s r}}{K}(e^{KL} - 1), \quad (4\text{-}11)$$

where K is defined as $K = -\alpha - j(k_1 - k_s \sin\theta)$. (4-12)

Expression (4-11) is very similar to the diffraction pattern function of an oblique plane wave illuminating a single slit, except that the contributions along the width of the aperture are exponentially decreasing instead of uniform. Similarly, the magnitude profile is a *sinc* function; and the optical intensity reaches its maximum when all leaky waves at angle θ arrives at the image plane in phase, which implies $k_1 = k_s \sin\theta$ in Figure 4-5. The simulations confirm this.

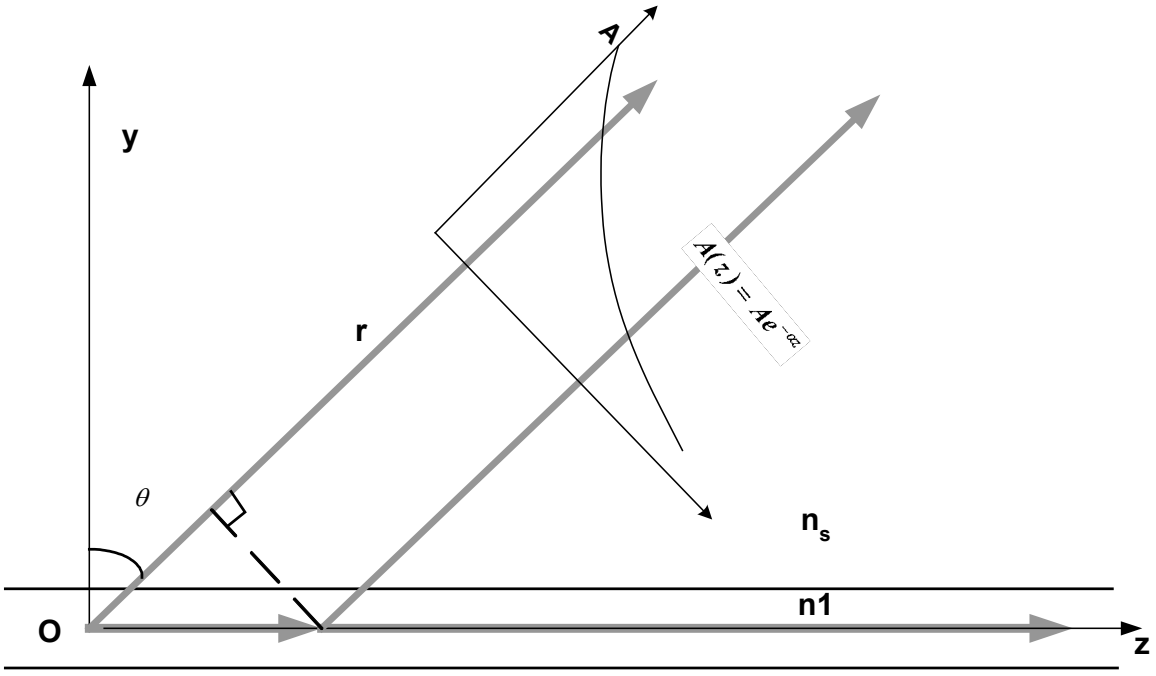

Figure 4-5: Beam analysis.

Figure 4-6 shows the intensity pattern of the image line under different loss coefficients with the same amplitude, A, at the origin. When n_1=2.137 and n_s=2.282, the maximum appears at θ=1.2127 rad, which is exactly the angle where the in phase condition gives θ =asin(n_1/n_s). Note that this angle is independent of the loss coefficient.

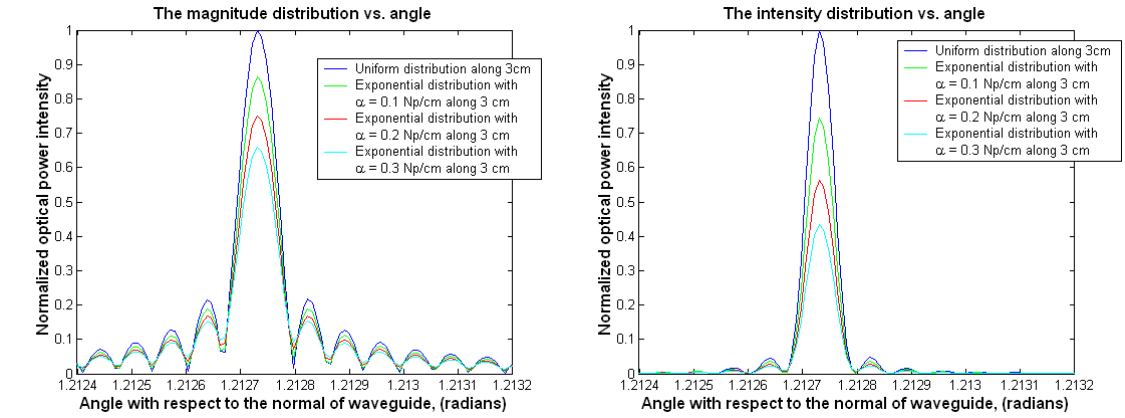

(a) (b)

Figure 4-6: Normalized optical magnitude (a) and power intensity pattern (b) as a function of angle for different loss coefficients.

The linewidth of the intensity function is determined by the total length of the leaky waveguide and the loss coefficient. If the optical wave magnitude is uniformly distributed, according to Fraunhofer diffraction theory the first zeros happen at:

$$\Delta\theta = \pm\frac{\lambda}{n_s L\cos\theta} \quad . \tag{4-13}$$

The zero-to-zero linewidth of a 3cm leaky waveguide at a wavelength of 1.55μm is 1.292×10^{-4} rad, and its half-maximum-full-width (HMFW) is 5.72×10^{-5}, close to half of the zero-to-zero linewidth. The linewidths are plotted vs. the length of leaky waveguide

in Figure 4-7 (left). It is clearly shown that a longer leaky waveguide leads to higher angular resolution.

In a weakly leaky waveguide, the linewidth is not sensitive to the loss coefficient. There is not a simple analytical expression for the image line intensity function of an exponentially decayed line source. The linewidths in are obtained by finding a numerical solution of equation (4-9). For example, when α=0.2 Np/cm, or 1.74dB/cm, 5.22dB of the optical power leaks out from the 3-cm waveguide and its angular minimum-to-minimum linewidth and HMFW are 1.3×10^{-4} and 5.786×10^{-5} rad, respectively. This shows that when the weakly leaky condition holds the linewidth is mainly determined by the diffraction limitation, which is inversely proportional to the length of the leaky waveguide. As shown in Figure 4-7, even when α=0.4 Np/cm, the linewidth is close to the ideal uniformly distributed case. For comparison, higher loss coefficients were also simulated. Since when α is not 0 there are no zeros in the intensity function, compares HMFW only. The simulation shows that the angular linewidth of a 3cm leaky waveguide changes from 5.72×10^{-5} rad when α=0 (uniform distribution) to 1.3×10^{-4} rad when α=2 Np/cm.

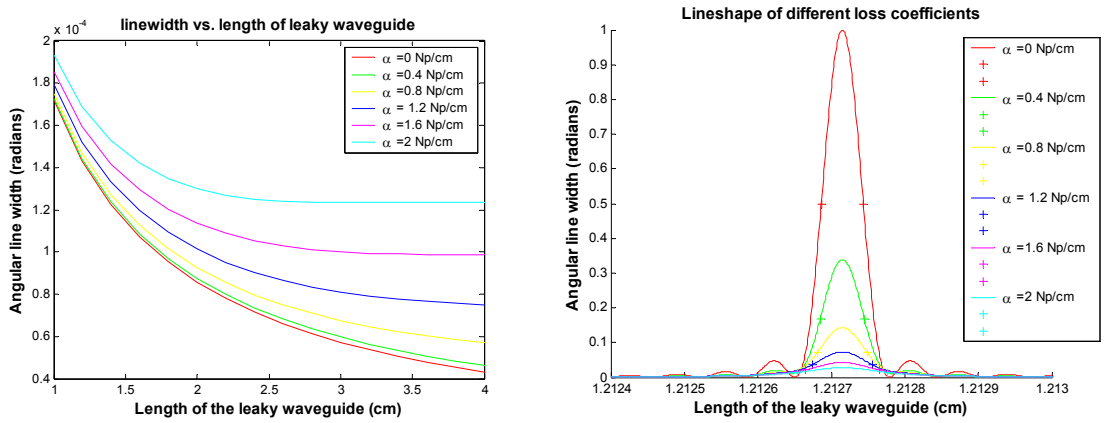

(a) (b)

Figure 4-7: The angular HMFW vs. the length of the leaky waveguide under different loss coefficients (a), and intensity pattern of different coefficient when the leaky waveguide is 3cm in length (b).

We chose the minimum-to-minimum angle as the linewidth throughout the thesis, so that when the size of collector apertures are designed to equal the linewidth of the image line we can still obtain a good distinction between code '1' and '0'. It is concluded that as one designs the waveguide for weakly leaky situations, its linewidth can be estimated using twice the Fraunhofer diffraction angle. It is useful to restate the linewidth clearly:

$$\delta\theta = \frac{2\lambda}{n_s L \cos\theta}. \tag{4-14}$$

4.3.4 Resolving power of the AOADC

The total number of resolvable image lines can be derived from equation (4-9) and (4-14):

$$N = \frac{d\theta}{\delta\theta} = \frac{\frac{1}{2}\frac{f(\theta_i)}{n_s \cos\theta} n_1^3 \gamma E_{FS}}{\frac{2\lambda}{n_s L \cos\theta}} = \frac{1}{4}\frac{n_1^3 f(\theta_i) L}{\lambda}\gamma E_{FS} \tag{4-15}$$

The resolution bit number is then $b=log_2N$. E_{FS} is the electric field induced by the full-scale voltage. Equation (4-14) indicates ways to achieve high resolution.

- Selection of materials: There are 2 parameters related to characteristics of the E-O material, the E-O coefficient, γ, and the refractive index, n_1. Two widely used materials are $LiNbO_3$, for which γ_{33} is 30 pm/V, and E-O polymers, for which γ is on the order of 100 pm/V. Note that polymers do not gain a factor of 3.3 in resolution because their refractive index is less than $LiNbO_3$. A typical improvement for polymers is 1.5 times greater swing angle.
- Design of incident angle at the superstrate/air interface: the magnification factor $f(\theta_i)$ at angles close to the total reflection angle can significantly increase the resolution. However the selection of θ_i must be made with the tradeoff in transmitted optical power in mind.
- Length of the leaky waveguide: The number of resolvable lines is proportional to the length of the leaky waveguide. However a very long interactive length generally limits the modulation bandwidth at $(f_{RF})_{max} = \frac{c}{4L(n_o - n_m)}$ [48], which arises from the velocity mismatch between the optical wave and RF wave. The selection of the length of the leaky waveguide shows the tradeoff between resolution and bandwidth of the AOADC.

Taking the simulation result from the previous section, the total angle swing is 5.5 mrad for a $LiNbO_3$ waveguide, and its linewidth is 1.3×10^{-4}rad. Theoretically, this swing covers more than 40 resolvable lines and enables an AOADC resolution of more than 6 bits.

4.4 RF bandwidth of the E-O leaky waveguide deflector

AOADCs operating at 40GS/s are capable of processing RF signals up to 20GHz. At 20GHz, the RF signal wavelength is 1.5cm in the air and even shorter in a dielectric media. Since the leaky waveguide is about 3cm in length, longer than the wavelength, traveling wave electrodes must be used. The approximate 3 dB modulation of the waveguide E-O modulator is given as:

$$f_{3dB}=\frac{1.4c}{\pi|n_m-n_o|L}, \text{ [49, 50],} \qquad (4\text{-}16)$$

where n_o and n_m are effective indices of refraction at optical and RF frequencies, respectively. To extend the bandwidth to 20 GHz, the difference in indices has to be less than 0.22, as implied by equation (4-16). $LiNbO_3$ is the most widely used electro-optic material. Its typical refractive index is about 2.2, but its permittivity at RF frequencies is ε_{r33}=29, corresponding to a refractive index of 5.4, much higher than that of the optical wave. Depending on the electrode configuration and superstrate material, the index of the RF signal is between the index of the $LiNbO_3$ substrate and the index of the superstrate because the electrodes are mainly surrounded by these two materials. Since the superstrate is a high refractive index material, the effective refractive index the RF signal sees along the electrodes is definitely higher than optical index in the waveguide, resulting in severe velocity mismatch in a $LiNbO_3$ waveguide covered by a superstrate.

To solve this problem, we proposed two approaches: one uses different materials and another uses a different configuration.

Table 4-1 compares 3 different E-O materials, $LiNbO_3$, E-O polymers and GaAs. Advanced polymer materials provide much lower dispersion in the index of refraction between infrared and RF frequencies, thus enabling broad bandwidth E-O devices. High-speed E-O polymer modulators operating up to 110 GHz have been demonstrated [51]. E-O polymers also feature superior E-O coefficients of more than 70 pm/V, and current reports have shown E-O coefficient as high as 126 pm/V [52], greatly enhancing the bandwidth-length product of E-O modulators. Moreover, their fabrication is compatible with semiconductor technologies, making polymers very promising in integrated optics.

Table 4-1: Property comparison of typical E-O materials

Properties	$LiNbO_3$	E-O polymer	GaAs
E-O coefficient (pm/V)	30	>70	1.5
Refractive index	2.2	1.6~1.7	3.5
Dielectric constant	29	2.5~4	10~12
Optical loss (dB/cm)	0.2	0.7~1.1	2
Maximum optical power	250mW	250mW	30mW

The E-O polymer material we use in the stripline electrode configuration has an optical refractive index of 1.62 and RF frequency dielectric constant of 3.0. The superstrate is assumed to feature indices of 1.7 and 2 for the optical waves and for RF frequencies, respectively. Also, the buffer layer has an optical refractive index of 1.55 and RF index of 2.5. By carefully designing the electrodes, a bandwidth of 40 GHz is possible. We will show the detailed design and analysis in the Chapter 5.

Although E-O polymers have many good properties and the technology is rapidly advancing, commercial products are still not widely available due to fabrication issues. Table 4-1 also shows a higher optical loss coefficient than $LiNbO_3$ due to *C-H* bond vibration overtones. In addition, their thermal stability still needs to be improved. As material technology advances, we can expect new polymer materials with improved performance. Therefore we have designed the AOADC based on E-O polymers. At the same time we also designed another leaky waveguide deflector based on $LiNbO_3$, currently the most popular E-O material.

As mentioned above, using the stripline electrode configuration shown in Figure 4-2 , a $LiNbO_3$ leaky waveguide is not able to achieve a velocity match of optical wave and the RF signal. To reduce its effective index at RF frequencies, the superstrate is removed so that the electrodes are partially exposed to the air, resulting in lower effective index. By carefully designing the electrodes, velocity match can be obtained over a broad band. Also, to keep the waveguide leaky, a high refractive index material is placed on the back of the $LiNbO_3$ substrate, as shown in Figure 4-8, so the optical waves will leak out from the back. Note that the configuration change does not affect its angular swing and resolution. The electrode configuration I choose to use is a coplanar waveguide (CPW), so that the waveguide positioned underneath the hot electrode experiences an RF field flux that is more concentrated. It has been shown that the CPW configuration results in a factor-of-two improvement in overlap between the RF and optical fields, relative to previous stripline configuration [53]. Therefore it is able to increase angular swing under given applied voltage.

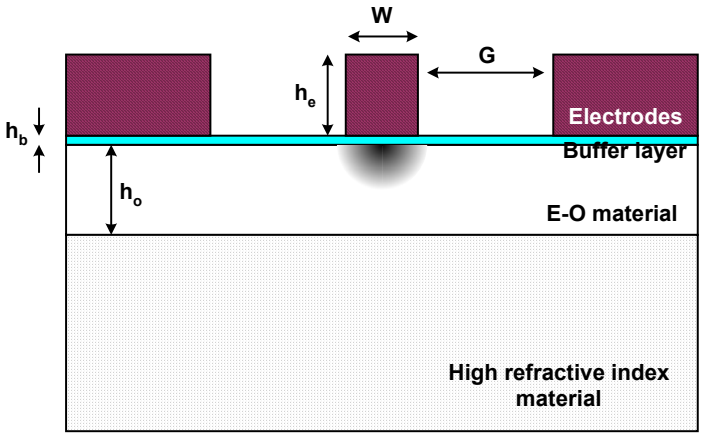

Figure 4-8: Cross section of leaky waveguide with high refractive index material on the back

In the next chapter we will discuss the detailed designs of these two configurations: E-O polymer waveguide with stripline electrodes and $LiNbO_3$ waveguide with CPW electrodes.

4.5 Challenges

The design has shown a capability of operating up to 40 GHz with at least 6-bits of resolution. The performance may be further enhanced by optimizing the design or using new materials. There are several challenges that must be addressed in improving its performance. Challenges in this section are mainly focused on the new components introduced in the novel AOADC: the electro-optical leaky waveguide deflector and the optical collector array.

4.5.1 Trade-off between resolution and sampling rate

As described in section 1.1.1, the AOADC's resolution is proportional to the length of the leaky waveguide, while the modulation bandwidth is inversely proportional to the length due to the transit time limitation. To increase the resolution-sampling rate product, the electro-optical leaky waveguide must be carefully designed to obtain velocity match between refractive indices at optical and RF frequencies. The benefit of resolution from increasing the length saturates when most of the optical power has leaked out from the waveguide, and extra length contributes less and less. The maximum length is also determined by fabrication techniques that affect how the process controls the waveguide profile, material uniformity and characteristics constant over a long range.

4.5.2 Trade-off between resolution and power dissipation

The total number of quantization levels is determined by the total angular swing under the full-scale voltage. Therefore, increasing the strength of the input signal can increase the angular swing and hence increase the number of resolution bits. However, to further increase resolution of the proposed AOADC by increasing the voltage, the input signal is first amplified, resulting in additional components and extra power dissipation. Moreover, increasing voltage leads to an undesirable square of the voltage increase in the power dissipation of the traveling wave electrodes. Therefore less driving voltage is always preferred.

4.5.3 Trade-off between resolution and leaky power

Optical power budget is another very important issue in the design. Before the leaked optical pulses reach the detectors, they have to propagate through various media and interfaces, and may lose a good amount of their power. Moreover the image is focused only in the transverse direction and spreads in the lateral direction, so the apertures of every bit just cover a portion of the image line and may not receive sufficient optical power. Therefore it is desirable to get more optical power leaking out from the waveguide, which means increasing the leaky coefficient for a fixed optical input power. But the simulation results in section 4.3 show that higher leaky coefficient actually leads to wider angular linewidth and, hence, lower resolution, so there is a compromise between optical power and resolution.

4.6 Conclusion

An AOADC based on an electro-optical leaky waveguide deflector was designed for 40 GS/s and 6-bits of analog-to-digital conversion. The waveguide structure of the E-O deflector has a lower driving voltage than GRISM and other prism-based AOADCs, resulting in lower power dissipation. The optical collector array is a passive quantizer and encoder that is able to generate any code easily. Also because of the AOADC's single channel configuration, it eliminates the channelization mismatch that many ADCs suffer from. The proposed AOADC is quite feasible. Advanced mode-locked laser technologies have shown capabilities to generate fast, accurate short pulses for AOADC applications, although we cannot pick up an exact product from the market yet. Photodetectors suitable for 40 GS/s quantization can be purchased as commercial products, though arrays are not commercially available. The electro-optical leaky waveguide deflector has been carefully

designed for high frequency operation. Finally, the optical collector array is proposed and will be shown later in Chapter 6. The analysis shows no major fundamental limitations to keep us from implementing the ultra fast AOADC. The deflector and the collector array were proposed and can be fabricated using advanced integrated optic technologies. However, there are many design issues to be addressed for designing the novel E-O leaky waveguide. In the next chapter we will show the key parameters in determining leaky coefficient, traveling wave electrodes impedance and velocity of RF waves, and provide estimated performance.

5. Analytical and Numerical Modeling for Design of the E-O Leaky Waveguide

The key enabling component of the proposed OADC is the E-O leaky waveguide deflector. Every detail of the deflector design affects the performance of the OADC. Its angular swing and linewidth determine the resolution of the OADC. Its electrode configuration limits the bandwidth of the OADC. And, as an active component, the E-O deflector consumes the majority of the power at the front end. In this chapter, we further analyze its optical properties and RF performance. An approximate leaky waveguide theoretical model is developed to work in parallel with numerical simulations. Two different structures, an electro-optical polymer waveguide using stripline electrodes and a *z*-cut Ti:$LiNbO_3$ waveguide using coplanar waveguide (CPW) electrodes, have been designed and compared.

5.1 Design issues

The major concerns in designing a leaky waveguide include deflector resolution, optical power budget, modulation bandwidth, and RF power dissipation. Among them the first two issues mainly involve optical design, while the last two are mainly electronic design issues.

5.1.1 Deflector resolution

Tracing down the path that the light travels in the OADC, we can see three factors affecting the overall resolution: the light source, the optical modulator, and the collectors. Among them the time jitter from the mode-locked laser and the spatial error from the collector array are less important in the design, since the time jitter from an MLL is a

given parameter for existing MLL technology, while the spatial error can be well controlled below the quantization noise in the OADC. It is the number of resolvable image lines of the deflector that impacts the overall characteristics most; therefore the design of the electro-optical leaky waveguide deflector is a major task in achieving a sufficiently high bit number in the OADC.

The number of resolvable lines of the leaky waveguide deflector has been given in equation (4-15):

$$N = \frac{d\theta}{\delta\theta} = \frac{1}{4}\frac{n_1^3 f(\theta_i)L}{\lambda}\gamma E_{FS}. \qquad (5\text{-}1)$$

When the E-O material is specified, there are just a few parameters that can be adjusted. The wavelengths we choose to use in the design are 1.55 μm for $LiNbO_3$ and 1.06 μm for the E-O polymer, respectively, following the wavelengths that typical $LiNbO_3$ and polymer E-O modulators employ.

The magnification factor $f(\theta_i)$ can be simply controlled by the shape of the superstrate wedge. As discussed in section 4.3, when the leaky waves hit the wedge edge at an angle near to the total reflection angle, $f(\theta_i)$, can be a value much greater than one, meaning that the angular displacement in output angle is much larger than that of the leaky waves in the superstrate. When the magnification increases as the incident angle approaches the total reflection angle, two problems arise. First, near the total reflection condition there is very little power coming out of the superstrate, making the OADC very inefficient in optical power budget. A solution is to coat the superstrate/air interface with proper anti-reflection (AR) films to reduce the reflection loss, since AR coatings do not change $f(\theta_i)$

but significantly increase the transmittance. In the designs we present in this chapter that $f(\theta_i)$ is chosen to be around 4~6, resulting in 60% of optical power reflection prior to having AR coatings. Second, at the steep edge of the curve of output angle vs. incident angle near total reflection, the function is away from its linear region. This problem can be solved by compensating for the nonlinearity at the collector array using variable apertures and spacing precisely following to the exact angular displacement function. In summary, the incident angle, or the shape of the superstrate prism, should be selected as a compromise between angular swing and available optical power.

The selection of the length of the leaky waveguide, L, involves issues of resolution in the optical domain and bandwidth in the RF domain as mentioned as a challenge in the Chapter 4. Here a quantitative estimation is provided for selecting the waveguide length. The amplitude of the leaky wave is an exponentially decaying function along the waveguide. The target leaky coefficient in our design is 0.1~0.3 Np/cm. The optical loss of a conventional Ti:$LiNbO_3$ waveguide modulator is usually 0.2 dB/cm, corresponding to 0.023 Np/cm, much smaller than the designed leaky coefficient. Generally the optical image line becomes narrower as the length increases. Figure 5-1 shows the angular linewidth in the worst case that total attenuation is 0.4 Np/cm, at which point only 1/10 of the total launched optical power remains after propagating 3 cm. For comparison, $\alpha=0$ is also plotted. It shows that when the length increases to about 10 cm in the presence of optical loss the linewidth saturated at around 5×10^{-5} rad and does not drop anymore, since almost no optical power remains at that distance. On the other hand, as the waveguide is made longer, the velocity match technique and fabrication process control over a long

length become more and more challenging. The selection of waveguide length shows the general trade-off between resolution and sampling rate in the OADC design. Throughout the design we use 3 cm as the waveguide length, because it provides sufficiently narrow linewidth and at the same time it is a typical length for most E-O modulators.

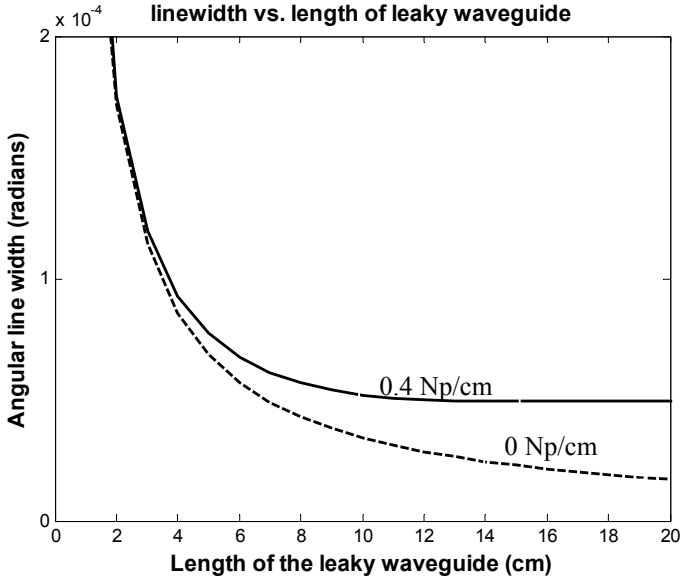

Figure 5-1: Comparison of the angular linewidth of the leaky waveguide for attenuations of α=0 and α=0.4 Np/cm

It is interesting to observe that the superstrate and buffer layer appear to have nothing to do with the resolution as shown in equation (5-1). Actually, the superstrate and buffer layer properties affect the resolution via the electric field, *E*. Given a fixed full-scale applied voltage, the electric field strength that the optical wave experiences in the waveguide is not only determined by the gap between electrodes, but also the dielectric constants of all media surrounding the electrodes, as well as the thickness of the buffer

layer. In order to avoid undesired optical loss due to absorption by the metal electrode, the gap must be much greater than the width of the waveguide, whose width is usually around 8 μm for Ti:$LiNbO_3$ waveguides and 6 μm for polymer waveguides. The electrode configuration will be determined by optimizing impedance matching and velocity matching given the superstrate and buffer layer properties.

5.1.2 Optical power budget

When an optical pulse propagates through the leaky waveguide, its power gradually leaks out to the superstrate, as shown in Figure 5-2. The leaky coefficient determines the available optical power that the OADC can use for sampling and quantization. The leaky coefficient, defined as α_L, is a very important parameter in the design of the OADC. Unlike the straightforward solution for leaky angle and its angular linewidth, which are obtained using ray optics, analysis of the leaky coefficient involves more wave theory, including solving for modes in a strip waveguide and determining evanescent waves. There are no explicit solutions for the propagation mode and leaky wave for a strip leaky waveguide. We will give a qualitative explanation in this section, and provide an approximate theoretical model and numerical simulation results later in this chapter.

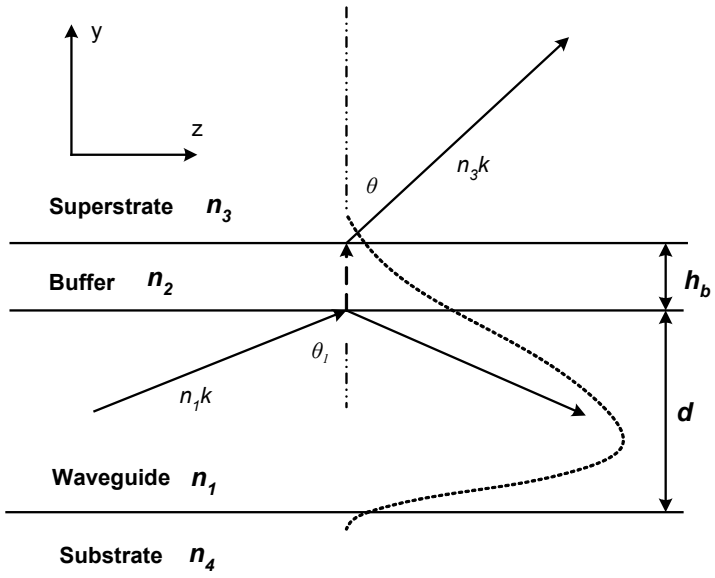

Figure 5-2: Side view of the leaky waveguide. θ is the leaky angle and θ_1 is the incident angle of the fundamental mode. The dotted line shows the field distribution of the fundamental mode.

The buffer layer plays a very important role in controlling the leaky coefficient. The refractive index of the buffer layer is less than the effective index of the propagation mode, n_{eff}. So the buffer layer working as a cladding that confines the optical wave in the waveguide and just allows a small portion of optical power to leak out, as shown in Figure 5-2. Intuitively, the leaky coefficient is inversely proportional to the thickness of the buffer layer. The buffer material also affects the leaky coefficient. Higher-index contrast results in better optical confinement, and hence leads to a lower leaky coefficient. As discussed in the previous section, the design of the buffer layer must also take into consideration the RF property requirements.

The superstrate controls the direction of the Poynting vector of the leaky wave, which can be expressed as $\theta = asin(\frac{n_{eff}}{n_s})$, where θ is the angle between the wave propagation direction and the *y*-axis. When n_s increases, the leaky wave is steered towards the *y*-axis and so the *y*-directed power density increases at a rate of $\cos\theta$. At the same time, as n_s increases, the index contrast between superstrate and the buffer layer increases, and the transmitted power from the buffer to the superstrate decreases because of higher reflectance. The final leaky power is a result of the competition between the increasing and decreasing factors, which sometime lead to a convex shape in a curve of leaky coefficient vs. superstrate index.

5.1.3 Modulation bandwidth and power dissipation

As described in Chapter 4, the major practice in enhancing the RF bandwidth of the E-O deflector is to reduce its effective index of refraction to match the refractive index of the infrared spectra. We have proposed two alternative solutions of a basic *x*-cut $LiNbO_3$ waveguide with stripline electrodes. The polymer waveguide provides inherent broadband operation up to 40 GHz. The *z*-cut $LiNbO_3$ waveguide with CPW electrodes is able to successfully reduce the effective index of refraction at RF frequencies by moving the superstrate with high dielectric constant away from the vicinity of the electrodes.

Using the traveling wave configuration, the electrodes of the E-O deflector must be loaded with a resistor that matches the characteristic impedance of the electrodes. The E-O deflector is designed for a 50 Ω system, meaning that the Z_0=R_L=50 Ω, where Z_0 is the characteristic impedance and R_L is the load resistance. If the characteristic impedance

deviates from 50 Ω, a portion of the signal from a 50 Ω front end will be reflected causing reduced delivered power and possible oscillation.

The designs for velocity match and impedance match are tightly entangled in the selection of gap, width and thickness of the electrodes and the thickness of the buffer layer. The electrodes are designed with the assistance of finite element analyses using High Frequency Structure Simulator (HFSS) available from Ansoft. The simulation results will be shown in section 5.3.

5.2 The theoretical model to study leaky coefficient

5.2.1 Slab leaky waveguide

A slab leaky waveguide is the simplest leaky structure. It is composed of four stacked layers which are, from the bottom to the top, substrate, slab waveguide, buffer layer and superstrate, as shown in Figure 5-2. Note that now the waveguide is an infinite large plate extending in the *x*- and *z*-direction instead of a strip. This model has been investigated in prism couplers, in which a prism is placed on the top of a film (slab waveguide) with an air gap of h_b to couple optical power into the film [54-56].

P. K. Tien and R. Ulrich derived the slab modes and the coupling coefficient using ray optics [54]. In this model the beam propagating along the waveguide hits the boundary with the buffer layer at an angle of θ_1, which it is then reflected with a complex refletion ratio of R. At the same time, a wave is excited in the superstrate at an angle of θ, because of penetration of the beam into the thin buffer and superstrate. The transmission

coefficient is defined as *T*. If the propagation constant in the *z*-direction, *β,* of this mode is known, the orthogonal propagation constants in media 1~3 can be found from:

$$k_{y1}^{\ 2} = (kn_1)^2 - \beta^2 \ ; \tag{5-2}$$

$$-k_{y2}^{\ 2} = \tau_2^{\ 2} = \beta^2 - (kn_2)^2 ; \tag{5-3}$$

$$k_{y3}^{\ 2} = (kn_3)^2 - \beta^2 . \tag{5-4}$$

Since $n_2<n_{eff}$, the propagation constant, k_{x2}, is an imaginary quantity indicating that the wave in the buffer layer is propagating along the *z*-direction with its amplitude decayed along the *y*-direction as $e^{-\tau_2 y}$. When the air gap is wide and finite, satisfying a weak leaky condition that $e^{-\tau_2 h_b} <<1$, an approximate expression of the transmittance, $|T|^2$, is given by Tien and Ulrich as:

$$|T|^2 \cong 4e^{-2\tau_2 h_b} \sin 2\Phi_{12} \sin 2\Phi_{32} . \tag{5-5}$$

Where $\tan\Phi_{12}= \tau_2/k_{y1}$, $\tan\Phi_{32}=p_2/k_{y3}$ for TE modes. So Φ_{12} and Φ_{32} are related to the *y*-components of the propagation constants. It can be easily derived that $2\Phi_{12}$ and $2\Phi_{32}$ are actually the phase shifts at the boundaries 1-2 and 3-2.

Using the transmittance, the leaky coefficient can be obtained as:

$$\alpha_L = \frac{|T|^2}{4d \tan\theta_1} = \frac{e^{-2\tau_2 h_b} \sin 2\Phi_{12} \sin 2\Phi_{32}}{d \tan\theta_1} . \tag{5-6}$$

Equation (5-6) shows that the leaky coefficient can be controlled by the refractive index and the thickness of the buffer layer if the superstrate material and the waveguide geometry are given. A typical buffer material is silicon dioxide, with an index of refraction of about 1.5. In a $LiNbO_3$ waveguide working at 1.55 μm, the decay factor, τ_2,

in the buffer is $\tau_2 = (\beta^2 - (kn_2)^2)^{1/2} \approx 6\times10^4$ Np/cm. Because of the fast decay of the optical intensity, the leaky coefficient is sensitive to the thickness of the buffer layer. As the design goal for the leaky coefficient is set as 0.1~0.3 Np/cm, the buffer layer is on the order of μm. The solid lines in Figure 5-3 shows plots of leaky coefficient vs. buffer layer thickness (left) and refractive index (right), respectively. The materials used in the model are $LiNbO_3$ with an effective index of 2.137 as the slab and ZnS with index of 2.282 as superstrate. Figure 5-3 also shows numerical simulation results as marks. The simulation package we use is BeamPROP from Rsoft. The computational core of the program is based on a finite difference beam propagation method [57, 58], which approximates the behavior of optical wave fields in media with microscopic variations in refractive index. It can be used to model devices that utilize evanescent coupling. The slab model matches the simulation very well at low leaky coefficients but differs from the simulation result at very high leaky coefficients. This is reasonable since the slab model is valid for a weak leaky condition, i.e. $\alpha_L << \beta$.

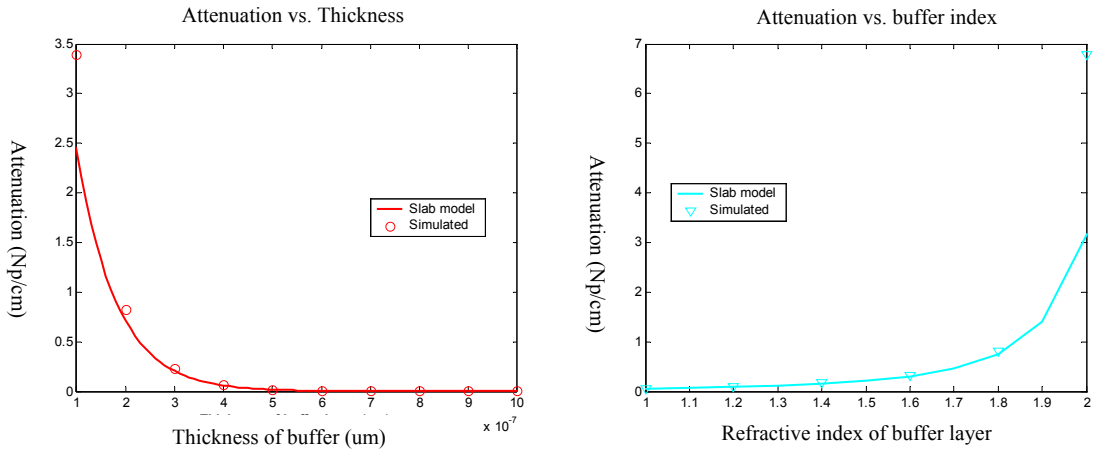

Figure 5-3: The leaky coefficient vs. buffer layer parameters for a $LiNbO_3$ waveguide.

Figure 5-4 shows a simulation result of relative optical power vs. propagation distance when the buffer is chosen to be SiO_2 with n_b=1.5 and thickness h_b=0.3 μm. The simulated leaky coefficient is 0.225 Np/cm, so after propagating 3 cm the optical power in the waveguide is reduced by about 6 dB (i.e., ¾ of power is leaked out). According to Tien's slab leaky model in equation (5-6), the calculated leaky coefficient is 0.232 Np/cm, close to the simulated result. Tien's slab leaky model provides a general guideline for selecting parameters for a more complicated embedded strip leaky waveguide, which is described in the next section.

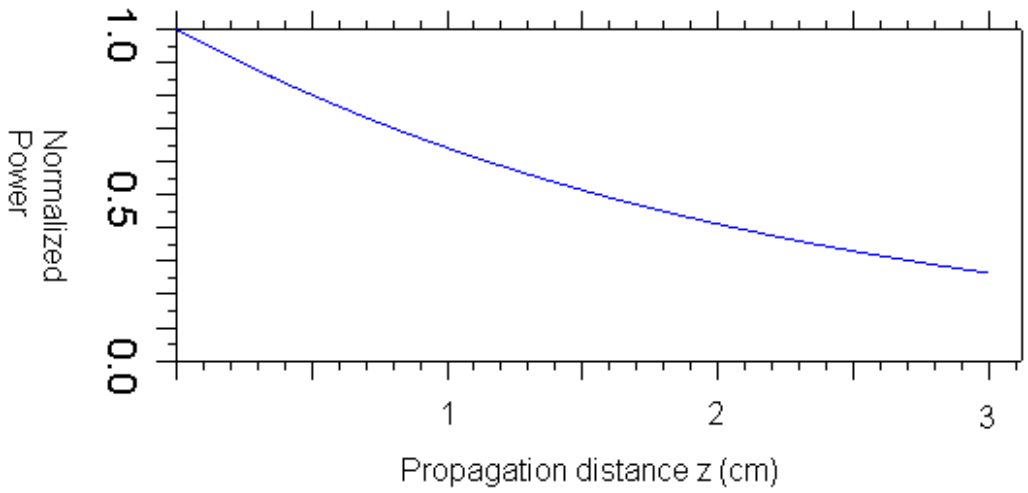

Figure 5-4: The relative power along the *z*-direction of a $LiNbO_3$ leaky waveguide. n_{sub}=2.137, n_1=2.145, n_b=1.5, n_s=2.282.

5.2.2 Embedded strip leaky waveguide model

The designed leaky structure is a 2-dimentional waveguide with a superstrate. The leaky coefficient can be determined by experiments or simulations, but in many cases we still need a theoretical model to understand the underlying physical principles and analyze its

behavior. Tien's model is based on ray optics and hence not very suitable for 2-dimensional structure analysis. Extending to 2 dimensions is very complicated. Also, it does not give solutions for the characteristic propagation constant, β, but instead it assumes β is known, so Tien's model is not quite straightforward when only the geometry of the waveguide is given. Therefore, we use EM field theory to develop an approximate model to analyze the design the leaky waveguide structure.

In a Ti:$LiNbO_3$ waveguide, the propagation channel is formed by a diffusion process, therefore the waveguide cross-section is approximately a semicircle with a graded index profile. Its mode solutions can be found only by using numerical methods. In an E-O polymer waveguide, the waveguide can be a simple rectangular strip, which we can approximately solve and find its characteristic propagation constant and leaky coefficient. In this section, we will develop an approximate solution for a rectangular embedded strip waveguide.

First, let's redraw the leaky waveguide cross-section in Figure 5-5. The height of the strip is *2b*, and its width is *2a*.

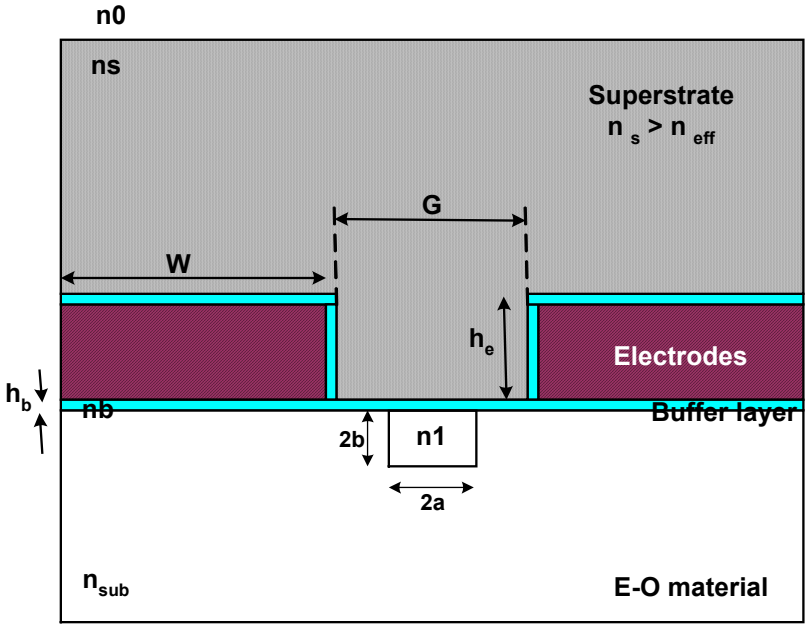

Figure 5-5: Cross-section of the rectangular strip waveguide.

There is no simple analytical solution for this structure [59]. To simplify the problem, we have to make the following assumptions:

1) The superstrate couples just a very small portion of the power out of the waveguide at every point along the waveguide but does not change the mode in the waveguide. This condition is valid in the design, since it is weakly leaky and the amplitude of the leaky wave is usually less than 1/1000 of that in the core region. With this condition satisfied we can assume that the buffer extends the upper half infinite space for solving the mode, so the problem is now to solve 9 regions in the space, as shown in Figure 5-6.

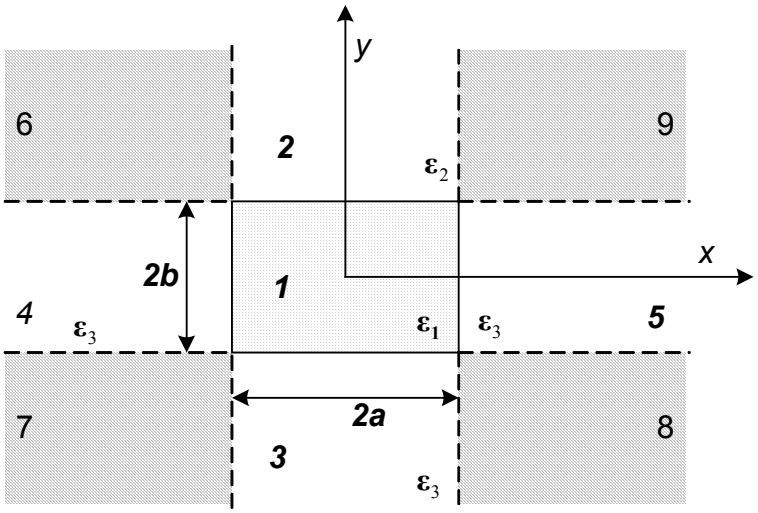

Figure 5-6: Strip waveguide solution regions.

2) The optical field is mainly concentrated in the core region (1). The optical powers in regions 2 through 5 are much less than that in the core region; and the optical powers in regions 6 through 9 is even less and, therefore, negligible. So the problem can be further simplified to 5 regions and 4 interfaces without considering the shaded areas in [59].

3) The propagation mode is far from cut-off, meaning that the incident angle of a wave is much larger than the critical angle of total reflection. This condition implies that the wave vector is almost parallel to the *z*-axis. Since the incident wave and the reflected wave are assumed to be plane waves, their EM fields are normal to the wave vector. Under this assumption, the transverse components of the EM field in the strip waveguide are much greater than its longitudinal components, and hence similar to a TEM mode, called quasi-TEM mode. There are two possible modes of a quasi-TEM wave according to the direction of the EM field: $E_{mn}^{(y)}$ mode, when E_y and H_x are much larger, and $E_{mn}^{(x)}$ mode, when E_x and H_y are much larger.

In the strip waveguide we designed, $\varepsilon_1 > \varepsilon_3 > \varepsilon_2$. We can assume the field distribution forms in different regions. In the core, i.e. region 1, the optical field is well confined and it is a standing wave in both *x*- and *y*-directions. Its transverse propagation constants are k_{x1} and k_{y1}. In regions 2 and 3, the fields are standing waves in the *x*-direction with propagation constants of k_{x2} and k_{x3}, respectively, and they are evanescent waves in the *y*-direction with decay factors of $jk_{y2}=\tau_2$ and $jk_{y3}=\tau_3$. Similarly, the fields in regions 4 and 5 are standing waves in the *y*-direction with k_{y4} and k_{y5}, and evanescent waves in the *x*–direction, with $jk_{x4}=\tau_4$ and $jk_{x5}=\tau_5$.

To satisfy the boundary conditions at the 4 interfaces, the longitudinal propagation constants in all regions must be the same,

i.e. $\beta_1=\beta_2=\beta_3=\beta_4=\beta_5=\beta$,

And the transverse propagation constants must satisfy:

$k_{x1}=k_{x2}=k_{x3}=k_x$, and

$k_{y1}=k_{y4}=k_{y5}=k_y$.

In every region *i, i*=1 to 5, the wave vectors satisfy dispersion relationship of:

$$k_{xi}^2+k_{yi}^2+\beta^2=k_i^2=w^2\mu_0\varepsilon_i. \qquad (5\text{-}7)$$

When the electrodes are arranged as shown in Figure 4-2, the electric field in the waveguide is mainly along the *x*-direction. To utilize the maximum E-O coefficient of γ_{33}, the *E*-component of the optical wave is parallel with the electric field, so the $E_{mn}^{(x)}$ modes should be excited in the designed structure. In the following derivation, we only

show the solution for $E_{mn}^{(x)}$ modes, or TE modes. The standing wave in the waveguide, i.e. region 1, can be expressed according to our assumption as:

$$E_{1x} = E_1 \cos(k_x x + \phi)\cos(k_y y + \psi)e^{-j\beta z}. \tag{5-8}$$

Following the derivation in [59] the orthogonal propagation constants in regions 1 to 5 can be found as:

$$\tan(2k_x a) = \frac{\varepsilon_1 k_x(\tau_5\varepsilon_4 + \tau_4\varepsilon_5)}{\varepsilon_4\varepsilon_5 k_x^{\,2} - \varepsilon_1^{\,2}\tau_4\tau_5} \tag{5-9}$$

$$\tan(2k_y b) = \frac{k_y(\tau_2 + \tau_3)}{k_y^{\,2} - \tau_2\tau_3} \tag{5-10}$$

τ_4 and τ_5 are related to k_x in $\tau_i^2+k_x^2=\omega^2\mu_0(\varepsilon_1-\varepsilon_i)$, i=4 or 5. Therefore equation (5-9) is actually a one-variable equation, and so k_x can be solved. Similarly, τ_2 and τ_3 are related to k_y in $\tau_i^2+k_y^2=\omega^2\mu_0(\varepsilon_1-\varepsilon_i)$, i=2 or 3. k_y can be found by solving (5-10). Figure 5-7 graphically shows the solution of equations (5-9) and (5-10). The first intersection other than the origin is the fundamental mode solution.

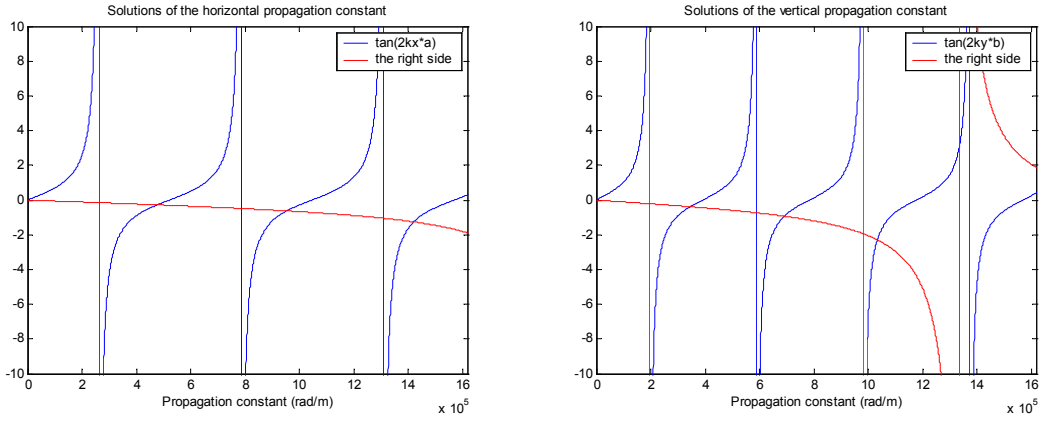

Figure 5-7: Graphic approach to solving equations (3-15) – horizontal; and (3-16) – vertical. (Assuming $2a$=8 μm, $2b$=6 μm.)

The two equations can also be solved by numeric methods. Consequently, the phase shift φ and ψ can be calculated. As the orthogonal components of the propagation mode are found, its longitudinal propagation constant is obtained by $\beta^2=k_1^2-k_x^2-k_y^2$.

For our leaky waveguide, we need to put another medium on top of region 2. Now we need to find the amplitude of the wave penetrating into the superstrate, which is separated from the strip waveguide region by a buffer layer, n_2, with a thickness of h_b. The amplitude of the electric field at the core/buffer interface, $y=\pm b$, can be calculated by satisfying the boundary condition that the tangential component, E_x, remains continuous at interface:

$$E_x(b) = E_1 \cos(k_y b + \psi). \tag{5-11}$$

Note that in the above expression the common part that represents the variations in the x- and z-directions is omitted, which are the same for region 1, 2, 3 and the superstrate. The wave in the buffer layer, i.e. region 2, is an inhomogeneous wave propagating in the z-direction and decaying in the y-direction. In the presence of the superstrate, part of the wave will be reflected at the buffer/superstrate interface. When a weakly leaky condition is assumed, the amplitude of the wave at the buffer/superstrate interface is very small and hence the reflected wave is even smaller, so the impact of the reflected wave on the mode propagating in the core is negligible. Calculation of the reflection follows the same rule as homogeneous waves:

$$T = \frac{2k_{y2}}{k_{y2}+k_{ys}} = \frac{2j\tau_2}{j\tau_2+k_{ys}}. \tag{5-12}$$

Therefore the electric field amplitude at the buffer/superstrate interface, $y=b+h_b$, is:

$$E_s = TE_x(b)e^{-jk_{y2}h_b} = TE_1\cos(k_y b + \psi)e^{-jk_{y2}h_b}\,. \tag{5-13}$$

The leaky wave in the superstrate region propagates along both +y- and +z-directions. Therefore the fields E_x and H_z can be expressed as:

$$E_{xs} = TE_1\cos(k_y b + \psi)e^{-jk_{y2}h_b}e^{-jk_{ys}(y-(b+h_b))} \tag{5-14}$$

$$H_{zs} = \frac{E_{xs}}{\eta_s}\cdot\frac{k_{ys}}{k_s}\,, \tag{5-15}$$

where η_s is the wave impedance, $\eta = \sqrt{\mu/\varepsilon}$, and k_{ys}/k_s is related to the leaky angle in $\sin\theta = k_{ys}/k_s$. Therefore the Poynting vector along the y-direction is:

$$S_s = E_{xs}H_{zs} = \frac{E_{xs}^{\,2}}{\eta_s}\sin\theta = \frac{1}{\eta_s}(TE_1\cos(k_y b + \psi)e^{-jk_{y2}h_b})^2\sin\theta\,. \tag{5-16}$$

The radiated power from the area corresponding to unit length in z and unit width in x is then:

$$P_L = S_s \times 1 unit\ area = S_s. \tag{5-17}$$

To compute the leaky coefficient, the z-directed power flow in the waveguide must be calculated. Similar to the calculation of the Poynting vector in the superstrate, the Poynting vector along the z-direction at a point of the cross section can be derived as:

$$S_{1z}(y) = E_x(y)H_y(y) = \frac{E_{1x}(y)^2}{\eta_1}\frac{\beta}{k_1} \approx \frac{E_{1x}(y)^2}{\eta_1} \qquad (\because \beta \approx k_1) \tag{5-18}$$

Note that, since the field distribution along the x-direction is same in region 1, 2, 3, and the superstrate, the integral along the x-direction can be omitted for conciseness.

Corresponding to a unit length in the *x*-direction, the power is an integral of the Poynting vector over the waveguide cross section:

$$P_{1z} = \int_{-b}^{b} S_{1z}(y)dy = \frac{E_1^2}{\eta_1}\int_{-b}^{b}\cos^2(k_y y+\psi)dy = \frac{E_1^2}{2\eta_1}\int_{-b}^{b}[\cos(2(k_y y+\psi))+1]\,dy$$

$$= \frac{E_1^2}{4\eta_1 k_y}\int_{2(-k_y b+\psi)}^{2(k_y b+\psi)}[\cos u+1]\,du = \frac{E_1^2}{4\eta_1 k_y}\{\sin 2(k_y b+\psi)-\sin 2(-k_y b+\psi)+4k_y b\}.$$

As assumed, the optical power is concentrated in the core region. It implies that the *E* and *H* fields at $y=\pm b$ are small, meaning that $\pm k_y b+\psi$ are close to $\pm n\pi+\pi/2$, where *n* is an integer. When the waveguide is operating in a single mode, i.e. $n=1$, $2k_y b\approx\pi$ there is only one field maximum near the center of the strip. The power flow in the *z*-direction can be estimated as:

$$P_{1z} \approx \frac{E_1^2}{4\eta_1 k_y}\{\sin(\pi)-\sin(-\pi)+2\pi\} = \frac{E_1^2\pi}{2\eta_1 k_y}. \qquad (5\text{-}19)$$

Therefore the optical power leaky coefficient can be derived by dividing equation (5-17) by (5-19). The optical power leaky coefficient is:

$$\alpha_{PL} = \frac{P_L}{P_{1z}} = \frac{\pi\eta_1 T^2}{2k_y\eta_s}\cos(k_y b+\psi)^2\sin\theta e^{-2\tau_2 h_b}, \qquad (5\text{-}20)$$

so the field leaky coefficient is half of the power leaky coefficient;

$$\alpha_L = \alpha_{PL}/2. \qquad (5\text{-}21)$$

Equation (5-21) shows that the leaky coefficient depends on the mode characteristic, buffer thickness and refractive index of the superstrate. The theoretical model helps us to

understand the behavior of the leaky waveguide and allows us to manipulate it by using proper design parameters.

5.3 Numerical analyses of the E-O leaky waveguide deflector

While the leaky coefficient should be finally analyzed by experiments, numerical analyses are powerful tools to investigate the characteristics of the leaky waveguide before pursuing an expensive fabrication. In our design, BeamPRO from Rsoft is employed to numerically simulate mode characteristics and leaky coefficient of the designed waveguides. Similarly, since there is no way to find an explicit theoretical formula to express the effective index of refraction and characteristic impedance at RF frequencies for complex electrode configurations, numerical approaches are also used in analyzing the RF performance. We use HFSS from Ansoft to simulate the electrical characteristics of the designed E-O deflector. In this section, we will show the numerical simulation results of polymer and *z*-cut Ti:$LiNbO_3$ leaky waveguides. Simulations of optical and electrical performance of an *x*-cut Ti:$LiNbO_3$ waveguide have been performed as well. But since it is not able to achieve velocity matching at 20 GHz, as we mentioned in the last chapter, we do not show its results in this chapter. Instead the simulation results are demonstrated in Appendix D for convenience of comparison.

5.3.1 E-O polymer leaky waveguide with CPW electrodes

5.3.1.1 Polymer leaky waveguide design

Nonlinear optical (NLO) polymers have been investigated for more than two decades and over 100GHz modulation have been demonstrated. Our simulation of the designed

polymer leaky waveguide uses some typical properties reported for E-O polymers. The proposed polymer leaky waveguide is designed as a rectangular embedded strip waveguide, as shown in Figure 4-2. The waveguide can be fabricated by photolithography and ion etching processes. After forming the proper shape of the waveguide, an electrode poling process is used to align the molecular dipolar electrets along the polling field. The poling process is necessary because the Pockel's effect requires the breaking of the centersymmetry of the material. Advanced polymer materials have shown E-O coefficients over 100 pm/V. We use 100 pm/V in our design to reflect state-of-the-art technologies. After the electrode poling process, the electrodes are removed and proper top buffer layer and modulation electrodes are deposited. Typical E-O polymers have higher absorption loss than $LiNbO_3$, especially around a wavelength of 1.55 μm, so most polymer E-O devices operate at shorter wavelengths. Therefore the designed waveguide is analyzed and simulated at 1.06 μm.

The refractive index of the waveguide depends on polymer materials and fabrication processes; it is usually 1.60~1.65. In our design we use 1.62 as a typical value. We will also demonstrate simulations of optical characteristics versus the core index change. The waveguide is 6 μm in width and 3 μm in height, which, again, is typical for E-O polymer modulators. The refractive index of the cladding and buffer layers is 1.55, and the index of the superstrate is 1.70. The thickness of the buffer layer is very important and it is chosen using equation (5-21) and simulations so that the field leaky coefficient, α_L, is between 0.1 to 0.3 Np/cm to obtain enough output optical power at a minor reduction in

the angular resolution. The thickness of the buffer layer we finally chose is 1.2 μm. The above parameters are summarized in a refractive index profile as drawn in Figure 5-8.

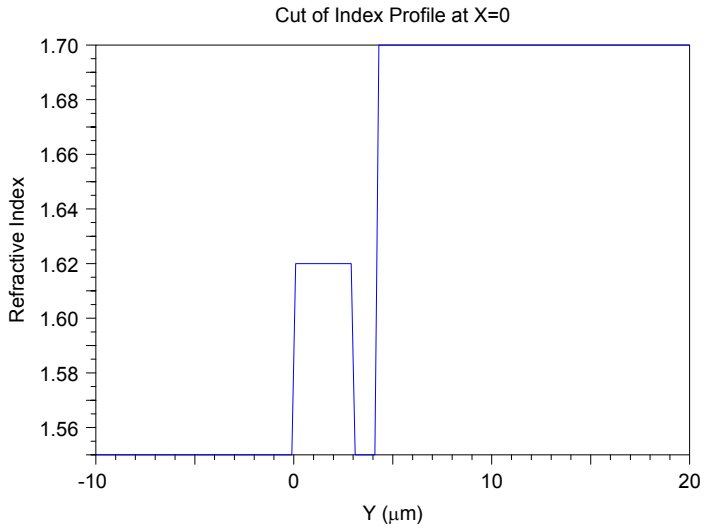

Figure 5-8: Refractive index profile of the E-O polymer leaky waveguide.

The simulated electric field amplitude distribution of the optical propagation mode is shown in Figure 5-9. The left image in the figure shows the field distribution in an E-O polymer waveguide without a superstrate. It implies, in principle, that the wave is totally confined and propagating mode without leakage, and the simulation verifies it. The simulated effective coefficient is n_{eff}=1.61177 as shown on the top of the figure. In this case n_{eff} is a real number, indicating not a leaky wave. Then when a superstrate with refractive index of 1.7 is placed on the top of the waveguide with a buffer layer of 1.2 μm, the mode becomes leaky, as shown in the field distribution on the right in the figure. The effective refractive index of the leaky mode is n_{eff}=1.611769+j3.224×10^{-6}, whose imaginary part represents the leaky characteristic of the mode. At a wavelength of 1.06 μm the complex propagation constant, Γ, is defined as $\Gamma=\beta+j\alpha_L=2\pi\ n_{eff}/\lambda$, which is

9.55×10^{4}+j 0.191 cm^{-1}, whose imaginary part is the leaky coefficient, which is 0.191 Np/cm for the leaky structure. The simulation also shows that the presence of the superstrate introduces just a minor change in the mode effective index, proving that the assumption we made in the theoretical analysis is correct.

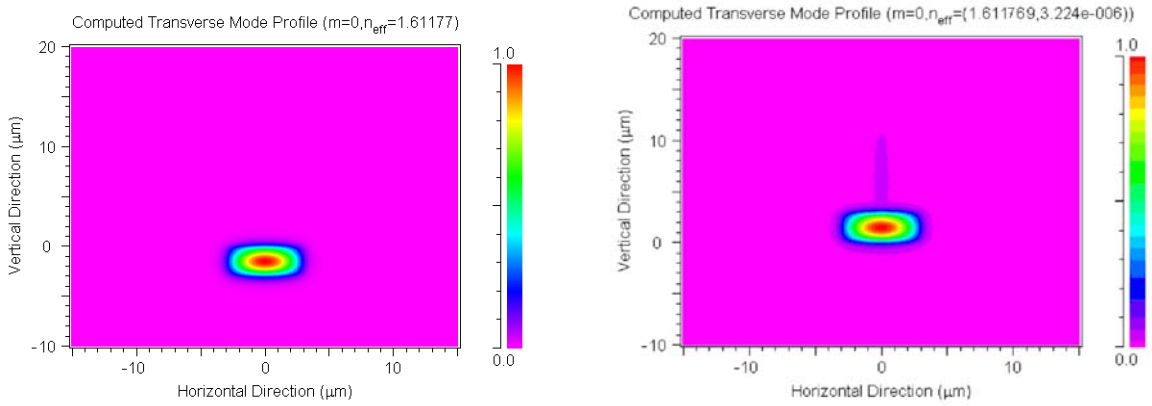

(a) (b)

Figure 5-9: Optical field distribution of non-leaky mode (a, without superstrate) and leaky mode (b, with superstrate).

As designed, the leaky wave is very weak, so it is barely seen in the color scale figure shown above. To illustrate the leaky mode clearly, we plot in Figure 5-10 the one-dimensional field distributions along the *x*- and *y*-directions crossing the waveguide center at x=0 and y=1.4μm.

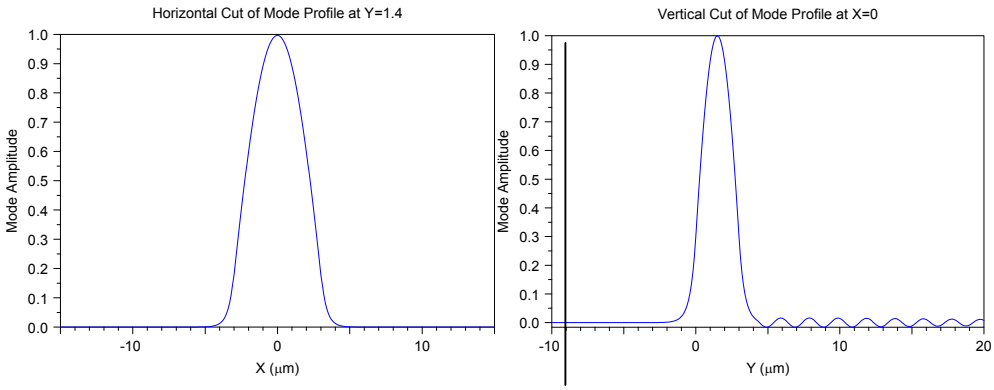

Figure 5-10: The field distribution profile along the *x*- and y-directions.

The figure shows a clear difference between the field distribution profiles in the *x*- and *y*-directions; there is an oscillation in the +*y*-direction, indicating radiation. That means part of the optical power will leak into the upper space. The undulation period is measured to be 1.95 μm, which is related to the radiation propagation constant in this direction, k_{ys}. Using the theoretical model, we can find the period by $\sqrt{n_s^{\,2} - n_{eff}^{\,2}}\,k_0$, resulting in *2* μm. The simulated value matches with the calculated result very well. Figure 5-11 shows the simulated optical power flowing in the waveguide. Due to the limitation of computation time and memory, the total propagating distance is set to be 1 cm, instead of 3 cm as we designed. After 1 cm, a significant part of the optical power leaked out from the waveguide and 67% of the total launched power still remains in the waveguide, corresponding to about 0.2 Np/cm attenuation. The mode simulation result and the propagation simulation result match each other perfectly. If the leaky waveguide extends to 3 cm, 70% of the total power will leak out.

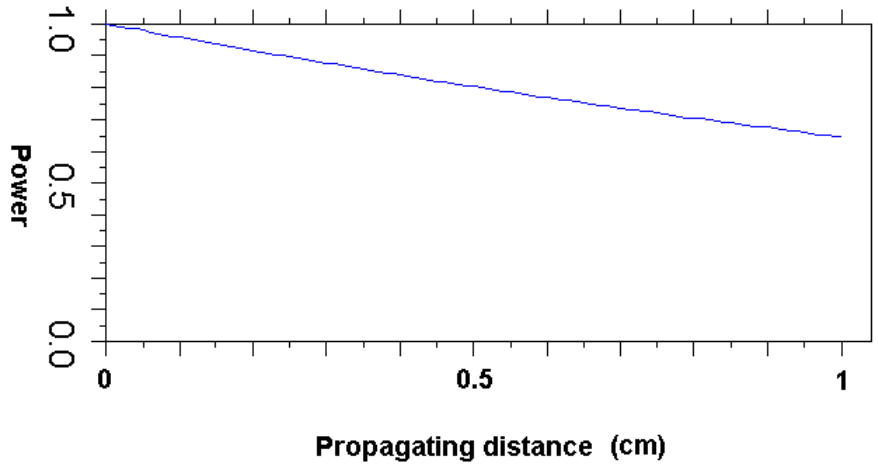

Figure 5-11 Optical power in the waveguide vs. propagating distance in the *z*-direction

5.3.1.2 Parametric analysis of optical properties

The leaky coefficient is a major concern in the optical power budgeting and affects the angular resolution of the deflector. The leaky coefficient, α_L, is affected by many parameters. Its sensitivity to those parameters determines whether or not it is feasible to achieve desirable properties by controlling practical fabrication conditions. This section will discuss how the leaky coefficient changes when altering core index, buffer layer thickness and superstrate material.

- Leaky coefficient vs. refractive index of the waveguide core

There are many types of polymer materials suitable for E-O devices. Their refractive indices are between 1.60 and 1.65. To investigate the effects of using possible different E-O polymer materials, the leaky waveguide is simulated versus refractive index. Figure 5-12 shows the effective refractive index change as the core index increases from 1.58 to 1.66 when the buffer layer thickness is 1.2 μm and the refractive index of the buffer and

superstrate are 1.55 and 1.70, respectively. The dashed lines are the simulated leaky coefficient (pink) and mode effective index (blue). The theoretical model developed in section 5.2 is applied to the structure and its calculated leaky coefficient results are plotted as a solid line in the figure. The calculated results fit the simulated data well when the core index is higher than 1.60 and the leaky coefficient is low. The leaky coefficient drops as the core index increases because of the following reasoning: when the index contrast between the core region and the buffer layer is higher, the optical wave is tighter confined in the waveguide, thus a lesser electric field extends into the superstrate, which results in a lesser leakage. The real part of the effective refractive index increases accordingly with increase in the core index, which is very reasonable. If the E-O polymer material and the waveguide geometry are given, the leaky coefficient can be designed by changing buffer layer thickness and superstrate index.

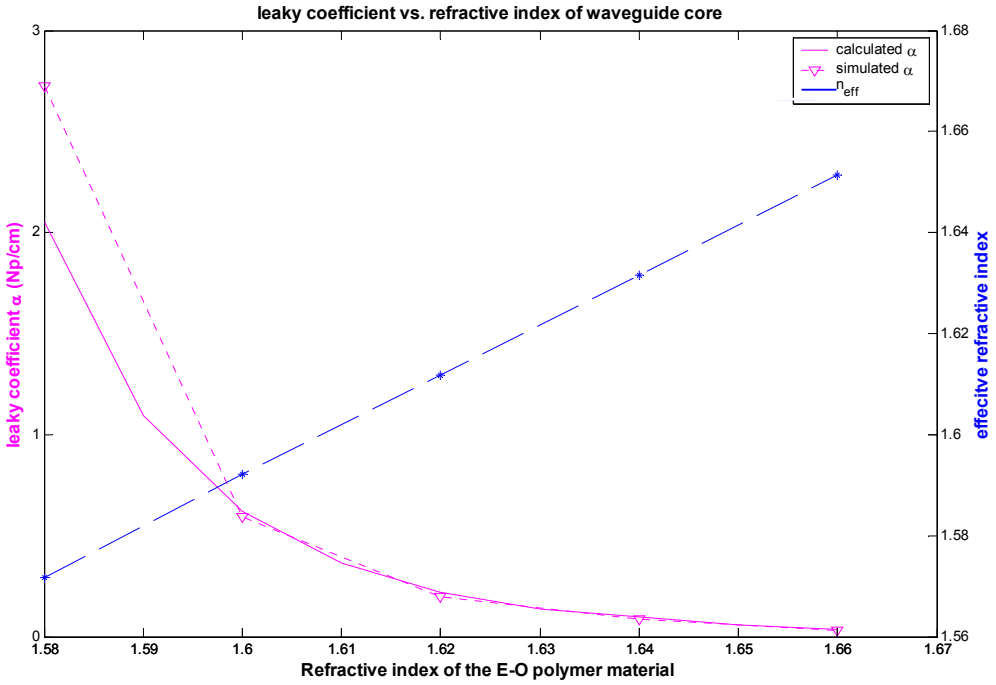

Figure 5-12: Real and imaginary parts of effective refractive index vs. the core index n_1.

- Leaky coefficient vs. buffer layer thickness

Changing the buffer layer thickness to modify the leaky coefficient is straightforward and simple. Under the previous assumptions of weak leakage, the thickness does not affect the real part of the effective refractive index. For the imaginary part, as shown in the theoretical model, the leaky coefficient decreases with the thickness at a rate of $e^{-\tau_2 h_b}$. In order to get enough optical power leaked out of the superstrate, the buffer layer should be quite thin. Figure 5-13 shows the electric field leaky coefficient, i.e. the imaginary part of the effective refractive index, vs. the thickness of the buffer layer as a dashed line. In the simulation the indices of the core, buffer and superstrate are respectively 1.62, 1.55 and 1.70. The solid line shows the calculated leaky coefficient following the theoretical model. The simulated data and the theoretical analysis results match each other very well.

As shown in the figure, the leaky coefficient drops rapidly as the thickness increases. Therefore the buffer layer thickness must be controlled carefully during its fabrication. A 10% variation in thickness of the buffer layer, which is designed to be 1.2 μm, changes the leaky coefficient by about 0.1 Np/cm, resulting in additional 2.6 dB power attenuation in the total leaky wave after 3 cm. Although the thickness significantly changes the available optical power, it does not impact the angular resolution much. As shown in Chapter 4, increasing the attenuation from 0 Np/cm to 0.4 Np/cm just causes a minor broadening in the angular beam width. Figure 5-13 also shows the real part of the effective refractive index, which just changes a little as the buffer layer thickness increases. It, again, verifies the validity of our weak leakage assumptions.

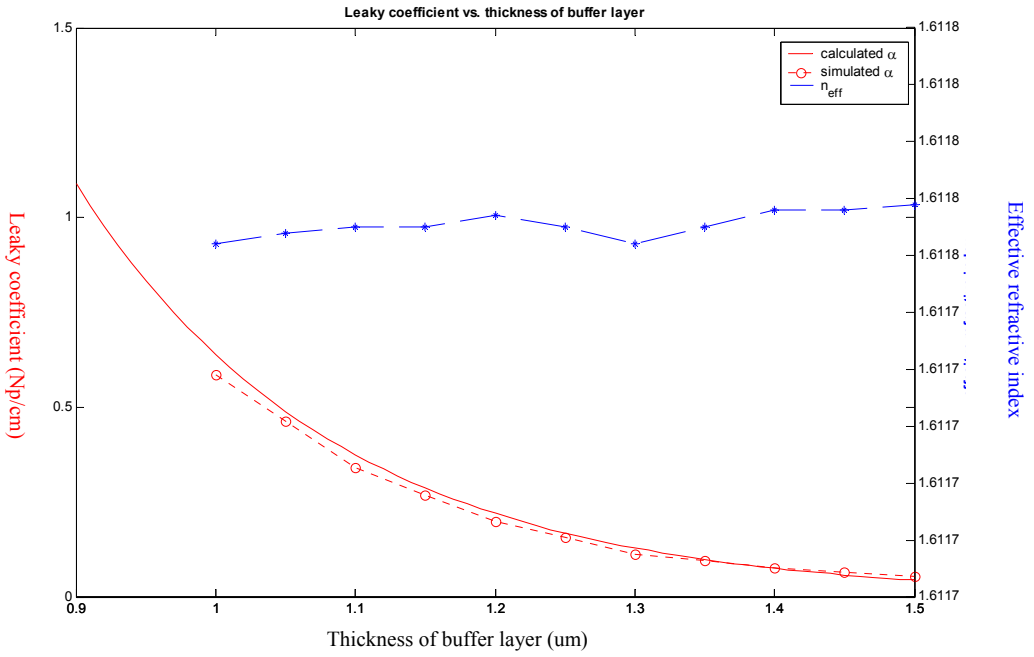

Figure 5-13: The real part and the imaginary parts of the effective refractive index

- Leaky coefficient vs. refractive index of the superstrate

According to the theoretical model, the refractive index of the superstrate changes the leaky coefficient in two aspects: altering the leaky angle and reflecting the evanescent wave from the buffer. These two effects change the leaky coefficient in opposite ways; therefore the leaky coefficient may reach a maximum in its curve vs. superstrate index, as shown in Figure 5-14. Both calculated and simulated plots show a convex shape near to n=1.70. The analytically calculated curve is about 0.05 to the left of the numerically simulated one in the superstrate refractive index axis. Both curves show that, if the waveguide core and buffer layer are given, the superstrate refractive index in a wide range changes the leaky coefficient by less than 0.15 Np/cm. This provides flexibility in selecting proper superstrate materials. The figure also verifies that the impact of the superstrate on the mode propagation characteristics is minor and the weak leakage assumption in the theoretical analysis is valid.

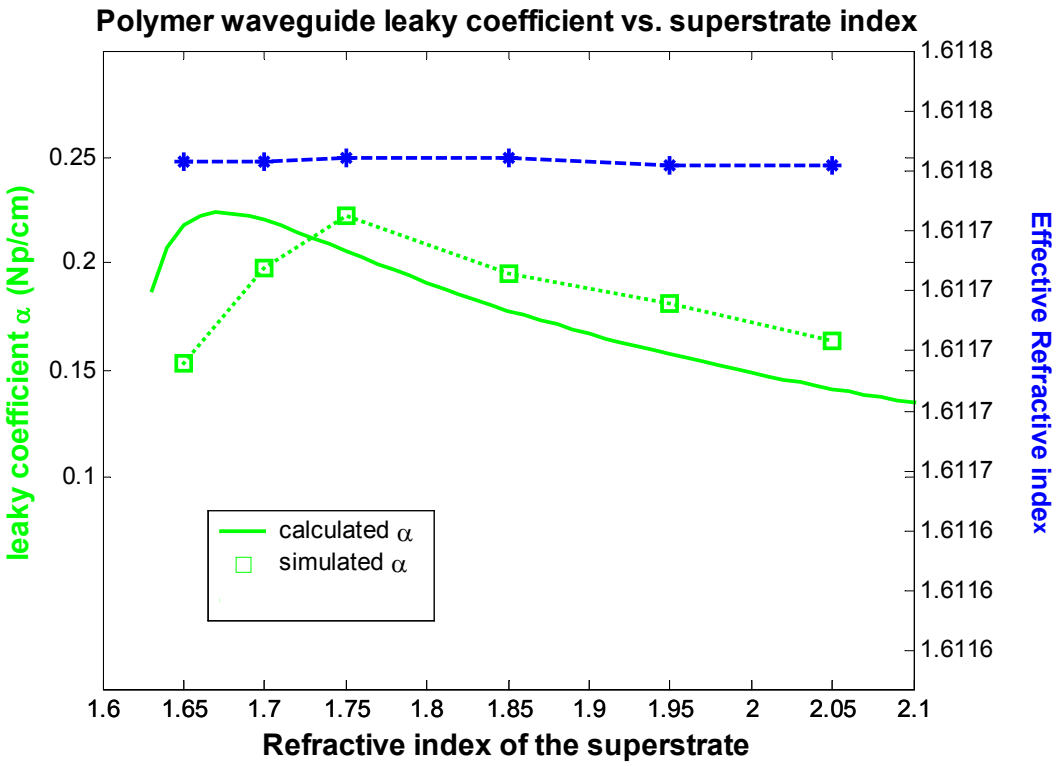

Figure 5-14: Real and imaginary part of effective refractive index vs. the superstrate index, n_s.

5.3.1.3 Electrical properties

As an E-O device, the electrode design affects the bandwidth, driving voltage and power dissipation of the EO leaky waveguide deflector. Its characteristic impedance, effective refractive index at RF frequencies and electrical loss are of interest in this design. The electrodes are designed for a 50 Ω system and 20 GHz bandwidth. The slot-line configuration, as shown in Figure 4-2, was simulated using HFSS from Ansoft, which employs a finite element method. The parameters of the structure are listed in the table below.

Table 5-1: Parameters of the waveguide.

Layer Name	Material	Thickness	Refractive index (optical)	Permittivity ε_r (RF)
E-O material	E-O polymer	3 μm	1.62	3
Superstrate	Polymer	2 cm	1.7	4
Buffer layer	Polymer	1.2 μm	1.55	2.5
Electrode	Gold	10 μm	N/A	4×10^7

The permittivity, ε_r, and characteristic impedance, Z_0, were simulated over frequencies from 2 GHz to 42 GHz. Because of the high frequencies, small meshes had to be used in the numerical analysis. Therefore a long transmission line will need a large computation time to be simulated. When the 3 cm waveguide was simulated, the computer actually ran out of memory and stopped simulation. Therefore the following simulations in this section were run for smaller segments. In principle, ε_r and Z_0 are determined by the cross section configuration if fringe effects are ignored. That means ε_r and Z_0 are independent of the length of the transmission line and can be found by simulating smaller segments. Simulations of segments with different lengths confirm this intuitive expectation. However, the RF attenuation is directly related to the length of the transmission line, but can be derived from the characteristics of smaller segments.

- Characteristic impedance

The simulated characteristic impedance at 20 GHz is 49.6 Ω. Figure 5-15 shows the magnitude and the real part of the impedance; both are close to 50 Ω and vary less than 2 Ω over 2 GHz to 42 GHz, indicating that the electrode configuration obtains impedance matching over a wide frequency range.

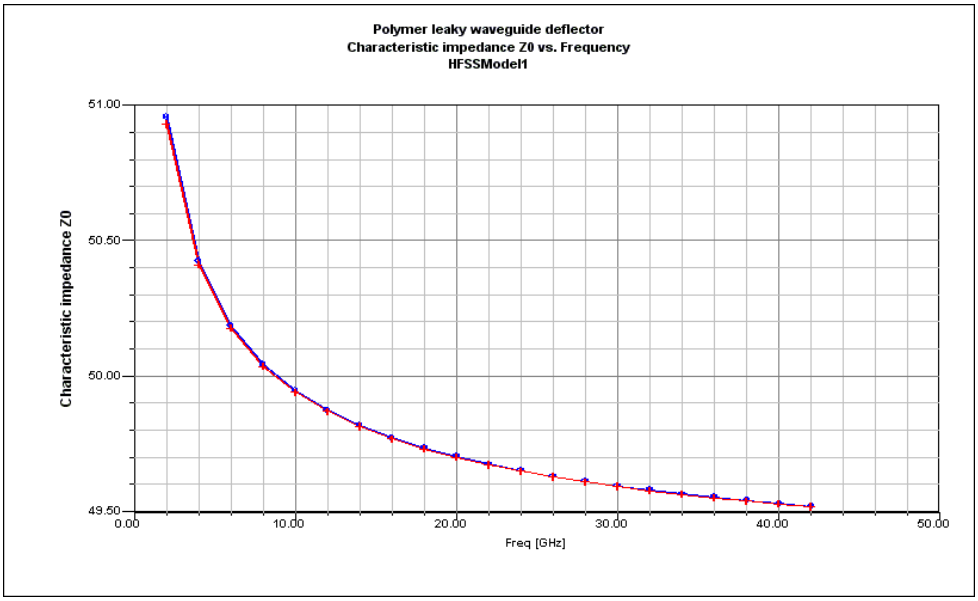

Figure 5-15: Characteristic impedance vs. frequency, simulated when the waveguide is 3 mm in length.

- Effective index of refraction, n_m

The effective permittivity, ε_r, was simulated using HFSS. Its corresponding effective index of refraction at RF frequencies, n_m, is related to ε_r by $n_m=\varepsilon_r^{1/2}$. Figure 5-16 plots the effective index of refraction vs. RF frequency along with its optical mode index, n_o, which is 1.62 for the designed polymer leaky waveguide structure. The dispersion of RF frequencies and infrared signals was evaluated by comparing it to a maximum index difference of 20 GHz operation, since the maximum modulation frequency of the leaky waveguide deflector is limited by its dispersion by, as mentioned in Chapter 4, $f_{3dB}=\frac{1.4c}{\pi|n_m-n_o|L}$. To operate above 20 GHz, the index difference between n_m and n_o must be less than 0.22. The simulated data in the figure show that the index difference over the frequency range of 2 GHz to 42 GHz is well below 0.22. For example, at 20

GHz, n_m is 1.71, a difference of 0.09, which limits the modulation frequency to about 45 GHz, and meets the 20 GHz requirement very well.

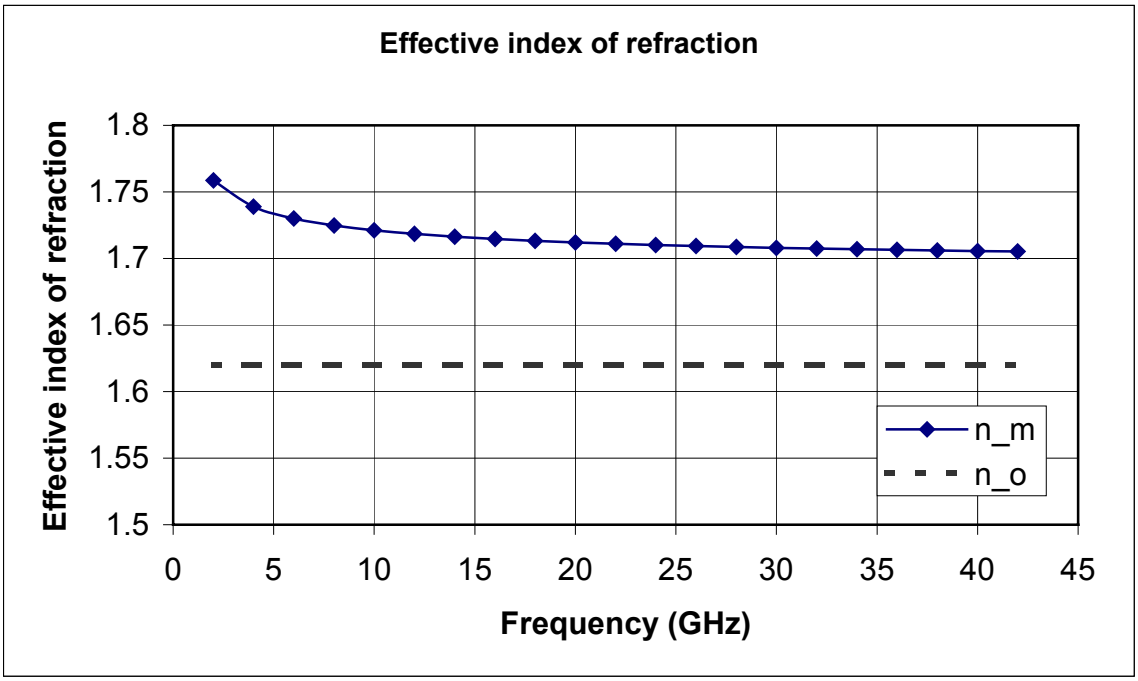

Figure 5-16: Effective index of refractive index vs. frequency when the waveguide is 3 mm in length.

- Electrical loss

The electrical loss of the E-O deflector is related to its forward scattering parameter S21. The RF modulation bandwidth is defined as the 3 dB bandwidth of its S21. Due to limited computation resources, S21 was not obtained by simulating a 3 cm waveguide directly. Instead, a simulation was performed for a 3 mm segment of the waveguide. Its S21 amplitude in dB and phase shift in degrees are shown in Figure 5-17 and S21 drops as frequency increases, meaning that the electrical loss increases at higher frequencies. At

the same time, the phase is linear in the frequency as shown in Figure 5-18, indicating very small dispersion over the frequencies of interest.

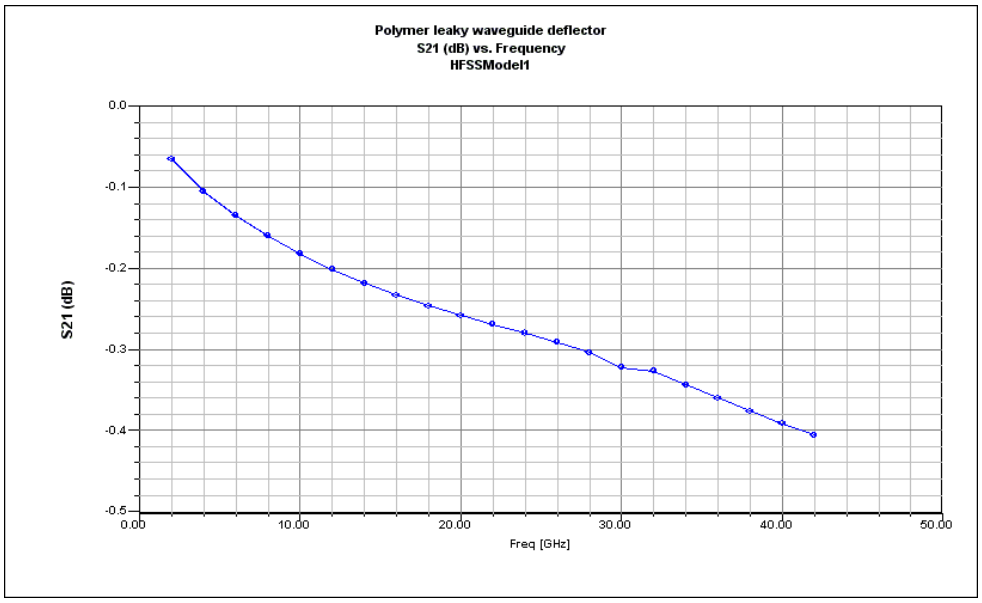

Figure 5-17: S21 (dB) vs. frequency when the waveguide is 3 mm in length.

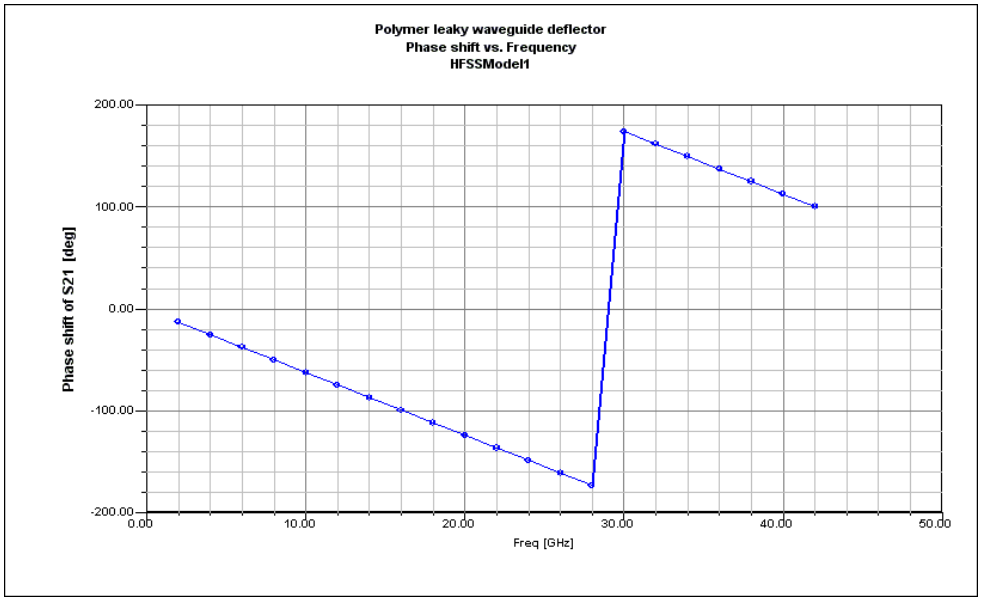

Figure 5-18: Phase of S21 vs. frequency when the waveguide is 3 mm in length.

In principle the attenuation of a transmission line increases linearly as length increases, so S21 for 3 cm electrodes can be derived from the result of the shorter segment. To verify this expectation, S21 was simulated vs. length, and the results shown in Figure 5-19. The figure demonstrates an approximately linear drop of S21 with increasing length. Therefore S21 of the 3 cm waveguide can be calculated from the simulation results of by multiplying it by 10, and the derived results are plotted in Figure 5-20. The 3 dB bandwidth can be found at S21 equal to –3 dB, which is about 28 GHz as indicated in the figure.

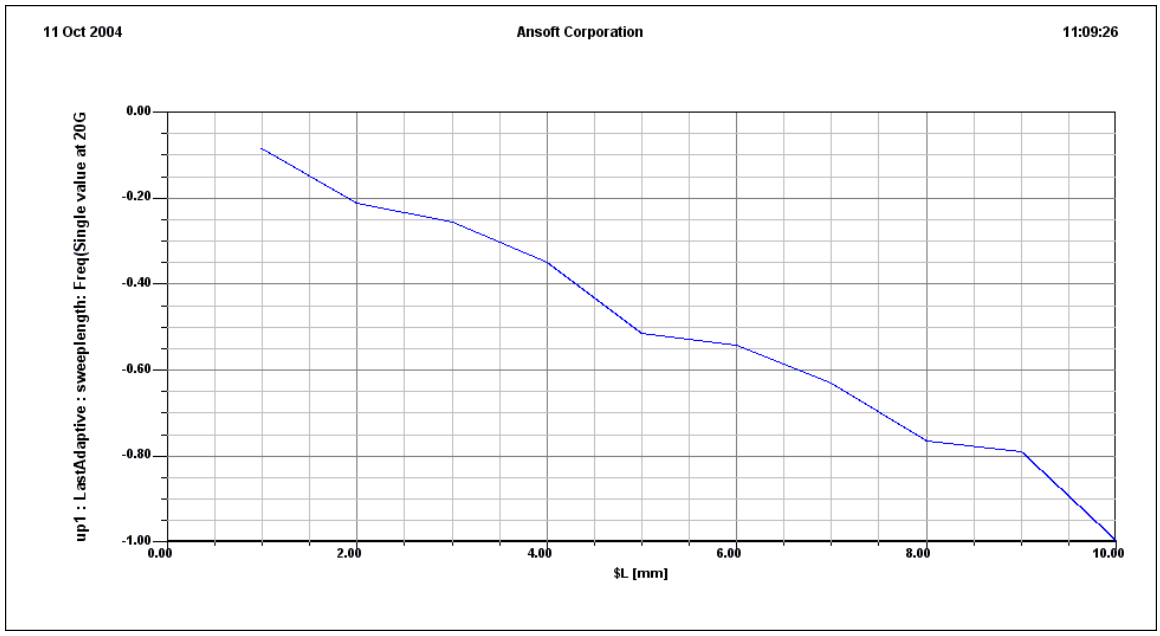

Figure 5-19: S21(dB) vs. length of the structure at 20 GHz.

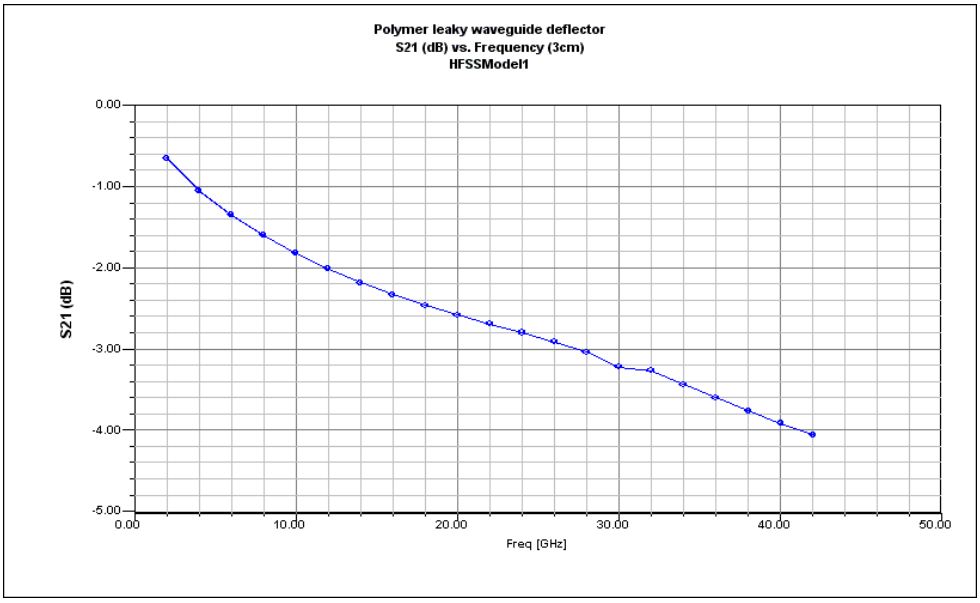

Figure 5-20: Calculated S21 vs. frequency for a 3cm waveguide.

5.3.1.4 Electro-optical properties

When a voltage is applied to the electrodes, an electric field is created that induces an index change in the E-O polymer. Figure 5-21 shows the electric field distribution and corresponding index change when a voltage of 20 V is applied between the two electrodes.

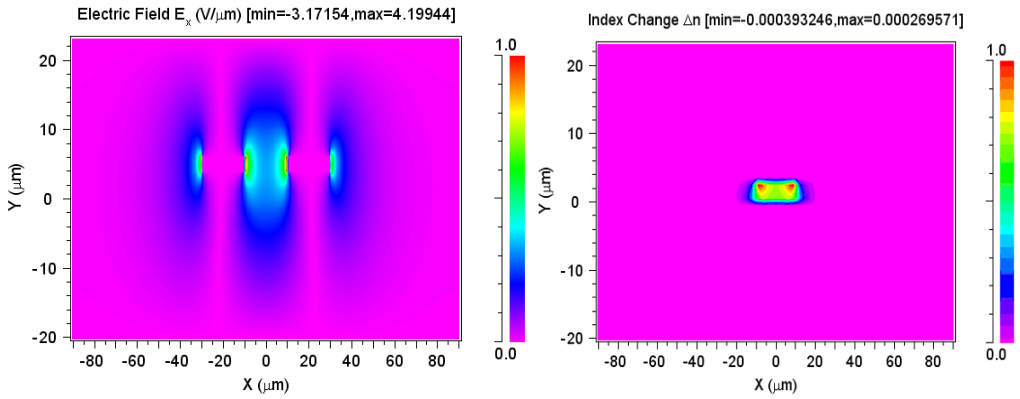

Figure 5-21: Electrical field E_x distribution (left) and corresponding index change (right).

The maximum electric field of about 4 V/μm is built around the edge of the electrodes. Since the maximum field is less than the breakdown of the E-O polymer, buffer or superstrate, a voltage of 20 V is safe for the E-O polymer leaky waveguide deflector. The right image shows that the index change is not uniform because the non-uniform electric field. The overall effect of the electric field is represented in the change of the effective refractive index of the propagation mode, since it is effective index that alters the leaky angle. The effective refractive index of the waveguide was simulated versus applied voltage using BeamPRO, as shown in Figure 5-22.

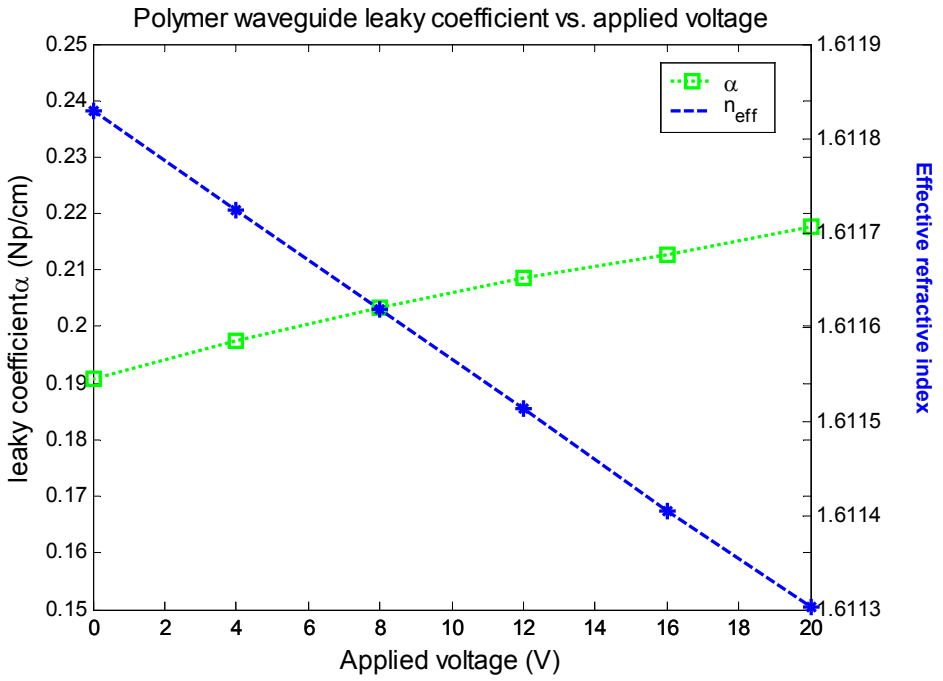

Figure 5-22: Effective refractive index vs. applied voltage in a polymer waveguide.

The real part of the effective refractive index changes linearly with respect to the applied voltage. Therefore it is proved that the electric field is able to steer the leaky angle linearly. The total change in the index is 5.27×10^{-4}, making the modulation efficiency 2.635×10^{-5}/V. The leaky coefficient, i.e. the imaginary part of the effective refractive index, changes as little as 0.027 when the voltage increases from 0 V to 20 V, resulting in almost no broadening in the angular linewidth. Therefore the error introduced by non-uniform beam width is negligible.

Combining the simulation data and the leaky angle analysis we described in Chapter 4, the displacement of leaky angle vs. applied voltage, as well as the final output angle are shown in Figure 5-23. This figure shows a linear translation of voltage into output angle. The angular swing at a voltage of 20 V is 2.8 mrad when the edge of the superstrate is at

60° with respect to the leaky waves. An RF signal with amplitude of 20 V varies between +20 V and –20 V, therefore the total angular swing of the full scale is 5.6 mrad.

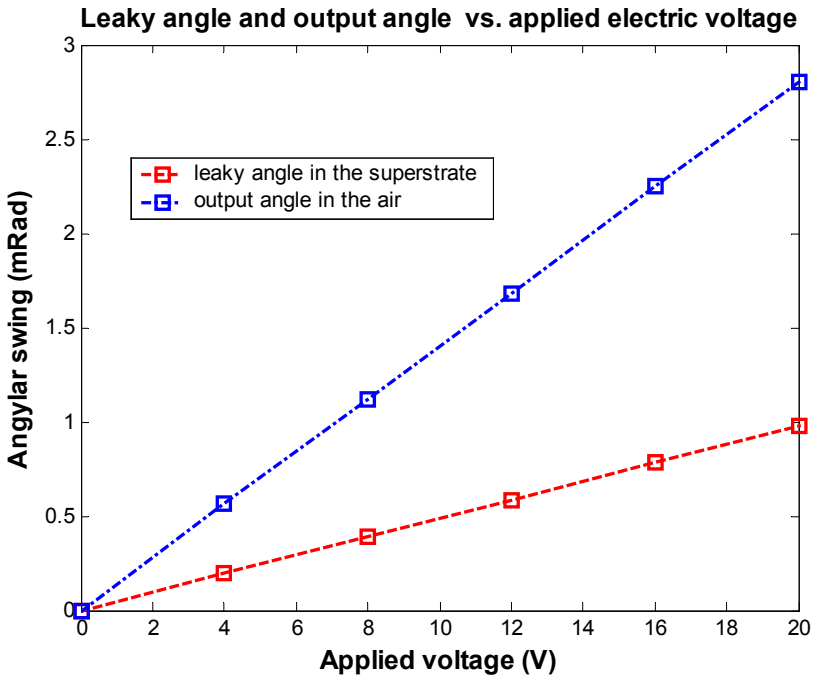

Figure 5-23: Leaky angle and output angle displacement introduced by the applied voltage.

As designed in the beginning of this section, the leaky coefficient is about *0.2* Np/cm. Additional attenuation during propagation in a polymer waveguide is usually 0.7~2 dB/cm [52], corresponding to 0.08 to 0.23 Np/cm, making the total attenuation of 0.28 to 0.43 Np/cm. If we choose the waveguide attenuation to be 0.1 Np/cm on top of the leakage loss of 0.2 Np/cm, 16% of the total launched power remains in the waveguide after propagating 3 cm. The total leaked optical power is 60% of the launched power. The total attenuation of 0.3 Np/cm leads to an angular resolution of 0.125 mrad. Therefore the total number of resolvable image lines is 45. In principle, it is sufficient to implement a 6-

bit OADC using binary code or approximately 7-bits using Gray code. The modulation bandwidth of the OADC is 28 GHz, sufficient for 40 GS/s A-to-D conversion, as long as the optical sampling pulses are fast enough.

5.3.2 Z-cut Ti:$LiNbO_3$ leaky waveguide deflector with CPW electrodes

5.3.2.1 Z-cut Ti:$LiNbO_3$ leaky waveguide design

Polymer devices have shown broad RF bandwidth and good compatibility with integrated semiconductor technologies. However, to be accepted in system applications, these E-O polymer devices must reduce their optical insertion loss and improve thermal stability. Conventional E-O crystalline materials have been investigated for decades and are commercially available. For example, $LiNbO_3$ devices have been well studied and widely used in optical communications. To make the designed OADC possible for current available mature technologies, a *z*-cut Ti:$LiNbO_3$ leaky waveguide was designed to meet the requirement of high frequencies. For convenience of discussion, a cross section of the *z*-cut Ti:$LiNbO_3$ leaky waveguide is redrawn in Figure 5-24.

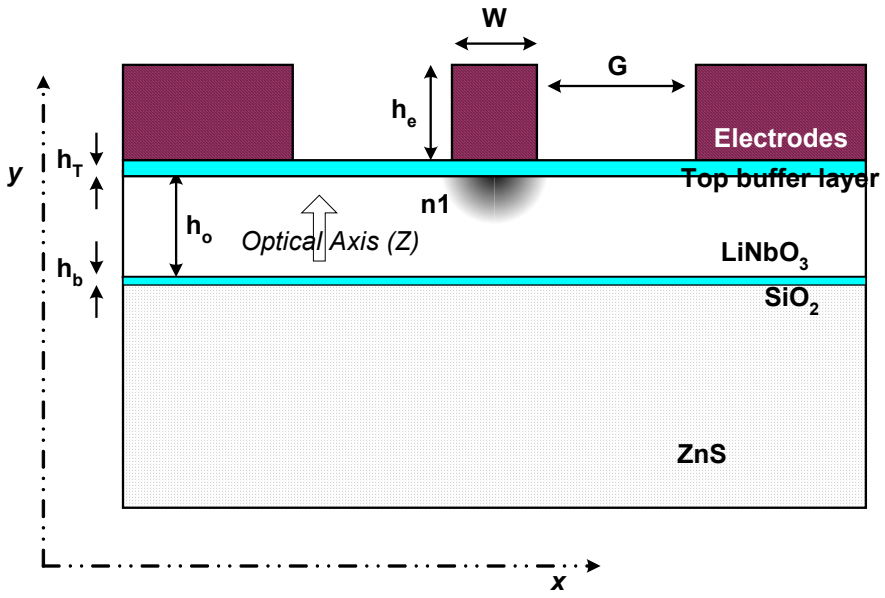

Figure 5-24: Cross section of the *z*-cut Ti:$LiNbO_3$ leaky waveguide.

In this design, a strip waveguide is formed by in-diffusing Ti into a *z*-cut $LiNbO_3$ substrate Presence of Ti in the crystal increases both the ordinary and the extraordinary indices of refraction. The waveguide region is usually 6~9 μm wide. In the simulation, the waveguide region is set to be 8 μm. The $LiNbO_3$ substrate is fabricated and placed so that its optical axis, i.e. the *z*-axis of the crystal, is parallel to the *y*-direction, so that when a voltage is applied to the electrodes the electric field underneath the hot (center) electrode is mainly parallel to the optical axis in order to achieve the maximum index change via the electro-optic coefficient, γ_{33}, of $LiNbO_3$. Therefore, the applied electric field changes the extraordinary index of refraction in $LiNbO_3$. To utilize this maximum index change, the E-field of the optical wave should be parallel to the applied electric field, so the *y*-dominant mode, $E^{(y)}$, should be excited and used in this configuration.

The high index material is selected to be Zinc Sulphide (ZnS), whose transmission window covers 1μm to 12μm. Its refractive index at 1.55 μm is 2.282, which is higher than the extraordinary refractive index of $LiNbO_3$ by about 0.1. The main reason to choose ZnS over other high refractive index optical materials is that its permittivity at RF frequencies is about 10, the smallest among many possible candidates. For example, we could have used a *z*-cut $LiNbO_3$ as the superstrate, since the *x*-polarized optical wave would yield the ordinary refractive index, which is slightly higher than its extraordinary refractive index, but its RF permittivity is 43, resulting in severe velocity mismatch between the RF traveling wave and the propagating optical waves. Another example is TiO_2, whose refractive index at 1.55 μm is about 2.4 while its permittivity is higher than 80.

In this design, a thin layer of lower refractive index material separates the prism from the $LiNbO_3$. Actually the use of this buffer layer is not necessary, since the $LiNbO_3$ substrate around the core region behaves like a cladding layer. But introducing a buffer layer to separate the prism and the waveguide makes control of the leaky coefficient flexible and reduces fabrication difficulties. The buffer layer in this design uses silicon dioxide (SiO_2), whose refractive index is about 1.5. Its thickness is chosen according to equation (5-21) and simulation so that the field leaky coefficient, α_L, is between 0.1 and 0.3 Np/cm. There is another buffer layer on top of the waveguide that is necessary to separate the optical waveguide from the metal electrode to avoid unwanted optical absorption. The final refractive index profile is drawn in Figure 5-25. The Ti in-diffused $LiNbO_3$ waveguide has a graded index profile, which is provided by Rsoft according to a typical

Ti diffusion process [58]. The buffer layer is 8 μm under the top surface and its thickness is 0.12 μm. The 8 μm size is about the mode size in the 8-μm-wide Ti:$LiNbO_3$ waveguide, so that the optical power can leak out efficiently.

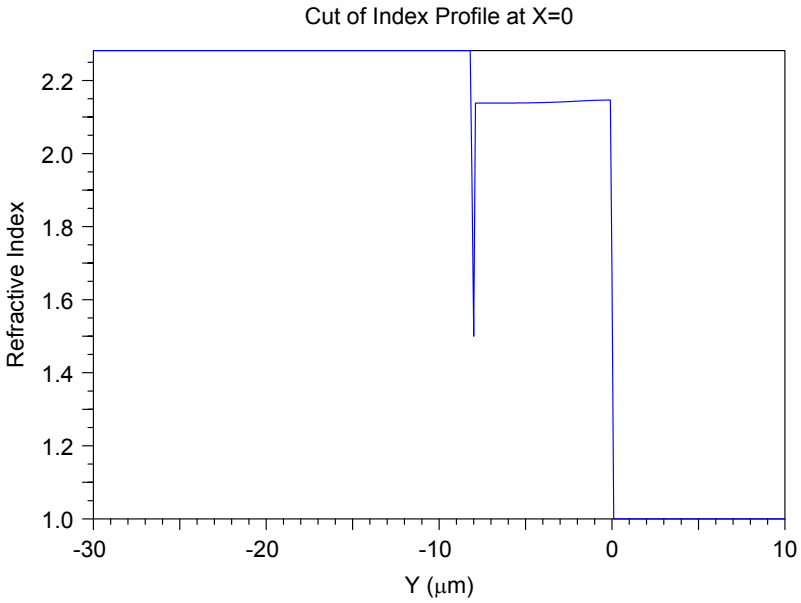

Figure 5-25: Refractive index profile of the *z*-cut Ti:$LiNbO_3$ leaky waveguide.

Figure 5-26 shows the simulated mode profile. Its effective refractive index of the leaky mode is n_{eff}=2.137397+j3.226×10^{-6}, corresponding to a leaky coefficient of 0.13 Np/cm. Therefore after propagating 3 cm, 55% of the total launched optical power will leak out from the bottom.

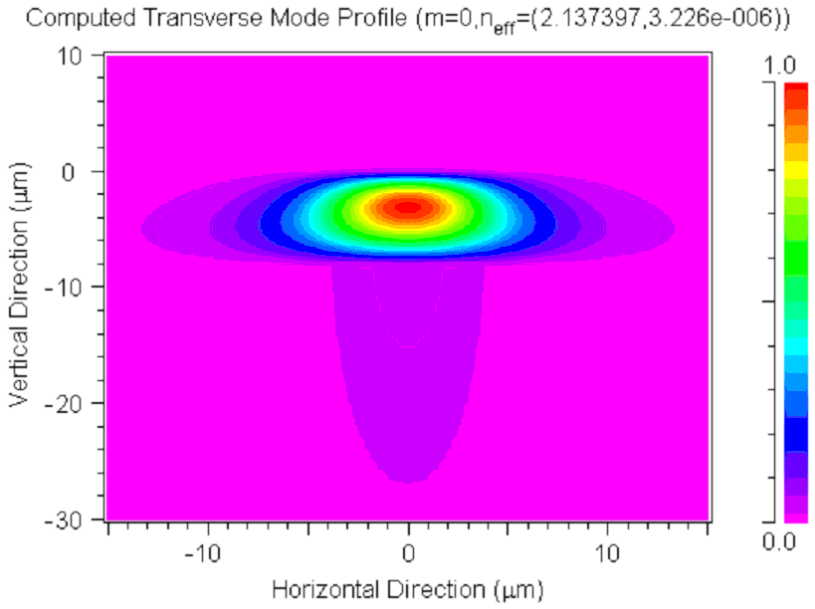

Figure 5-26: Optical field distribution in the Ti:$LiNbO_3$ leaky waveguide

The leaky wave is designed to be very weak. To illustrate the leaky mode clearly, we show the one-dimensional field distribution along the *x* and *y*-directions crossing the waveguide center in Figure 5-27.

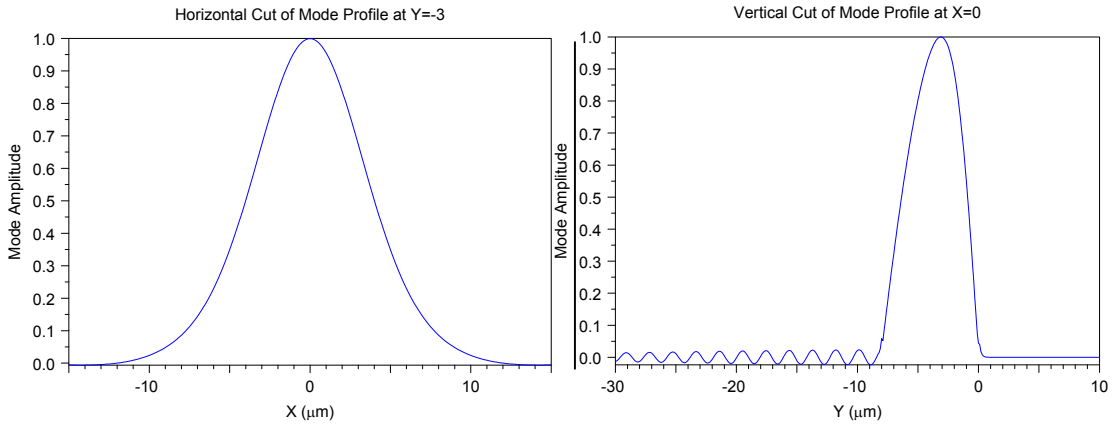

Figure 5-27: The field distribution profile along the *x* and *y*-directions.

The figure shows a clear undulation in the *y*-direction, indicating radiation from the bottom. That means part of the optical power will leak to the lower space. The undulation oscillation period is 1.91 μm. It also can be found by calculation following the theoretical model, $\sqrt{n_s^2 - n_{eff}^2} \cdot 2\pi / \lambda$, resulting in 1.93 μm. The simulated value matches the calculated result very well.

5.3.2.2 Parametric analyses of optical properties

This section will show how the leaky coefficient changes with respect to the refractive index and thickness of the buffer layer, as well as the index of the prism. Because the Ti:$LiNbO_3$ waveguide has a graded index profile, the strip model we developed in section 5.3 is not applicable so we just show the simulated data without comparing it to a theoretically calculated result. But the general effects of the buffer and the prism can be still explained by the theoretical model.

- Leaky coefficient vs. refractive index of the buffer layer

In this simulation, the material and the geometry of the Ti:$LiNbO_3$ waveguide is given. The buffer layer material can be chosen arbitrarily as long as its refractive index is less than that of $LiNbO_3$. Figure 5-28 shows the simulated effective refractive index versus index of the buffer layer when the index of the buffer layer increases from 1 to 2. Similar to the simulation of the polymer waveguide, in which we change the core index, the leaky coefficient increased when the index contrast between the core region and buffer layer decreased since the optical field extends more into the cladding, buffer and prism. Compared to the polymer waveguide, the leaky coefficient in the *z*-cut Ti:$LiNbO_3$ leaky

waveguide changes more slowly versus the index contrast because of the presence of the $LiNbO_3$ substrate.

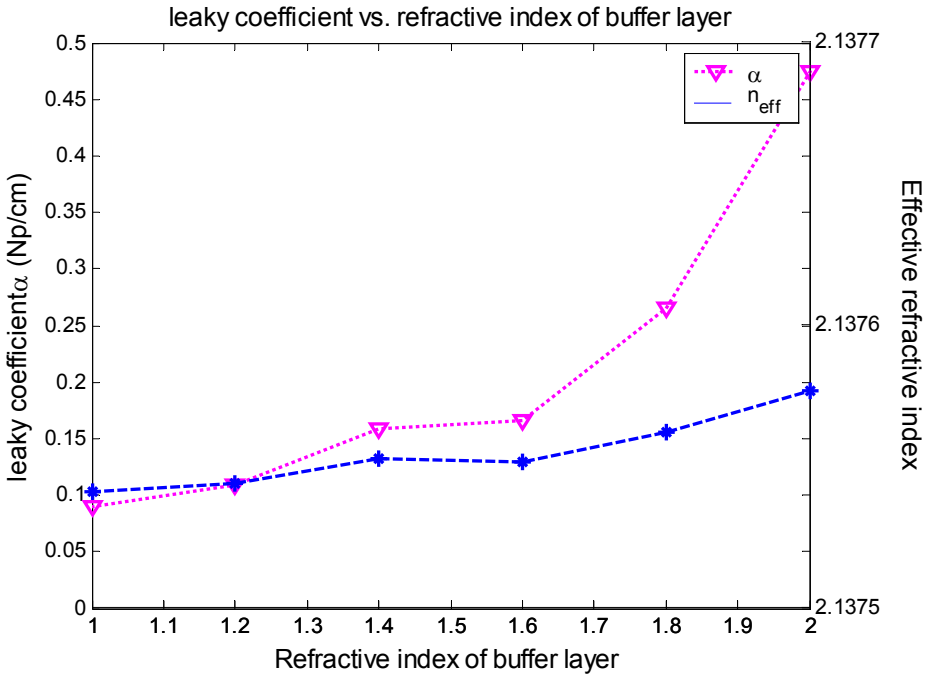

Figure 5-28: Real and imaginary parts of the effective refractive index vs. the refractive index of buffer layer.

- Leaky coefficient vs. thickness of the buffer layer

The leaky coefficient drops rapidly at a rate of 12 Np/μm as the thickness of the buffer layer increases, as shown in Figure 5-29. According to equation (5-21) the leaky coefficient changes as $e^{-2\tau_2 h_b}$. We can derive τ_2 from the real part of the effective refractive index and the buffer layer as $\tau_2 = k_0\sqrt{n_{eff}^{\ 2} - n_2^{\ 2}}$, which equals 6.17 cm^{-1}, making the drop rate, $2\tau_2$, 12.3 Np/cm, matching the simulated data very well. Due to the large difference between the indices of the core and the buffer, τ_2 is much greater than

that of the polymer waveguide, so the leaky coefficient is quite sensitive to the thickness. Therefore deposition of the buffer layer must be well controlled during the fabrication.

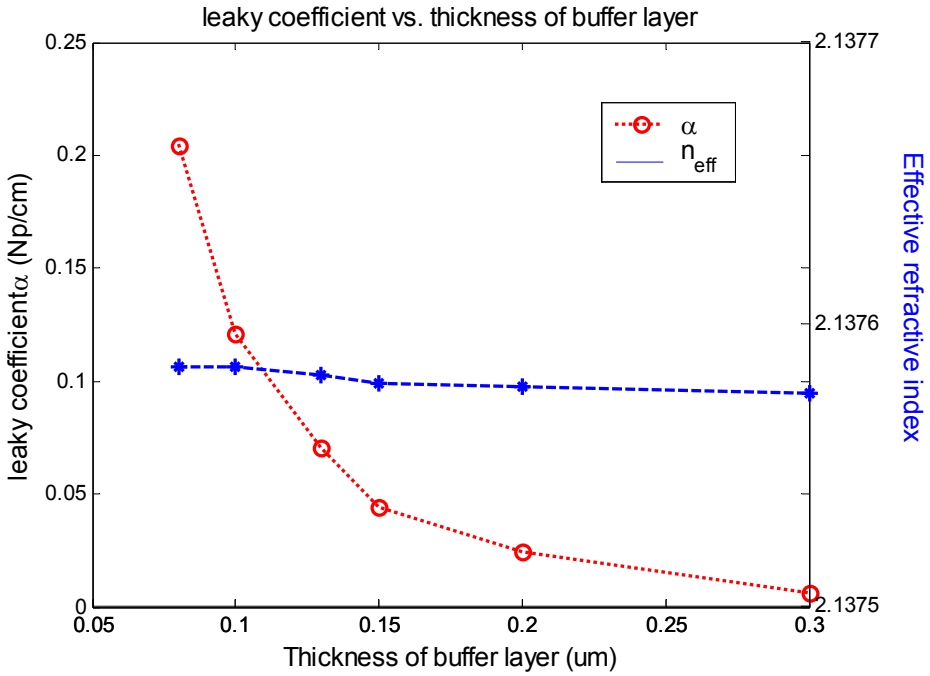

Figure 5-29: Real and imaginary parts of the effective refractive index vs. thickness of the buffer layer.

- Leaky coefficient vs. prism index

Figure 5-30 shows the simulated leaky coefficient vs. the refractive index of the prism. The leaky coefficient increases monotonically in the index range of 2.2 to 2.8. It implies that the effect of increased leaky angle is dominant over the decreased transmittance in the change of leaky coefficient within this range. Similar to what has been shown in the polymer leaky waveguide; the change of leaky coefficient is slower and provides flexibility in selecting different prism materials.

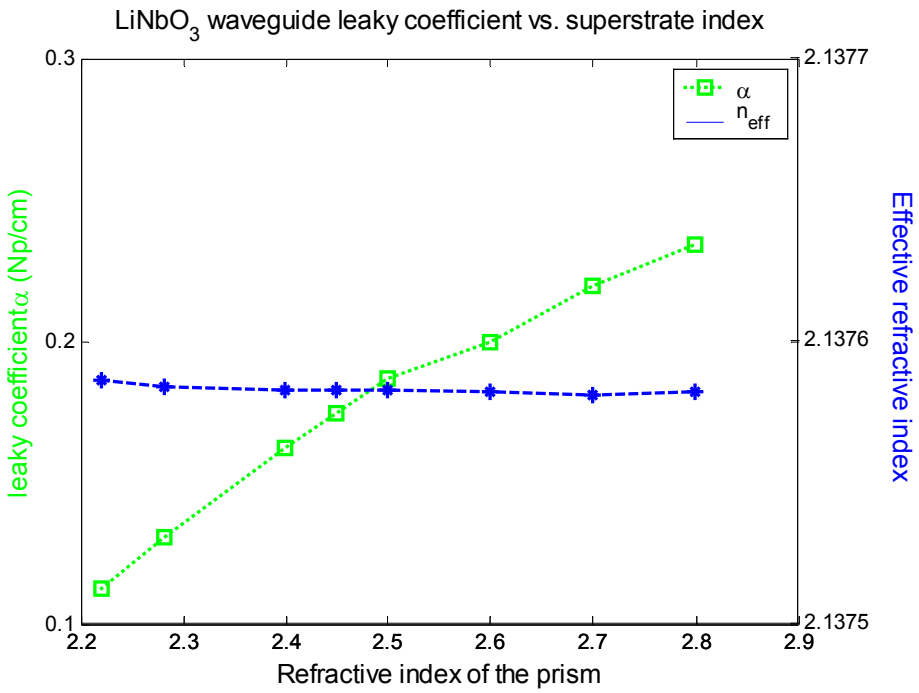

Figure 5-30: Real and imaginary parts of the effective refractive index vs. prism index

5.3.2.3 Electrical properties

The *z*-cut Ti:$LiNbO_3$ leaky waveguide employs a coplanar waveguide (CPW) electrode configuration. The electrodes are designed so that the effective refractive index at 20 GHz is close to 2.137, which is the effective refractive index of the propagation mode. At the same time the characteristic impedance is designed to be 50 Ω. The cross section of the waveguide along with the electrodes has been shown in Figure 5-24. The parameters of the waveguide are listed in the table below:

Table 5-2: Parameters of the waveguide

Layer Name	Material	Thickness	Refractive index (optical)	Permittivity ε_r (RF)
E-O material	$LiNbO_3$	8 μm	2.2	29
Prism	ZnS	2 cm	2.282	10
Buffer layer	SiO_2	0.12 μm	1.5	4
Buffer layer (top)	SiO_2	1.3 μm	1.5	4
Electrode	Gold	8 μm	N/A	4×10^7

The width of the center electrode, *W,* is 8 μm; the gap between center and ground electrodes, *G,* is 15 μm. The effective refractive index at RF frequencies is a weighted average of the index of all media near to the electrodes. The thick electrodes, which are 8 μm in the design, pull some electric field out of the high index material and are characterized by lower effective index of refraction. At the same time, the thick gold electrodes also provide lower RF attenuation.

The permittivity, ε_r, and characteristic impedance, Z_0, were simulated over the range 2 GHz to 42 GHz. Due to limited computation resources, S21 was obtained by running the simulations for short length.

- Characteristic impedance

Figure 5-31 shows the amplitude and the real part of the characteristic impedance, which vary less than 3 Ω around 50 Ω over the frequency range of 2 GHz to 42 GHz. At 20 GHz the simulated impedance is 50.7 Ω.

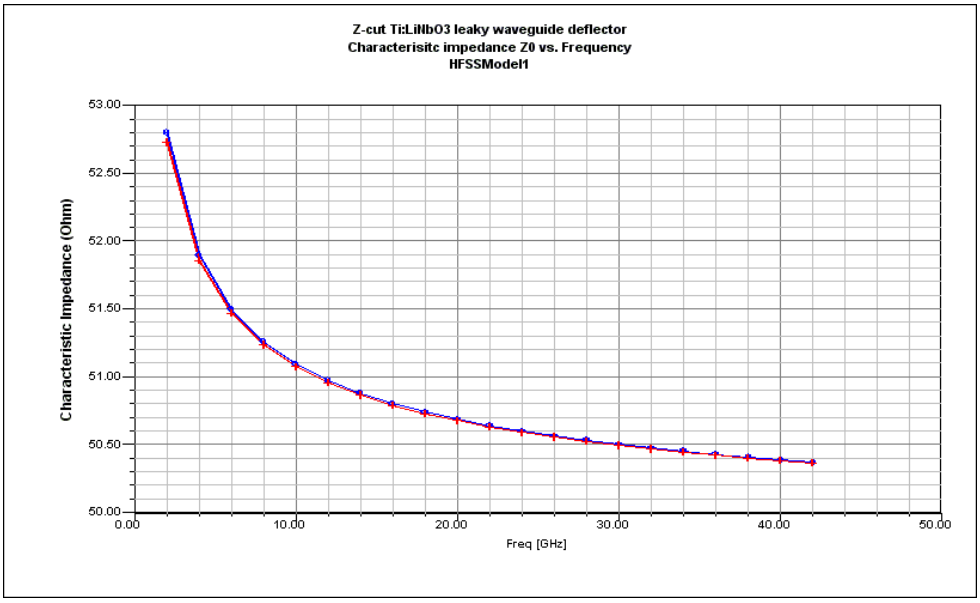

Figure 5-31: Characteristic impedance vs. frequency, simulated when the waveguide is 3 mm in length

- Effective permittivity, ε_r

Figure 5-32 plots the effective index of refraction vs. RF frequency along with its optical mode index, n_o, as a reference, which is 2.137 for the Ti:$LiNbO_3$ waveguide. It is seen in the figure that the index difference over the frequency range of 2 GHz to 42 GHz is well below 0.22, the critical dispersion for velocity match at 20 GHz. For example, at 20 GHz n_m is 2.15, higher than the optical index by only 0.013. That means the RF signal and optical wave travel at almost the same velocity.

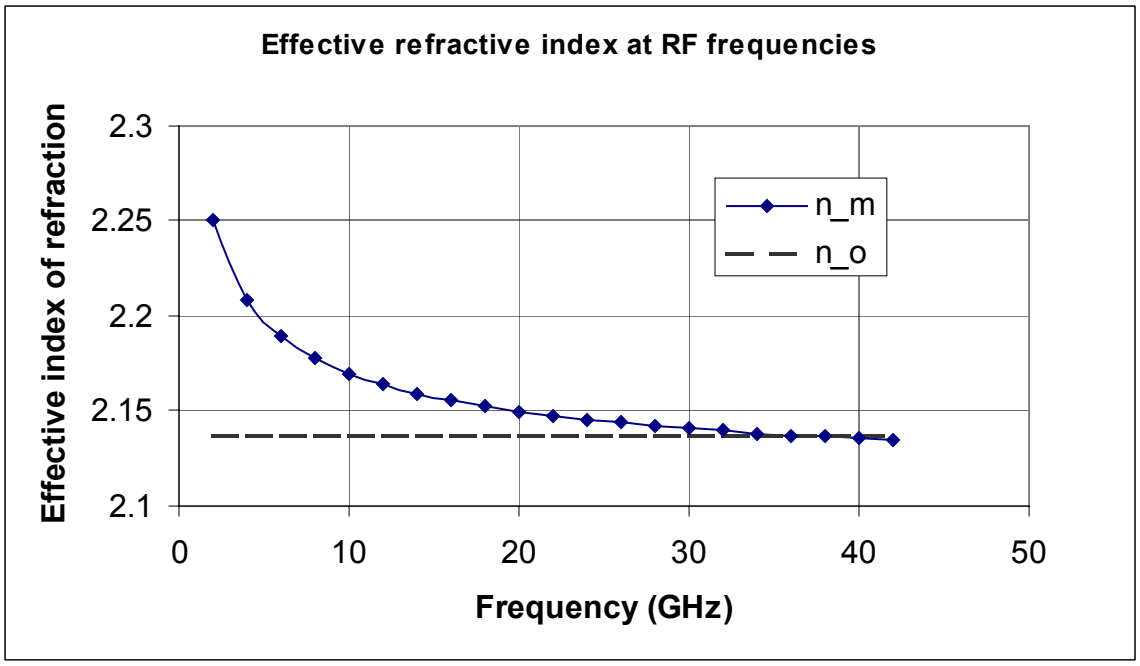

Figure 5-32: Effective index of refractive index vs. frequency when the waveguide is 3 mm in length.

- Electrical loss

S21 of the electrodes of the Ti:$LiNbO_3$ leaky waveguide deflector is found by the same approach as in the simulation of the polymer waveguide. S21 is calculated from a simulated result of a 3-mm segment by magnifying the result 10 times. The result is plotted in Figure 5-33. The figure indicates an electrical loss of 5.7 dB at 20 GHz and a 3 dB bandwidth of 12 GHz around 20 GHz. Also shown in the figure, typical electrical loss of current $LiNbO_3$ M-Z modulators is 0.5 dB/cm/$GHz^{1/2}$ [53], corresponding to -6.7 dB at 20 GHz, which is 1dB lower than the calculated value.

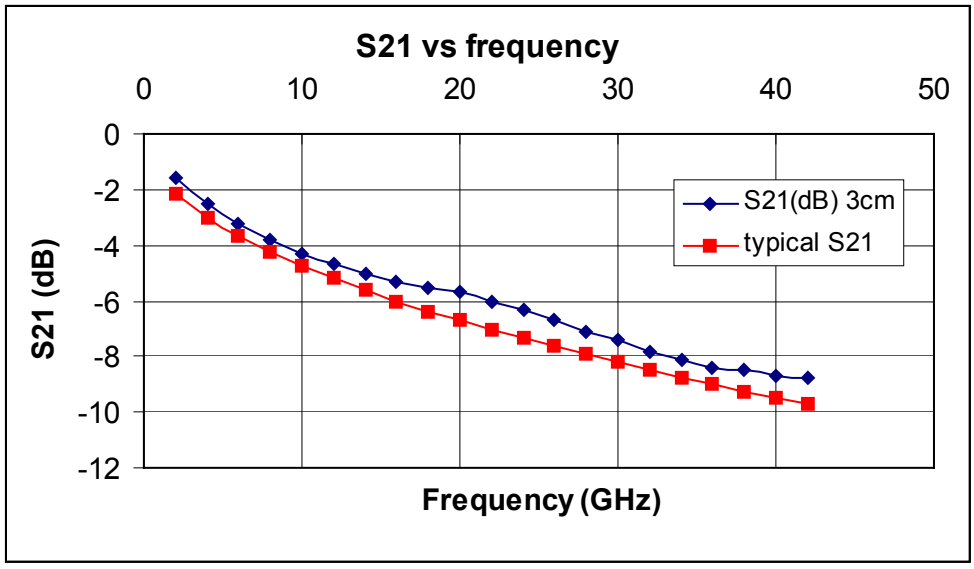

Figure 5-33: Calculated S21 vs. frequency (blue), when the waveguide is 3 cm in length, and typical electrical loss of current $LiNbO_3$ modulator (red).

5.3.2.4 Electro-optical properties

When a 20 V signal is applied to the center electrode, an electric field is produced between the center electrode and the two ground plates. Figure 5-34 (left) shows the electric field distribution and corresponding refractive index change in the $LiNbO_3$ region (right). With a gap of 15 μm, the average strength of the electric filed is 1.33 V/μm, less than the dielectric breakdown of air. But the electric fields at the edges of the electrodes are about 25V/μm, exceeding the breakdown field. Two ways can be used to avoid dielectric breakdown in the air. First, we should make the edges with a smooth round shape to avoid extremely large field at sharp corners. Second, since the extreme field only happens in a very small region close to the very edge, we can deposit a thin layer of material with high dielectric breakdown field on the surfaces of the electrodes to avoid damage.

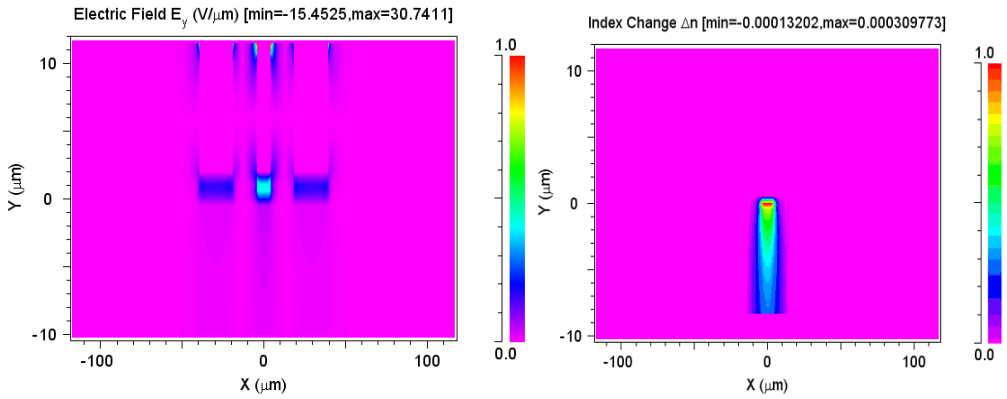

Figure 5-34: Electric field distribution and induced index change

The refractive index modulation vs. applied voltage is plotted in Figure 5-35, which shows a linear response of the index to the applied voltage. As the applied voltage increases from 0 to 20 V, the real part of the refractive index changes 0.00015, corresponding to 7.5×10^{-6}/V. The leaky coefficient changes only 0.004, so the linewidth does not have a noticeable change as voltage increases.

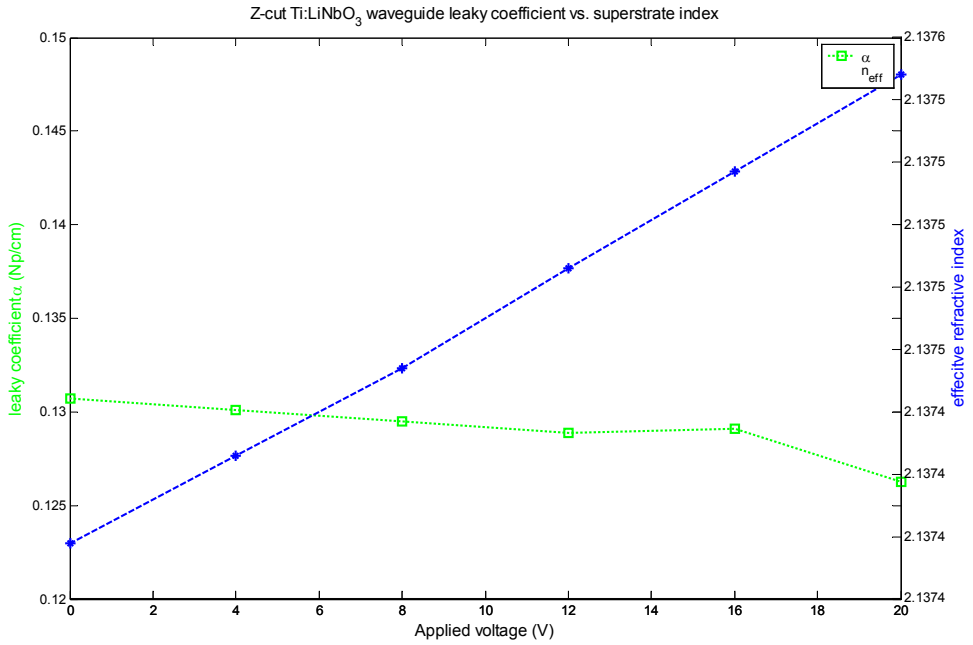

Figure 5-35: The effective index and leaky coefficient vs. applied voltage.

The corresponding angular displacement vs. applied voltage is shown in Figure 5-36. A 20V signal induces 0.95 mrad in angular displacement. Therefore when the RF signal's full-scale is from –20V to +20V, the total angular swing is 1.9 mrad.

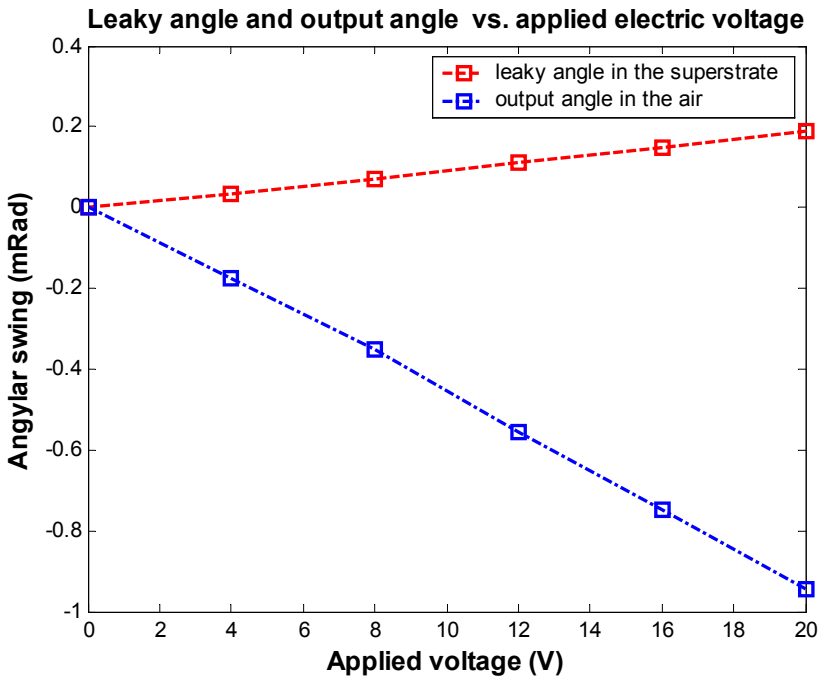

Figure 5-36: Angular displacement vs. applied voltage.

The leaky coefficient is simulated as 0.13 Np/cm as shown in the beginning of this section. Other terms contributing to attenuation during propagation result in a typical $LiNbO_3$ waveguide loss of about 0.2 dB/cm, corresponding to 0.023 Np/cm, which is negligible compared to the loss coefficient due to the leaky waves. As the optical wave propagates along the waveguide with an attenuation of 0.13 Np/cm due to the leaky coefficient, 54% of the total launched power leaks out of the waveguide after propagating 3 cm. The calculated angular resolution is 0.115 mrad. Therefore the total number of resolvable image lines is 17. In principle, this is sufficient to implement a 5-bit OADC using binary code or 6-bit using Gray code. Its resolution is lower than the polymer structure, because, a) the electro-optic coefficient is lower, and, b) voltage drops in the top buffer layer. As shown in the previous section, the modulation bandwidth of the $LiNbO_3$ leaky waveguide OADC is 12 GHz around 20 GHz.

5.4 Summary

This chapter discusses how the E-O leaky waveguide deflector is designed. Its optical properties are analyzed by an approximate theoretical model, as well as numerical simulations. The theoretical model helps to adjust the leaky coefficient by changing parameters. Simulations are performed for two structures, an E-O polymer leaky waveguide with stripline electrodes and a *z*-cut Ti:$LiNbO_3$ leaky waveguide with CPW electrodes. Their leaky coefficients were simulated vs. buffer index, buffer thickness and superstrate index using OptiBMP from Rsoft, angular resolution using Matlab, RF impedance, bandwidth and loss using HFSS from Ansoft. Their estimated performance is compared in following table:

Table 5-3: Comparison of E-O leaky waveguide deflectors of polymer and $LiNbO_3$.

		Polymer	$LiNbO_3$
Structure		E-O polymer leaky waveguide with stripline electrodes	Z-cut Ti:$LiNbO_3$ leaky waveguide with CPW electrodes
Bits resolution	Binary	6 bits	5 bits
	Gray	7 bits	6 bits
Velocity mismatch at 20 GHz		n_m-n_o= 0.09 < 0.22	n_m-n_o= 0.013 < 0.22
3-dB bandwidth		0 to 28GHz	14 to 26GHz
Leaky coefficient		~0.19 Np/cm	~0.13 Np/cm
Other optical attenuation		0.08 to 0.2 Np/cm	~0.02 Np/cm
Electrical loss at 20 GHz		2.7 dB	5.7 dB

In the comparison, the E-O polymer deflector has higher resolution because of its high E-O coefficient. It also features lower electrical loss and broader 3-dB modulation bandwidth, since it employs wider electrodes. On the other hand, the $LiNbO_3$ deflector

had less velocity mismatch and lower waveguide attenuation. Generally, $LiNbO_3$ E-O devices are mature, more thermally stable and more accessible.

6. Optical Collector Array and Other Enabling Components

The proposed approach of implementing the AOADC requires 4 critical enabling components: E-O deflector, optical collector array, mode-locked laser (MLL), and photodetectors. The deflector has been investigated and proved feasible. The optical collector array is another new device that needs to be designed and evaluated. The following section will discuss its operation, spatial error sources, a static test and a possible implementation. Another two components, the MLL and the photodetectors, are common devices and have been used in existing optical ADCs. This chapter will discuss their required performance and availability.

6.1 The design of collector array

6.1.1 Operation and coding scheme

When the deflected beam is projected on the optical collector array, all bits share the same steering image lines, making the collector array more compact. Figure 6-1 shows the aperture arrangement for binary code and Gray code respectively.

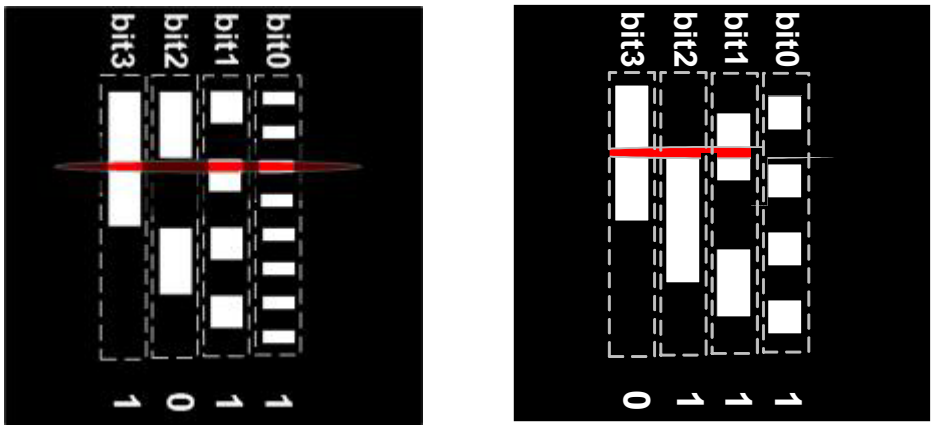

(a) (b)

Figure 6-1: Optical collector aperture array for 4-bit binary and Gray code encoding. The white blocks represent opening apertures, while the black portion blocks light. a) Binary code: the digitized code is 1101, b) Gray code: the digitized code is 0111.

A cylindrical lens can be used to focus the steered beam into the single image line. The line moves up and down according to the applied voltage, as illustrated in the figure. Each column of the aperture array corresponds to a bit of the AOADC result. The apertures in each column are arranged so that the size of each aperture are of equal spacing. All apertures of a bit are combined together and connected to a single photodetector. Similar to the analysis of *N* spectral line and a single collector, by using *N* openings, the full-scale displacement is divided into *2N* quantization levels. When the steering beam falls into any of the apertures of a bit at a sampling instance, the detector receives a short optical pulse. If the collected optical power exceeds a previously set threshold, the detector outputs a digital code '1'. In this way the positions on the image plane are projected onto a code, from which the original voltage information can be restored. Figure 6-1 shows an example: the image line falls into apertures of bit 0, 1 and 3, so its binary output is '1101'. When the line move from the bottom (representing the

minimum voltage input) to the top (maximum), the 4-bit digital output changes from ‘0000’ to ‘1111’. Thus the AOADC digitalizes the signal in the spatial domain. The spatial error associated with the size and position of the apertures will impact the quantization noise level.

The combined collectors work like an ‘OR’ function. Any encoding scheme can be implemented easily. Actually the apertures of the collectors work like a series of barcodes at fixed positions; a specific position corresponds to certain code. Figure 6-1 shows simple binary code and the Gray code. To generate the Gray code, we just need to have openings at the ‘1’ positions and the light blocked at the ‘0’ positions. The similarity of and is clear demonstrated. It is also shown that the aperture and spacing of the LSB of the Gray code are twice that of the binary code. Therefore the Gray code may allow twice the line width, or in another word, the Gray code may increase the resolution of an AOADC by a factor of 2 for a given line width, if the quantizer can accurately detect and discriminate the received power.

If necessary, more complicated codes, can be implemented by simply put openings and blocks at ‘1’ and ‘0’ positions respectively as long as the encoded word maps to the information bits 1-by-1. This makes the encoding procedure effortless and the optical signal is immediately ready for distribution without extensive processors.

Table 6-1: 4-bit binary code and Gray code

Input level (respect to full scale)	Binary code				Gray code			
	Bit3 (MSB)	Bit2	Bit1	Bit0 (LSB)	Bit3 (MSB)	Bit2	Bit1	Bit0 (LSB)
15/16	1	1	1	1	1	0	0	0
14/16	1	1	1	0	1	0	0	1
13/16	1	1	0	1	1	0	1	1
12/16	1	1	0	0	1	0	1	0
11/16	1	0	1	1	1	1	1	0
10/16	1	0	1	0	1	1	1	1
9/16	1	0	0	1	1	1	0	1
8/16	1	0	0	0	1	1	0	0
7/16	0	1	1	1	0	1	0	0
6/16	0	1	1	0	0	1	0	1
5/16	0	1	0	1	0	1	1	1
4/16	0	1	0	0	0	1	1	0
3/16	0	0	1	1	0	0	1	0
2/16	0	0	1	0	0	0	1	1
1/16	0	0	0	1	0	0	0	1
0	0	0	0	0	0	0	0	0

6.1.2 Selection of aperture size

To generate a clean optical digital signal, the opening and spacing of the LSB are generally required to be equal or greater than the beam width at the image plane, although, theoretically, aperture sizes smaller than the beam width also works, as long as the threshold is carefully chosen and the detector is very accurate and sensitive. Figure 6-2 shows output pulse shapes for 3 cases. The first one is the extreme case of ideally infinite narrow beam (blue line). When this beam moves across the collector array with a constant velocity, the aperture collects either the narrow line or nothing; therefore the

output pulses are perfect evenly spaced square shape. When the beam width is finite but narrower than the aperture size (red line), the output is still a clean digital-like pulse with good extinction ratio. Its threshold is set at half of the maximum to discriminate between '0' and '1'. When the beam width is wider than the aperture size (green line), the collected optical power never reaches 0, so the threshold has to be set at the mid point between the maximum and minimum. Moreover, because the transit of the output pulses is slower, it is more vulnerable to noise and threshold errors. Therefore for practical use, the aperture size of the LSB equal to the beam width is set as a criterion of minimum aperture size.

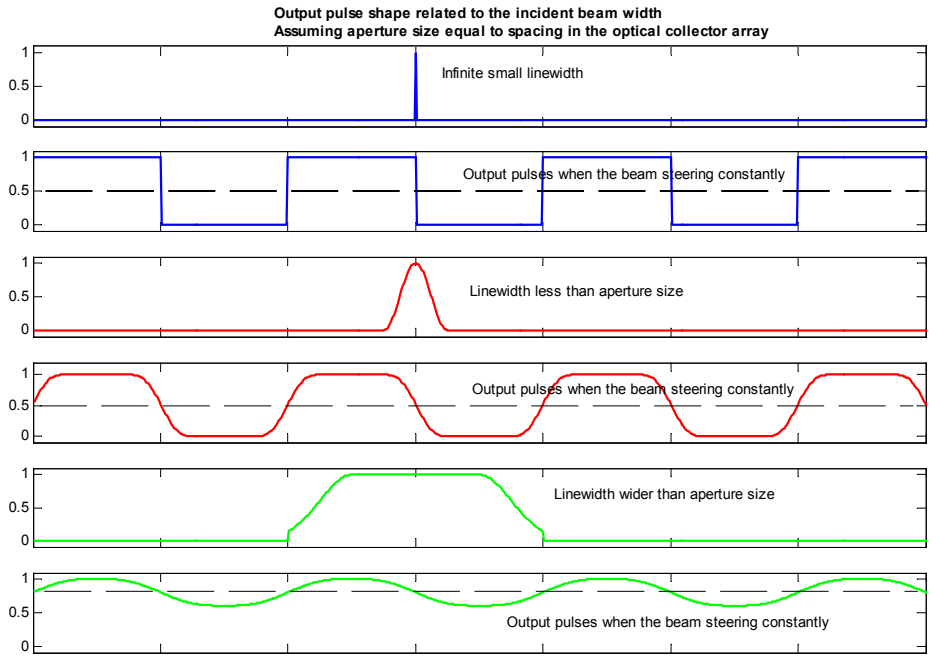

Figure 6-2: The collected optical pulse shape, when the incident beam is a) infinitely narrow compared to the aperture size of the collectors, (plots 1, 2), b) narrower than the aperture size (plots 3, 4), c) wider than the aperture size (plots 5, 6).

These thresholds may be set differently for one bit to the next bit, since the beam width and power intensity may varies at different positions along the length of the image line. In the beam shape shown in Figure 6-1, the focused beam image is wider and more intense in the middle, while narrower and weaker at the ends, so the threshold should be set according to local beam width and power intensity, which should not be a challenge for the AOADC.

6.1.3 Spatial errors of the size and position

The collector array works as a quantizer. The optical quantizer could be cast as electrical quantizer and introduce operational errors in a same manner. Particularly its spatial accuracy impacts the performance of the AOADC directly. The possible spatial errors includes: a) offset error, b) gain error, c) differential nonlinearity (DNL) error, and d) integral nonlinearity (INL) error. They cause deviations of the quantization transfer function from the ideal function.

If the entire aperture array is away from its ideal position, a shift of the transform function from the ideal one occurs. This is defined as offset error, as shown in Figure 6-3 (a). Offset errors will result in DC shift in the reconstructed signal. If all the aperture array size is larger or smaller than the ideal size, it causes an error called gain error. The gain error appears as a change in slope of the transfer curve, as demonstrated in the right graph of Figure 6-3 (b).

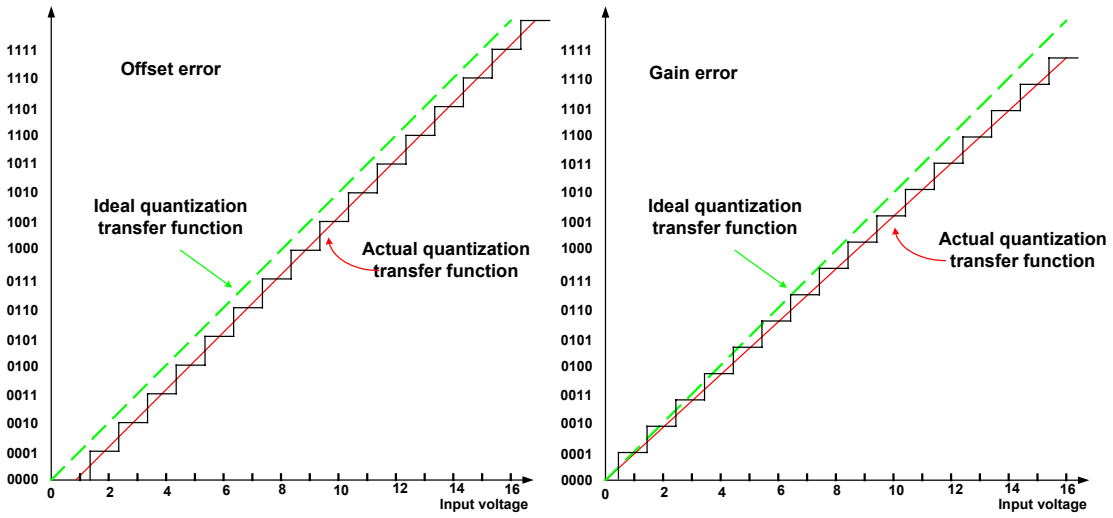

(a) (b)

Figure 6-3: Impact of spatial errors in the collector array. a) offset error and b)gain error

Differential nonlinearity is a measure of the quantization size error of each quantization step. It is defined as the maximum deviation from the ideal step size of 1 LSB. It can be expressed as DNL=max(ΔV_i-ΔV). In the collector array, it is the variation of aperture size and spacing of the collector apertures, as shown in Figure 6-4. If the differential nonlinearity is greater than ±1 LSB, then the A-to-D converter is missing a code. In other words, as the voltage increases across the whole input range, there is a digital output value that never appears.

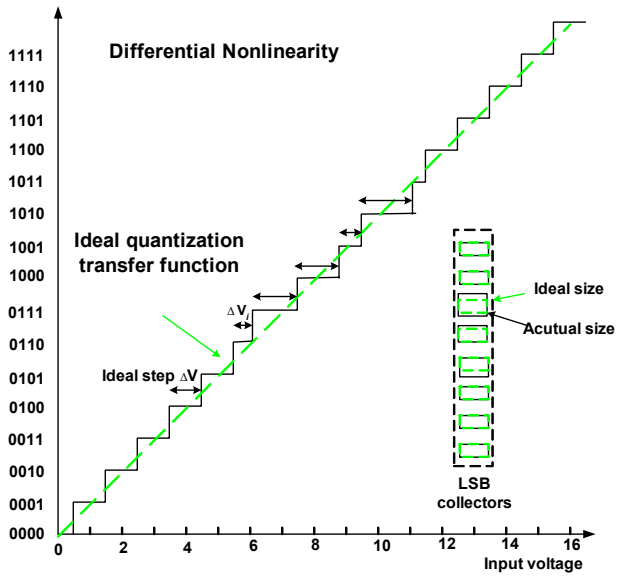

Figure 6-4: Differential nonlinearity

The integral nonlinearity is a measure of the deviation of the actual transfer function from the ideal transfer function, and it is the accumulation of all of individual differential errors. It can be expressed as INL=max(V_i-V), as graphically shown in Figure 6-5.

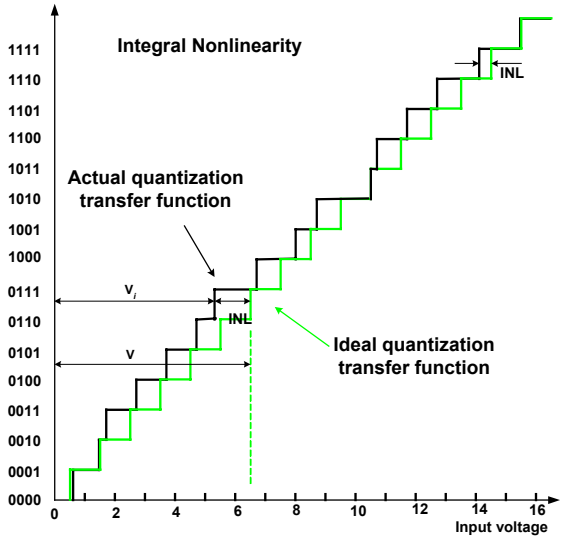

Figure 6-5: Graphical description of integral nonlinearity

The DNL and INL errors are usually caused by imperfect fabrication of apertures and usually are uncorrelated errors. The noise caused by the DNL and INL is added on top of the inherent quantization noise and degrades overall performance of the AOADC. Assume the maximum INL is Δ_{INL}, and the INL of individual steps is uniformly distributed between [$-\Delta_{INL}/2$, $\Delta_{INL}/2$]. If the LSB quantization step is Q, the maximum quantization error due to imperfect step sizes is then $Q/2+\Delta_{INL}/2$ and the error is random between [$-(Q+\Delta_{INL})/2$, $(Q+\Delta_{INL})/2$]. Therefore the total quantization noise can be calculated as:

$$\sigma_q^{\,2} = \int_{-(Q+\Delta_{INL})/2}^{(Q+\Delta_{INL})/2} \frac{1}{Q+\Delta_{INL}} e^2 de = \frac{(Q+\Delta_{INL})^2}{12}, \tag{6-1}$$

resulting in a signal-to-quantization noise ratio of:

$$SQNR = \frac{\sigma_x^{\,2}}{\sigma_q^{\,2}} = \frac{\frac{Q^2}{8}\cdot 2^{2b}}{\frac{(Q+\Delta_{INL})^2}{12}} = \frac{Q^2}{(Q+\Delta_{INL})^2}\cdot 3\cdot 2^{2b-1}. \tag{6-2}$$

Comparing equation (3-10) with the SQNR of a perfect *b*-bit quantizer, the SQNR is by a factor of $\frac{Q^2}{(Q+\Delta_{INL})^2}$. For instance, when Δ_{INL} is equal to the LSB, the SQNR is reduced by 3dB, or other words, the effective number of resolution bits is reduced by 1 bit. It also shows that the spatial error of the optical collector array is very important to the overall performance of the AOADC.

In ADC design, it is usually required that the DNL and INL combined error is less than the LSB. For example, in a 6-bit AOADC using Gray code the LSB contains 16 ($16=2^{b-2}$,

b=6 bits) collector apertures, so the aperture size is 1/32 of the full span. If the maximum angle swing is 5 mrad, as estimated in Chapter 5, this angle spans 500 um at the image plane when the focal length is 100 mm. So the aperture size, as well as the spacing, is 1/32 of 500 um, which is 16 um. So the spatial error due to INL and DNL is required to be less than 16 um, which is not a major challenge for advanced microfabrication technologies.

6.1.4 The proof-of-concept experiment

An experiment was performed to evaluate the static performance of the concept of the optical collector aperture array. A dynamic test would require a fast optical deflector with a frequency of GHz, which is far beyond the capabilities of any commercial deflector in absence of a leaky wave deflector product, which is yet to be fabricated. Therefore, only a static test has been conducted to demonstrate the system performance.

The experiment utilized basic laboratory components. This static test setup is shown in Figure 6-6. It includes 3 parts: a) a steerable light source, b) an optical aperture based on binary or Gray encoding, and c) a CCD camera as detector array. To work as a movable light source and imitate the optical deflector, an LED is mounted on a micropositioner driven by precise motors. The micropositioner is able to move the beam along the x-direction with an accuracy of 0.1um. The beam is projected onto an aperture array. The 5-bit aperture array is arranged in Gray code and printed on a transparency. The beam comes from a laser pointer with a long elliptical Gaussian beam (i.e. line-shape pattern). The output optical power of the laser is about 2 mW and the beam width at the aperture array plane is measured to be 1.56 mm. Behind the aperture array, there is a CCD camera

to record the image of the collected pattern. The 'OR' function of combining collected optical power is accomplished by post image processing in a Matlab© program. This approach is capable of showing the static characteristics saving the cost of waveguide array and coupling.

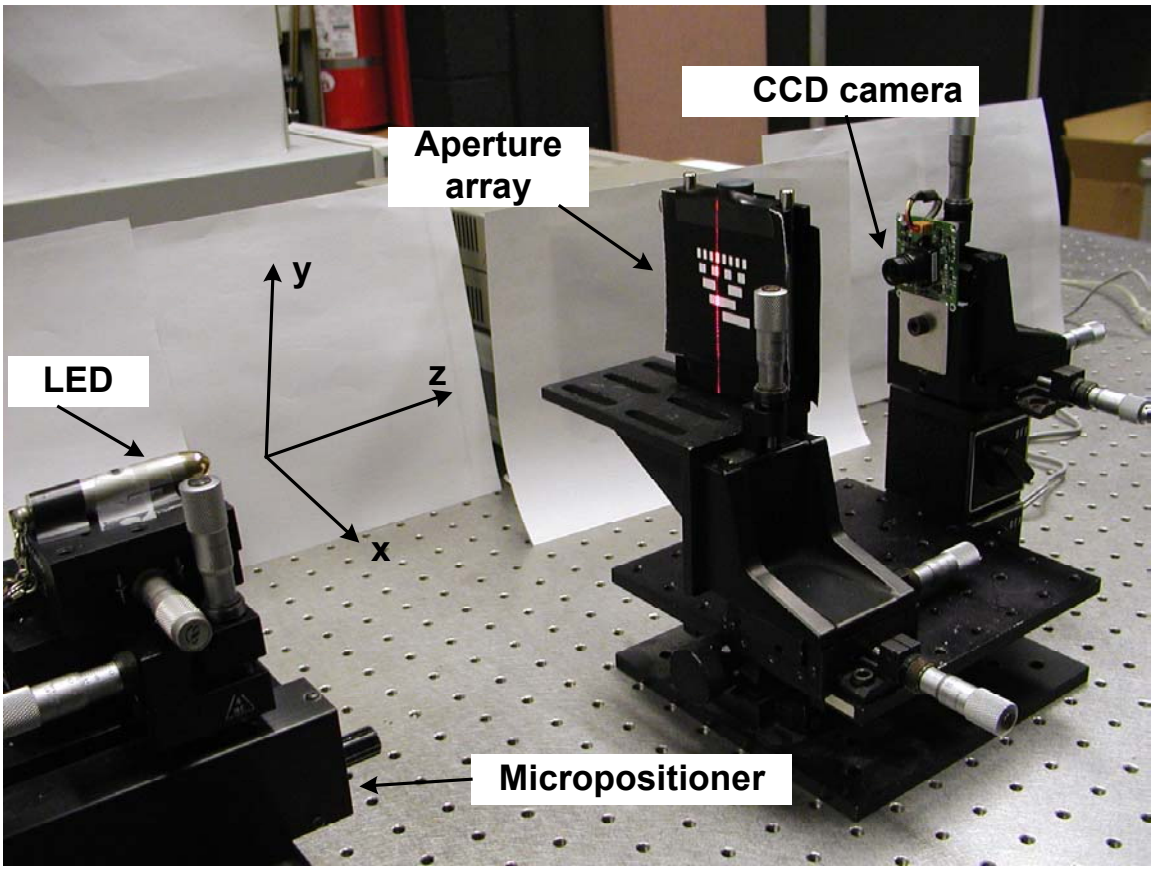

Figure 6-6: The experiment setup of static test of aperture array.

The 5-bit Gray code aperture array is shown in Figure 6-7 (a). The beam is moving along x-direction, so the apertures of each bit are located in a row horizontally. The size of the openings of the LSB, as well as their spacing, is 2 mm, so the widths of Bit1-Bit4 are

4mm, 8mm, 16mm and 16mm respectively. When the beam is moving across the aperture array, the continuous images were captured by the CCD camera at 15 frames/second. As examples, Figure 6-7 shows clips at 3 different positions: 00011, 11001 and 10011, corresponding to binary codes of 00101, 10001, and 11101 respectively.

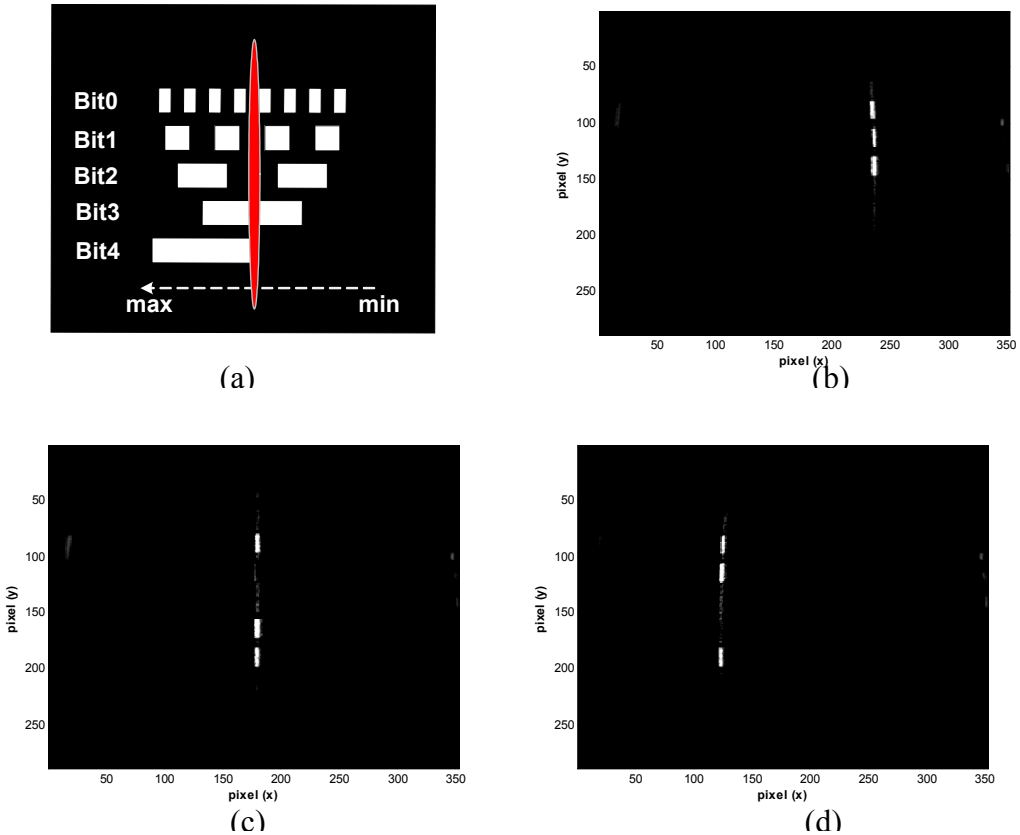

Figure 6-7: The aperture array of a Gray code pattern (a) and the images of a line-shape beam pass through the apertures: (b) 00111, (c) 11001 and (d) 10011

The CCD collects a movie composed of a series of Gray scale images. These images are then processed by a Matlab program. In the Gray scale the color code is proportional to the power intensity on the pixel. Therefore the program just needs to sum up the color

code of all pixels in the aperture region of each bit. The summation is the combined collected optical power of that bit. This power information is then compared with a threshold to obtain digital code '1' or '0'. The obtained 5-bit output Gray code is graphically shown in Figure 6-8. The code maps to a normalized quantization level within [0 1] in Figure 6-9. The transfer function matches the ideal functional behavior very well. It shows that both DNL and INL are less than ½ LSB.

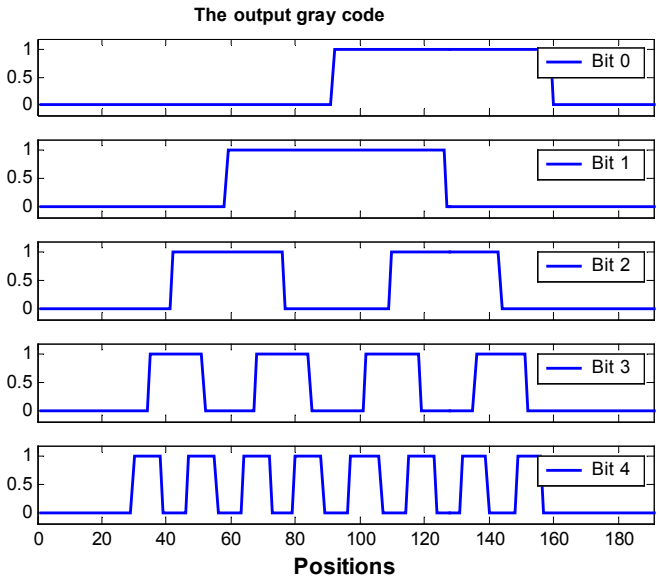

Figure 6-8: The output Gray code obtained from post image processing

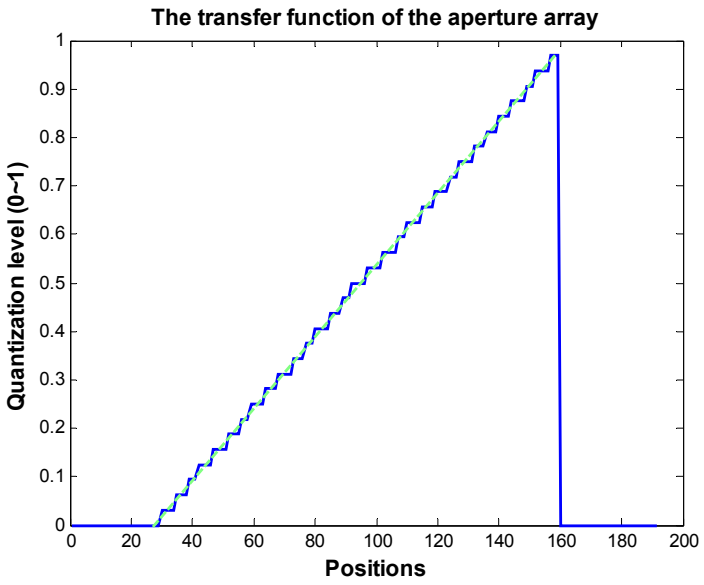

Figure 6-9: The quantization transfer function of the aperture array

6.1.5 Possible implementation

The concept of an optical collector array is novel, simple and efficient. The major challenges for this component are mainly fabrication issues. Since the angular swing is in the range of only a few mrad and the linewidth is usually in the order of one tens of mrad, to collect and detect the image line requires either very small sizes of the apertures or a very long separation of image plane to the leaky waveguide. In order to keep the whole system compact, the former approach is preferred. Implementation of aperture sizes as small as 10 μm is not difficult for current integrated optics technologies. The optical collector array can be implemented by an arrayed waveguide, as proposed in Figure 6-10. The input waveguides of one bit merge to a single output waveguide and deliver the collected optical power to a remotely located photodetector. This waveguide array structure is very similar to the planar arrayed waveguide grating (AWG), which has been employed in WDM (Wavelength Division Multiplexing) for years. Input access aperture

as small as 6 μm [60] has been reported. One challenge may be that in AWG the waveguides are arranged in one dimensional, while in the proposed collector array, the planar waveguides have to be stacked up for different bits. Additionally, the waveguide apertures must be quite accurate in size and position.

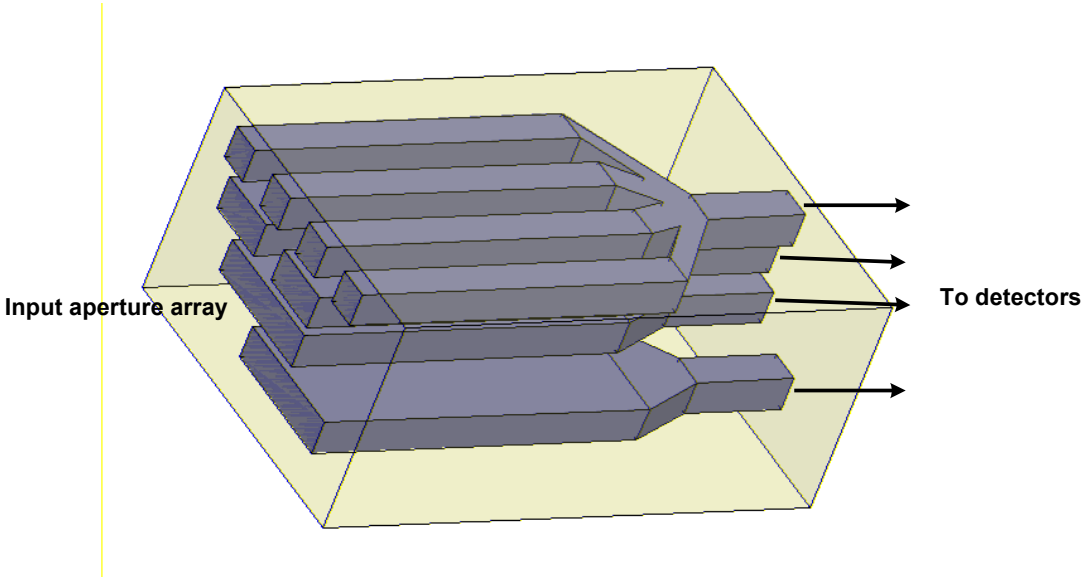

Figure 6-10: Drawing of 4-bit Gray code arrayed waveguide

6.2 Mode-locked laser

Fast pulse generation provided by advanced mode-locked lasers is the reason that optical ADCs appear promising. Besides high repetition rate, optical sampling also requires very stringent time jitter. Finding an MLL with high repetition rate and small time jitter is a common challenge of any optical ADCs, both hybrid and all-optical. Since mode-locked lasers with repetition rate as high as 100GHz have been successfully used in other optical ADC systems, 40GHz pulses should be an easy task for state-of-the-art mode locked lasers.

The proposed AOADC is designed to operate at 40GS/s with at least 6 bits of resolution. There are three specifications characterizing a pulse train that need to be addressed to achieve desirable performance of the AOADC: repetition rate, time jitter and pulse width. According to the aperture jitter limitation we derived in Chapter 2, to ensure equivalent noise due to the jitter less than the 6-bit quantization noise, the time jitter of a 40GHz pulse train is required to be less than 40 fs. At the same time, the pulse width must be keep short so that a single pulse covers not more than 1 LSB, otherwise the least significant bit is meaningless. It is easy to image that when a pulse lasts too long, the image line may sweep across two of the collector apertures, so the detector will collect two or more short pulses successively and causes errors. To avoid this problem, the pulse width must be less than the shortest time that the image line sweeps over a single aperture, i.e. a LSB. If the input is a 20GHz sinusoidal signal, the fastest sweep happens when it crosses zero, where the slope is $A\omega$, where A is the amplitude and ω is the angular frequency. A LSB is then $2A/32$ if the apertures are arranged as Gray code. Therefore it takes $1/16\omega$ to change from a quantization level to another around the zerocrossing, so the pulse width is required to be less than $1/16\omega$, which is 0.5 ps in our design. Therefore the requirements for the MLL can be summarized as: repetition > 40GHz; time jitter < 40fs; and pulse width < 0.5ps.

Repetition rate is not a big challenge for mode locked lasers. Pulse generation at more than 100 GHz has been achieved by using a passive mode locking technique [61]. Even THz mode-locked laser has been reported by using harmonic passive mode-locked DFB

lasers [62, 63]. Active mode-locked lasers providing lower time jitter at more than 100 GHz have been also reported [61]. Monolithically integrated DFB lasers with electro-absorption (EA) modulators have been demonstrated [64]. This interesting optical transmitter has been fabricated with one or two EA modulators. EA modulators are inherently very high speed, and mode-locked devices based on this structure have been used to produce pulses up to 120 GHz.

Figure 6-11 depicts the structure of a source with two EA modulators, which is employed for pulse code modulation at rates as high as 40 Gb/s. A version of this structure where only one modulator is used has also been used to demonstrate external modulation for Ka-band sub-carrier modulation [65], where a spurious free dynamic range of SFDR≥105dB $Hz^{2/3}$ has been demonstrated without the use of any linearization technique. The superior performance and potential low cost of fabrication makes this device an attractive candidate to implement the proposed AOADC.

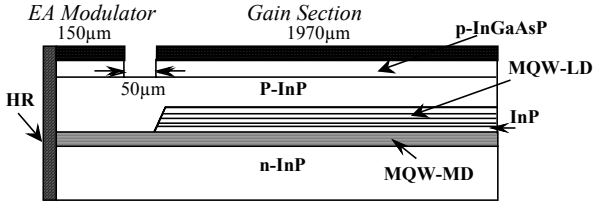

Figure 6-11: Physical structure of monolithically integrated DFB laser with EA modulator. [64]

The 40fs time jitter requirement is quite challenging for current high frequency MLLs. However it is not prohibitive; very low time jitters have been reported for relatively low

rate pulse generation. Timing jitter less than 10 fs at 10 GHz with a mode-locked fiber laser [66] and 1 fs at 10 GHz with a mode-locked Cr:YAG microchip-laser [67] have been reported. At ultra high repetition rates, very impressive 140fs of time jitter at 480GHz using CPW-LD (Colliding pulse mode-locking laser diode) [68], 230fs of time jitter at 102 GHz using a semiconductor mode-locked laser [69], and 93fs in 160GHz optical clock extraction [70] have been reported.

Subpicosecond short pulse generation has been demonstrated by using a variety of techniques; 850fs at 40GHz and 250fs at 300GHz have been reported recently [71, 72]. A combined performance of pulse width of 580fs and time jitter of 140fs at 850GHz is achievable in ultra high-speed AOADCs [73]. It is concluded that pulse generation is not a limitation for the proposed AOADC.

6.3 RF Broadband photodetectors

The broadband photodetector is another common challenge for any ultra high-speed optical ADC. The ADC's quantizing post-sampled optical pulse in intensity requires not only broad bandwidth but also high sensitivity. But in the proposed AOADC, which is working in the spatial domain, the photodetector connected to the optical collector array only needs to tell whether the collected power is higher than a preset threshold. The digital-like operation greatly reduces requirements for detector sensitivity and linearity. Therefore speed is the major concern for photodetectors in the proposed AOADC.

High-speed photodetectors up to THz have been demonstrated. Photodetectors with 40GHz of RF bandwidth have been commercially available from many manufacturers. In

commercial products, Discovery Semiconductors has delivered an InGaAs PIN Diode (part number: DSC10W) with bandwidth as large as 75 GHz [74], which is the best in the market, and NTT has developed ultra high frequency UTC-PDs (Uni-Traveling-Carrier Photodiode). NTT's photodetector model at 120 GHz [75] and photodiode with bandwidth of 310 GHz [76] has been demonstrated, so commercial parts have been able to meet our requirements for the AOADC As photodetectors keep improving, they should be able to support even higher sampling rates. The noise performance of the photodetectors, as well as the spatial error of the optical collector array, impacts the resolution of the overall AOADC system.

6.4 Summary

This chapter shows the feasibility of the proposed AOADC in terms of its enabling components. A spatial quantizer is proposed and analyzed. It is able to generate any code without adding additional hardware. A static experiment shows that the quantizer-induced error is minor when the beam size is about half of the aperture size. The collector array can be implemented by waveguide array technologies and a possible structure is given. As for the active components, MLL and photodetectors, current technologies can provide the necessary performance to make the proposed AOADC feasible.

7. Conclusions and Future Work

7.1 Technical Contributions

To address the inherent limitations of current electronic and optical ADCs, we proposed spatial based OADC. Two designs of prism based and leaky wave structures werer presented. Both designs are proposed for the first time, however, the leaky waveguide based AOADC does not suffer from a high voltage requirements as the steerable grating based topology.

Initially we studied a possible spatial sampler using a steerable grating, which could be implemented by E-O GRISM. Potential advantage of using gratings is that it can generate more angular displacement for the same index change by using grating is that it can generate more angular displacement for the same index change by using high diffraction order and hence achieve higher resolution. We completed a system level design of 10-bit AOADC by manipulating the multiple lines in the spectral domain and the size of the optical collector array in the spatial domain. However, also because of the using of gratings, spectral components were split and because CW beams in multiple directions, and the multibeams were steered across the sensor array continuously. Therefore the detector would receive extremely fast short optical pulses, which cannot be sensed and discriminated by existing photodetectors. After carefully analyzing the problem, we proposed two approaches, which are solvable through complicated. Inspired by this initial study, we finally changed the whole design of spatial sampler and found a good solution

that retains the advantages of spatial domain AOADC and eliminates the CW beam problem at the same time.

The proposed ADC is able to convert a multi-GHz electrical analog signal to optical digital codes in the spatial domain by using a traveling wave leaky waveguide deflector. This is a unique AOADC concept with a feasible implementation. In contrast to existing all-optical ADCs that depend heavily on the availability of high performance components, my design took into consideration all the practical issues from the beginning. The work has accomplished a conceptual design, system level analyses, identification of enabling components, detailed component design and some preliminary tests. The thesis made significant technical contributions in the following aspects.

For the first time this thesis investigated spatial domain AOADCs as a new distinct category of ADCs. Compared to various other types of ADCs, the thesis concluded that spatial domain AOADCs have greater immunity from optical intensity fluctuations and shot noise, hence it is potentially a high resolution solution. Its bit resolution is mainly determined by MLL timing jitter, spatial error of the spatial quantizer, maximum deflection and image line width of the spatial sampler; the former two are fairly small and the latter two were found to be the major limitations of the overall resolution. As advanced MLLs and photodetectors have demonstrated frequencies as high as 100 GHz, the sampling rate of a spatial domain AOADC is mainly determined by the spatial sampler, where a compromise between sampling rate and resolution must be made. Based

on a system level analysis, we set my design goal as 6 bits at 40 GS/s, one of the best among all-optical ADCs.

Corresponding enabling components and required component specifications were identified. Since the proposed AOADC can share the same MLLs and photodetectors, which have been used in other reported high-speed AOADCs, the optical sources and detectors are not a barrier hence was not discussed in great detail in this thesis. The critical parts to be designed are the spatial sampler that translates the amplitude of an RF signal into a unique deflection angle, and the spatial sensor array that quantizes the angular displacement and encodes it into an electrical digital parallel bit streams. Finally, design of both critical parts successfully leading to the required specification is presented in this thesis.

The solution is the E-O leaky waveguide deflector. Proposed for the first time, this unique structure of a leaky waveguide driven by traveling wave electrodes enables operation above 20 GHz. Because of its strip channel configuration, driving voltage as low as 20 V can be used, compared to KV for conventional E-O deflectors. The traveling wave electrodes have a characteristic impedance of 50 Ω over a wide frequency range. Moreover, since the image line of the leaky waves is essential the 0^{th} order, the multiple spectral components appear at the same position with their phase locked, as the original optical pulses from the MLL. We designed two practical implementations for the E-O leaky waveguide deflector: a) E-O polymer leaky waveguide with stripline electrodes, and b) a *z*-cut Ti:$LiNbO_3$ leaky waveguide with CPW electrodes. Numerical analyses

have shown 7 bits from DC to 28 GHz for a), and 6 bits from 14 to 26 GHz. Both show the capability to achieve the design goal of 6-bit at 40 GS/s.

The thesis provided detailed designs in terms of material selection, optical and RF geometry, and RF driving schemes. Moreover, we offered an approximate theoretical model of a strip leaky waveguide so that the leaky coefficient can be found from a simple yet effective analytical equation. The calculated results using the model matched the simulation data well. The model helped me to understand the behavior of the leaky waveguide and provide a guideline in designing the leaky waveguide deflector. The design procedure can be summarized as following:

1) Select proper E-O material and superstrate materials so that the refractive index of the superstrate is slightly higher than that of the E-O material.
2) Design the strip waveguide geometry so that the waveguide supports single mode operation at given wavelength.
3) Design the shape of the superstrate so that the incident angle of the leaky waves at the superstrate/air interface is close to the total reflection angle. The incident angle must be selected as a compromise between the angular magnification factor and transmitted optical power. Then select proper anti-reflection layers to make maximize power transmitted to the detectors.
4) Find a proper length in order to obtain the desired angular resolution.
5) Choose proper buffer layer material and thickness using the analytical model to obtain a leaky coefficient so that 50% to 70% of the optical power leaks out after

propagating the selected length. Then use a numerical modeling tool to verify and optimize the design in order to achieve the desirable result.

6) Adjust the gap, width, and thickness of the RF electrodes so that its effective index of refraction of the propagating RF signals is close to that of the optical signals. At the same time ensure that the characteristic impedance of the traveling wave transmission lines is 50 Ω. With these two conditions satisfied, try to make the gap between the electrodes as small as possible in order to reduce necessary driving voltage.

These steps may need to be repeated in an iterative method to achieve the optimized performance.

Finally, this thesis also covered a simple yet flexible optical collector array to collect the deflected optical energy and encode the position of the image line. The collector array is able to generate digital-like optical pulses for all bits by using a single image line, therefore it effectively eliminates bit-to-bit mismatch. In addition it can compensate for any nonlinearity in the deflector easily by carefully arranging the collector apertures. We analyzed the impact of spatial errors in the collector array and investigated the static properties in a preliminary experiment. To sense the very small angular swing and resolution of the E-O deflector, we have proposed an integrated implementation using a 2-D waveguide array.

7.2 Future work

The thesis has investigated the leaky waveguide based AOADC and provided complete and quantitive designs for future implementations. A good start for future research would

be to build a prototype of the proposed AOADC. Among the necessary enabling components, the E-O leaky waveguide deflector and the optical collector array must be manufactured, while the MLL and photodetectors may be found from the market or research laboratories.

7.2.1 Manufacture and test of the E-O leaky waveguide deflector

At the end of Chapter 6, we showed that both an E-O polymer leaky waveguide and $LiNbO_3$ leaky waveguide can be used for the spatial sampler. Either can be chosen and manufactured following the designs provided in the thesis. Although the leaky waveguide looks very much like a conventional E-O modulator using polymer or $LiNbO_3$, it cannot be built by simply adding a higher-index of refraction material to an existing modulator. Both structures must be developed from the substrate.

- Using E-O polymer

Currently existing polymer based E-O modulators usually employ configurations with electrodes above and beneath the waveguide, as depicted in Figure 7-1, so the electrodes will block leaky waves on both top and bottom. Therefore we cannot simply take an existing polymer E-O modulator and convert it into a leaky waveguide. In the designed E-O polymer leaky waveguide deflector slot-line design should be implemented on top of the waveguide. In order to achieve maximum index modulation under the electrode configuration, during the fabrication the poling process should be done under the same configuration with high voltage. One should work closely with the manufacturing experts to determine and control the entire process.

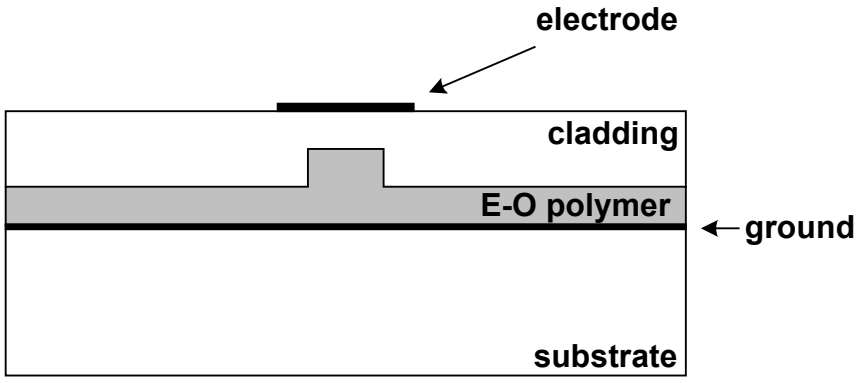

Figure 7-1: Typical electrode arrangement for polymer E-O modulators.

- Using $LiNbO_3$

In the design of a *z*-cut Ti:$LiNbO_3$ leaky waveguide deflector the optical waves leak out from the bottom and hence require the $LiNbO_3$ to be as close to the vertical mode size of the propagation mode, which is typically about 10 μm. However typical $LiNbO_3$ wafers used in conventional $LiNbO_3$ modulators are 300 to 500 μm in thickness, or 100 μm at minimum. Therefore extra thickness must be removed from the backside. The thin $LiNbO_3$ crystal is a challenge in two aspects: a) mechanical strength is reduced and hence it is fragile; b) the removal process may result in rough surfaces and cause undesired scattering loss. A Ti:$LiNbO_3$ waveguide with 10 μm substrate thickness around the channel region has been demonstrated using micromachining technology with KrF excimer laser ablation [77]. The process should be investigated in terms uniformity and surface quality to ensure that the desired leaky coefficient could be obtained. Similar to the simulation of the structures, the manufactured E-O deflector should be tested to determine its deflection angular swing, angular resolution, leaky coefficient, RF bandwidth and characteristic impedance.

7.2.2 Manufacture and test of the optical collector array

In order to sense the small angular swing and narrow image line from the deflector the apertures of the collector array needs to be on the order of microns. The most likely solution is to use an integrated 2-D waveguide array as proposed in the Chapter 6. To implement the collector array we must extend the integrated waveguide manufacturing technology from 1-D to 2-D. This technology is not available yet; so the first step may be to investigate the manufacturing process. As the optical collector array is manufactured, static and dynamic tests should be performed to determine its spatial error and corresponding impact on the quantization.

7.2.3 OADC system evaluation

When the leaky waveguide E-O deflector and optical collector array are manufactured and high-speed MLL and photodetectors are purchased, the AOADC should be assembled according to the configuration shown in the Chapter 4. The selection of lenses and distance of the image plane from the deflector can be determined by measured the angular resolution of the deflector and the aperture size of the optical collectors. The AOADC system should be tested with regard to static and dynamic performance. In terms of static tests, the offset, gain error, INL and DNL should be found. Regarding its dynamic performance, as the sampling rate is determined by the MLL, the quantization resolution should be determined by measuring the SNR and the SFDR at different RF frequencies. Its total power dissipation, stability and cost should be evaluated as well.

7.2.4 Possible Improved implementations

The design uses separate E-O deflector, lens and collector array, therefore it may not be suitable for practical applications in some harsh environments. An integrated configuration will benefit the system in both compact size and stability. As integrated optics is advancing, it is possible to implement all these components on a single substrate. At the same time, we should keep our eyes on new materials, especially advanced E-O materials. For example, Strontium Barium Nitrate ($Br_xSr_{1-x}Nb_2O_6$), or SBN, has demonstrated an electro-optical coefficient as large as $\gamma_{63}=1400\times10^{12}$ m/V, which is 10 times higher than that of E-O polymers [42]. The extremely strong electro-optical effect could lead to a very large angular swing and resulting in 3-4 additional resolution bits in the AOADC. The thesis did not explore a possible implementation by using SBN because it also shows extremely high dielectric constant ($\varepsilon \approx 880$), which would result in difficulty in achieving RF and optical wave velocity matching [78, 79]. This thesis, however, has significantly contributed to developing a feasible structure that is capable of achieving good performance using commercially available materials. The general design guideline provided by the thesis will help in the direction of further enhancing the performance by taking advantages of new structure and materials.

List of References

1. B. L. Shoop, "Photonic Analog-to-Digital Conversion", Springer 2001.
2. FCC news releases, http://ftp.fcc.gov/Bureaus/Engineering_Technology/News_Releases/2002/nret0203.pdf
3. J. Mitola, "Software radios-survey, critical evaluation and future directions," *Telesystems Conference*, 1992. NTC-92, National, 19-20 May 1992, pp. 13/15 - 13/23
4. R. L. Thompson, M. J. Degerstrom, W. L. Walters, M. E. Vickberg, P. J. Riemer, E. L. H. Amundsen, and B. K. Gilbert, "An 8-bit 2.5 gigasample A/D converter multichip module for all-digital radar receiver for An/APS 145 radar on Navy E2-C airborne early warning aircraft," in *Proc. 1997 IEEE Multi-Chip Module Conf.*, Santa Cruz, CA, Feb.4-5, 1997, pp. 20–26-5.
5. R. H. Walden, "Analog-to-Digital Converter Survey and Analysis", IEEE Journal of selected areas in communications, vol. 17, No. 4, April 1999, pp539-550
6. H. F. Taylor, "Electro-Optic A/D Converter, US patent 4058722
7. D. K. Brock, O. A. Mukhanov, and J. Rosa, "Superconductor digital RF development for software radio," IEEE Commun. Magazine, pp. 174-179, Feb. 2001.
8. X. Hou, A. S. Daryoush, R. Lachenmaier, W. Rosen, "Challenges of a GS/s All-Optical Analog-to-Digital Converter", *Proceedings of the IEEE Sarnoff Symposium*, Princeton, NJ, pp289-292 , March 2003.
9. X. Hou, A. S. Daryoush, W. Rosen, "A Novel All-Optical Analog-to-Digital Converter", *Proceedings of the 8th Optoelectronics and Communications Conference (OECC)*, Shanghai, China, pp603-604, Oct. 2003.
10. A. S. Daryoush, X. Hou, W. Rosen, "All-Optical ADC and its Applications in Future Communication Satellites", International Topical Meeting on Microwave Photonics, invited paper, Oct. 2004, to be published.
11. X. Hou, A. S. Daryoush, W. Rosen, H. Burstyn, P. Zalud , "Design of a Novel All-Optical Analog-to-Digital Converter Using Grating Coupler", *Proceedings of 2004 IEEE Radar Conference*, pp523-526, April 2004.
12. C. E. Woodward, K. Konkle, M. L. Naiman, "A monolithic voltage-comparator array for A/D converters", *IEEE Journal of solid state circuits*, Sc-10, No. 6, pp392-399, Dec 1975.

13. K. Poulton, R. Neff, B. Setterberg, B. Wuppermann, T. Kopley, R. Jewett, J. Pernillo, C. Tan, A. Montijo; "A 20 GS/s 8 b ADC with a 1 MB memory in 0.18um CMOS", *2003 IEEE International Solid-State Circuits Conference*, *Digest of Technical Papers*. *ISSCC*, pp.318 – 496, 2003.

14. Data sheet. http://www.maxim-ic.com/quick_view2.cfm/qv_pk/2092

15. Data sheet. http://www.rsc.rockwell.com/highspeed/files/PB_0040XA1-1104.pdf

16. Data sheet. http://www.rsc.rockwell.com/highspeed/files/PB_0032XA1-1104.pdf

17. Data sheet. http://www.atmel.com/dyn/resources/prod_documents/doc2101.pdf

18. C. Baringer, J. Jensen, L. Burns, B. Walden, "3-bit, 8 GSPS flash ADC", Indium Phosphide and Related Materials, 1996; 21-25 Apr 1996; pp 64 -67

19. P. Xiao, et al., "A 4b 8GSample/s A/D converter in SiGe bipolar technology," ISSCC Digest of Technical Papers, February 1997, pp. 124 – 125

20. T. Broekaert, W. Ng, J Jensen, D. Yap, D. Persechini, S. Bourgholtzer, C. Fields, Y. Brown, B. Shi, and R. Walden, "InP HBT Optoelectronic Integrated Circuits for Photonic Analaog-to-Digital Conversion," *IEEE J. Solid State Electron*, Vol. 36, no. 9, Sept. 2001

21. R. Yu, et al, "Multi-Gigasample per second Analog-to-Digital Converters and Digital-to-Analog Converters Implemented in an AlGaAs/GaAs HBT Technology," *IEE Conference on Advanced A/D and D/A Conversion Techniques and their Applications*, July 1999

22. K. Poulton, K. Knudsen, J. Corcoran, K. Wang, R. Nubling, R. Pierson, F. Chang, P. Asbeck, R. Huang, "A 6-b, 4GSa/s GaAs HBT ADC," *IEEE Journal of Solid-State Circuits*, Vol. 30, No. 10, Oct. 1995

23. F. Vessal, C. Andre T. Salama,"An 8-Bit 2-Gsample/S Folding-Interpolating Analog-to-Digital Converter in SiGe Technology", *IEEE Journal Of Solid-State Circuits*, Vol. 39, No. 1, pp. 238-241, Jan. 2004.

24. J. S. Rieh, B. Jagannathan, et al, "SiGe HBTs with cut-off frequency of 350 GHz", *International Electron Devices Meeting, 2002. IEDM '02. Digest*. pp. 771 – 774, Dec. 2002.

25. W. Hafez, Jie-Wei Lai, and M. Feng, "InP/InGaAs SHBTs with 75 nm collector and f/sub T/>500 GHz", *Electron. Letts*., Vol. 39 , Issue: 2, pp.1475 – 1476, Oct. 2003.

26. Y. Yamashita, A. Endoh, K. Shinohara, K. Hikosaka, T. Matsui, S. Hiyamizu, T. Mimura, "Pseudomorphic $In_{0.52}Al_{0.48}AsIn_{0.7}Ga_{0.3}/As$ HEMTs with an ultrahigh f_T of 562 GHz**",** IEEE Electron Device Letters, Vol. 23, Issue: 10 , Oct. 2002, Pp. 573 – 575

27. Twichell, J.C.; Juodawlkis, P.W.; Wasserman, J.L.; Williamson, R.C.; Betts, G.E. , "Extending the performance of optically sampled time-demultiplexed analog-to-digital converters **",***Conference on Lasers and Electro-Optics*, 2000. (CLEO 2000), pp. 624 –625, 2000.

28. Juodawlkis, P.W.; Twichell, J.C.; Betts, G.E.; Hargreaves, J.J.; Younger, R.D.; Wasserman, J.L.; O'Donnell, F.J.; Ray, K.G.; Williamson, R.C, "Optically sampled analog-to-digital converters" Microwave Theory and Techniques, IEEE Transactions on , Volume: 49 Issue: 10 Part: 2 , Oct. 2001 Page(s): 1840 -1853

29. T. R. Clark, J. U. Kang, R. D. Esman, " Performance of a time- and wavelength-interleaved photonic sampler for analog-digital conversion "IEEE Photonics Technology Letters , Volume: 11 Issue: 9 , Sept. 1999, pp 1168 –1170

30. S. Bhushan, P. V. Kelkar, B. Jalali, O. Boyraz and M. Islam, "130-Gsa/s Photonic Analog-to-Digital Converter with Time Stretch Preprocessor", IEEE Photonic Technology Letters, Vol. 14, No. 5, May 2002, pp684-686

31. F. Coppinger, A. S. Bhushan, B. Jalali, "Photonic Time Stretch and Its Application to Analog-to-Digital Conversion", IEE Transactions on microwave theory and techniques. Vol 47. No. 7, Jul. 1999, pp1309-1314

32. B. Jalali and Y. M. Xie, " Optical folding-flash analog-to-digital converter with anlog encoding", Optics letters, Vol. 20, No. 18, pp1901-1903

33. M. J. Hayduk, "Photonic Analog-to-Digital Conversion Using Light Absorption" US patent 6326910

34. M. J. Hayduk and R. J. Bussjager, "Photonic Analog-to-Digital Conversion", webpage http://www.ieee.org/organizations/pubs/newsletters/leos/feb01/hottopic.htm

35. J. T. Gallo, "Photonic A/D converter using parallel synchronous quantization of optical signals", US patent 6188342

36. Zmuda, H.; Toughlian, E.N.; Li, G.; LiKamWa, P., "A photonic wideband analog-to-digital converter**",** Aerospace Conference, 2001, IEEE Proceedings. , Volume: 3 , 2001 Page(s): 3/1461 -3/1472 vol.3

37. M. Johansson, B. Löfving, S. Hård, L. Thylén, M. Mokhhtari, U Westergren, and C. Pala, "Study of an ultrafast analog-to-digital conversion scheme based on diffractive optics", Applied Optics, Vol. 39, No. 17, June 2000, pp2881-2887

38. L. Brzozowski and E. H. Sargent, "All-Optical Analog-to-Digital Converters, Hardlimiters, and Logic Gates", Journal of Lightwave Technology, Vol. 19, No. 1, Jan. 2001, pp114-119

39. M. Currie, T. R. Clark and P. J. Mathews, "Photonic Analog-to-Digital Conversion by Distributed Phase Modulation", IEEE Photonics Technology letters, Vol. 12, No. 12, Dec. 2000, pp1689-1691

40. E. Donkor, et al, "A 5 Gigabit/sec All Optical Parallel Analog-to-Digital Converter", CLEO 2001, pp182-183

41. B. L. Shoop, E. C. Shaffer and G. P. Dudevoir, "Distributed Photonic A/D Conversion Using a Neural Network, Oversaampling, and Spectral Noise Shaping", Optical Fiber Communication Conference and Exhibit, 2001. OFC 2001 , Volume: 3 , 2001 Pp WDD51 -WD1-3 vol.3

42. W. C. Nunnally, "Electro-optical analog to digital conversion method and device", US patent 6714149

43. P. Rabiei, and A. F. J. Levi, "Analysis of hybrid opto-electronic WDM ADC," IEEE J. *Lightwave Technol.,* pp. 1264-1270, 2000.

44. Y. Ninomiya, "High S/N-Ratio electrooptic prism-array light deflectors," *IEEE J. of Quantum electronics*, vol. QE-10, no. 3, pp. 358-362, Mar. 1974.

45. D. A. Scrymgeour, Y. Barad, V. Gopalan, K. T. Gahagan, Q. Jia, T. E. mitcheall, and J. M. Robinson, "Large-angle electro-optic laser scanner on $LiTaO_3$ fabricated by in-situ monitoring of ferroelectric-domain micropatterning," *Appl. Optics*, vol. 40, no. 34, pp. 6236-6241, Dec. 2001.

46. L. Sun, J. Kim, D. An, X. Lu, Q. Zhou, J. M. Taboada, R. T. Chen, J. J. Maki, S. Tang, H. Zhang, W. H. Sterier, C. Zhang, "Polymeric waveguide prism-based electro-optic beam deflector," *Opt. Eng*., vol. 40, no. 7, pp. 1217-1222, Jul. 2001.

47. T. Khayim, A. Maruko, K. Shibuya, A. Morimoto, and T. Kobayashi, "Ultrafast unidirectional beam deflection using an electrooptic traveling phase grating with periodic domain inversion", *IEEE J. of Quantum electronics*, vol. 37, no. 8, pp. 964-969, Aug. 2001.

48. Yariv, "Optical Electronics", Fourth edition, Saunders Colledge Publishing, 1991

49. M. Nancy, Marcos A. R. Franco, and A. Passaro, "Analysis of a x-cut Ti:$LiNbO_3$ electrooptic modulator with a ridge structure," Procedings of SBMO/IEEE MTT-S IMOC'99, pp. 144-148, 1999.

50. H. Nishihara, M. Haruna, and T. Suhara, Optical integrated circuits, 1st ed., McGraw-Hill, 1989, pp. 109-111

51. D. Chen, H. R. Fetterman, A. Chen, W. H. Steier, L. R. Dalton, W. Wang, and Y. Shi, "Demonstration of 110 GHz electro-optic polymer modulators," *Appl. Phys*. Lett., vol. 70, no. 25, pp. 3335-3337, Jun. 1997.

52. M. Oh, H. Zhang, C. Zhang, H. Erlig, Y. Chang, B. Tsap, D. Chang, A. Szep, W. H. Steier, H. R. Fetterman, and L. R. Dalton, "Recent advances in electrooptic polymer modulators incorporating highly nonlinear chromophore," *IEEE J. on Selected Topics in Quantum Electronics*, vol. 7, no. 5, pp. 826-835, Sept/Oct. 2001.

53. E. L. Wooten, K. M. Kissa, A. Yi-Yan, E. J. Murphy, D. A. Lafaw, P. F. Hallemeier, D. Maak, D. V. aAttanasio, D. J. Fritz, G. J. McBrien, and D. E. Bossi, "A review of lithium niobate modulators for fiber-optic communication systems," *IEEE J. selected topics in quantum electronics*, vol. 6, no. 1, pp. 69-82, Jan/Feb. 2000.

54. P. K. Tien, and R. Ulrich, "Theory of prism-film coupler and thin-film light guides," *J. Optical Society of America*, vol. 60, no. 10, pp. 1325-1337, Oct. 1970.

55. R. Ulrich, "Theory of the prism-film coupler by plane-wave analysis," *J. Optical Society of America*, vol. 60, no. 10, pp. 1337-1350, Oct. 1970.

56. P. K. Tien, "Light waves in thin films and integrated optics," *Appl. Opt.,* vol. 10, no. 11, pp. 2395-2414, Nov. 1971.

57. M. Geshiro, M. Hotta, and T. Kameshima, "Coupled-mode analysis of leaky waves in channel waveguides consisting of anisotropic material," *IEEE Trans. on Microwave Theory and Techniques,* vol. 41, no. 6/7, pp. 1159-1164, Jun/Jul. 1993.

58. E. Strake, G. P. Bava, I. Montrosset, "Guided modes of Ti:$LiNbO_3$ channel waveguides: a novel quasi-analytical technique in comparison with the scalar finite-element method," J. of Lightwave Technol., vol. 6, pp. 1126-1135, 1988.

59. Marcus, *Dielectric optical waveguide*,

60. K. Takada, M. Abe, T. Shibata, and K. Okamoto, "A 25-GHz-Spaced 1080-Channel tandem multi/demultiplexer covering the S-, C-, and L-bands using an arrayed-waveguide grating," *IEEE Photonics Technol. Lett.,* vol. 14, no. 5, pp 648-650, May 2002.

61. S. Arahira, S. Sasaki, K. Tachibana, and Y. Ogawa, "All-optical 160-Gb/s clock extraction with a mode-locked laser diode module," *IEEE Photonics Technol. Lett*., vol. 16, No. 6, pp1558-1560, Jun. 2004.

62. B. S. Kim, Y. Chuang, S. Lee, S. H. Kim, K. N. Kang, and S. S. Choi, "THz-class short-pulse generation in mode-locked laser diodes with periodically sampled gratings," *ECOC'98*, pp. 479-180, Sept. 1998.

63. S. Arahira, S. Oshiba, T. Sunii, Y. Matsui, and Y. Ogawa, " Generation of 1.54 THz pulse train by harmonic passive mode-locking in DBR lasers," *14th IEEE international semiconductor laser conferences,* pp. 12-13, Sept. 1994.

64. J-H, Lee, A. S. Daryoush, K. Sato, "Pulse to pulse coherency of actively mode-locked laser diodes," *MWP '99 International Topical Meting on Microwave Photonics,* pp. 69-72, 1999

65. A. S. Daryoush, K. Sato, K. Horikawa, H. Ogawa, " Efficient optoelectronic mixing at Ka-band using a mode-locked laser," *IEEE Microwave and Guided Wave Lett.* Vol. 9, no. 8, pp.317-319, Aug. 1999.

66. T. R. Clark, and M. L. Dennis, " Toward a 100-Gsample/s photonic A-D converter," *IEEE Photonics Technol. Lett.*, vol. 13, no. 3, pp. 236-238, March 2001.

67. T. R. Schibli, T. Kremp, U. Morgner, F. X. Kartner, R. Butendeich, J. Schwartz, H. Schweizer, F. Scholz, J. Hetzler, and M. Wegener, " Mode-locking of Cr^{4+}: YAG micro-chip lasers," *CLEO 2001*, pp. 504-505, 2001.

68. S. Arahira, S. Kutsuzawa, Y. Matsui, and Y. Ogawa, "Higher order chirp compensation of femtosecond mode-locked semiconductor lasers using optical fibers with different group-velocity dispersions," *IEEE J. of Selected Topics in Quantum Electronics*, vol. 2., no. 3, Sept. 1996.

69. K. Sato, A. Hirano, N. Shimizu, I. Kotaka, "High-frequency and low-jitter optical pulse generation using semiconductor mode-locked lasers," IEEE Trans. On Microwave Theory and Techniques, vol. 47, no. 7, pp. 1251-1256, 1999.

70. Y. Ogawa, and S. Arahira, "Generation and stabilization of ultrafast optical pulses by mode-locked laser diodes," *15th Annual Meeting of the IEEE Lasers and Electro-Optics Society, LEOS 2002,* vol. 2, pp. 714-715, Nov. 2002.

71. M Nakazawa, and E. Yoshiba, "A 40-GHz 850-fs regeneratively FM mode-locked polarization-maintaining erbium fiber ring laser," *IEEE Photonics Technol. Lett.*, vol. 12, no. 12, pp1613-1615, Dec. 2000.

72. N. Stelmakh, A. Azouz, J. –M.Lourtioz, "Trains of 250fs pulses at sub-intrinsic-cavity roundtrip intervals from chirped mode-locked laser diodes," *15th IEEE Semiconductor Laser Conference*, pp. 113-114, Oct. 1996.

73. B. Y. Lee, T. Kobayashi, A. Morimoto, T. Sueta, "High-speed electrooptic deflector and its application to picosecond pulse generation," *IEEE J. of Quantum Electronics*, vol. 28, no. 7, pp. 1739-1744, Jul. 1992.

74. Data sheet: http://www.chipsat.com/products/photodiodes/datasheet.php

75. Data sheet: http://www.phlab.ecl.ntt.co.jp/eng/theme/2002/e2002a_12_2.pdf

76. Data sheet: http://www.phlab.ecl.ntt.co.jp/eng/theme/2004/e2004_04_03.pdf

77. J. Kondo, A. Kondo, K. Aoki, S. Takatsuji, O. Mitomi, M. Imaeda, Y. Kozuka, and M. Minakata, "High-speed and low-driving-voltage X-cut $LiNbO_3$ optical modulator with two step backside slot," *Electron. Lett*., vol. 38, no. 10, pp. 472-473, May 2002.

78. J. M. Marx, O. Eknoyan, H. F. Taylor, and R. R. Ncurgankar, "GHz-bandwidth optical intensity modulation in self-poled waveguides in stronitium barium niobate (SBN)," *IEEE Photonics Technol. Lett*., vol. 8, no. 8, pp. 1034-1035, Aug. 1996.

79. O. Kwon, O. Eknoyan, H. F. Taylor, and R. R. Neurgaonkar, "Low-voltage electro-optic modulatior in SBN:60," *Electron. Lett.,* vol. 35, no. 3, pp. 219-220, Feb. 1999.

Appendix A. Design of a 10 bit AOADC based on steerable gratings

A.1 Original design of AOADC based on steerable gratings:

An all-optical ADC (AOADC) was originally proposed for direct digitization using electro-optically steerable gratings. As shown in the general system diagram in Figure A. 1, the received RF signal is applied to a parallel array of electro-optically steerable (tunable) diffraction gratings. This signal modulates the refractive index of the electro-optic material. The electrical signal is linearly converted into a unique diffraction angle according to its amplitude by steering via Pockel effect.

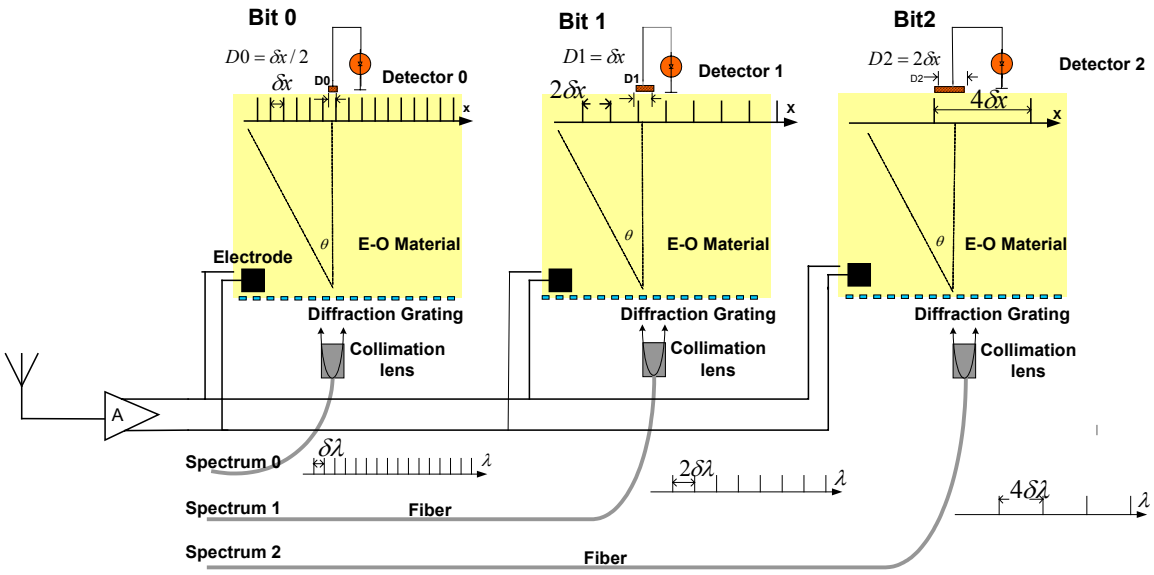

Figure A. 1: System diagram of the proposed all-optical ADC.

Quantization for each bit of resolution is carried out by setting the optical apertures of the detectors to half of the line spacing of the diffracted pattern. As shown in Figure A. 2, if the line spacing of the diffraction pattern of LSB is δx, then the optical aperture of the corresponding detector is chosen as half of the space, $D_0=\delta x/2$. Whenever the optical collector receives optical power more than a preset threshold, it indicates that a line is being collected and the digital output is '1'. When the diffracted pattern of N lines is swept by the applied electric field at RF frequency, the detector will observe alternate digital levels '1' or '0'.

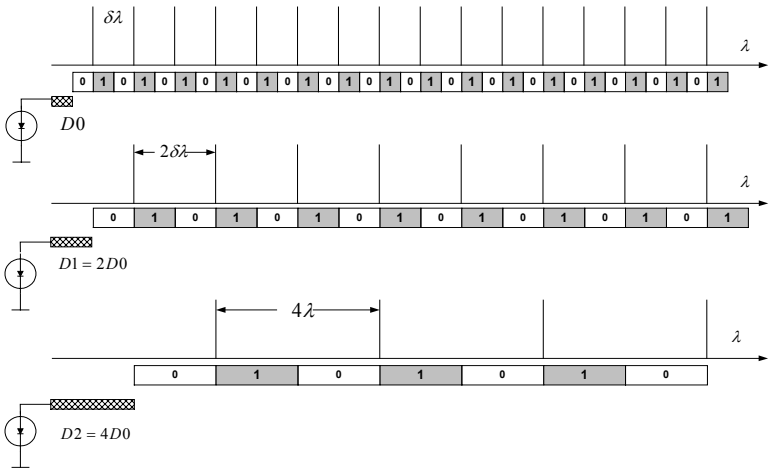

Figure A. 2: Folding spectrum of the first 3 bits.

The geometry shown in represents a simple conceptual implementation of the AOADC. The electric field required to achieve high resolution for this structure can be quite high since the full-scale voltage is proportional to $\delta\lambda \times 2^{n-1}$ (line spacing × number of lines). For example, to shift 512 lines (for 10 bits of resolution for binary code) with spacing of 50 GHz, i.e. 400 nm tunable range, the required electrical field is about 1500 V/um using

$LiNbO_3$ gratings, which is far beyond the material breakdown electric field. However, by using a high electro-optic coefficient polymer material, it may be reduced by 1 order of magnitude.

A.2 Generation of denser spectral lines:

To reduce the required electric field, a denser spectrum can be generated. For example, a Mach-Zehnder modulator may be used to generate multi-order sideband spectral lines around the MLL spectrum, as shown in Figure A. 3. By AM modulating the signal with a 3.125 GHz RF signal, 16 evenly spaced lines are generated between two spectral lines, so the required electric field is reduced by a factor of 16. The disadvantage of this scheme is that the sideband spectral lines deffer in intensity, so the dynamic range of the detectors has to be large.

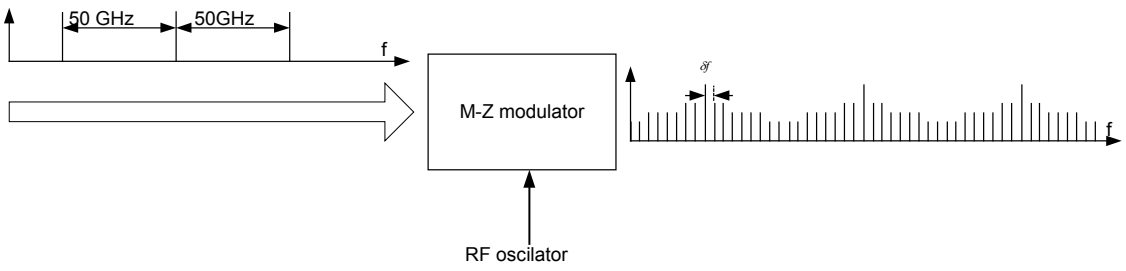

Figure A. 3: Generating side band spectral lines using a Mach-Zehnder modulator.

An alternative solution is the use of combined collectors. Instead of using dense spectral lines, this method uses combined collectors closely located to each other. The system diagram is shown in Figure A. 4.

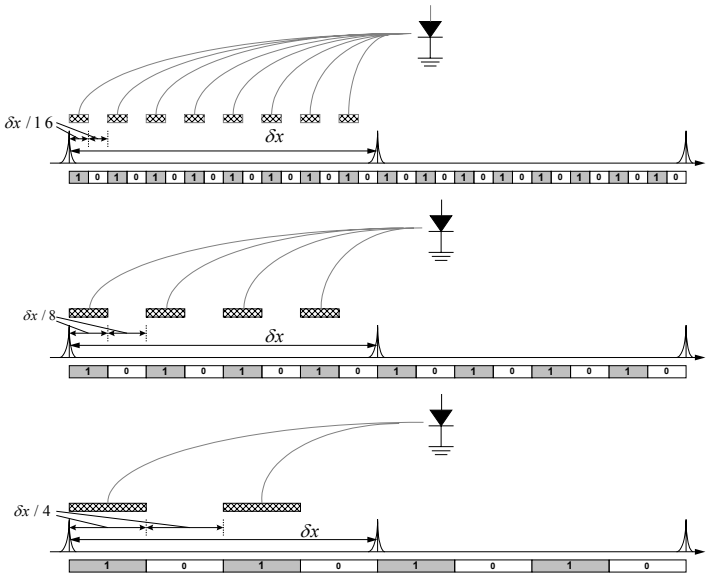

Figure A. 4: ADC implementation using combining collectors.

Several collectors (optical windows) are placed so that the spacing between the collectors is equal to the optical aperture size. Whenever any collector picks up a spectral line, the detector indicates a digital "1." For example, as the spectrum is shifted across the space by a ramp voltage, the detector will read binary code "10101010…" Using 2^m collectors, it is equivalent to having a dense spectrum with spacing of $\delta\lambda/2^m$. Therefore the tuning range and the required electric field are reduced by a factor of 2^m.

By employing a combination of the two implementations described above the total tunable range can be reduced dramatically. However, we may still need a number of lasers with different spectrum combined to cover the whole tunable range. The number of laser sources can be reduced by using multiple collectors separated by δX, which covers the total diffracted pattern of the existing laser. This is shown in Figure A. 5. The collected signals are combined and sent to a single detector. Whenever any detector

senses a line, it will indicate a "1." Using L collectors and one source with N spectral lines is equivalent to using $L \times N$ spectral lines. As the diffraction gratings shift the spectrum, at any given time, there is at most one collector that receives light. This scheme will reduce the number of lasers by a factor of L. It is interesting to note that in this method the spatial domain can be used to achieve a desired effective spectrum without affecting the design of the MLL.

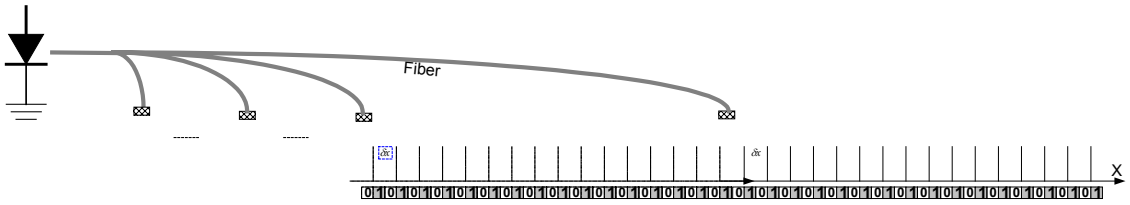

Figure A. 5: multiple collectors to reduce the number of required lasers.

A.3 Generation of Gray code:

The resolution of the ADC may be increased by a factor of 2 for a given spectral density and aperture geometry through the use of a Gray code, since N spectral lines cover $4N$ quantization segments, instead of $2N$ segments in binary code. The Gray code for 5 bits and corresponding optical spectrum are shown in Figure A. 6. Note that the spectral lines shown in Figure A.6 may be generated by placing and combining optical collectors in the same manner described above; the Gray code representation is obtained without any additional processing or alteration to the spectrum.

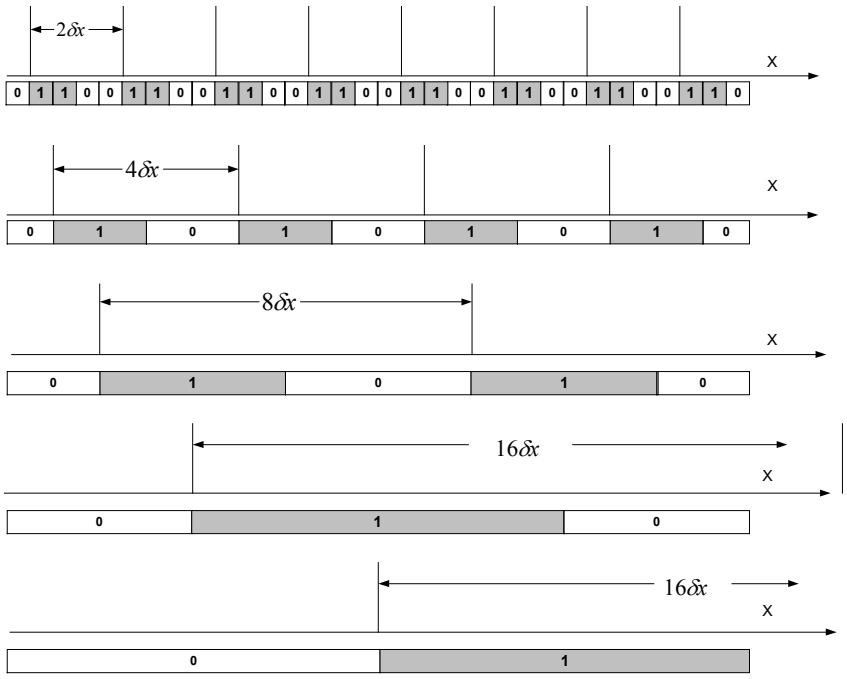

Figure A. 6: 5-bit Gray code and the corresponding spectrum.

A.4 Novel Optical Source Design:

It is desirable to use just a single mode-locked laser instead of multiple CW lasers to generate the multiple-wavelength spectrum. In a mode-locked laser the line spacing is equal to the pulse rate. However, the line spacing for the more significant bits may be much larger 50 GHz even though a dense spectrum or combined detectors is employed. For example, if the effective line spacing is 3.125 GHz, the most significant bit for a 10-bit resolution requires a line spacing of 1.6 THz, which is impossible to generate by directly using a mode-locked laser. The spectrum for the most significant bit can be obtained by removing lines using Fabry-Perot cavity filters. But simply removing spectral lines may result in undesired pulses in the time domain. For instance, a line spacing of 100 GHz corresponds to pulses spaced 10 ps apart in the time domain. Consequently the time interval for higher bits is much smaller. This will result in interference coming from

undesired pulses. Also the power is reduced due to removing a large number of spectral lines. A possible solution is to remove a cluster of lines from the original spectrum (cf. Figure A. 7 (b)) rather than removing every other line (cf. Figure A. 7 (a)). The resulting spectrum and collector arrangement is shown in Figure A. 7.

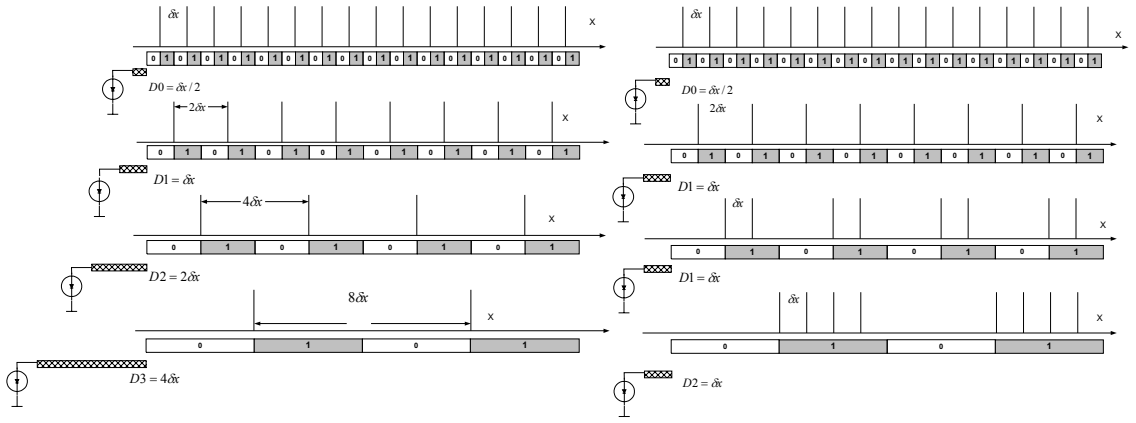

(a) (b)

Figure A. 7: Diffracted pattern and detector arrangement of original design (a) and modified design (b).

Line clusters of 1, 2, and 4 … are removed by proper filters for higher bits respectively. In addition, all the collector apertures (except for the LSB) are the same, which are double that of the LSB. The effective behavior of the AOADC is the same as that of the original concept shown in Figure A. 8. Due to the removal of some spectrum lines undesired pulses will still appear in the time domain (cf. Figure A. 8). However these sideband pulses are smaller than those obtained by simply removing any other line. Therefore less overlap or crosstalk is introduced in the cluster spectrum. The detector only “reads” every 20 ps while ignoring any other pulses. An additional benefit is that the sizes of the collector apertures are identical for all higher bits.

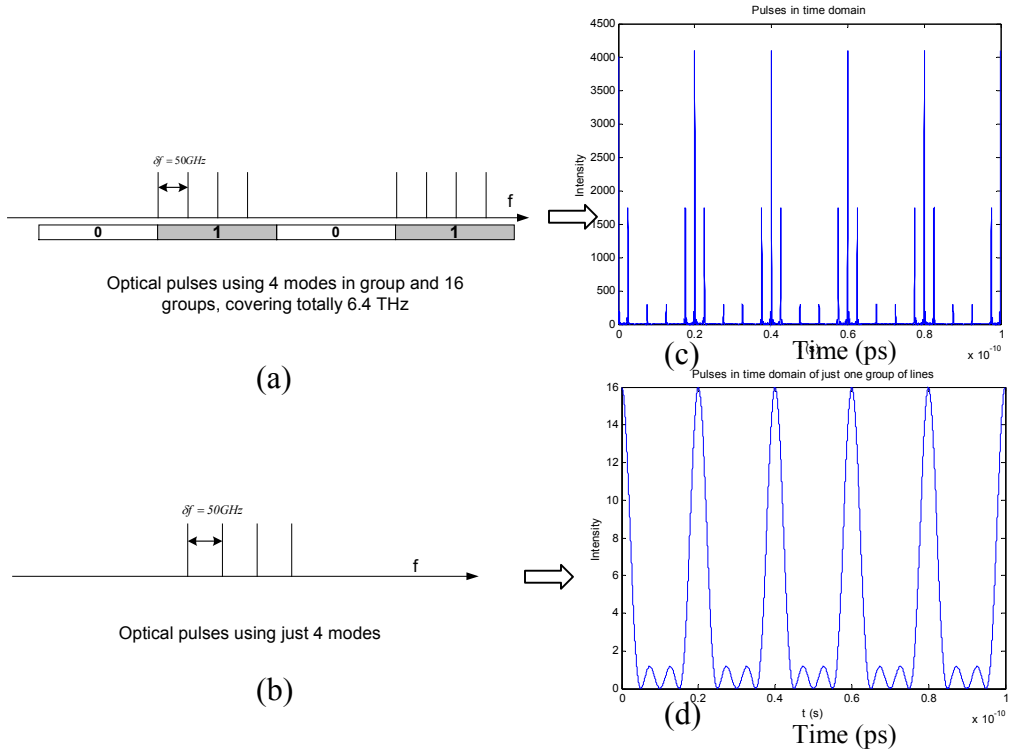

Figure A. 8: Time domain pulses corresponding to cluster of spectrum lines.

Combining all spectra and collector arrangements, a comprehensive arrangement of a 10-bit AOADC is shown in Figure A.9.

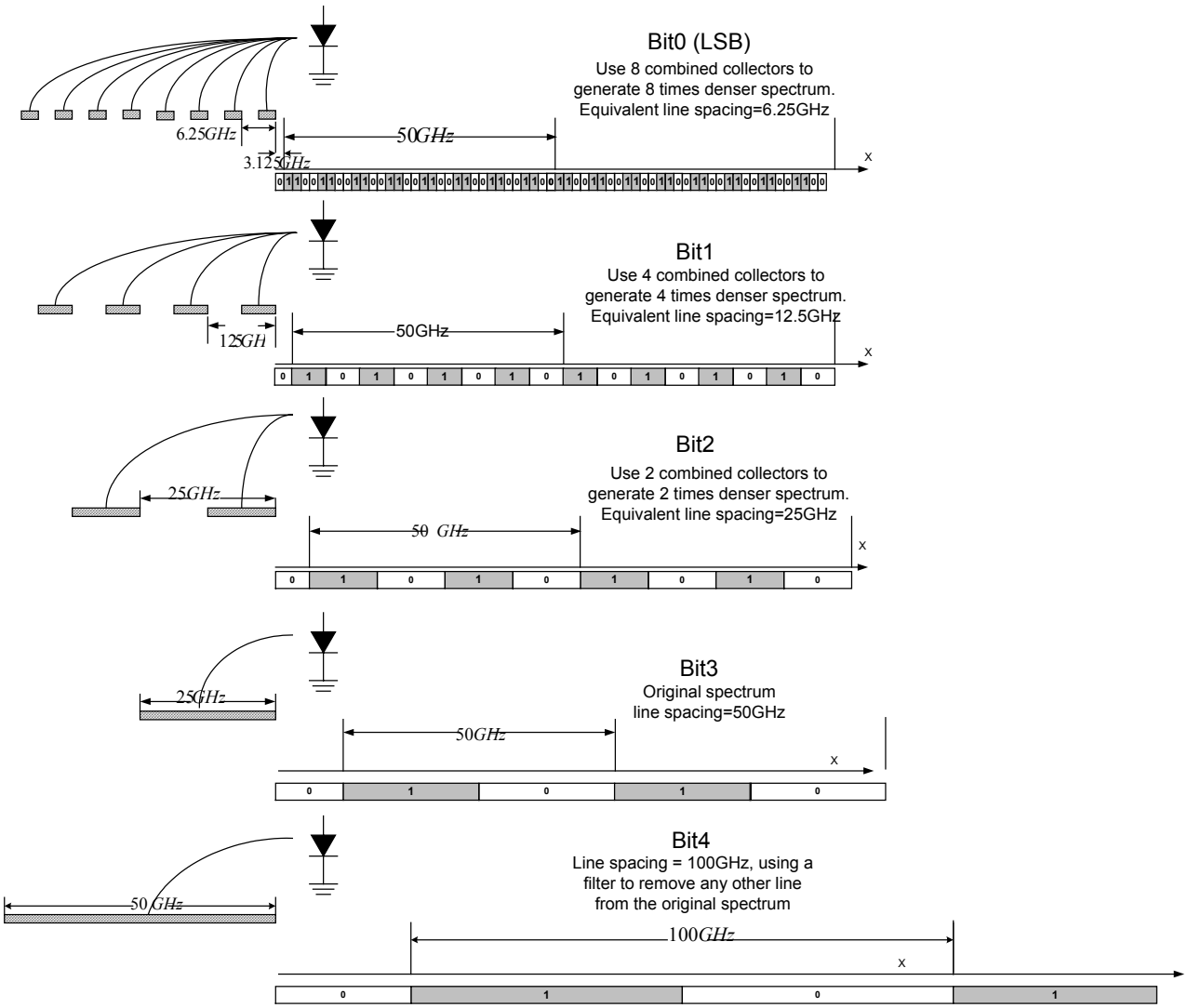

(a) Spectra and optical collector arrangement of bit0-bit4. (Line spacing is 50GHz in the original spectrum of a mode-locked laser source.)

Figure A. 9: arrangement for a 10-bit AOADC.

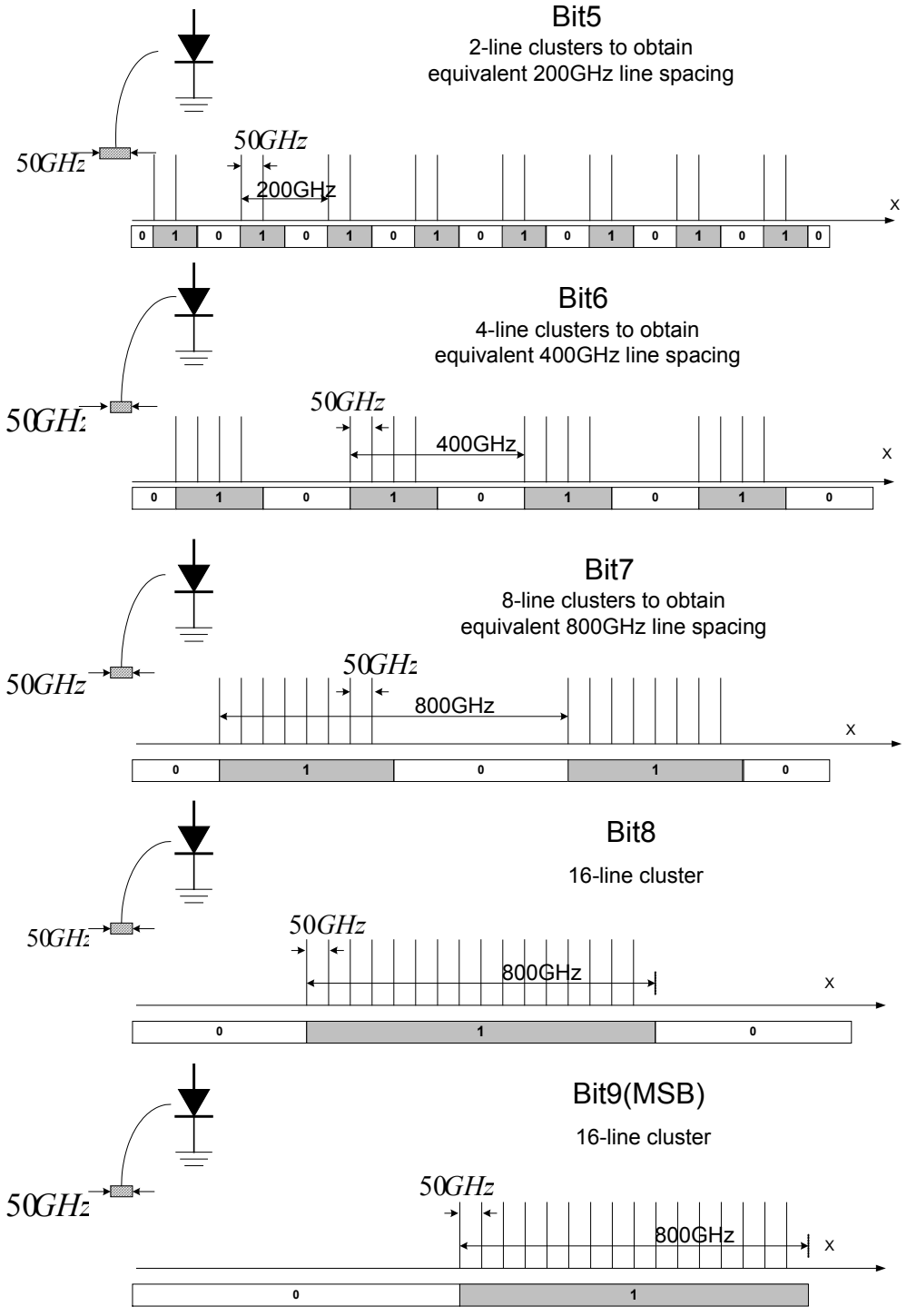

(b) Spectra and optical collector arrangement of bit5-bit9. (Line spacing is also 50GHz in the original spectrum, but shown in a larger scale for showing many lines.)

Figure A. 9: arrangement for a 10-bit AOADC. (Continued)

In this example, only 32 spectral lines are required, instead of 512 lines as in the design for a binary code without using combined collectors. A factor of 2 comes from the Gray code, which saves half the number of lines. Another factor of 8 comes from the combined collector scheme, since the line spacing of the LSB is 8 times less than the spectrum from the 50GHz MLL. As for the steerable gratings, we proposed to use GRISMs, as demonstrated in the Chapter 3.

A.5 Challenge: ultra fast pulses at detectors:

A diffraction grating splits spectral components into different directions. This means that only a single spectral component is available at certain angle at any given time. Hence, irrespective of whether the optical sources are CW lasers or mode-locked lasers, every diffracted beam is always single frequency, i.e. it is continuous wave. As shown in Figure A. 10 the steerable grating scans the multiple beams across the space continuously.

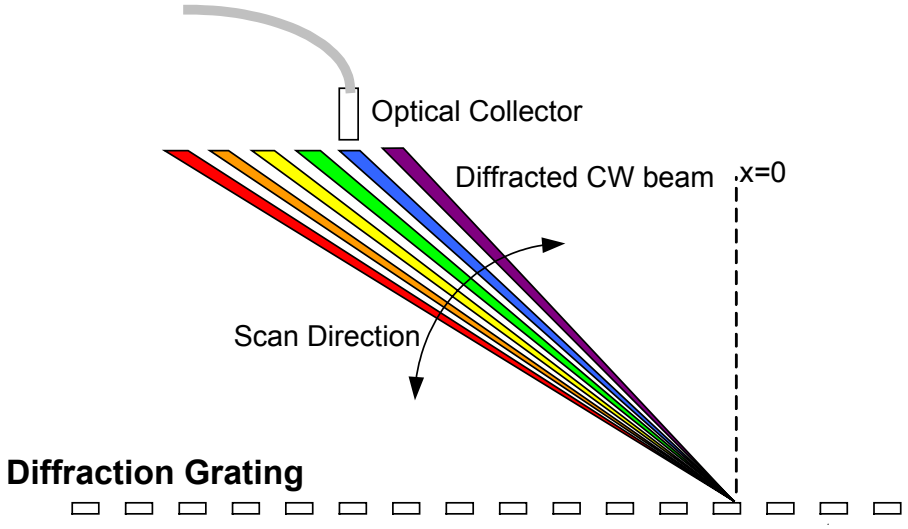

Figure A. 10: The diffracted beams are CW light and they are scanned continuously by the input electrical signal.

The continuous-wave beams generate ultra-fast pulses that cannot be correctly detected by the optical collector. For example, when a 25 GHz ramp signal is applied to the steerable grating, the diffracted beams are shifted from their minimum angle to the maximum angle in 40 ps. For a 10-bit Gray code AOADC, there are 256 effective spectral lines. The 256 lines will sweep across the collector aperture successively in the 40 ps period, therefore the received pulse rate is *40ps/256=156fs*. This extraordinary pulse rate is beyond the capabilities of available photodetectors. As a result, a bandwidth-limited photodetector acts as an integrator and the output varies indistinctly around its received average power level. Therefore other approaches must be introduced to avoid this problem. Two approaches were proposed to solve this problem.

a) Gated continuous wave (sampling first and then quantizing) is depicted in Figure A. 11. This approach uses *N* independent continuous-wave (CW) lasers to

generate a multi-wavelength spectrum. The combined WDM optical beam is then sent to a switch, which is controlled by an optically pulsed signal from a mode-locked laser. Thus the switch turns the beam on and off at the pulse rate. Every wavelength component is now like a pulse and can sample the RF signal at the rate of the MLL pulses. The purpose of this approach is to break the coherent phase relation between different wavelengths. In this approach, independent CW lasers generate the desired spectra, while the switch works as a shutter to generate the sampling pulses. In this way, the electrical voltage is converted into the corresponding diffracted angle only at the sampling instance. The collectors can then sense and quantize the position of the optical pulses as described in the original design.

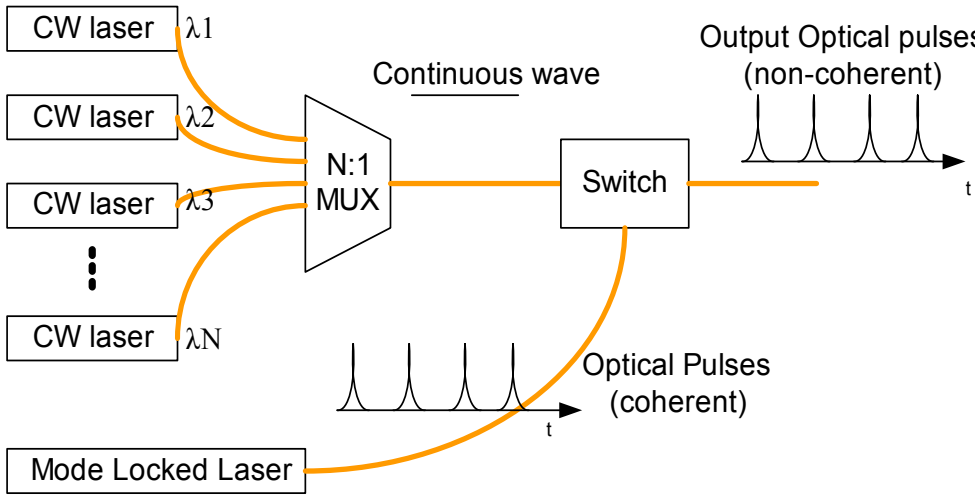

Figure A. 11: Generate non-coherent pulses by gating CW light.

Advantages:

- The pulses collected by optical collectors are already digitized, so it does not require complicated synchronization schemes.

Disadvantages:

- It requires multiple CW lasers.
- It is difficult to find an optical switch design that is fast in speed and low in time jitter. The switch may be turned on and off by optical pulses, but no existing optically controlled switches meet the required speed and time jitter.
- The gated pulses must be very short (on the order of *fs*); otherwise the detectors will receive more than one pulse within a pulse duration, which generates errors. Significant optical power is also lost in the gating operation. For example, if the pulse duration is 40 fs and pulse rate is 20 ps, only 0.2% of the total power will go through the optical switch.

b) Vernier Arrangement (quantizing first and then sampling) is depicted in Figure A. 12, where an example of the LSB vernier is shown. In this scheme multiple detectors are used for a single bit, and the collectors are placed in different distances from the spectral lines, which are 2D, 4D, 6D and 8D respectively. As shown in the figure, the spectral line spacing is 8D, while the collector spacing is 10D. Every collector is connected to a separate photodetector. Thus each detector deals with only one spectral line. When the diffracted pattern is shifted to different positions, the light will be picked up by different collectors, so every

detector observes an N times slower pulse rate, where N is the number of detectors. The purpose of the vernier arrangement is to split the ultra fast pulses into multiple detectors, so that each individual detector receives pulses at a slower rate. Since the diffracted beams are continuous waves, the voltage is converted into its diffraction angle continuously without sampling. For example in order to obtain the resultant digital code at 50 GS/s, the outputs of detectors must be sampled every 20 ps to read either a "1" or "0." High-speed photoconductive devices can be used as the sampling components.

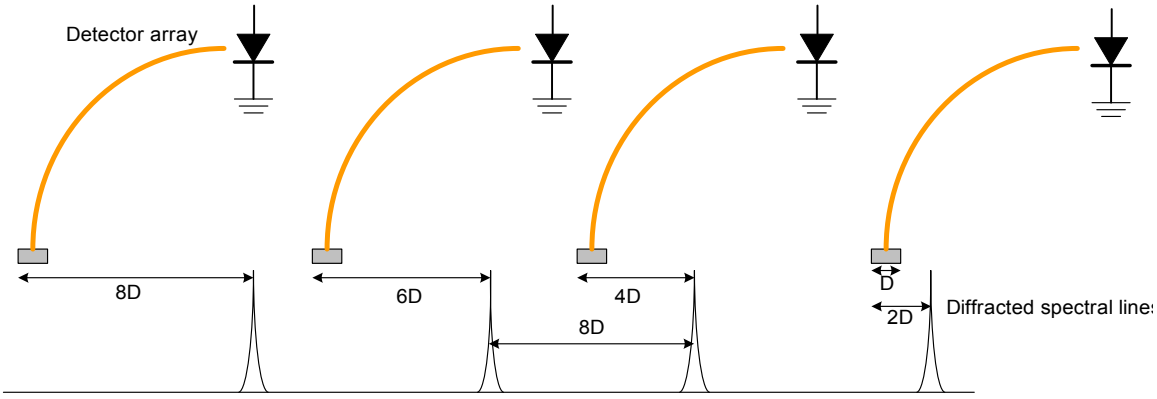

Figure A. 12: Vernier arrangement.

Advantages:

- It just uses one mode-locked laser to generate all spectral lines, which are more accurate in line spacing and narrower in pulse width.
- The quantization requires a single-bit quantizer (a simple comparator), even though it is supposed to work at 50 GHz.

Disadvantages:

- It requires a number of high-speed photodetectors. To significantly lower the pulse rate at every detector in a 10-bit 50 GS/s AOADC system, more than 50 detectors may be needed to make the received pulse rate less than 100 GHz.
- It requires a circuitry for every bit to convert the multiple outputs of the detectors into a single digital bit.
- The outputs of the detectors should be sampled at the same time; therefore it requires stringent timing matching between deferent detectors.

A.6 Summary:

The first design of the AOADC was based on steerable gratings. It combines operation in the spectral and spatial domains. It shows the advantages of immunity from optical intensity fluctuation and flexibility of the spectrum arrangement. However, this approach is more conceptual as it faces several feasibility issues.

Appendix B. Bibliography of Patents on Photonic Analog-to-Digital Converter

http://www.uspto.gov/patft/index.html

Patent No	Date	Inventers	Method
6801147	10/5/2004	Thylén at al.	OPTICAL SYSTEM AND METHOD FOR PERFORMING ANALOG TO DIGITAL CONVERSION Amplitude of the electric signal is modulated into wavelength of optical signals. The beam is diffracted by a grating to different angle, where different binary pattern is placed.
6714149	3/30/2004	W.C. Nunnally	ELECTRO-OPTICAL ANALOG TO DIGITAL CONVERSION METHOD AND DEVICE Amplitude is converted into angular displacement. It uses collector array to quantize.
6700517	3/2/2004	K. K. Kellar	PHOTONIC ANALOG-TODIGITAL CONVERTER It is an optical flash ADC. Modulated optical power is split into 2^N path and yield different attenuation. It is encoded by interferometers.
6661362	12/9/2004	M. F. Lewis et al.	HIGH SPEED OPTICAL ANALOG TO DIGITAL CONVERTER AND DIGITAL OPTICAL WAVEMETER
6525682	2/25/2003	Yap et al.	PHOTONIC PARALLEL ANALOG-TO-DIGITAL CONVERTER It is a hybrid optical ADC using parallel channels of sampling and quantization. The electronic ADC it uses is Δ-Σ ADC
6420985	7/16/2002	Toughlian et al.	PHOTONIC WIDE-BAND ANALOG TO DIGITAL CONVERTER AND METHOD An analog electrical signal is first converted to an optical signal having a wavelength that is a function of the amplitude of the analog electrical signal, which is then filtered in a plurality of optical filter.

6404366	6/11/2002	Clark, et al.	PHOTONIC ANALOG-TO-DIGITAL CONVERTER UTILIZING WAVELENGTH DIVISION MULTIPLEXING AND DISTRIBUTED OPTICAL PHASE MODULATION It is a hybrid optical ADC
6404365	6/11/2002	Heflinger	FULLY OPTICAL ANALOG TO DIGITAL CONVERTERS WITH COMPLEMENTARY OUTPUTS The amplitude of the electrical signal is converted into wavelength of optical signals. A plurality of interferometers with unequal arms is used deliver a complementary sinusoidal signals, which are the digital outputs.
6326910	12/4/2001	M.J.Hayduk	PHOTONIC ANALOG-TO-DIGITAL CONVERSION USING LIGHT ABSORPTION Signal is sampled by a coherent light source, then distributed in parallel to N (bit) absorbers, which has variable light-absorption coefficient with each significant bit.
6292119	9/18/2001	J.C.Carillo	DELAYED PULSE SATURABLE ABSORBER-BASED DOWNWARD-FOLDING OPTICAL A/D Downward-folding successive approximation conversion scheme that employs subtraction of optical channel. Signal is sampled with time interleaving then quantized using thresholding device.
6288659	9/11/2001	B. Jalali	DATA CONVERSION USING TIME MANIPULATION Signal is sample with dispersed light source, then demuxed to 4 channels in time domain. Channelized signals then are time-stretched and quantized using electrical A/D converter.
6265999	6/24/2001	P.R. Prucnal	HIGH-SPEED SERIAL-TO-PARALLEL AND ANALOG-TO-DIGITAL CONVERSION Input OPTICAL signal is sampled by a mode-locked laser, then splitted based on time interleaving. Parallel signals are converted by electrical ADC
6219172	4/17/2001	A. Yariv	SAMPLING AND PROCESSING SIGNALS BY USING OPTICAL PULSES Signal is sampled by optical pulsed then demux to multiple channels, then quantized using electrical ADC

6188342	2/13/2001	J.T.Gallo	PHOTONIC A/D CONVERTER USING PARALLEL SYNCHRONOUS QUANTIZATION OF OPTICAL SIGNALS Input OPTICAL signal is sampled and quantized by photodetectors with different sensitivities.
6175320	1/16/2001	D.G.Heflinger	ALL OPTICAL ANALOG-TO-DIGITAL CONVERTER EMPLOYING AN IMPROVED STABILIZED IOTICAL INTEREFEROMETER Based on M-Z interferometer
6121907	9/19/2001	R.A.Fields	UPWARD-FOLDING SUCCESSIVE-APPROXIMATION OPTICAL ANALOG-TO-GITAL CONVERTER AND METHOD FOR PERFORMING CONVERSION It is composed of a plurality of optical stages with different comparator thresholds.
6118397	9/12/2000	D.G.Heflinger	FULLY OPTICAL ANALOG TO DIGITAL CONVERTERS WITH COMPLEMENTARY OUTPUTS Based on M-Z interferometer
6118396	9/12/2000	W.S. Song	OPTICALLY SAMPLING DEMULTIPLEXING, AND A/D CONVERTING SYSTEM WITH IMPROVED SPEED Based on M-Z interferometer
6100831	8/8/2000	M.Y. Frankel	OPTOELECTRONIC ANALOG-TO-DIGITAL CONVERTER USING WAVEWLENGTH MULTIPLEXING Signal is sampled by a optical source with separated spectrum then sent to wavelength division demultiplexer. Channelized signals are quantized using electrical ADC
6064325	5/16/2000	R.A. Fields	FREQUENCY MODELATION-BASED FOLDING OPTICAL ANALOG-TO-DIGITAL CONVERTER It is composed of multiple stages based on downward-folding successive approximation approach. Signal is ampled by optical FM modulator and bandpass filter with different bandwidth.
5995875	9/21/1999	J.C.Twichel	LINEARIZED OPTICAL SAMPLER Based on differential M-Z interferometer

5381147	1/10/1995	W. Birkmayer	PROCESS FOR THE ANALOG-TO-DIGITAL CONVERSION OF MICROWAVE SIGNALS Based on M-Z interferometer
5264849	11/23/1993	H.Kondoh	OPTICAL A/D CONVERSION USING ASYMMETRICAL-NEURAL-NETWORKS Based on optical computing
5010346	4/23/1991	M.C.Hamilton	ELECTRO-OPTICAL ANALOG-TO-DIGITAL CONVERTER AND METHOD FOR DIGITIZING AN ANALOG SIGNAL Optical pulses are sent to a 1:5 splitter followed by M-Z modulator.
4058722	11/15/1977	H. F. Taylor	ELECTRO-OPTIIC ANALOG/DIGITAL CONVERERTER

Appendix C. Challenges of AOADC using prism-based E-O deflector

C.1 The experimental setup to prove the concept of building an AOADC using a prism-based E-O deflector

In the experimental setup shown in Figure C.1, a conventional prism-based E-O deflector was designed to steer the input optical beam into an angle according to the input electric field. However driving the prisms at frequencies on the order of GHz is difficult. This study actually shows the general challenges that conventional prism-based E-O deflectors encounter. The goal of the design was to show a 3 or 4 bit conversion at 20 GS/s, corresponding to a RF bandwidth of 10 GHz.

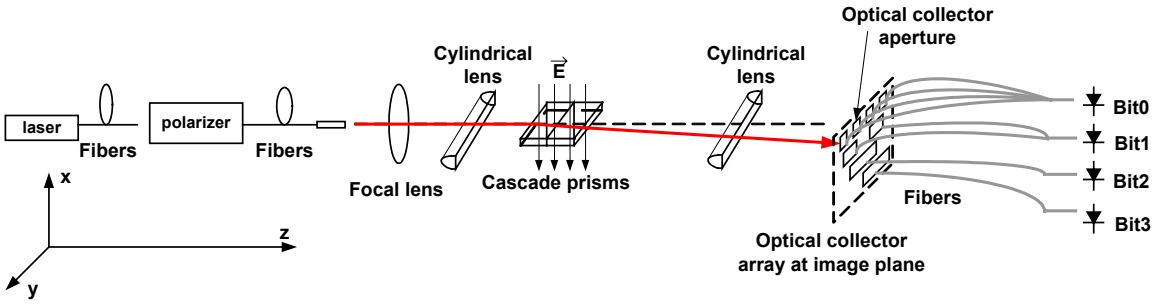

Figure C. 1: The system diagram of the proposed experimental setup.

In this setup, optical sampling pulses generated from a mode-locked laser are first polarized in a direction parallel to the applied electric field on the prisms. The polarized and collimated beam is then focused in only one dimension by using a cylindrical lens so

that the beam is focused at the center of the prisms. This technique is called pre-focusing. In Figure C.1, the optical beam is steered in the *y*-direction and then focused on the image plane where an optical collector array is placed.

As shown in Figure C.2, the cascade prisms are arranged such that adjacent prisms have opposing crystal directions. As a result, when an electric field is applied, the index changes alternately thus achieving a larger angular deflection. The total number of resolvable spots of the E-O deflector is $N = \frac{\Delta\theta_{\max}}{\delta\theta}$, where $\Delta\theta_{max}$ is the maximum angle, and $\delta\theta$ is the angular spot size determined by the Rayleigh refraction limitation.

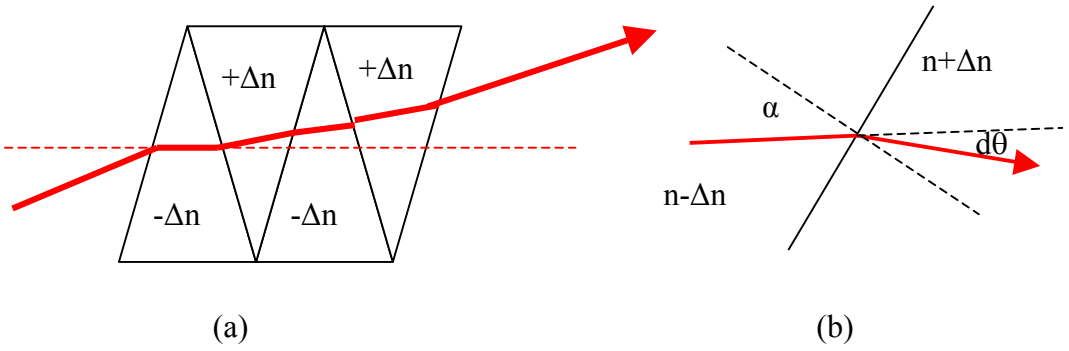

Figure C. 2: The cascade prisms (a) and the beam refraction at the interface of adjacent prisms (b).

Integrated cascade prisms have been demonstrated on $LiTaO_3$ wafers, but they are only available in a few research laboratories. Therefore we acquired 4 pieces of discrete $LiNbO_3$ prisms and put them side-by-side. The dimensions of the prisms are drawn in Figure C.3.

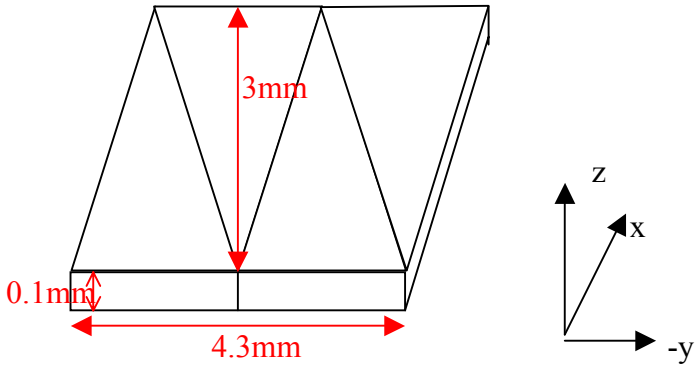

Figure C. 3: Dimensions of the prisms.

At every interface as shown in Figure C.2 (b), the deflection angle satisfies $(n+\Delta n)\sin(\alpha - d\theta)=(n-\Delta n)\sin\alpha$. When 10 V/um of electric field is applied to the prisms, $\Delta n = \frac{1}{2}n^3 r\Delta E = 0.0016$, resulting in $\frac{\Delta n}{n} = 7.26\times10^{-4}$. The calculated $\theta max = 3.56\times10^{-3}$. The image linewidth is determined by the aperture size in the x direction by Fraunhofer diffraction. Since the dimension in the x direction is 2 mm, the angular size of an image line at wavelength of 1.5 μm is $\delta\theta \approx \frac{1.2\lambda}{W} = \frac{1.2\times1.5\times10^{-6}}{2\times10^{-3}} = 9\times10^{-4}$, where W is the optical aperture size in x. Although it only provides $N=4$ resolvable image lines, corresponding to 4 bits in Gray code, it is good to demonstrate the concept. By using shorter wavelength, the spot size can be further reduced.

The electrodes should be deposited on the top and bottom sides of the prisms. Since the dielectric breakdown of the air is only 3 V/um, which is much smaller than the applied electric field in the $LiNbO_3$ crystal (10V/um), there are margins of 0.5mm for both electrodes, as shown in Figure C.4. However the major challenge is to drive this deflector

at high frequencies with sufficiently high voltage. Many driving schemes have been investigated, and their problems are summarized in following sections.

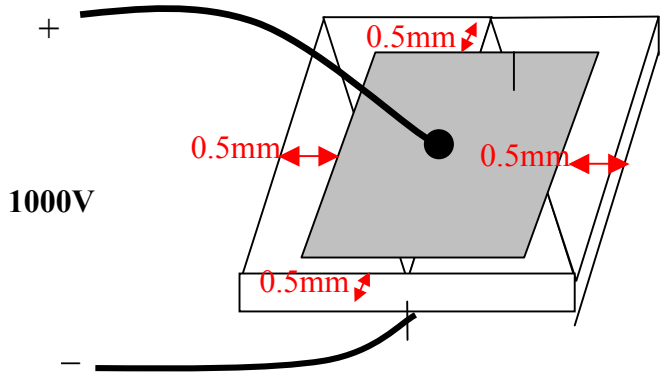

Figure C. 4: electrodes on the cascade prism.

C.2 High Voltage driving schemes

The cascade prism structure requires a driving voltage of about 1KV to obtain 4 bits of resolution. In order to meet the requirements of a high driving voltage and the broad bandwidth (of the order of 10 GHz) the driving scheme is critical. This section describes different approaches that have been investigated. It has been shown that the challenges faced by the experimental setup are also the common challenges faced while using a prism-based E-O deflector in a high-speed optical AOADC system.

1) Driving without load - Lumped element model

If the electrodes are not loaded, they behave like a lumped capacitor. In principle no power is consumed in the deflector and its modulation bandwidth is determined by the capacitance of the electrodes.

When the electrode metal covers the area of the top and bottom of the crystals as shown in Figure C.4, the capacitance is calculated as:

$C = \frac{\varepsilon A}{d}$, ε_r=29, A=3.3 × 2 mm^2, d=0.1mm ➔ C=17 pF.

This large capacitance corresponds to an RC time of *0.85 ns* for a source resistor of 50 Ω. Also the lumped element model is valid only when the dimension << wavelength. At 10 GHz the wavelength in the $LiNbO_3$ is only 5.57 mm (calculated using both parallel plate waveguide model and micro stripline model in ADS LineCalc tool). This is comparable with the dimensions of the cascade prisms. Hence the electrodes actually behave as a transmission line with open circuit as investigated in the transmission line model discussed below.

2) Transmission line model

At high frequencies the structure shown in Figure C.1 is modeled as a piece of parallel plate waveguide transmission line. The EM field travels along the -*y* direction (*w=3.3mm, d=0.1mm, l* = 3.3 mm = 0.59λ@10 GHz) as shown in Figure C.1, and its characteristic impedance is

$Z_0 = \sqrt{\frac{\mu}{\varepsilon}}\frac{d}{w} = \frac{1}{\sqrt{29}}\sqrt{\frac{\mu_0}{\varepsilon_0}}\frac{0.1mm}{3.3mm} = 2.2\Omega$ for the lowest mode.

The calculated characteristic impedance is very small compared to the impedance of the standard RF source, which is 50 Ω or 75 Ω. The severe impedance mismatch causes problems in power delivery and dissipation. For example, if we could design a system of

2.2 Ω, the 1KV driving voltage would result in 226K watts! Even if it could be matched and loaded with 50 Ω, the structure would consume 10K watts, which is not feasible in currently available laboratory conditions, so we tried to use the open circuit approach. A few possible solutions have been explored.

- Approach 1: Using high voltage RF source directly.

Theoretically, 1KV of voltage can be delivered to the 2.2 Ω transmission line as long as a proper matching circuit is applied. Leaving the electrodes open-circuit, as shown in Figure C.5, we can connect the electrodes to a 50 Ω transmission line by using a taper.

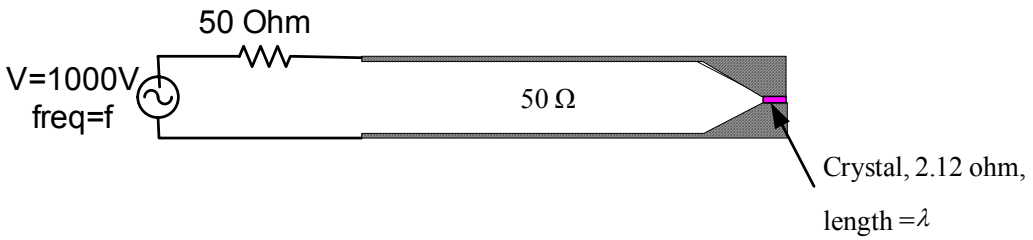

Figure C. 5: Applied high voltage to the prisms using a 50 Ω transmission line and a taper.

Since the load is an open circuit, the incident wave will be reflected at the open end and will form a standing wave in the crystals. The electrode length and the wavelength of the RF wave are selected so that the length of the electrode equals one wavelength. As a result the standing wave with peak amplitude of 1000 V is built at the center of the crystal, as shown in Figure C.6. If the light goes through the peak region, it is reflected by the maximum electric field. Although it is theoretically possible, it is not feasible to use a 1 KV RF source at 10 GHz and apply it to such a small structure in the laboratory.

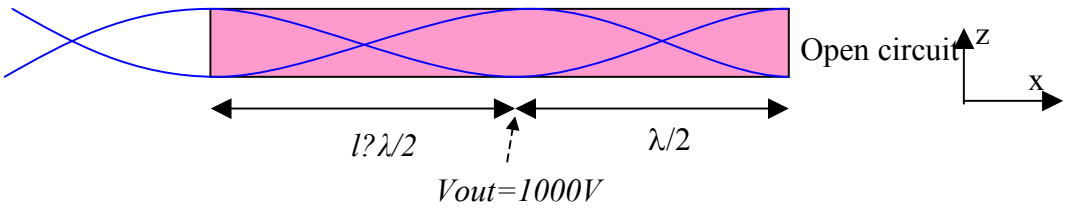

Figure C. 6: Standing wave in the crystal to achieve 1000 V in the center.

- Approach 2: Using a medium voltage source and a transformer

The structure using a double slug tuner is shown in Figure C.7. The dual dielectric slug transformer is used to boost the voltage from 100 V at the source to 1000 V in the crystal. In order to achieve a transformer ratio of R=10, the dielectric coefficient is chosen as $\varepsilon_r=10$. Therefore the characteristic impedance of the dielectric part of the transmission line is 50 Ω/$\sqrt{10}$ =15.6 Ω. The transmission line length in the crystal region is equal to wavelength λ, so that a peak of the standing wave appears at the center of the crystal, similar to approach 1.

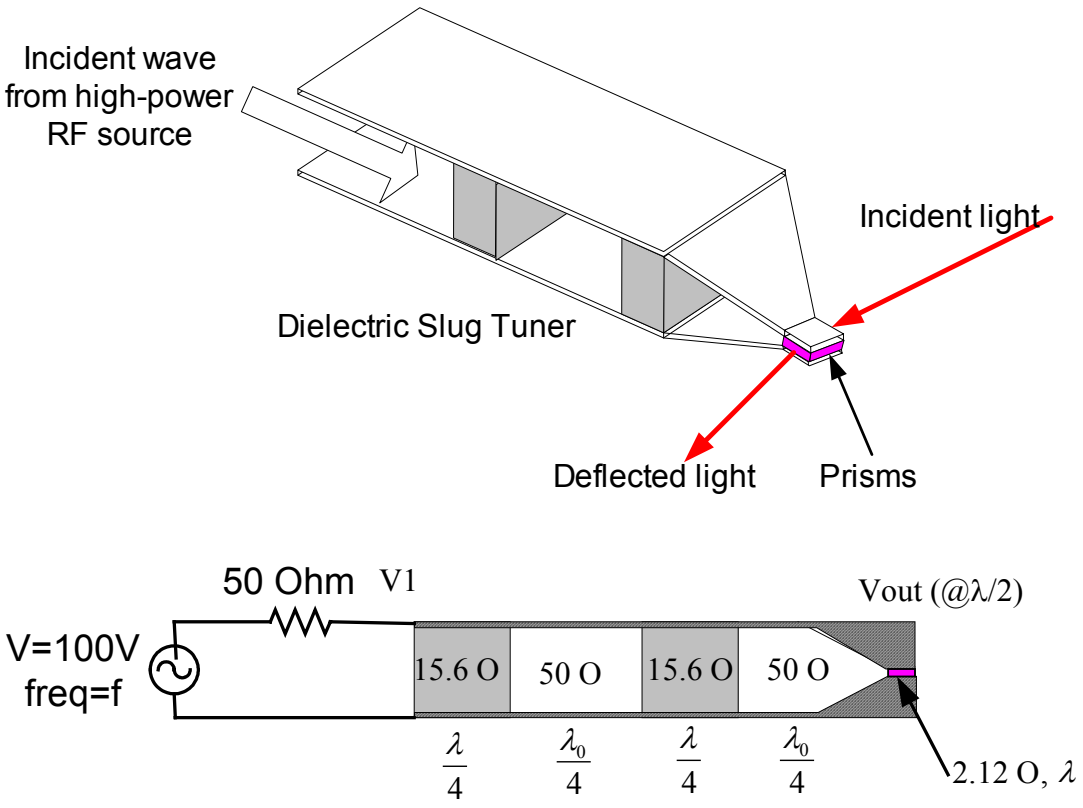

Figure C. 7: The structure using transformer to boost the source voltage to 1 KV.

Theoretical it is possible to boost the voltage 10 times as shown in the ADS simulation result in Figure C.8. However this structure is extremely sensitive, due to multiple sections made up of quarter wavelengths or one wavelength. If any of the sections wavies away from its accurate value, the output voltage drops rapidly. The sensitivity can be represented by the input impedance at point V1 in Figure C.9. The impedance mismatch will determine the power delivered. Figure C.9 shows an ADS simulation of the input impedance at 10 GHz. It is almost open at 10 GHz; however the bandwidth is extremely narrow, which is on the order of KHz.

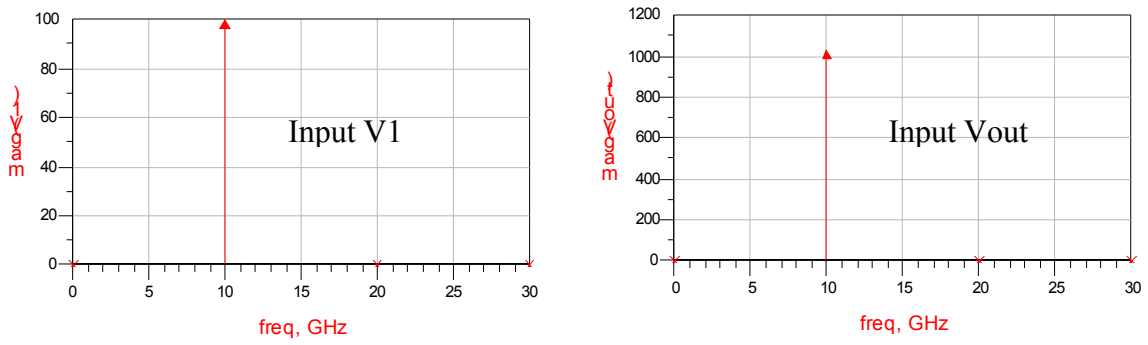

Figure C. 8: The simulated voltage at output of voltage source and the center of the deflector.

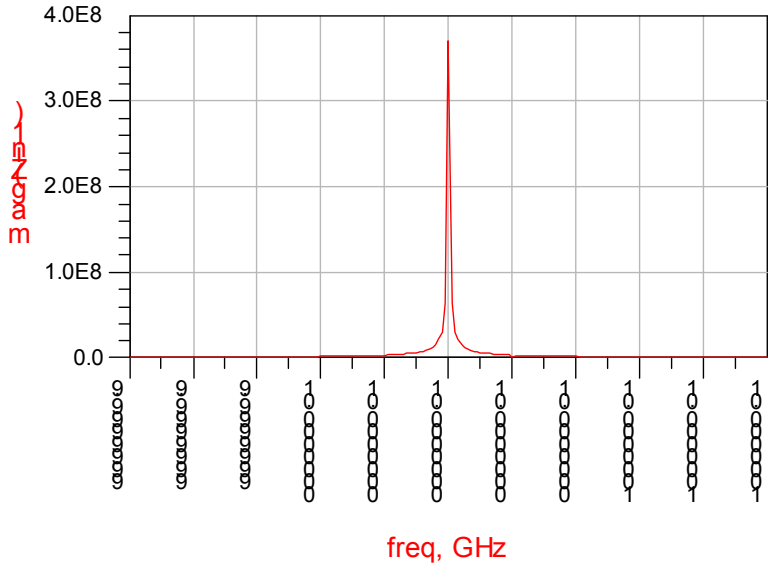

Figure C. 9: Input impedance at the input of the dual-slug transformer.

Apart from the challenges described above, both approaches 1 and 2 also face some similar problems:

a) The amplitude at the center of the crystal is not the signal to be digitized as this amplitude at time *t* is a superposition of the signal at time *t* and the reflected signal at time *t*-*T*, where *T* is the round trip time of traveling λ/2.

b) The unevenly distributed field across the optical aperture at *xz* plane induces wave front distortion. Since waves at different positions yield different deflection, the actual optical aperture is no longer 2 mm anymore but the small region around the peak where the electric field is approximately even. According to Fraunhofer diffraction limitation, $\delta\theta \approx \frac{1.2\lambda}{W}$, the angular image line width is much wider than the previous calculation and this makes the resolution very low.

- Approach 3: Loading the transmission line with a large resistor (power absorber)

If 1KV could be delivered to a load of 50KΩ, the structure absorbs only 100W of power. This design can be translated into a matching problem of 50KΩ to a 50Ω system as shown in Figure C.10. With such a high ratio of 1000 (50KΩ/50Ω), the matching circuit would be more sensitive and difficult to construct. At the same time, this approach also faces transit time limitation. The traveling time of the optical waves through a 3.3mm crystal is 24 ps, while the traveling time of the RF signal is simulated as 59 ps. The difference 35 ps, is more than a quarter of a period of the electrical signal (100ps @ 10GHz). This indicates that the optical beam experiences a significant change of electric field along its way.

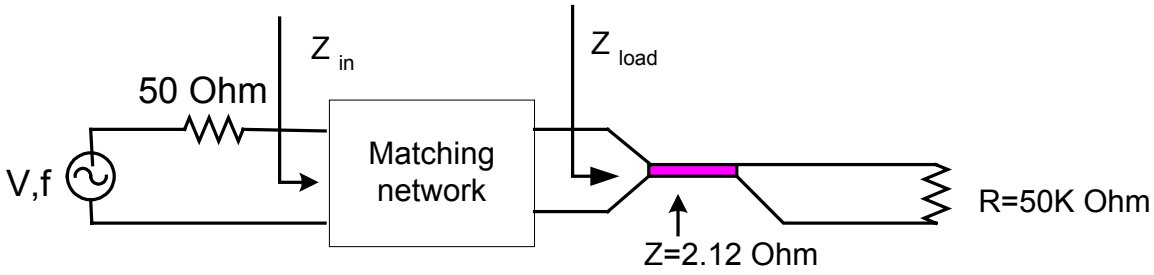

Figure C. 10: Loaded scheme.

C.3 Summary:

This appendix investigated a variety of approaches to drive a prism-based deflector at frequencies above 10 GHz. However, none of them are feasible to deliver a 1 KV, 10 GHz signal to the crystals. The study is consistent with the literature review of prism-based E-O deflectors, among which the fastest E-O deflector operates at 1 GHz while others are far behind. But 1 GHz would fail to show an A-TO-D conversion capability better than electronic ADCs, therefore we did not pursue experimental setup working at lower frequencies.

The general problem encountered by the prism-based E-O deflectors is the high voltage requirement. Moreover high-power microwave sources are hard to access and handle. Efforts have been made to reduce the driving voltage by using integrated prisms. However even for the prisms that are fabricated on a wafer, the space between the electrodes, i.e. the thickness of the prisms, is at least 100 μm. Since the E-O effect is very weak, KV of voltage must be applied to the electrodes to achieve sufficient index modulation and angular deflection. Secondly, the width of the electrodes is usually of the

order of *mm*, leading to a very small impedance at RF frequencies. The severe impedance mismatch makes the input voltage very difficult to be delivered to the prisms.

This study has shown the challenges in implementing a prism-based E-O deflector for high-speed operation. It led to our current effort of designing a novel E-O deflector, which requires much less driving voltage and is capable of working at frequencies of the order of 10 GHz. This is presented as the electro-optical leaky waveguide deflector in Chapter 4 of the thesis.

Appendix D. X-cut LiNbO3 Ti diffused leaky waveguide simulation

D.1 X-cut LiNbO3 Ti diffused leaky waveguide design:

In this design, a strip waveguide is formed by in-diffusion of Ti into a x-cut $LiNbO_3$ substrate. The waveguide region is usually 6 to 9 μm in width. In the simulation, the waveguide region is set as 8 μm. The cross section of the leaky waveguide along with its electrodes is shown in Figure D. 4.

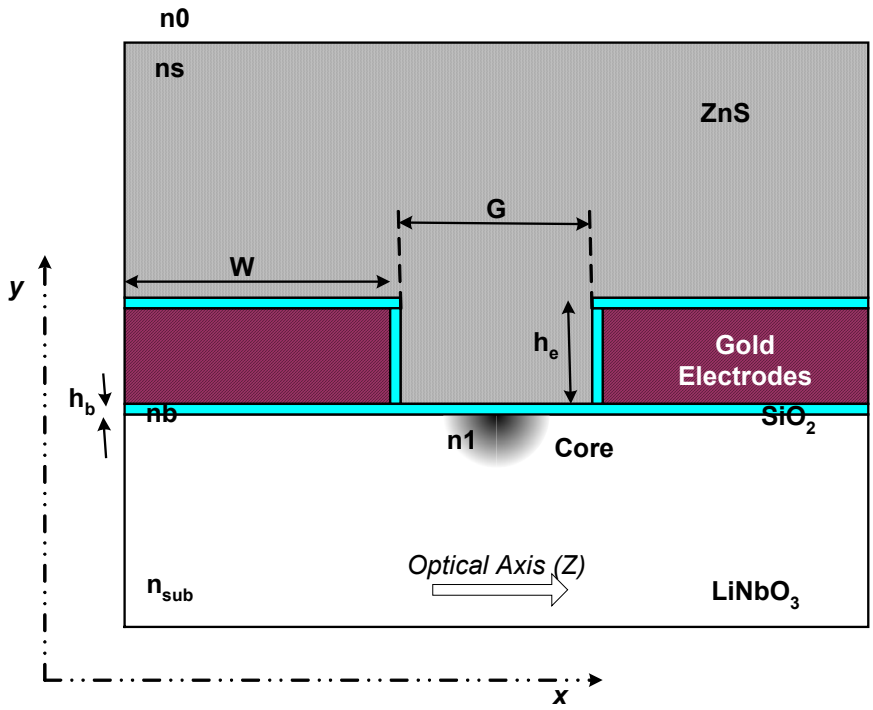

Figure D. 4: Cross section of an X-cut LiNbO3 Ti:diffused leaky waveguide.

The $LiNbO_3$ substrate is placed so that its optical axis, i.e. the z-axis of the crystal, is parallel to the *y*-direction, so when a voltage is applied to the gold electrodes, the electric

field is mainly parallel to the optical axis in order to achieve the maximum index change via the electro-optic coefficient component, γ_{33}, of $LiNbO_3$. The applied electric field changes the extraordinary index of refraction of $LiNbO_3$. To utilize this maximum index change, the E-field of the optical wave should be parallel to the optical axis as well, so the x-dominant mode $E^{(x)}$ should be excited and used in this configuration.

The superstrate is selected to be Zinc Sulphide (ZnS) with refractive index of 2.282; the buffer layer is silicon dioxide (SiO_2), whose refractive index is about 1.5. The thickness of the buffer layer is chosen according to equation (5-21) and simulation so that the field leaky coefficient, α_L, is between 0.1 and 0.3 Np/cm to obtain enough output optical power at minor cost of the angular resolution. The final refractive index profile is drawn in Figure D. 5. The Ti diffused $LiNbO_3$ waveguide has a graded index profile, which is provided by Rsoft according to typical Ti diffusion process. The thickness of the buffer layer is 0.3 μm.

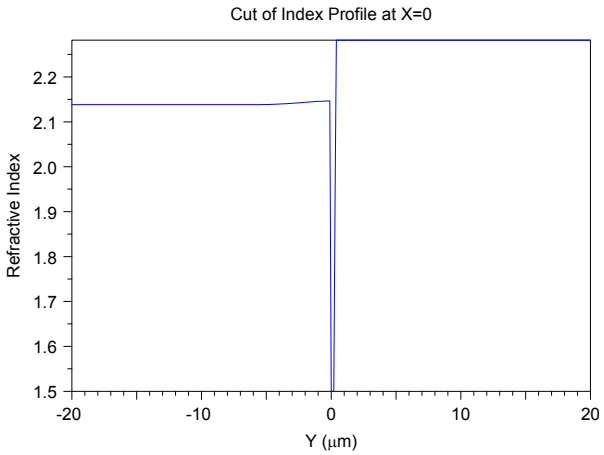

Figure D. 5: Refractive index profile of x-cut Ti: diffused $LiNbO_3$ leaky waveguide.

Figure D. 6 shows the electric field distribution of the waveguide without and with the superstrate. The simulated effective coefficient is n_{eff}=2.138101 when the superstrate is absent. When a superstrate with a refractive index of 2.282 is placed on the top of the waveguide, the mode becomes leaky as shown on the right in Figure D. 6. The effective refractive index of the leaky mode is $n_{eff}=2.137344+j3.612\times10^{-6}$, corresponding to a leaky coefficient of *0.15 Np/cm*. The simulation also shows that the presence of the superstrate introduces just a minor change in the mode effective index, proving that the assumption we made in the theoretical analysis is correct.

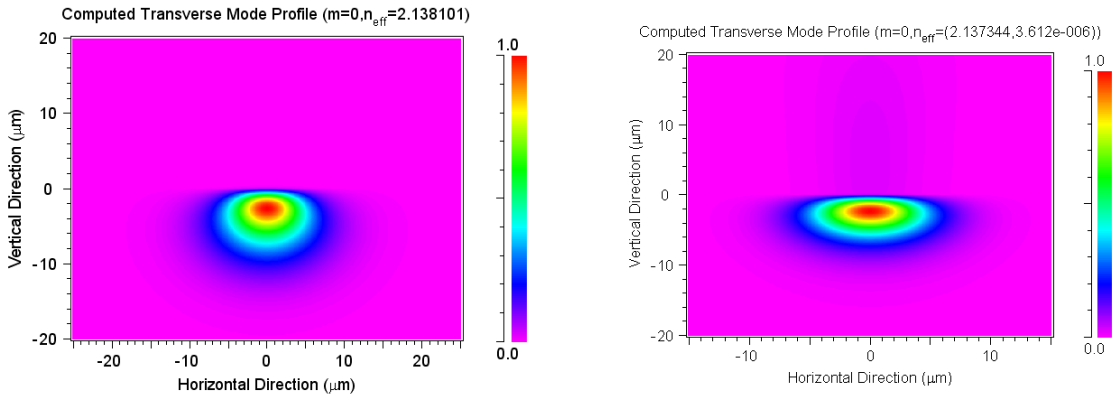

Figure D. 6: Optical field distribution of non-leaky mode (left, without superstrate) and leaky mode (right).

The leaky wave is designed to be very weak. To illustrate the leaky mode clearly, we show the one-dimensional field distribution along the *x*- and *y*-directions crossing the waveguide center in Figure D. 7. The figure shows a clear oscillation in the +*y*-direction, indicating a radiation loss.

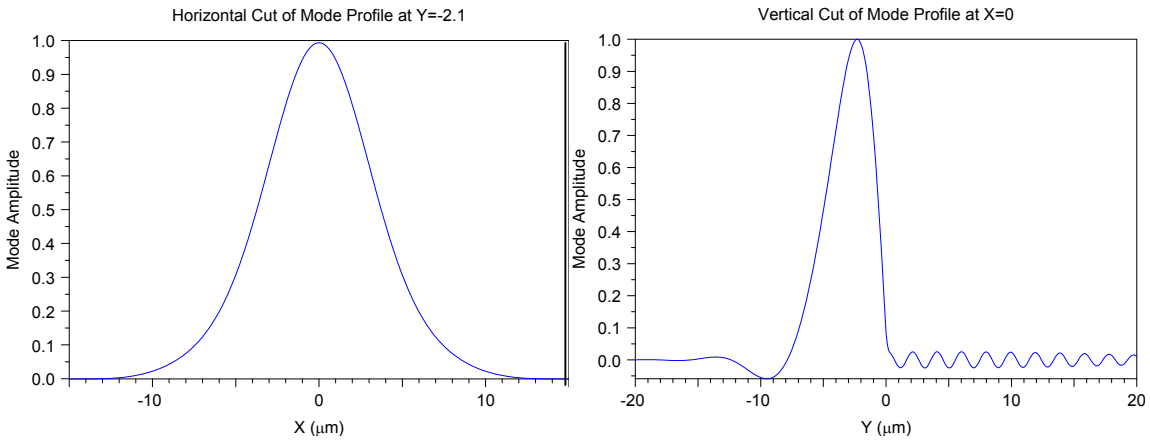

Figure D. 7: The field distribution profile along x- and y- directions.

D.2 Parametric analyses of optical properties:

- Leaky coefficient vs. thickness of the buffer layer

Changing thickness to modify the coefficient is straightforward. The leaky coefficient decreases with the thickness as a rate of $e^{-\tau_2 h_b}$, as shown in Figure D. 8. When the real part of the effective refractive index is 2.137, as simulated, the decay factor, τ_2, is on the order of $4\times10^4\ Np/cm$. Therefore every 1 μm increase in buffer layer thickness results in a 54-time increase in the leaky coefficient.

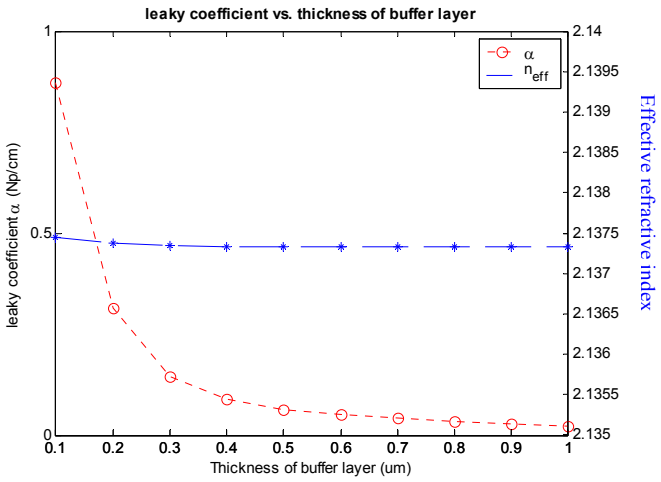

Figure D. 8: Real and imaginary parts of the effective refractive index vs. thickness of the buffer layer.

- Leaky coefficient vs. refractive index of the buffer layer

Figure D. 9 shows the simulated effective refractive index versus index of the buffer layer, when the index increases from 1 to 1.7. It is seen that when the index contrast between the core region and the buffer layer decreases, the leaky coefficient increases, since more optical field extends into the cladding, buffer and the superstrate.

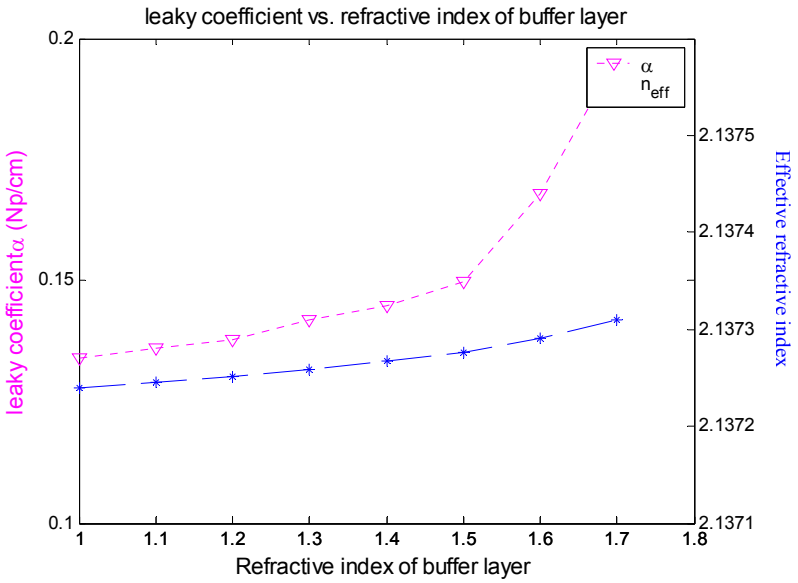

Figure D. 9: Real and imaginary parts of the effective refractive index vs. index of the buffer layer.

- Leaky coefficient vs. superstrate refractive index

Figure D. 10 shows the simulated leaky coefficient vs. the refractive index of the superstrate. The leaky coefficient increases monotonously in the index range of 2.2 to 2.8. It implies that the effect of the increased leaky angle is dominant over the decreased transmittance within this index range. Similar to what has been shown in the polymer leaky waveguide; the change of leaky coefficient is slower and provides flexibility in selecting different superstrate materials.

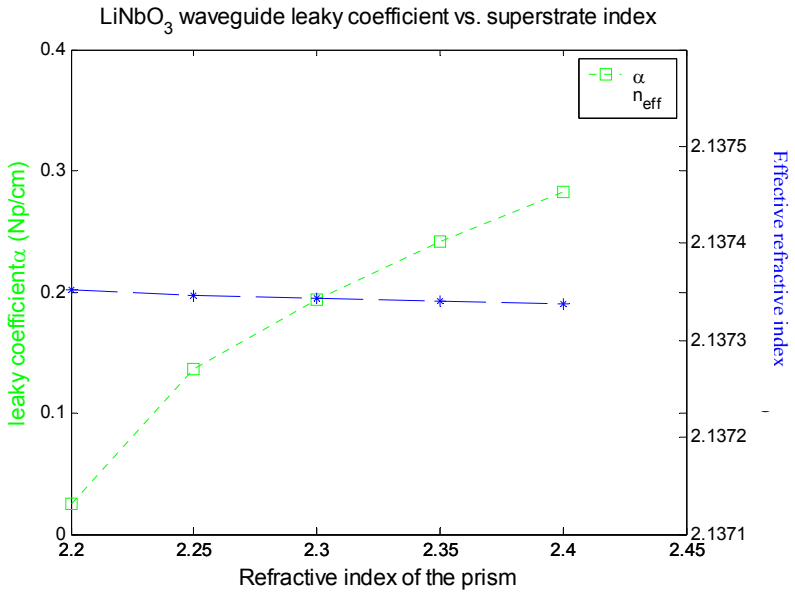

Figure D. 10: Real and imaginary part of the effective refractive index vs. prism index.

D.3 Electric Properties

The x-cut Ti:$LiNbO_3$ leaky waveguide is simple and feasible. However, since the electrodes are surrounded by the high-index materials of $LiNbO_3$ (n=5.38) and ZnS (n=3.16), the effective index at RF frequencies is much higher than the optical refractive index (n=2.137). The severe velocity mismatch prohibits the x-cut Ti:$LiNbO_3$ leaky waveguide from operating at very high frequencies. This section shows the effective index of refraction when the characteristic impedance is 50 Ω. The parameters of the electrodes and the waveguide are listed in the following table.

Table D.1: Parameters of the x-cut Ti:$LiNbO_3$ leaky waveguide.

Layer Name	Material	Thickness	Refractive index (optical)	Permittivity ε_r (RF)
E-O material	$LiNbO_3$	100 μm	2.2	29
Superstrate	ZnS	2 cm	2.282	10
Buffer layer	SiO_2	0.3 μm	1.5	4
Electrode	Gold	8 μm	N/A	

The characteristic impedance is plotted vs. frequency in Figure D. 11. Both amplitude and the real part of the characteristic impedance vary less than 3 Ω around 50 Ω over the frequency range of 2 GHz to 42 GHz. At 20 GHz, the simulated impedance is 50.7 Ω.

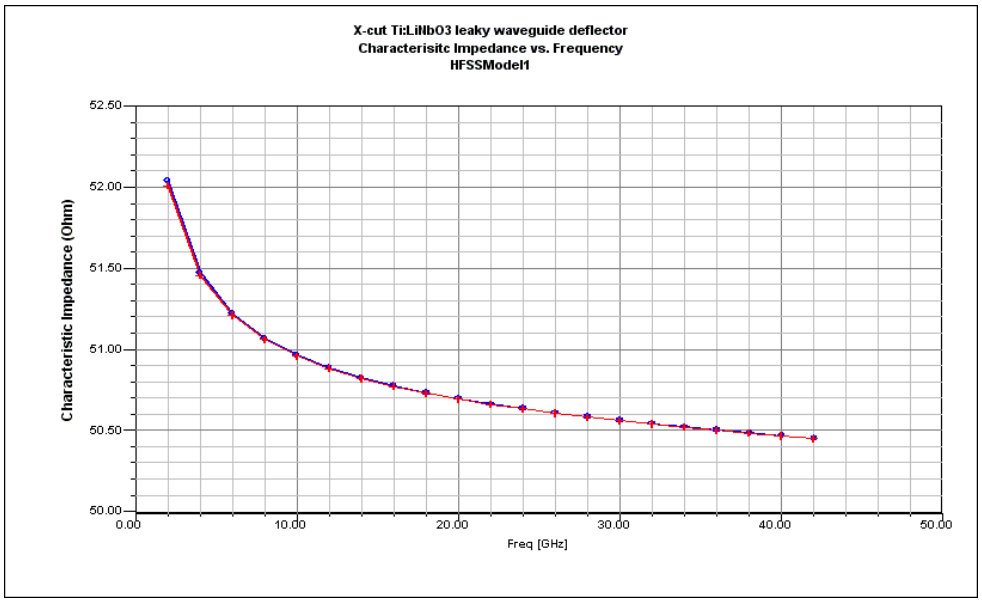

Figure D. 11: Characteristic impedance vs. frequency, simulated when the waveguide is 3 mm in length.

Figure D. 12 plots the effective index of refraction vs. RF frequencies along with its optical index n_o as a reference. It shows that the effective index of refraction at RF frequencies is around 3.5, higher than the optical refractive index by about 1.2. The large

index difference limits the modulation bandwidth to about 3.3 GHz, far from the required 10 GHz of bandwidth. This is the reason why we do not use an x-cut Ti:$LiNbO_3$ leaky waveguide in the thesis.

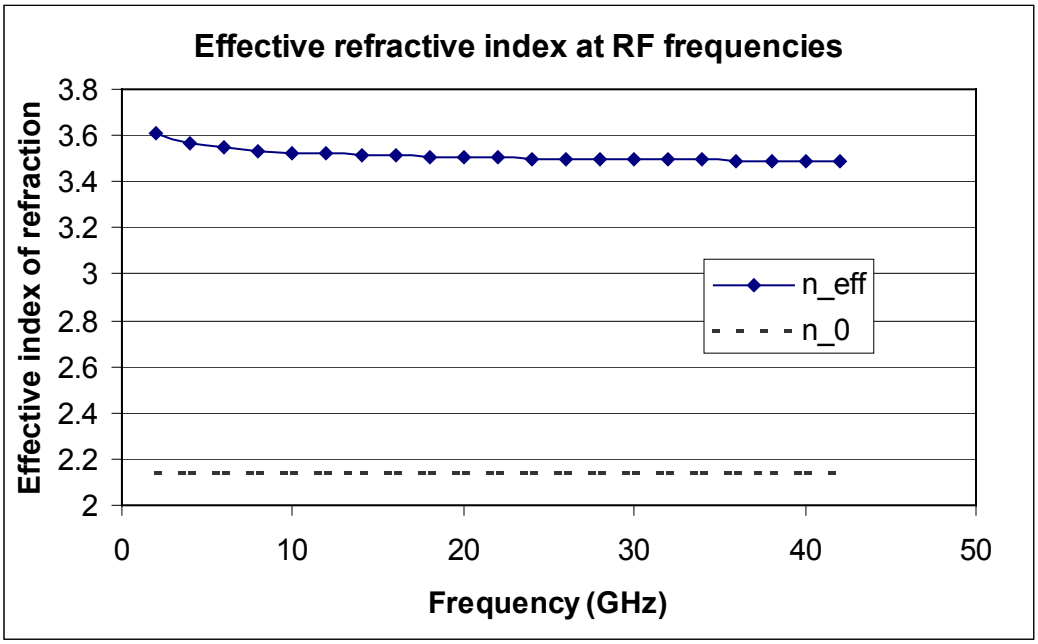

Figure D. 12: Effective index of refractive index vs. frequency, when the waveguide is 3 mm in length.

D.4 Electro-optic properties

The static index change and angular displacement vs. applied voltage were simulated to complete the analysis. The refractive index modulation is plotted in Figure D. 13, showing a linear change in the index vs. the applied voltage. As the applied voltage increases from 0 to 20 V, the real part of the refractive index changes 0.00021, corresponding to 1.05×10^{-5}/V.

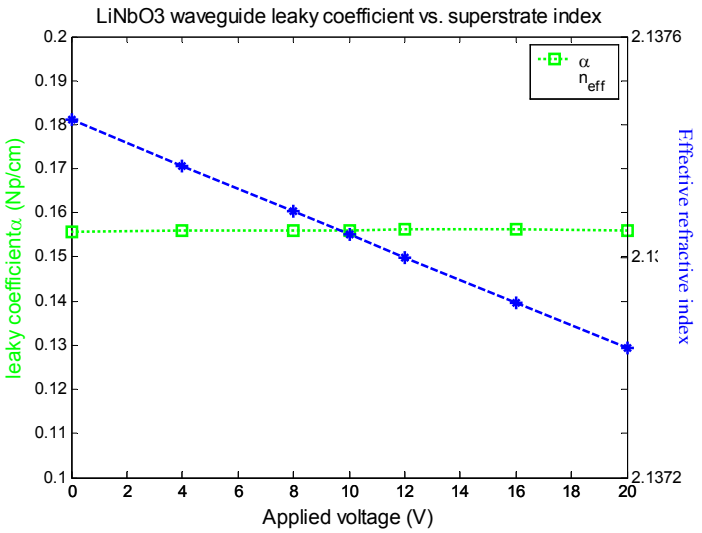

Figure D. 13: The effective index and leaky coefficient vs. applied voltage.

The corresponding angular displacement vs. applied voltage is shown in Figure D. 14. A 20 V signal induces 1.3 *mrad* of change in the deflection angle. Therefore when the RF signal's full-scale is from –20V to +20V, the total angular swing is *2.6 mrad*.

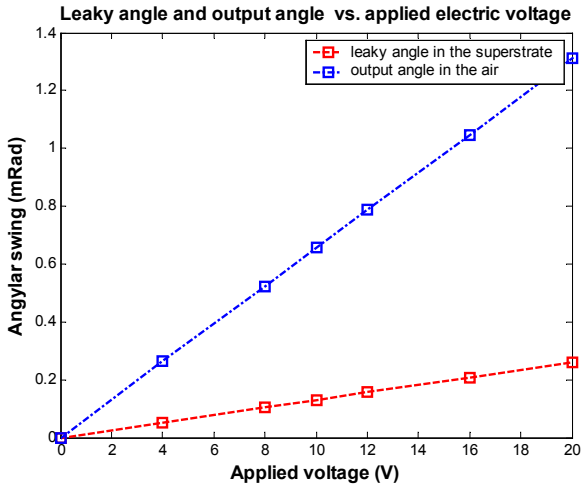

Figure D. 14: Angular displacement vs. applied voltage.

The leaky coefficient is simulated as *0.15 Np/cm* as shown in the beginning of this appendix. Other attenuation during propagation of a typical $LiNbO_3$ waveguide is about 0.2 dB/cm, corresponding to *0.023 Np/cm*, which is negligible compared to the loss coefficient due to the leaky waves. As the optical wave propagates along the waveguide at the attenuation of *0.15 Np/cm*, *60%* of the total launched power leaks out of the waveguide after propagating 3 cm. Similar to the z-cut $LiNbO_3$ waveguide, the calculated angular resolution is *0.115 mrad*, so the total number of resolvable image lines is 22. In principle, it is sufficient to implement a 5-bit AOADC using binary code or 6-bit using Gray code. However its RF bandwidth is only about 3 GHz.

D.5 Summary

An x-cut Ti:$LiNbO_3$ E-O leaky waveguide was designed and simulated. The severe velocity mismatch of the RF signal and the optical wave prevents this scheme from implementing a high frequency E-O deflector. It was the study of x-cut Ti:$LiNbO_3$ leaky waveguide that led to the novel design of the z-cut Ti:$LiNbO_3$ leaky waveguide deflector, as shown in Chapter 4 and 5.

VITA

Xiaobo Hou was born in Guilin, China, on April 8, 1974. Ms. Hou graduated with a bachelor degree in electrical engineering and a Mater degree majoring electrophysics and optoelectronics from Tsinghua University, Beijing, China, in 1997 and 2000, respectively. Her master thesis, "Magnetron sputtering of SiO_2 in ITO transparent conductive glass", has won a number awards including Award of Technology Advancement of Beijing 2004. After receiving her Master's degree, Ms. Hou started her Ph.D. program in Drexel University in September 2000. She was involved in many research activities including electrooptical device and high-speed electronic IC design. She has designed and developed a 10 Gbps serializer/deserializer (serdes) and a 2.5 Gbps phase and frequency detector. Her work on all-optical analog-to-digital converter won the second prize in IEEE Sarnoff symposium 2003 student paper contest, NJ. Ms Hou also won the Allen Rothwarf Outstanding Graduate Student Award from Drexel University in 2004.